Characterization of cell uptake and intracellular trafficking of exosomes by quantitative live cell imaging: towards biomimetic delivery vehicles of therapeutic RNA

Inauguraldissertation
zur
Erlangung der Würde eines Doktors der Philosophie
vorgelegt der
Philosophisch-Naturwissenschaftlichen Fakultät
der Universität Basel
von

Wolf Heusermann

aus
Deutschland

Basel 2017

Genehmigt von der Philosophisch-Naturwissenschaftlichen Fakultät
auf Antrag von

Nancy Hynes, Nicole Meisner-Kober, Matthew Wood

Basel, den 15.09.2015

Prof. Dr. Jörg Schibler
Dekan

The experimental part of this thesis was carried out in the laboratory of Dr. Nicole Meisner-Kober at the Novartis Institutes for Biomedical Research, under supervision of Dr. Nicole Meisner-Kober, and Prof. Dr. Nancy Hynes of the Friedrich Miescher Institute of Biomedical Research.

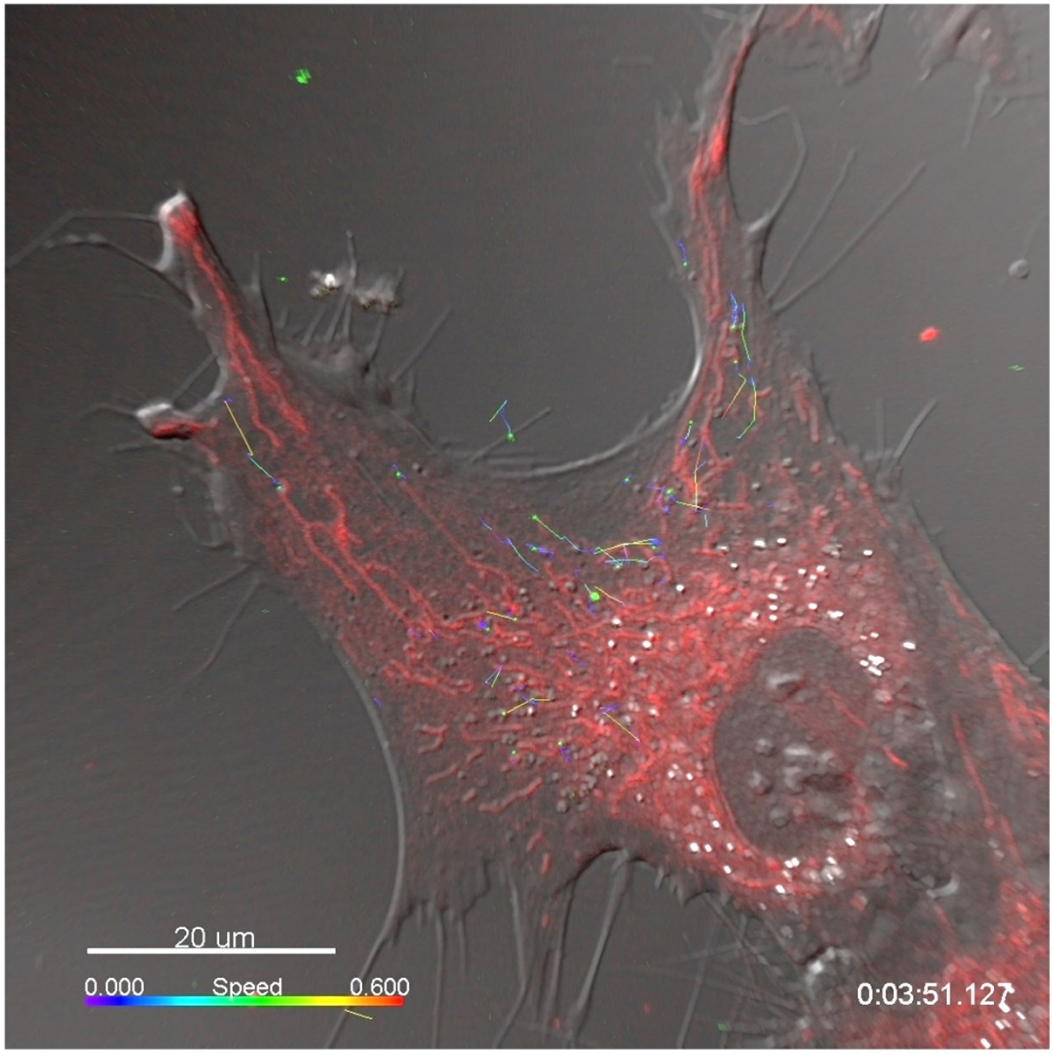

Fluorescence and DIC live cell microscopy: Exosome tracks and ER-labeling in Huh7 cell

ISBN
Printed in Switzerland by
Basel 2017
Distributor: Basel University

Summary

Exosomes are biological nanoparticles which play a role in long distance cell-to-cell communication. These 40-100 nm sized vesicles are released by virtually all cells and derive from the multivesicular bodies within their parent cells. They modulate their target cell fate by induction of cell signaling as well as RNA and protein cargo transfer. Exosomes have also moved into the spotlight of clinical research, with potential use as biomarkers or next generation therapeutic delivery agents.

Exosomes are thought to be highly efficient intercellular messengers but quantitative characterization is lacking. Also, their routes of cell uptake and subcellular fate within recipient cells remain elusive. This work introduces an in depth and quantitative characterization of exosome cargo, physicochemical properties, labeling, isolation and their recipient cell interaction at the single cell – single vesicle level.

Basic protocols for exosome purification were revisited in order to allow for isolation of exosomes with sufficient yields and in as native state as possible to enable functional studies. Since exosome integrity and recovery yields after differential ultracentrifugation (UC), the most commonly used protocol for exosome isolation, turned out to be poor and unreproducible, we describe an alternative protocol based on ultrafiltration (UF) with subsequent gel filtration (GF) for recovering exosomes relatively selectively, with intact biophysical and functional properties and significantly higher yields.

Next we establish methods for specific exosome labeling using fluorescent marker proteins transiently expressed in parent cells, which led to a focus on FP tagged CD63 constructs. CD63-emGFP labeled exosomes were extensively characterized and showed identical properties compared to unlabeled exosomes based on sucrose density gradient, CryoTEM microscopy and proteomics analysis.

Furthermore, we successfully adapted fluctuation correlation spectroscopy for characterization of fluorescently labeled exosomes.

In another part of this work we describe a high content screen for exosome uptake which we use to provide a first systematic and quantitative profiling of exosome uptake across a panel of exosome parent recipient cells, including HEK293, Huh7, B16F10 as parental cells and additional primary fibroblasts, primary keratinocytes, iPS derived motor neurons and HUVEC primary human endothelial cells as recipient cell lines. These quantitative profiling data reveals preferences in exosome internalization by different cell types and suggests that specific receptor ligand interactions may determine tissue specificity.

Finally, we address one of the fundamental questions in the field of cellular communication: how exosomes released by one cell enter and interact with their recipient cell. Our data quantifies for the first time the cell uptake dynamics of exosomes at the single vesicle and single cell level and reveals a quantitative efficiency paralleling that of infective pathogens rather than artificial delivery vehicles. We demonstrate that exosome uptake is largely mediated by active recruitment and surfing on filopodia to reach endocytic hotspots for their internalization at the filopodia base. This provides a cell biological explanation for the remarkably high efficiency of exosomes in targeting recipient cells and discovers a new parallel to some viruses and other pathogens. We propose that the process of filopodia surfing may have evolved as a highway for exosomes into the cell, being hijacked by certain pathogens for host cell interaction. This data does not support the previously reported exosome uptake by vesicle fusion with the plasma membrane or cargo release by endosomal escape. Instead we observe intact exosome uptake to enter endocytic vesicles, which then scan along the endoplasmic reticulum (ER) and end up in lysosomes. Our data suggest a model of controlled cargo delivery to defined subcellular localizations like the ER, rather than vesicle fusion and free release into the cytoplasm.

Paper and Manuscripts which are included in this thesis

Paper I. *Ultrafiltration with size-exclusion liquid chromatography for high yield isolation of extracellular vesicles preserving intact biophysical and functional properties* (Nordin J, Lee Y, Vader P, Mäger I, Johansson H, **Heusermann W**, Wiklander O, Hällbrink M, Seow Y, Bultema J, Gilthorpe J, Davies T, Fairchild P, Gabrielsson S, Meisner-Kober NC, Lehtiö J, Smith E, Wood MJA, EL Andaloussi S) Nanomedicine *11*, 879–883 (2015).

Manuscript I. *Quantitative profiling of exosome parent-recipient cell pairing by high content screening using CD63-emGFP vesicle labeling.* (**Heusermann W**, Hean J, Trojer D, von Bueren S, Graff-Meyer A, Genoud C, Steib E, Voshol H, EL Andaloussi S, Wood MJ, Meisner-Kober NC) manuscript submitted.

Manuscript II. *Exosomes surf on filopodia to enter cells at endocytic hot spots, and shuttle with endosomes to scan the endoplasmic reticulum – a highway to the cell.* (**Heusermann W**, Hean J, Trojer D, von Bueren S, Graff-Meyer A, Genoud C, Martin K, Voshol H, Morrissey DV, EL Andaloussi S, Wood MJ, Meisner-Kober NC), manuscript submitted.

Manuscript III. Note: The introduction of this thesis was compiled into a book chapter (editor: Wood MJA, publisher Wiley)

Further papers and manuscripts in the appendix

Paper II. *The rough endoplasmatic reticulum is a central nucleation site of siRNA-mediated RNA silencing* (Stalder L, **Heusermann W**, Sokol L, Trojer D, Wirz J, Hean J, Fritzsche A, Aeschimann F, Pfanzagl V, Basselet P, Weiler J, Hintersteiner M, Morrissey DV and Meisner-Kober NC). The EMBO Journal 2013.

Manuscript IV. *An easily accessible wide field based fluorescence imaging platform for ultrafast screening of one-bead one-compound libraries using a novel image subtraction approach*. (**Heusermann W**, Ludin B, Weidemann T, Meisner-Kober NC, Pham N, Auer M and Hintersteiner M), manuscript in preparation

Papers and manuscripts which are not included in this thesis

Manuscript V. *Elucidation of exosome subpopulations: a lysosome derived species of extracellular microvesicles* (**Heusermann W**, Hean J, Beketova E, Nyfeler B, Trojer D, von Bueren S, Graff A, Genoud C, Meisner-Kober NC) manuscript in preparation.

Paper III. *Biophysical properties of chitosan/siRNA polyplexes: profiling the polymer/siRNA interactions and bioactivity* (Holzerny P, Ajdini B, **Heusermann W**, Bruno K, Schuleit M, Meinel L, Keller M), J Control Release 2012

Table of contents

List of tables

List of figures

Abbreviations

Abbreviation	Description
Aa	Amino acid
Ago2	Argonaute2 (removed ago2)
Amp	Ampicillin
BBB	Blood brain barrier removed BBB
CD	Cluster of differentiation
CFSE	Carboxyfluorescein succinimidyl ester removed from text
DC	Dendritic cell
DiD	1,1’-dioctadecyl-3,3,3',3'-tetramethylindodicarbocyanine perchlorate
DiI	1,1’-dioctadecyl-3,3,3',3'-tetramethylindocarbocyanine perchlorate
DiO	3,3’-dioctadecyloxacarbocyanine perchlorate
EBV	Epstein Barr virus
eCFP	Enhanced Cyan Fluorescent Protein
eGFP	Enhanced Green Fluorescent Protein
ERK1/2	Extracellular signal-related kinase 1/2
eYFP	Enhanced Yellow Fluorescent Protein
FACS	Fluorescence-activated cell sorting
Fc	Fragment, crystallisable
FCCS	Fluorescence Cross Correlation Spectroscopy
FCS	Fluorescence Correlation Spectroscopy
FIDA	Fluorescence Intensity Distribution Analysis
FLIM	Fluorescence Lifetime Imaging Microscopy
FM4-64	N-(3-Triethylammoniumpropyl)-4-(6-(4-(Diethylamino) Phenyl)Hexatrienyl) Pyridinium Dibromide
FP	Fluorescent protein
GFP	Green fluorescent protein
GM3	Monosialodihexosylganglioside
GW4869	N,N'-Bis[4-(4,5-dihydro-1H-imidazol-2-yl)phenyl]-3,3'-p-phenylene-bis-acrylamide dihydrochloride
HEK	Cell line derived from Human Embryonic Kidney
HIV-TAT	Human immunodeficiency virus trans-activator of transcription
Hsp27	Heat shock protein 27
HSPG	Heparan sulphate proteoglycan receptor
LFA-1	Lymphocyte function-associated antigen 1
mAbs	Monoclonal antibody
MFG-E8	Milk fat globule protein E8
MHCII	Major histocompatability complex II
miRNA	microRNA
PAGE	Polyacrylamid gel electrophoresis
PBS	Phosphate Buffered Solution
PCR	Polymerase Chain Reaction
p-Hsp27	Phosphorylated Hsp27

Abbreviation	Description
PI3kinase	Phosphatidylinositol-4,5-bisphosphate 3-kinase
PKH-x	Paul Karl Horan (dye inventor)
PS	Phosphatidyl serine
R18	Octadecyl Rhodamine B Chloride
Rab27a	Ras-related protein 27a
siRNA	Short interfering RNA
SV40	Simian vacuolating virus 40
TAMRA	N, N-, N', N'- Carboxy-tetramethylrhodamine
TFSM	TopFluor-Sphingomyelin
Timx	T-cell immunoglobulin- and mucin-domain-containing molecule
U0126	1,4-diamino-2,3-dicyano-1,4-bis(2-aminophenylthio)butadiene

1 Introduction

1.1 Exosomes

1.1.1 Background

Exosomes were initially discovered in the early 1980s [1,2], when they were primarily assigned a role in cellular waste disposal. This appeared plausible due to their intracellular origin from the endo/lysosomal system where they arise by inward budding of the endosomal membrane, giving rise to so called into the Multivesicular bodies (MVB). Upon fusion of the MVB with the plasma membrane, exosomes are released into the extracellular space. Their secretion thus inherently results in depletion of intracellular components. Waste removal by exosomes in response to changing environmental conditions has been repeatedly demonstrated over three decades, such as in studies on the elimination of transferrin receptors during reticulocyte maturation [1], excretion of materials into urine during nephric clearance [3] or the balancing of cholesterol levels [4].

The view that trash disposal is the primary function of exosomes changed dramatically when a study by Raposo and co-workers showed that exosomes from B-cells stimulate T-cell proliferation via recognition of MHCII receptors on the exosome surface [5], which suggested a specific function in cell-to-cell signalling. This discovery was followed by an avalanche of studies demonstrating further examples of exosomal signalling in various physiological processes including the inflammatory response [6–8], immune tolerance [9–11], anti-tumor immune response [12,13], chemotaxis [14,15], intercellular signaling within the tumor microenvironment [16], non-synaptic communication in the nervous system [16,17], and in retroviral as well as prion pathology [18,19].

The complex composition of cell recognition molecules presented on the exosome surface, including tetraspanins, MHC Class I and/or Class II antigens, integrins and other cell-adhesion molecules, already indicates a propensity for delivery to and uptake into recipient cells in a very specific manner. In addition the physiochemical properties of exosomes like their small size and fluidity allow them to reach virtually all types of tissue and even (be engineered to) penetrate tight barriers such as the blood brain barrier [20,21].

Today it is widely recognized that exosomes play an important role in cell-to-cell and tissue-to-tissue signaling. This has recently called for new terminology, introducing ‘microvesicular signaling’ for this specific form of intercellular communication, alongside with the well-established forms of autocrine, paracrine, endocrine, and juxtacrine signaling [22–24].

Since the initial findings of Raposo and co-workers, it has been demonstrated that microvesicle- and exosome-signaling goes beyond the initially revealed interaction between cell- and vesicle-surface antigens: exosomes can also transfer their cargo to recipient cells to exert a function within the host cell – almost in analogy to viruses. A breakthrough discovery was published in 2006 [25] when exosomes from embryonic stem cells were demonstrated to shuttle messenger RNA into haematopoietic progenitor cells and undergo translation to produce the encoded proteins. Shortly after, Valadi and coworkers demonstrated functional exosome-based transfer of mRNA between mouse and human mast cells [26]. It has become a widespread notion that exosomes do indeed shuttle functional cargo of virtually every class of biological macromolecules: cholesterol [4], protein [27–29], retrotransposon DNA elements [30], messenger RNA [26,27], microRNA [26,31–41] as well as exogenously introduced siRNA [21,42–44]. Also, there are increasing data suggesting that the repertoire of exosome cargo is under dynamic control and thereby directly depends on parent cell type and state.

Apart from their increasingly apparent role in the homeostasis of a living organism and physiological cell-cell communication, exosomes have also been implicated in pathological cell communication. As a potential collateral damage of their cell-to-cell communication capabilities, exosomes were found to contribute to spreading of toxic proteins in neurodegenerative proteinopathies (reviewed in [45]), including alpha synuclein in Parkinson's disease [21,46,47] or tau in Alzheimer's disease [48]. Furthermore, a growing body of work has suggested a central role of exosomes secreted by solid tumors in cancer progression, such as by priming pre-metastatic niches [49–53]. Even various parasite exosome interactions have been reported (reviewed in [54]). Studies reveal cell-autonomous defense programs to monitor subcellular compartments for infection and to evoke counter-responses which are connected to extracellular vesicle release through lysosome exocytosis to clear recalcitrant pathogens. [55].

1.1.2 Exosome Isolation and Differentiation/ Biogenesis

Basically all body fluids as well as *in vitro* cell culture supernatants contain a variety of Extracellular Vesicles (EV), which are classified into three types based on their biogenesis. **Ectosomes** are shedded from the plasma membrane; **Exosomes** arise from intracellular MVBs. **Apoptotic bodies** are vesicles heterogeneous in size and content which are released during the process of programmed cell death. All classes of EV are double lipid membrane enclosed vesicles and have similar or at least partially overlapping physicochemical properties. The isolation of exosomes on the complex background of other

extracellular particles is thus still a major challenge in the field. For many years, the gold standard protocol for isolation of exosomes was based on their sedimentation properties during differential ultracentrifugation [56] which however is increasingly recognized to co-purify a number of other extracellular particles [57]. To address this, typical protocols in the literature later started to include either additional ultracentrifugation steps or a sucrose gradient fractionation which retrieves exosomes relatively selectively at a typical sedimentation density of 1.14-1.17 g/ml sucrose[56]. A different approach is based on polymer mediated precipitation which is now commercialized by different manufacturers. Finally, also affinity based purification using antibody capture through extravesicular marker proteins are now being increasingly implemented [58]. All methods have their limitations either in the purity, the yield, the integrity or the irreversible binding to beads which may enable analytical characterization, but is incompatible with the requirements for functional studies. There is still a lack of data on the potential bias that different isolation procedures may introduce, in particular since we haven't been able to study exosomes in their native state upon release from their parent cells without any enrichment or purification steps. The first part of this work aims to address the issue of isolating exosomes in high purity, sufficient quantities for functional studies and retained integrity. This resulted in a new exosome isolation protocol which we thoroughly characterized and benchmarked against standard methods, as published in a joint effort with the labs of Dr. Wood (Oxford University) and Dr. El Andaloussi (Karolinska Institute) and included in the results of this thesis (Paper I, *Nordin J et al, Nanomedicine 2015*).

1.1.3 Exosome Characterization and Quantification

A large variety of cell lines and tissues release microvesicles, and associated with these is an equally large diversity in reported and anticipated functions, behavior, markers and content of exosomes. This complicates the transition of this young and dynamic field into one of uniform definitions. In 2011 the international Society for Extracellular Vesicles (ISEV) was founded as a communication platform. Databases like ExoCarta [59], EVpedia [60] or Vesiclepedia [61] were installed to facilitate the exponentially growing interest and research in this exciting field, and align the relevant conventions. ExoCarta provides a resource for the most commonly used markers for exosome identification. These comprise chaperone proteins such as HSPA8 or HSP90, proteins of the ESCRT complex such as Alix and TSG101, proteins involved in transport and fusion like Annexins (ANXA2) or Rabs (Rab11, Rab7, Rab2), and tetrapanins like CD63, CD9 and CD81.

Gene Symbol	Number of times identified		Gene Symbol	Number of times identified
CD9	98		LDHA	72
ALIX	96		EEF1A1	71
HSPA8	96		YWHAZ	69
GAPDH	95		PGK1	69
ACTB	93		EEF2	69
ANXA2	83		ALDOA	69
CD63	82		HSP90AB1	67
SDCBP	78		ANXA5	67
ENO1	78		FASN	66
HSP90AA1	77		YWHAE	65
TSG101	76		CLTC	64
PKM	72		CD81	64

Table 1) List of top 24 proteins that are often identified in exosomes *(ExoCarta status March 2015)*

Beside such relatively ubiquitous and generally highly abundant exosome markers, more than 170`000 molecules were identified in exosome samples as a result from ca 260 high throughput data sets and 6800 publications including exosome profiling data to date (*EVpedia*- status March 2015).

High-throughput studies	High-throughput datasets	Molecules	Publications	Principal investigators
168	263	172,080	6,879	3,336

Table 2) Publication statistics for exosome content related high-throughput studies

Due to the heterogeneity and low concentrations on one side but also the overlapping characteristics of different EV populations on the other side there is a need to fill the gap between the molecular and micrometer scale characterization, which is driving the development of more sophisticated technologies. Tunable resistive pulse sensing (TRPS) based on a tunable elastomeric pore sensor, size adapted flow cytometry and nanoparticle tracking analyses (NTA) based on single particle light scattering are more recent developments to address the needs of exosome research. However, the most

commonly used methods for exosome characterization still largely encompass transmission electron microscopy for size and shape determination, the detection of exosome marker proteins by western blotting, as well as density characterization by sucrose gradient fractionation. In consequence there is still a general lack of quantitative characterization in exosome biology. A quantification of exosomes based on total protein content is entirely non-representative and reproducible due to the highly variable co-purification of proteins and other vesicles, and gives no information about numbers of vesicles.
In this work, we have addressed this issue and provide the first quantitative characterization of exosomes and their interaction with recipient cells at the single vesicle level, which is part of the publication I (*Ultrafiltration with size-exclusion liquid chromatography for high yield isolation of extracellular vesicles preserving intact biophysical and functional properties*) and the manuscripts I (*Quantitative profiling of exosome parent-recipient cell pairing by high content screening using CD63-emGFP vesicle labeling.*) and manuscript II (*Exosomes surf on filopodia to enter cells at endocytic hot spots, and shuttle with endosomes to scan the endoplasmic reticulum – a highway to the cell.*) included in the results part of this thesis.

Finally, the field has suffered from a lack of reagents to modulate exosome production or release from parent cells which might provide more stringent and functional controls. Recently emerging strategies such as sphingomyelinase expression modulation or pharmacological inhibition through GW4869 [33], or Rab27a expression modulation [62] will thus become of increasing relevance for future studies. On this background we need to be aware of a critical perspective with respect to current understanding of heterogeneity of microvesicle preparations, analytics, controls and the validity of an assignment of activities to exosomes versus potential other extracellular microvesicles or particles.

1.2 Horizontal transfer and functional delivery of RNA into recipient cells by exosomes

Following the initial discovery that mRNA can get shuttled by exosomes and is translated within recipient cells [25,26], Valadi and coworkers also revealed the presence of miRNAs within exosomes - a discovery which led to an eventual explosion of the field. However, a function of exosomal miRNA within recipient cells still remained elusive for a few years. A subsequent report that certain miRNAs are enriched in exosomes [27] and that the miRNA profile differs between

cell types suggested an active sorting mechanism. This finding still supported the two theories, a means to dispose of "unwanted" miRNAs or a functional relevance of the small RNA cargo within recipient cells. In 2010, three groups independently reported that intercellular transfer of miRNAs contained in exosomes results in silencing of target gene expression in the recipient cells [31,33,37]. Zhang et al [37] presented that THP-1-derived microvesicles delivered miR-150 into human HMEC-1 endothelial cells, resulting in elevated exogenous miR-150 levels in recipient cells concomitant with knockdown of c-Myb expression and enhanced cell migration – established downstream effects of miR-150. Pegtel and colleagues demonstrated that Epstein-Barr-Virus (EBV) encoded mature miRNAs were secreted via exosomes by infected B-cells; In co-cultures with infected B-cells the authors demonstrated silenced expression of EBV host cell target genes as well as viral miRNA luciferase reporters in non-infected MoDC recipient cells [31]. As this study monitored miRNA function in recipient cells upon exposure to full conditioned medium using a co-cultivation of parent and recipient cells, the assignment of the miRNA delivery to exosomes, albeit plausible, was however still indirect. More direct evidence was finally presented in an independent study by Kosaka and coworkers in which miR-146b was loaded into exosomes by transient overexpression of a pri-miR146b expression construct in COS7 parent cells. Exosomes purified by ultracentrifugation from conditioned medium then resulted in silencing of a miR-146b luciferase reporter but not a seed mutated control reporter in HEK293T recipient cells. The same study revealed that exosome release is dependent on nSMNase activity, and used nSMNase knockdown as control for assigning the functional reporter gene silencing to exosomes [33 63].

An intriguing advantage of exosomes is the ability to transfer packages of macromolecular cargo in a targeted manner across physical distances. However there are also reports for an involvement of exosomes in trans-synaptic transfer of cargo, including miRNAs, in the immune system [36,64], and potentially also the central nervous system (CNS) [65,66]. In immune synapse formation, transfer of miRNAs from the T cell to the antigen presenting cell by CD63 positive exosomes has been reported to occur in an antigen dependent and unidirectional manner, resulting in silencing of a miRNA luciferase reporter gene in the recipient cells [36]. Although there has still been no direct evidence for exosomal transfer of miRNAs and other functional cargo across synapses in the CNS, it is intriguing to speculate that this is happening since exosomes, released by neurons depending on synaptic activity, were found to be recaptured by other neurons [17]. These vesicles might be an excellent means for anterograde and retrograde information transfer between synaptically coupled neurons.

A new facet of high relevance for any functional studies of exosomal miRNA came from a study by Arroyo et al, which revealed that circulating miRNAs are not restricted to vesicles [67]. Instead, more than 80 % of miRNA detected in plasma and

serum was found to be associated with non-vesicular, protease sensitive Ago2 containing complexes. Interestingly, profiling data showed that certain miRNAs were exclusively associated with either the vesicles or the non-vesicular complexes, whereas some miRNAs were found in both. The authors speculate that vesicle-associated versus Ago2-complex-associated miRNAs in the circulation might originate from different cell types specialized for distinct release mechanisms.

1.3 Engineered exosomes as nucleic acid delivery bio-vehicles

The parent cell fingerprint of exosome cargoes and receptors and their tissue homing capability has not only opened an entirely new avenue in the diagnostics and biomarker field [27] but has also leveraged great interest in miRNA and RNA therapeutics research [44]. Due to their natural function in transferring macromolecular cargo across cells there is increasing interest in translating exosome biology towards next generation drug delivery vehicles [68 69] . The current gold standard for therapeutic siRNA delivery is largely based on liposomal vehicles. These synthetic nanovesicles share a number of physicochemical features in common with exosomes, such as encapsulation of the RNA cargo by a lipid bilayer, similarity in size, shape and content of certain lipids such as cholesterol and neutral lipids. Despite the extensive and growing knowledge base on the structure-activity-relationship (SAR) of liposomal siRNA formulations, the elucidation of mechanisms and routes for the most efficient functional cell uptake and subcellular distribution of liposome delivered cargo is still a holy grail in nucleic acid therapeutics development. Exosomes therefore appear as a highly attractive role model to guide the development of next generation, biomimetic delivery vehicles.
Intrigued by the idea of using exosomes themselves as biological delivery vehicles for siRNA and other nucleic acid therapeutics whilst avoiding immunogenicity [69]. Wood and coworkers have pioneered a strategy for loading exosomes from mouse DCs with siRNA *in vitro* and allografting them to animals from the same species. In addition, tissue directed delivery was achieved by introducing targeting peptides on the surface of these exosomes as fusions with surface markers transiently expressed in the parent cells. This successfully allowed to obtain systemic delivery of siRNA into specific tissue or even across the BBB and knockdown of targets in the brain [70] .

The therapeutic potential of exosomes has been further underlined by reports of successful delivery of exosome encapsulated anti-inflammatory drugs to the brain

by intranasal administration in mouse models of LPS-induced inflammation [20], or tumor targeted delivery of chemotherapeutics loaded into exosomes in breast cancer models [71]. It has been proposed that in mesenchymal stem cells, transfected synthetic miR-143 gets repackaged into exosomes which then mediate functional transfer of the synthetic miRNA into osteosarcoma cells in in vitro models [72]. This suggests that potential secondary spreading through exosomes might be exploited to deliver therapeutic siRNA indirectly to tissues and organs that are hard to target directly by current synthetic formulations, making use of repackaging into exosomes with preferred homing propensities from one to another tissue. However it has also been described that microvesicles originating from mesenchymal stem cells induce apoptosis and necrosis of certain immortalized cell lines in vitro and in vivo [73], suggesting that the observed outcomes of repackaged miR-143 within exosomes may be a consequence of cellular toxicity. Furthermore, it is not established yet whether transfection reagents have an impact on exosome biogenesis, which may influence their contents and cellular interaction, or even contaminate exosome samples isolated from the transfected cells. Therefore, to corroborate this idea, further studies on repackaging and secondary spreading of artificially delivered siRNA or miRNA through exosomes remain to be done, in particular also with careful controls for the impact of lipid transfection reagents on recovered exosomes.

Prior to the translation of these revolutionizing basic discoveries into a therapeutic application however, there are still a number of hurdles to be taken, including a thorough assessment of safety profiles as well as viable strategies for exosome manufacturing. Also the loading process of therapeutic cargo into exosomes without compromising their integrity and function requires further research [74,75]. The availability of exosome based drugs on the market therefore appears as an exciting but rather long term vision. However, in the short term an in depth understanding on their mechanism in tissue targeting and cell uptake may be of high impact for the tailoring of improved synthetic liposomal delivery vehicles [69], potentially allowing for reverse engineering of vesicular cell entry strategies employed by nature.

1.4 Strategies for monitoring exosome uptake

While the body of literature on functional delivery of exosomes and their cargo has become extensive, we are still only at the very beginning of unravelling structural features or surface markers of exosomes that determine their tissue targeting, the underlying cell uptake pathways as well as the subcellular fate of the vesicles and their cargo within the recipient cell. Certain questions such as the study of exosome uptake receptors and pathways may already be answered by quantitative endpoint measurements of exosome uptake in fixed cells. This bears the advantage to non-invasively stain exosomes within the target cells post-fixation, provided that a differential marker or cargo is available that is not expressed within the recipient cell. This strategy was used in exosome uptake studies using methods of varying levels of resolution, ranging from FACS [76,77], fluorescence microscopy and high resolution microscopy, to electron microscopy [78,79].

The method of choice to monitor exosome uptake *dynamics* is by fluorescence microscopy in live cells. A prerequisite for this approach is to trace the vesicles already prior to its interaction with recipient cells with fluorescent lipid stains, surface markers or cargo. While fluorescent labelling of microvesicles via fluorescent polymer beads has been well established for quantitative analysis of exosomes by flow cytometry [76,80] the labelling of exosomes for functional studies does demand for less invasive approaches. A relatively straightforward approach is to stain exosomes post isolation with lipophilic carbocyanine dyes such as DiI, DiO or DiD. These compounds are lipid-like molecules with fluorescent head groups and long aliphatic tails capable of inserting into the vesicle membranes. Alternative lipid stains that might be used are FM4-64, R18, CFSE, PKH-26 [81], PKH-67 [78], Top Fluor Sphingomyelin or Top Fluor Cholesterol (data not shown). Employing lipophilic carbocyanine dyes is relatively straightforward and allows for the use of synthetic fluorophores with optimal photophysical properties as well as flexibility over the entire spectral range. This strategy has meanwhile been used in several fluorescence microscopy based studies of exosomes [51,78,82–84]. Furthermore, one could potentially also apply this strategy to integrate other synthetic ligands into exosomes such as PET tracers or even small molecule ligands targeting a receptor of choice. The major drawback of lipophilic tracers however is that they are not exosome specific and indiscriminately stain all vesicles and lipid fragments contained within the sample. To complicate matters, additional washing and ultracentrifugation steps are needed to remove unincorporated tracers which potentially introduce further bias and yield issues. Also, the integration of non-natural lipids might alter the physicochemical properties of the exosome membrane and thereby affect their functionality. Thus, careful optimization of labelling ratios as well as monitoring changes of exosome size and

zeta potential may be required to allow for the least perturbing conditions. Another difficulty is that in salt-containing buffers or media most of these lipid stains rapidly form micelles or aggregates themselves. Since these particles can have similar physiochemical properties as exosomes they may not be easily removed by washing and may require more sophisticated purification steps. Even if such micelles generally appear to have a poor efficiency in cell staining at least for nonphagocytic cells [85], thorough control experiments need to be done to unambiguously assign the observed signals to exosomes.

A second strategy is to label the exosomes at the protein receptors; this might either be done post-purification based on random protein conjugation at primary amines by using standard succinimide chemistry [86,87], or at cysteines using maleimide [88,89] – activated dyes. This approach also allows for flexibility in choice of synthetic fluorophores (or ligands) and might be slightly less invasive than inserting synthetic lipids into the lipid bilayer; however, it still has drawbacks in lack of exosome specificity and potential interference with protein receptor function. A more specific and less invasive approach to visualize exosomes therefore seems the expression of fluorescent protein (FP) fused exosome surface markers such as CD-63 [36] or CD-9 [90] in parent cells prior to exosome isolation. This may even allow for real time tracing of exosomes directly upon their release such as in trans-well experiments or in animal models. To limit a potential interference with exosome uptake function, the fluorescent proteins may be integrated at the luminal side of a transmembrane marker which should not or only minimally affect extra-vesicular membrane-membrane interactions with the target cell. Apart from a limitation to fluorescent proteins, another potential issue may be the non-physiological overexpression of FP-tagged receptor in the parent cells which may influence exosome biogenesis, release as well as their composition due to cell stress or simply altered surface marker abundance. Therefore, a careful analytical characterization of labelled versus unlabeled exosomes is crucial. These issues were addressed in this work and are summarized in manuscript I (*Quantitative profiling of exosome parent-recipient cell pairing by high content screening using CD63-emGFP vesicle labeling)*.

A third option for visualizing exosomes is by introducing labelled cargo post-isolation, such as by electroporation [42,43,50]. In theory this should leave the outer surface unchanged. However, it remains to be shown whether this method results in exclusive encapsulation of the cargo within the vesicles and not additionally promote sticking to the outside or formation of self-aggregated nanoparticles of the cargo such as has been encountered during siRNA loading [74]. Alternative techniques for post purification cargo loading, or loading of FP-conjugated protein cargo overexpressed within the parent cells still remain to be investigated.

Finally, double labelling of exosomes by combining either of the strategies mentioned above may allow mitigating some of the issues in specificity, as for

example allowing for discrimination of cell derived micro vesicles from lipid-dye micelles. Also, double labelling may give additional mechanistic information such as on when cargo gets released within the recipient cell, or how long a single vesicle stays intact (i.e. [82]).

1.5 Initial contact of exosomes to the recipient cell surface

The increasingly emerging model is that exosomes specifically bind to cell surface receptors prior to their internalization, and several such receptors have been identified to date. One of the first efforts to identify exosome uptake receptors was published in 2004 [78] and was based on a study of bulk uptake of PKH67 lipid labelled exosomes from mouse bone marrow derived dendritic cells (BMDC) into BMDC by FACS. In this system and as repeatedly observed in later studies, the vesicle uptake efficiency was dependent on the presence of serum and Mg^{2+} and sensitive to reduced temperature, which suggests a specific and energy dependent process. Using monoclonal antibodies (mAbs) to specifically block a number of candidate receptors in the recipient cells resulted in partial (up to 40 %) inhibition of uptake when simultaneously blocking either several a5 and b3 integrins (CD51 and CD61), CD11a and its ligand CD54 or the tetraspanins CD9 and CD81. Complement receptors (CD11b/c, CD18) on the other hand did not seem to be involved. Significant uptake inhibition was also observed when adding a soluble analogue of phosphatidyl serine (PS), O-phospho-L-serine but not the control stereoisomer. This observation was particularly interesting since PS is known to play a central role in recognition and phagocytosis of apoptotic cells or expelled nuclei during erythroproeisis when exposed as an “eat me” signal at the outer membrane leaflet. Also, these results established a connection to a previous study that had postulated the soluble molecule MFG-E8 (milk fat globule protein E8) in serum to function as an opsonin that docks exosomes to target cells [91]. A plausible scenario might be that MFG-E8 functions as a bifunctional ligand that recognizes PS on the exosomes by its two factor V/VIII domains and simultaneously binds a5b3/5 integrins on host cells via its RGD (Arg-Gly-Asp) domain. Supporting this hypothesis, an agonistic anti-mouse MFG-E8 antibody increased, whereas addition of an RGD containing hexapeptide reduced exosome uptake in BMDC cell [78]. In a search for phosphatidylserine binding receptors, Miyanishi and coworkers screened a library of hamster mAbs against mouse peritoneal macrophages for blocking phagocytosis of apoptotic cells and identified Tim1 (T-cell immunoglobulin- and mucin-domain-containing molecule) and Tim4 as key receptors in binding of PS and engulfment of apoptotic cells. The same study showed that PS recognition by Tim1 and Tim4 also plays a role in

binding and potentially also uptake of exosomes into phagocytic cells. Using a bead-based binding assay, the authors showed that exosomes mediate indirect association of Tim1-Fc with Tim4-Fc suggesting that exosomes can be bound by both receptors simultaneously. Moreover, overexpression of these receptors in Ba/F3 cells also increased the binding of immunogold labelled exosomes to the cell surface, suggesting similar mechanisms are involved in target cell binding of exosomes, at least in phagocytic cells. Finally, evidence that PS may play a role in exosome uptake also in non-phagocytic cells was presented in a study addressing tissue factor exchange between breast cancer cells [29]. Exosome mediated transfer of tissue factor from MDA-MB-231 to MCF-7 cells was blocked by over 70 % by pre-incubation of the vesicles with AnnexinV, which should shield phosphatidylserine exposed on the exosome membrane – suggesting that phosphatidylserine might play a more general role in the interaction of exosomes with target cells not only in phagocytic cells.

A different angle was presented in a study characterizing the requirements for exosome transfer of MHCII/peptide complexes during cognate T-cell / DC interaction [92]. While the recruitment of DC exosomes to T-cells was generally dependent on T-cell activation, surprisingly it was independent of the antigen specificity - suggesting that the T-cell receptor itself was not involved in mediating exosome transfer. Rather the authors provided evidence supporting a direct interaction with LFA-1 based on a substantial (> 80 %) blocking of DC exosome uptake by LFA-1 specific neutralizing mAbs. Addition of Mn^{2+} to resting T-cells dose dependently induced exosome uptake in absence of T-cell activation. The authors assigned this activity to a Mn^{2+} mediated induction of a high-affinity state of LFA-1 and concluded that LFA-1 activation was sufficient to provoke DC exosome binding and uptake in T-cells during immunological synapse formation.

Since exosomes are particularly rich in tetraspanins that, promiscuously, associate with integrins, Rana and coworkers assessed the involvement of Tspan8 complexes in receptor-mediated uptake of exosomes in endothelial cells [93] and rat pancreatic adenocarcinoma cells [94]. By comparing *in vitro* and *in vivo* target cell and tissue selectivity of exosomes isolated from parent cells overexpressing different combinations of tetraspanins the authors suggest that the tetraspanin web contributes to the homing preferences of exosomes originating from different sources. This theory appears enticing since it directly suggests a future scenario where profiling the receptor portfolio might enable to predict target selectivity and ultimately tailor exosomes for drug delivery, however many more systematic studies will be required.

Finally, recent work by Christiansson and colleagues has investigated exosome uptake from the perspective of conceptional analogies to the uptake of viral particles. Since virus derived cell penetrating peptides such as HIV-TAT as well as Lipoproteins are known to enter cells through heparan sulphate proteoglycan

receptor (HSPG) dependent pathways, the authors specifically investigated a putative role of the HSPG receptor in uptake of exosomes [95]. Using lipid labelled exosomes from U87 glioblastoma cells, the uptake into GBM and CHO cells was monitored by fluorescence microscopy under different conditions of HSPG modulation. Indeed, exosome uptake was partially inhibited by addition of heparin and heparan sulphate derivatives but not the close analogue chondroitin sulfate. In addition, genetic modification of the HSPGs of both, the syndecan and glypican type, enzymatic depletion of cell-surface HSPG by xyloside as well as pharmacological inhibition of endogenous proteoglycan biosynthesis all significantly attenuated exosome uptake. Interestingly, HSPG receptors were also identified to be present on the surface of the exosomes themselves opening for the possibility of bidirectional recognition. However, the authors convincingly conclude that the exosome HSPGs are not directly involved in contacting the recipient cell since enzymatic depletion of receptors from exosomes by xylosidase did not impact uptake. Of note, inhibition of exosome uptake by heparin has most recently also been observed in other systems by us (data not shown) and others [81], again suggesting a more general relevance of HSPG receptors beyond the initially used glioblastoma cells.

To summarize, a number of different receptor/ligand interactions are emerging to play a role in exosome uptake, including phosphatidylserine, tetraspanins, integrins as well as the HSPG receptor (see also overview in Table 1). As a unifying hypothesis it appears plausible that, in line with the diversity of exosome parent and recipient cells, there is not just one way for exosomes to bind to target cells, but that several types of receptors are selectively involved for different exosomes to target different recipient cell types under different conditions. Hence there is a clear demand for a better understanding of how these vesicles target and enter their recipient cells, and how they deliver their cargo to reach its subcellular site of action.

1.6 Exosome internalization

As outlined above a variety of receptors and ligands have been associated with the cellular uptake of exosomes. Accordingly, a variety of different uptake routes for exosomes have been described, some of which were noted to be cell specific. In agreement with the established receptor-based contact of exosomes to the cell surface, the current leading model suggests that exosome uptake occurs by energy-dependent, receptor-mediated endocytosis [78,79,82,87]. A fairly extensive study performed by Svensson and colleagues demonstrated that PKH26-labelled exosomes generated by glioblastoma (GBM) cells were taken up by a variety of

cell lines (HeLa, CHO, MEF, HUVEC and U87 GBM cells). Uptake was found to be saturable and dose dependent as determined by competition with unlabeled exosomes [79]. Based on a co-localization with the known lipid raft marker cholera toxin B, the authors addressed the possibility of lipid raft mediated endocytosis and confirmed that depletion of cholesterol-rich lipid rafts by simvastatin (an inhibitor of cholesterol synthesis) decreased uptake of GBM exosomes. Consistently, GBM exosome uptake was significantly inhibited by the addition of filipin III, an inhibitor of lipid raft-dependent and caveolar endocytosis. This study also demonstrated that exosome uptake is negatively regulated by caveolin-1, a lipid raft-associated protein. Caveolin-1 is described to regulate the signaling of membrane protein extracellular signal-regulated kinase 1/2 (ERK1/2) and heat shock protein 27 (Hsp27), both of which - as well as their downstream targets - were found to be phosphorylated and upregulated up to 4.5 fold during exosome uptake in the same study. Inhibition of ERK1/2 signaling using the small molecule ERK1/2 inhibitor U0126 decreased exosome uptake alongside with reducing p-Hsp27 in a dose-dependent manner. While it remains unclear how exosomes, caveolin-1 and ERK1/2 interact, this study is the first to relate exosome uptake to specific intracellular signaling pathways in the host cells. This introduces another important question to the field: Is exosome uptake dependent on the cell signaling / activation status of the recipient cell? A question that likely will be subject to further research in the near future.

In contrast to the findings of Svensson et al 2013, an earlier report by Parolini and co-workers had described that exosomal uptake is primarily mediated by fusion with the plasma membrane under acidic pH conditions such as typically encountered within the tumor microenvironment [96]. The authors used Octadecyl rhodamine B (R18)-labelled exosomes and observed a fluorescence increase of the dye in the recipient cells. Such an effect would be consistent with a fusion of exosomes with the plasma membrane thereby leading to an unquenching of the dye highly concentrated and self-quenched within the exosomes. In addition, R18 from the exosomes co-localized with PKH67 in pre-stained recipient cells. While the authors conclude that this reflects an exosome / parent cell mixing event, such an effect would be consistent not only with plasma membrane fusion but also with co-localization or fusion with intracellular vesicles or potentially even recycling of exosomal lipids downstream of an initial uptake by endocytosis or other routes. Curiously, this study also demonstrated elevated levels of caveolin-1 within the exosomes generated under acidic conditions, which was incorporated into caveolin-1 naïve recipient cells. Caveolin-1 is postulated to promote tumor progression [97], however was also demonstrated to negatively regulate exosome uptake in the study mentioned above [79]. Further elucidation of the relationship between exosomes and caveolin-1 is required, which may reveal a dynamic

feedback relationship between exosome uptake and exosome-delivered caveolin-1.

Of note, uptake by fusion had also been reported in an earlier study describing microvesicle uptake into platelets [98]. In this paper, exosomes were generated carrying different donor-acceptor pairs of lipid dyes and the fluorescence within recipient cells was monitored over time by live cell confocal microscopy. Since unquenched donor fluorescence was observed as early as 3 minutes after uptake this would support a dilution of the lipids, consistent with membrane fusion taking place already during the initial phase of uptake.

The question remains whether such a fusion might be a phenomenon limited to special systems such as platelets or exosomes released and/or taken up in the tumor microenvironment. In this light it is interesting to note that Parolini and coworkers indeed reported a number of specific differences in both, exosome properties as well as their uptake efficiency under acidic conditions. For example, melanoma-derived exosomes demonstrated enhanced delivery to metastatic tumor cells compared to primary tumor cells, while overall exosome uptake was more efficient under acidic conditions. Melanoma exosomes derived under acidic conditions were also shown to undergo enhanced cellular uptake compared to exosomes released by parent cells under physiologic conditions, regardless of the environmental pH of the recipient cells, suggesting a change in the constitution of exosomes themselves. Consistently, exosomes generated under an acidic environment displayed increased sphingomyelin/ganglioside GM3 content and were described as having significantly lowered membrane fluidity – a change in properties that might plausibly alter the preferred uptake mode.

Yet an alternative route of exosome cell entry was reported by Feng and colleagues for cells of the monocyte lineage (Feng 2010). Leukaemia-derived (K562 and MT4 cell lines) PKH26 labelled exosomes were incubated with a series of phagocytic as well as non-phagocytic cells and, after washing with citric acid buffer and trypsinization to remove surface bound exosomes, uptake was quantified by flow cytometry. Exosomes were taken up by phagocytic cells (THP-1 myelomonocytic cells, U937 lymphblasts, RAW 264.7- and J774.1-macrophages) by about 3 orders of magnitude more efficiently than by non-phagocytic cells (NIH 3T3, Jurkat, T, 293T, COS-7 and HEL299). Fluorescence microscopy revealed that the phagocytic cells internalized labelled exosomes together with phagocytic latex beads and uptake was inhibited by dynamin2 knockdown, confirming that exosomes were indeed taken up through phagocytosis in these cells. Furthermore, this type of uptake was dependent on actin cytoskeleton and PI3kinase, as well as susceptible to antibodies blocking Tim4, but not when blocking Tim1 receptors. This work does not address however whether this form of exosome internalization is just a consequence of phagocytosis as a generic

function of macrophages, or whether exosomes employ more specific strategies to hitchhike phagocytic routes for functional cargo delivery to these cell types.
The diversity in current exosome uptake data may also corroborate the assumption that exosome-recipient cell interaction is largely governed by parent cell derived receptors or physicochemical properties, which would further enhance the potential for the development of tissue targeted, exosome-based therapeutics.

1.7 Intracellular fate of exosomes in recipient cells

The fate of the vesicles and their cargo upon internalization and their intracellular trafficking within recipient cells has not been extensively documented to date, and much additional research will be required. Current studies agree that once internalized, exosomes are sorted and shuttled to various vesicular and endosome-associated organelles within the cell, ultimately with their markers targeted to the lysosome. Morelli and co-workers labelled bone-marrow dendritic cell (BMDC) -derived exosomes with KPH67 and monitored co-localisation with different organelle markers in dendritic cells using confocal microscopy. Within five minutes of adding the labelled exosomes, KPH67 could be detected within early endosomes and after two hours the dye was located within late endosome/lysosome structures. It was also demonstrated that BMDCs were able to process the contents of allogeneic exosomes, and subsequently display the processed peptides on the surface of the cell. This suggests that cells such as DCs are capable of processing exosomal content specifically for surface display and immune stimulation, implying a trafficking of cargo to the ER. A study by Tian and colleagues demonstrated exosome uptake and trafficking during live cell microscopy [82,87]. Rat pheochromocytoma (PC12) derived exosomes were labelled with the fluorescent lipophilic marker, DiD, and vesicle surface proteins with TAMRA using succinimidyl ester chemistry. Similar to the findings of Morelli, this study demonstrated an initial localization of labelled exosomes in endocytic vesicles near the cell periphery at the early phases of uptake, after which components of the labelled exosomes were increasingly directed to the perinuclear region. Using single particle tracking (SPT) of double labelled exosomes, the authors also derive that exosomes undergo various stages of trafficking and sorting. Initially, labelled exosomes were observed to exhibit slow drifting at the plasma membrane surface, possibly through the action of retrograde actin flow. This phenomenon has been reported previously during virus attachment to receptors at the cell surface [99]. After uptake, exosome movement was confined, followed by a rapid transport (possibly along actin). A

second phase of rapid movement ensued, directed to the perinuclear region of the cell (possibly along microtubules). The final stage of confinement resulted in the separation of the exosomal markers; the TAMRA marker directed to the lysosomes suggesting that the protein contents of the exosomes are degraded, while the lipid DiD label was recycled back to the cell periphery. This study reported no evidence for fusion using R18 labeling in parent cells which is known to recycle into mitochondria from the plasma membrane, which in this study was not observed; instead also the R18 dye was trapped within endocytic vesicles, further supporting endocytosis as the primary uptake route, at least in this system.

The current literature of exosome uptake and intracellular transport contains several contradicting reports, possibly highlighting the disparity in the methods used to generate, isolate and analyze exosomes. In addition, this may relate to some of the key issues relevant to exosome biology which requires extensive elucidation. Are all exosomes equally proficient with respect to the uptake routes they can take, and is exosome uptake governed by the recipient cell type and state? Or, in turn do exosomes differ in preferred entry routes based on their origin and respective surface receptor repertoire? There is a growing body of evidence to suggest that exosomes do vary not only between cell types but that further subspecies even exist within the population of vesicles released from the same cell type [62,100,101]. Along these lines, it is conceivable that even within the same recipient cell and for exosomes from the same parent cell, multiple entry routes co-exist at a given time. Mechanisms as to how exosomes deliver and release their cargo remain elusive. The diverse set of cargo is likely functional at different subcellular sites, which makes a model appear plausible where exosomes take a defined trafficking route within the recipient cell shuttling between various ‘bus stops’ to differentially release cargo targeted to different addresses. Alternatively, all cargo might be released in one compartment such as by vesicle fusion and then trafficked on to their respective final destination independently.

The need for a better understanding of how exosomes target and deliver their cargo into recipient cells in order to translate their biology into medical application were the seed of this thesis.

contact type	binding partner	presented on	parent cell (Exosome)	target cell	literature
tetraspannin	CD151	Exosome	rat pancreatic adenocarcinoma cells	endothelial cells	Rana 2011
	Tspan8	Exosome	rat pancreatic adenocarcinoma cells	endothelial cells	Rana 2011
	CD9	Exosome	BMDC	BMDC	Morelli 2004
	CD9	Exosome	DC	APC, Tcells	Thery1999
	CD81	Exosome	BMDC	BMDC	Morelli 2004
HPSG	HPSG receptor	plasma membrane	U87 glioblastoma cells	GBM and CHO cells	Christianson 2013
phosphatidyl serine (PS)	PS	Exosome	BMDC	BMDC	Morelli 2004
	(MFG)–E8/ lactadherin	Exosome	BMDC	BMDC	Morelli 2004
	MFG-E8 (opsonin)	Exosome	DC		Thery 1999
	Tim1 and Tim4	plasma membrane	Ba/F3 (phagocytic cells)	Ba/F3 cells	Miyanishi 2007
	Tim4	plasma membrane	K562 or MT4	RAW 264.7 macrophages	Feng 2010
	PS	Exosomes	MDA-MB-231	MCF-7	Lima 2013
	PS	Exosomes	U373/EGFRvIII-GFP cells glioma cells HUVECs	U373 (human astrocytoma)	Al-Nedawi 2008
selectin	P-selectin (CAM)	plasma membrane	blood-derived monocytes, THP-1 cells , Plasma	platlets	Ian del Conde, 2005
	PSGL-1	Exosomes	blood-derived monocytes, THP-1 cells , Plasma	Platlets	Ian del Conde, 2005
integrin	LFA-1	n.d.	DC	T-cell	Nolte-t Hoen 2009
	LFA-1	plasma membrane	bone marrow-derived dendritic cells	CD8+ dendritic cell	Segura 2007
	CD51 a5 integrins	plasma membrane	BMDC	BMDC	Morelli 2004
	CD61 b3 integrins	plasma membrane	BMDC	BMDC	Morelli 2004
	CD11a (ITGAL)	plasma membrane	BMDC	BMDC	Morelli 2004
	CD54 (ICAM-1)	plasma membrane	BMDC	BMDC	Morelli 2004
	CD11B (Mac-1)	Exosome	DC		Thery1999
	CD11a (ITGAL)	Exosome	BMDC	BMDC	Morelli 2004
	CD54 (ICAM-1)	Exosome	BMDC	BMDC	Morelli 2004
lipid raft	not specified	plasma membrane	glioblastoma(GBM)cells, U87 MG	HUVECs & U87MG cells	Svensson 2013
	sphingomyelin/ganglioside GM3	Exosome	Mel1	Mel1 & PBMCs	Parolini 2009

Table 3) Receptors for interaction of exosomes with target cells:
Different classes of receptors are listed which were reported to be involved in the binding and uptake of exosomes into recipient cells. Of note, an early study [91] *came already to propose several uptake receptors purely based on MS-proteomics profiling of exosomes, several of which were later confirmed to be involved in exosome uptake by other groups.*

mode of uptake	recipient cell	parent cell	Exosome label	literature	uptake inhibition
Phagocytosis	various monocyte & macrophage lines vs. Jurkat, , HEK, COS, 3T3	K562 or MT4, T-cell leukemia cells	PKH26	Feng 2010	dynamin2 knockdown, tim4 mAbs
Phagocytosis	macrophages	Human saliva, plasma and breast milk	PKH67	Lässer 2011	no inhibition
Hemifusion, phagocytosis	melanoma	DC	R18	Montecalvo 2012	4°C, cytochalasin D, bafilomycin A1
Fusion	melanoma cells	Mel1 cells	R18	Parolini 2009	pretreatment with proton pump inhibitors
Fusion	U373 cells (human astrocytoma)	U373/EGFRvIII-GFP cells, glioma cells, HUVECs	EGFRvIII fused at C-terminus to a GFP	Al-Nedawi 2008	AnnexinV, Co-incubation of exosomes, blocking antibodies specific for various integrins, adhesion molecules or tetraspanins
Fusion	activated platelets	blood-derived monocytes, THP-1 cells , Plasma	parent cell - NBD-PE, Rh-PE, DOTAP	Ian del Conde 2005	annexin V, antibody to PSGL-1
Receptor mediated endocytosis	BMDCs	BMDCs	PKH67	Morelli 2004	simultaneous inhibition of CD51 & CD6, CD11a & CD54, CD9 and CD81 mAbs, soluble analog of PS, O-phospho-L-serine,
Receptor mediated endocytosis	PC12	PC12	DiD & amine-conjugation (TMR-NHS), R18	Tian 2010 & 2011	4°C & CytoD
Receptor mediated endocytosis	HeLa, CHO, HUVEC; MEF, U87 GBM	GBM	PKH67	Svensson 2013	MbCD, filipin III, simvastatin, CAV1 knockout MEFs and kd
Endocytosis	SKOV3	SKOV3, HEK293 , H4 cells	CFSE	Escrevente 2011	chlorpromazine, cytochalasin D, methyl-beta-cyclodextrin

Table 4) Different routes of cell uptake reported for exosomes

2 Thesis and objectives

This PhD project aimed to investigate exosomes as delivery vehicles and potentially identify learnings form the natural delivery routes which may eventually be transferred to synthetic formulations for systemic siRNA delivery. The starting point of this project was complicated by inconsistent literature on exosome isolation and characterization. Our first goal was therefore to generate a toolbox for thorough analytical characterization and thereby benchmarking different isolation methods Furthermore, we planned to establish methods for studying cell uptake and trafficking. In particular, we would like to characterize the major routes of cell uptake, fate within the target cell, directed cell-cell pairing (e.g. cancer cell- immune cell, mother milk – epithelial cells) and tissue specific exosome homing. The focus will be on quantitative and mechanistic characterization of exosome mediated cell uptake & intracellular trafficking.

3 Extended methods

3.1 Cell culture

3.1.1 Parent cells

HeLa (ATCC), Human hepatocellular carcinoma cells (Huh7, ATCC), human embryonic kidney cells (HEK293T, ATCC), rat pheochromocytoma PC12 cells, a mouse neuroblastoma cell line N2A (ATCC) and a mouse melanoma cell line (B16F10, ATCC) were cultured in complete media comprised of Dulbecco's Modified Eagle Medium (DMEM, Life Technologies), supplemented with 10 % fetal bovine serum (FBS, Cellgro) and penicillin/streptomycin (5 mg/ml, Cellgro). Human colon cancer cell line HCT-116 (ATCC) were grown in RPMI1640 supplemented with10% FBS and penicillin/streptomycin (5 mg/ml, Cellgro).

Human monocyt derived Dentritic cells (hum moDC) were isolated from buffy coats and differentiated with rhGM-CSF (100 ng/ml) and rhIL-4 (80 ng/ml) according to the protocol from Perrine Loesle (Amanda Littlewood-Evans's Lab) and Sophie Muller from Karl Welzenbach's laboratory. Briefly: First peripheral blood mononuclear cells (PBMCs) were isolated from a buffy coat by performing a Ficoll gradient. Buffy coat/ whole blood was diluted with PBS in a ratio 1:5 and transferred to 50ml Falcon tubes. 30 ml of diluted blood was underplayed with 10ml Ficoll and centrifuged at 2200rpm at room temp for 20 min in a swinging rotor. Then lymphocytes/peripheral blood mononuclear cells were collected from

the interphase ring with a transfer pipette and transfer into a fresh 50 ml Falcon tube.
Cells were washed cells twice with PBS-/- and then centrifuge at 1400 rpm for 5 min. Pellets were pooled and cell number was determined with a Casty count. For cell adhesion 2x10^6 PBMCs/ml were resuspended in RPMI 1640-glutamax supplemented with 10 % FCS and 1 % penicillin/streptomycin and plated out with 5ml/well in a 6 well plate (costar). After 2 hour incubation monocytes adhere to the plastic whereas lymphocytes remain non-adherent. Non adherent cells were removed and monocytes were washed twice with 5ml medium. Finally, 5 mL X-Vivo 15/well supplemented with rhGM-CSF (100 ng/ml) and rhIL-4 (80 ng/ml) were added for differentiation and immature moDC were harvested 5 to 7 days after isolation.
For bone marrow derived monocytic Dentritic Cells cultivation cells were isolated from Mouse tibias and femurs. The bones were removed from mice into ice cold PBS and tissue and muscle excess were removed. The bone marrow was flushed out of the bone in fresh DMEM medium using a 1 ml 27-gauge syringe. Then cells were filtered through a cell strainer (40um), using the back of the plunget to pass any large bone marrow pieces. After one washing step by centrifugation clear bone marrow cell pellet was resuspended and cultured in DMEM Glutamax (Gibco-BRL), 10% FCS and antibiotics, supplemented with 10ng/ml murine GM-CSF for differentiation. For human and mouse moDC exosome isolation medium was exchanged after differentiation and subsequent collected at 48h.
For fluorescent labeled exosome isolation, typically 5-8 x 10^6 HEK293, 4-5 x 10^6 Huh7 or 4-5 x 10^6 B16 cells were seeded in a 15 cm culture dish with complete media and transfected with CD63 expression constructs the next day. Cell transfection was done in complete medium using Lipofectamine2000 (Life Technologies; 1 ug DNA/2.2 ul LF2000) following the manufacturer's instructions. After 4 hours, cells were washed and medium was replaced by OptiMEM (Gibco-BRL). Conditioned media were collected at the time point as indicated in the experiments for exosome isolation. Typically, 100-200 ml of 48h conditioned medium (pooled from multiple dishes) was used in most experiments.
All cells were cultured at 37°C with 5 % CO2

3.1.2 Recipient cells

Human primary fibroblasts from a healthy donor (Life Technologies, #C-013-5C) were grown in MEM (Life Technologies) supplemented with 15 % fetal bovine serum and penicillin/streptomycin (5000 □g/ml, Cellgro) in 0.1% gelatine (Sigma Aldrich) coated T150 flasks. For exosome uptake experiments, cells were either plated in 8-well slides (ibidi) at a density of 40-60 % (confocal and DIC live cell imaging experiments) or 96-well plates (ibidi) at a density of 60 % (exosome uptake screening assay).

Transient expression of BacMam actin RFP in human fibroblast and other cells was obtained by adenoviral transduction as described in the manufacture protocol. Also transient expression of Adeno-Lifeact-mCherry in human fibroblast cells was obtained by adenoviral transduction, and cells were seeded onto line substrates or 2D substrates (Fibronectin coated coverslips) at least 6 hours prior to TIRF life cell imaging. Line substrate microfabrication was performed as described elsewhere [102]. Human primary keratinocyte progenitors (CELLnTEC Advanced Cell Systems AG, Bern, Switzerland) were kindly provided by Gabi Schutzius (Novartis Basel) and cultured in Epithelial Culture Medium (CELLnTEC Advanced Cell Systems AG) under sub-confluent culture conditions to prevent differentiation. For the exosome uptake assay cells at passage 6 were detached with Accutase (CELLnTEC Advanced Cell Systems AG), and plated 48 hours prior to exosome addition at a density of 20'000 cells per 96-well. Human iPS cells from a healthy donor (Coriell) were kindly provided by Claudia Merk (Novartis Basel) and differentiated into motor neurons following a protocol adapted from [103,104], plated in Matrigel coated 96-well plates (ibidi) and cultivated for 3 weeks prior to exosome uptake studies. HUVEC primary human endothelial cells (Promocell) were kindly provided by Giorgia Jurisis (Novartis Basel) cultivated in Endothelial Cell Growth Medium (Promocell) and plated in 96-well plates (ibidi) coated with Collagen (50 ug/ml, PureCol™ Advanced BioMatrix). HEK293 cells (ATCC), B16-F10 cells (ATCC), Huh7 cells (HSRRB) and HeLa cells (ATCC) were cultivated in DMEM (Life Technologies) supplemented with 10 % fetal bovine serum and 1x L-Glutamine 200 mM (100X; Life Technologies) and penicillin/streptomycin (Life Technologies) and plated in 96-well plates (ibidi) at a cell density of 40-60 % confluency one day prior to exosome addition.

3.2 Fluorescent labeling

3.2.1 Exosome labeling

For lipid labeling of exosomes, parent cell line MVBs were stained by TopFluor Sphingomyelin, TopFluor Cholesterol or Dioleoyl sn Glycero 3-Phosphoethanol Emine-N-Lissamine Rhodamine B-Sulfonyl (NRhPE/NFlPE) [105] [106] [107] treatment. TopFluor Sphingomyelin (Avanti Polar Lipids) and TopFluor Cholesterol (Avanti Polar Lipids) was dissolved in Dichlormethanol 1mg/100ul. For Parent cell labeling the TopFluor labeled lipid was further diluted 1:20 in PBS by extensive vortexing. The stain- PBS emulsions was dripped on the cell medium. A few drops per 10cm dish were enough for a strong staining. The TopFluor Sphingomyelin and the Cholesterol did form permanent drops in the medium. After the incubation time of 8 to 24h cells were washed extensively and fresh medium was added.

3.2.2 Cell organelle labeling for life cell imaging

For Antibody labeling eukaryotic cells were fixed, permeabilized and immunostained in 96 well plates with the following procedure: First cells were washed three times with OptiMem and once with PBS. Then cells were fixed with 4% PFA (NBK) for 10-15min at 4°C. Fixation was stopped by PBS, BSA 0.15 % washing step. Permeabilisation was achieved by 100 ul/well 0.1 % Triton X-100 (Sigma) incubation for 10-15 min at RT followed by a PBS, BSA 0.15 % washing step. Then non-specific binding sites were blocked at least for 60 min at RT (Albumin, Bovine serum, fraction V, low heavy metals (Calbiochem) before the primary antibody CD63 polyclonal-rabbit (1:200 dilution in PBS def / BSA 0.15 %) incubation was started. After 30-60 min at RT cells were washed 4 x with PBS def / BSA 0.15% to remove unbound primary antibody. Secondary antibody diluted in PBS def / BSA 0.15% was incubated also for 30-60 min at R.T. and cells were subsequently washed at least 4 x with 200 µl / well PBS def. / BSA 0.15 % to remove unbound secondary antibody, thereby reducing the background signal. Optionally a nuclear staining by Hoechst followed and then supernatant was removed and PBS or Vectashield added for imaging.

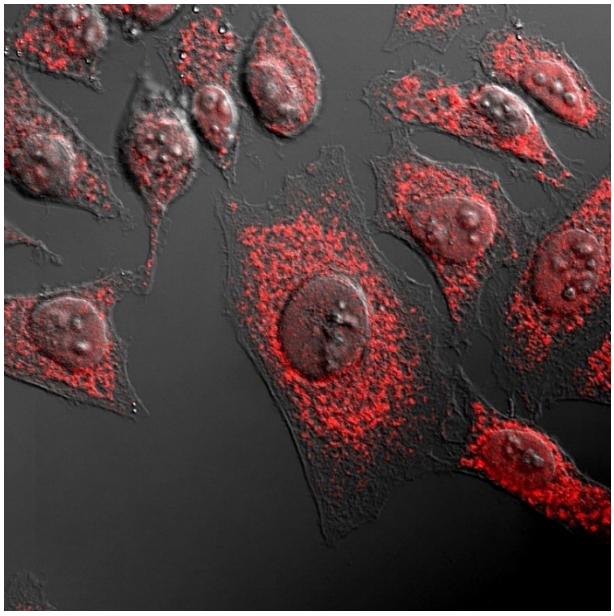

Blocking Buffer (prepare 50 ml, store at 4 °C)

Endconc. Reagent	Amount
1 % (w/v) BSA	0.5 g
0.05 % (v/v) Tween 20	250 µl
5 mM (v/v) EDTA (stock: 0.5 M)	0.5 ml
1 % (v/v) FCS	0.5 ml
PBS def. up to 50 ml	~ 48 ml
Total	50 ml

Figure 1) Endogenous CD63 IF staining in HeLa cells

3.3 Cloning

3.3.1 Lysosomal-associated membrane protein - Lamp2

Lamp2 is known as an exosomal marker [108 69 109]. The goal is to label exosomes for their characterization, quantification and in vitro quantitative Imaging. Using molecular cloning techniques, the HuR region of the vector pSecTag 2A HuR GFP

and pSecTag 2A HuR mCherry (originally psecTag2 A of Invitrogen, Cat.-No. V900-20) was replaced by a lamp2b domain.

The lamp2b domain (expasy.ch P13473, NCBI Genebank ref sec 13992) was amplified from a cDNA library with PCR and gene specific primers (Microsynth).

			L	Tm	Tm (overlap)	%GC	RE
Lamp2b F1	AATAATGCTAGCCACCATGGTGTGC TTCCGCCTCT	1096885	35	73.5	54.4	51.4	NheI
Lamp2b F2	AATAATGCTAGCCACCATGGTGTGC TTCCGCCT	1096886	33	72.4	50.8	51.5	NheI
Lamp2b R1	AATAATTTCGAACAGAGTCTGATATC CAGCATAACTTTTTCTTCTGCCAA	1096887	50	73.1	69.8	34	BstBI
Lamp2b R2	AGGAGGTTCGAACAGAGTCTGATAT CCAGCATAA CTTTTTCTTC	1096888	44	71.2	59.9	40.9	BstBI

Table 5) Lamp2b primer design

The cDNA library was generated by reverse transcription of mRNA which was isolated from HeLa cells by a Trizol RNA purification. Subsequently, the flanking sites were cleaved by restriction endonucleases and ligated into the linearized (and dephosphorilized) vector pSecTag2A. The DNA vectors were amplified in *E. coli*, column purified and controlled by site specific restriction digestion as well as DNA sequence analysis. The DNA constructs were stored at - 20° C.

3.3.2 CD63-GFP, CD63-mCherry, CD63-GFP-mCherry

For alternative fluorescent exosome labeling, the full length coding sequence of human tetraspannin CD63 isoform A (RefSeq NM_001257390.1) was TOPO cloned into the pcDNA 6.2 N-emGFP vector (Promega) to result in an N-terminal fusion of emGFP to CD63. Single-standed cDNA was synthesized from total RNA using the High Capacity cDNA Reverse Transcription kit.

Primer design for CD63 in TOPO-EmGFP-Vector (invotrogen):

fwd1:	AAGCTTGCGGTGGAAGGAGGAATG	
rev1:	CTACATCACCTCGTAGCCACTTCTG	
Sequencing primers:		
fwd1 (in kit):	AAAGCAGGCTCCGAATTCGC	1629-1648
fwd2 (lst19):	ATCATGTTGGTGGAGGTGGC	1932-1951
fwd3 (lst20):	AGGGCTGTGTGGAGAAGATTGG	2221-2242
rev1 (lst21):	ACCCACGGCAATCAGTCCCAC	1751-1731

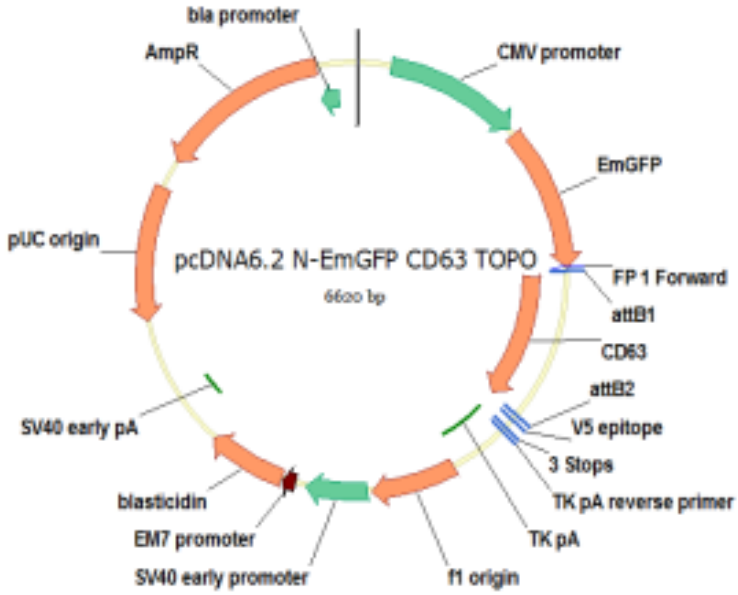

Figure 2) CD63-emGFP vector map

pcDNA 6.2 N-mCherry-CD63 and N-mCherry-emGFP-CD63 vectors were then subcloned by replacing the emGFP CDS by gene synthesized inserts (Solvias) comprising the CDS of either mCherry or an emGFP-mCherry fusion.
For DNA amplification and sequence modification, PCR reactions were performed by using the PCR Phusion Master mix.

CD63 2nd loop GFP

The CD63 2nd loop eGFP was kindly provided by Yiqi Seow (Agency for Science, Technology and Research, Singapore). Murine CD63 was cloned into peGFP-C1 vector. The sequence is shown below with yellow highlighting the transmembrane regions and cyan the extracellular loops. Bold marks the sequence which has been removed from CD63 to insert the construct.

atggcggtggaaggaggaatgaagtgtgtcaagttttgctctacgttctcctgctggccttctgcgcctgtgcagtgggat
tgatcgccattggtgtagcggttcaggttgtcttgaagcaggccattacccatgagactactgctggctcgctgttgcctgt
ggtcatcattgcagtgggtgccttcctcttcctggtggcctttgtgggctgctgtggggcctgcaaggagaactactgtctc
atgattacatttgccatcttcctgtctcttatcatgcttgtggaggtggctgtggccattgctggctatgtgtttagagacc
aggtgaagtcagagtttaataaaagcttccagcagcagatgcagaattaccttaaagacaacaaaacagccactattttgga
caaattgcagaaagaaaataactgctgtggagcttctaactacacagactgggaaaacatccccggcatggccaaggacaga
gtccccgattcttgctgcatcaacataactgtgggctgtgggaatgatttcaaggaatccactatccatacccagggctgcg
tggagactatagcaatatggctaaggaagaacatactgctggtggctgcagcggccctgggcattgcttttgtggaggtctt
gggaattatcttctcctgctgtctggtgaagagtattcgaagtggctatgaagtaatgtag

MAVEGGMKCVKFLLYVLLLAFCACAVGLIAIGVAVQVVLKQAITHETTAGSLLPVVIIAVGAFLFLVAFVGCCGACKENYCL
MITFAIFLSLIMLVEVAVAIAGYV**FRDQVKSEFNKSF QQQMQ NYLKDNKTATILDKLQKENNCCGASNYTDWENIPGMAK
DRVPDSCCINITVGCGNDFKES**TIHTQGCVETIAIWLRKNILLVAAAALGIAFVEVLGIIFSCCLVKSIRSGYEVM

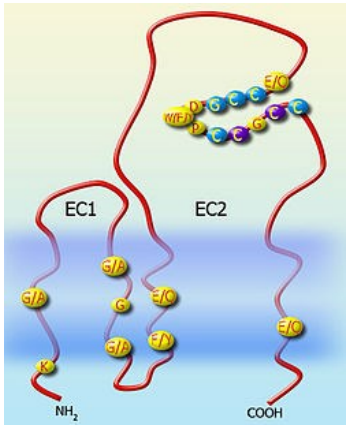

Figure 3) Tetraspanin a transmembrane protein
Tetraspanins have four transmembrane domains, two extracellular loops and contain a series of highly conserved amino acid residues. The key features are four or more cysteine residues in the EC2 domain, with two in a highly conserved 'CCG' motif. (Source: Wikipedia) These are removed in the construct so it abrogates its normal functions.

eGFP was cloned in between XhoI and and EcoRI. The sequence of the pmCD63-eGFP is shown below with eGFP highlighted in green

GCTAGCacacc**atg**gcggtggaaggaggaatgaagtgtgtcaagttttgctctacgttctcctgctggccttctgcgcctg
tgcagtgggattgatcgccattggtgtagcggttcaggttgtcttgaagcaggccattacccatgagactactgctggctcg
ctgttgcctgtggtcatcattgcagtgggtgccttcctcttcctggtggcctttgtgggctgctgtggggcctgcaaggaga
actactgtctcatgattacatttgccatcttcctgtctcttatcatgcttgtggaggtggctgtggccattgctggctatgt
gggagg**CTCGAG**Gagcaagggcgaggagctgttcaccggggtggtgcccatcctggtcgagctggacggcgacgtaaacggc
cacaagttcagcgtgtccggcgagggcgagggcgatgccacctacggcaagctgaccctgaagttcatctgcaccaccggca
agctgcccgtgccctggcccaccctcgtgaccaccctgacctacggcgtgcagtgcttcagccgctaccccgaccacatgaa
gcagcacgacttcttcaagtccgccatgcccgaaggctacgtccaggagcgcaccatcttcttcaaggacgacggcaactac
aagacccgcgccgaggtgaagttcgagggcgacaccctggtgaaccgcatcgagctgaagggcatcgacttcaaggaggacg
gcaacatcctggggcacaagctggagtacaactacaacagccacaacgtctatatcatggccgacaagcagaagaacggcat
caaggtgaacttcaagatccgccacaacatcgaggacggcagcgtgcagctcgccgaccactaccagcagaacaccccatc
ggcgacggccccgtgctgctgcccgacaaccactacctgagcacccagtccgccctgagcaaagaccccaacgagaagcgcg
atcacatggtcctgctggagttcgtgaccgccgccgggatcactctcggcatggacgagctgtacaag**GAATTC**ggtggcat
ccatacccagggctgcgtggagactatagcaatatggctaaggaagaacatactgctggtggctgcagcggccctgggcatt
gcttttgtggaggtcttgggaattatcttctcctgctgtctggtgaagagtattcgaagtggctatgaagtaat**gGATCC**

MAVEGGMKCVKFLLYVLLLAFCACAVGLIAIGVAVQVVLKQAITHETTAGSLLPVVIIAVGAFLFLVAFVGCCGACKENYCL
MITFAIFLSLIMLVEVAVAIAGYVGGSRIHPSGVTGLVPSLGDREKRDSLCPQGKYVHSKNNSICCTKCHKGTYLVSDCPSP
GRDTVCRECEKGTFTASQNYLRQCLSCKTCRKEMSQVEISPCQADKDTVCGCKENQFQRYLSETHFQCVDCSPCFNGTVTIP
CKETQNTVCNCHAGFFLRESECVPCSHCKKNEECMKLCLPPPLANVTNPQDSGTEFGGIHTQGCVETIAIWLRKNILLVAAA
ALGIAFVEVLGIIFSCCLVKSIRSGYEVMD

3.4 Exosome isolation

Different cell lines were plated in 15 cm dishes and transfected at ca 50 % confluency with CD63-EGFP using Lipofectamine 2000 in DMEM supplemented with 10 % FBS. After 4 hours, cells were washed and medium was replaced with OptiMem (GIBCO, 25 ml per dish) and cultivated for further 24 to 72 hours according to the experimental setup.

3.4.1 Ultracentrifugation (UC) for isolation of EVs

The EV isolation method by UC was adapted from Théry et al [56]. Supernatants were collected and subjected to two low speed spins, 300g for 5 min followed by 3000g for 10 min to get rid of cell debris and larger particles. The supernatant was subsequently filtered through a 0.22 µm filter. Syringe filters (Merck Millipore), 50ml Steriflip (Merck Millipore), or 250/500ml Stericups (Merck Millipore) were used. The final ultracentrifugation step was done at 120,000g for 70 min with a Beckman Coulter ultracentrifuge with Type 45 Ti fixed angel Rotor and 70ml Polycarbonate Bottle/Assembly. When indicated the EV pellet was resuspended in PBS and subjected to an additional PBS wash at 120,000g for 70 min. The final pellet was resuspended in 200-500ul PBS.

3.4.2 Ultrafiltration (UF) for isolation of EVs

The UF protocol involves the same initial low-speed spins and 0.22um filtration as that of the UC protocol. Instead of a high-speed ultracentrifugation at the final step, the cell culture supernatants were either spun at 3,500g for 15 min in 100-kDa molecular weight cut-off (MWCO) Amicon spin filters (Merck Millipore) or for larger volumes enriched in Amicon ultrafiltration devices of the appropriate size. In the standard procedure a 50 ml Amicon device was used with a 100-kDa molecular weight cut-off (MWCO) millipore membrane and N2 or argon 5bar gas pressure with up to 4 refills (200ml total volume/membrane) to enrich the ECV. The flow through was discarded after NTA loss of particle control and ECV were recovered from the membrane by 500ul – 1000ul PBS wash. In some cases, membrane was washed with 2 x 50ml PBS prior ECV recovery to further protein clearance.

3.4.3 Sucrose gradient (SG) for isolation of EVs

For exosome isolation via sucrose gradient, ten 350ul sucrose fractions with increasing (8-80%) sucrose was overlaid via freezing in dry ice between each step and topped with 12ml conditioned medium in 17ml Polyallomer Beckman tubes. The gradient was centrifuged after defrosting at RT for 65 hours at 120’000 g at 4 °C in a Beckman Optima Max ultracentrifuge and fractions were collected by quick freezing the gradient in dry ice, removing the tube and slicing 10- 20 frozen

“salami” fractions from the bottom with a razor blade. Each fraction was defrosted in an Eppendorf 1.5ml tube and sucrose content was determined by refractrometry. For subsequent FCS measurements 10ul sample were diluted 1:10 in PBS or water since 0- 8% sucrose does not have significant impact on diffusion time or molecular brightness. Alexa488 measurements in a sucrose dilution row confirmed that under these conditions changes in measured translational diffusion times due to viscosity and refractive index changes were negligible.

3.4.4 Gel Filtration with prior ultrafiltration (UF/GF) for isolation of EVs

Exosome isolation via UF/GF was essentially performed as described in Paper I (Ultrafiltration with size-exclusion liquid chromatography for high yield isolation of extracellular vesicles preserving intact biophysical and functional properties). Typically, 100-200 ml of the pre-cleared conditioned medium was then concentrated to a volume of 0.5-1 ml on an AMICON ultrafiltration device as described above. Enriched medium was then loaded onto a Superdex200 column (GE Healthcare) connected to an ÄKTA prime FPLC instrument (GE healthcare) equipped with a UV flow cell. 0.5 to 1 ml ECV were loaded via loading loop in the circuit of the ÄKTA. Gel filtration was performed at 4°C using sterile filtered 50 mM Tris-buffer (flow rate 0.5 ml/min). Ninety-six individual fractions of 200 □l each were collected and NTA and/or FCS was performed in at least every second fraction. For Western blotting, fractions were pooled (4 fractions each, omitting one fraction in between pools) and further concentrated to a volume of 30 ul on an Amicon 10-kDa MWCO spin columns (Millipore).

3.4.5 Exosomes isolation using ‘ExoQuick’

Conditioned cell culture medium was collected in sterile Falcon tubes and centrifuged at 3,000 g for 15 minutes at 4°C to remove dead cells and cell debris. The supernatant was transferred to a new sterile Falcon tube and was supplemented with ExoQuick exosome precipitation solution (SBI, #EXOQ20A-1). 1 volume of ExoQuick to 2 volumes of Cell medium were incubated overnight (min 12h) at 4°C. The solution was subsequently centrifuged at 1,500 g at 4°C for 30 minutes. The supernatant was discarded and the remaining drops were collected at the bottom of the tube by centrifugation at 1,500 g at 4°C for 5 minutes. The remaining solution was discarded, without disturbing the pelleted material. The precipitated material was resuspended in 1/10 of the original volume in PBS or water (GIBCO, #20012019) supplemented with protease inhibitors (Roche, #11873580001). The resuspended material was then subjected to TEM, to an NP40s-dependent FCS analyses and further experiments.

3.5 Exosome characterization

3.5.1 Western Blotting

Aliquots of sucrose gradient fractions or pooled and spin column concentrated gel filtration fractions were heated in SDS sample buffer for 10 minutes at 70°C and electrophoresed on 4-12 % NuPage gels (Life Technologies). Proteins were transferred to Protran nitrocellulose membranes (Whatman) using a SD Transblot system (BioRad) and blocked for 1 hour in PBS with 5 % (w/v) milk powder (BioRad) at RT prior to primary antibody incubation either for 2 hours in blocking buffer at RT or overnight at 4°C. Immune complexes were visualized using HRP-conjugated secondary antibodies (Santa Cruz) on a Biorad XRS system.
Antibodies: CD63 (sc-15363, Santa Cruz, 1/500); PDC6I/Alix (ab117600, Abcam, 1/500 dilution), Tsg101 (ab83, Abcam, 1/500 dilution); Lamp2 (ab25631, Abcam, 1/500 dilution); Calnexin (ab22595, Abcam, 1/10'000 dilution); GFP (ab290, Abcam, 1/1000 dilution); Calreticulin (A301-130A, Bethyl laboratories, 1/10'000 dilution); Ago2 (clone 11A9 Ascenion, 1/1000 dilution; 4G8, Wako Chemicals, 1/1000 dilution); b4-GalT1 (HPA010807, Atlas, 1/500 dilution); SmB (S0698, Sigma, 1/1000 dilution).

3.5.2 Nanoparticle Tracking Analysis (NTA)

Label-free particle size and concentration determination was performed on a LM NTA instrument (NanoSight). For each sample a dilution row of 1:100 to 1:10'000 was prepared with pre-filtered PBS in 2ml glass vials and analyzed. Measurements of 1 - 4 x 10^8 particles/ml are most valid and represent the dynamic range of the instrument. With a camera gain of 500, full detection range and 90 second recordings all camera settings as well as analyses parameters (detection threshold of 2, minimum expected particle size of 50 nm, fixed minimal track length of 4) where kept constant throughout all measurements to make these comparable.

3.5.3 MS-Proteomics

UF-GF isolated exosomes were separated by SDS-PAGE on a NuPAGE 4-12 % (Life Technologies) gel and stained with a Colloidal Coomassie stain (Sigma). Sixteen equal sized slices were excised from each of the gel lanes. In-gel digestion and subsequent identification by liquid chromatography coupled with tandem mass spectrometry was performed as described [110], with the exception that a mix of Trypsin and Endopeptidase Lys-C (Promega) was used instead of trypsin alone. Database searches were done with Mascot (version 2.4, Matrix Science) against the UniProt database (release of April 2013) concatenated with a reversed version and supplemented with known contaminants (such as trypsin, BSA and commonly used tags). Protein identifications were validated and summarized in Scaffold (version 4.0.3, Proteome Software Inc.), setting the protein identification

threshold at a 1 % false discovery rate (FDR) in the reversed database. At these settings peptide FDR was 0.05 %. The resulting protein list is provided as Supplementary Table 1 of manuscript I (*Quantitative profiling of exosome parent-recipient cell pairing by high content screening using CD63-emGFP vesicle labelling)*. Keratin contaminants were removed and are listed separately. Trypsin and Lys-C were also removed from the list. Total spectral count is provided as a semi-quantitative measure, as well as the number of unique peptides for each protein. The spectral count is shown without correction for the total number of assigned spectra in each sample (24'626 for GFP-CD63 and 21'234 for the untransfected sample).

3.5.4 Fluorescence Correlation Spectroscopy (FCS)

FCS was performed on a Clarina II Reader (Evotec Technologies) with 488 nm argon ion laser excitation at 50 µW, a 40x water emersion 1.15 N.A. objective (UAPO Olympus), a 488/633 nm major dichroic mirror in the excitation path and a HQ535/50m filter in the emission path. In-focus light was collected through a 50 µm pinhole using a SPCM-AQR-13FC avalanche photodiode (Perkin-Elmer Optoelectronics). The confocal volume was calculated in approximation according to [111] using the measured diffusional correlation time τ_{diff} of fluorescent Alexa488 free dye standard, the known translational diffusion coefficient of Alexa488 (Molecular probes; D = 280 µm^2/s) and the axis ratio fitted from calibration measurements.

FCS data analyses: Typically for each sample, several dilutions were made and measured in a 96-well glass bottom plate (Whatman, GE Healthcare) with 30 repetitive measurements of 10 s each. NP-40S at 1% v/v (Cambridge Bioscience, Cambridge, UK) was used to induce vesicle disruption. Disruption of vesicles was confirmed by dynamic light scattering. Autocorrelation curves were fitted with a one- or two-component two-dimensional diffusion model [112] [113] to extract translational diffusion times, particle numbers and molecular brightness's. For a two-component two-dimensional diffusion model we made the assumption that the two major CD63-EGFP positive components in the isolations are intact EVs/large vesicles and a secondary subpopulation of smaller, potentially disrupted vesicles. We then analyzed all detergent treated samples with a one component fit to derive the translational diffusion time of disrupted vesicles. Alexa488 measurements in an EV sample with and without NP40s confirmed that under these conditions changes in measured translational diffusion times due to viscosity and refractive index changes were negligible.

The average value from these measurements was then defined as the translational diffusion time of the putative small, disrupted particles in a two-component fit of the detergent free samples. This allowed to fit the data with

significantly improved Chi2 and delivered a reasonably homogeneous second population with translational diffusion times corresponding to a hydrodynamic radius in the range of ca. 70-100 nm.
FCS measurements from gel filtration samples were typically analyzed with a one component fit since this method already separates the fluorescent subpopulations by size. In contrast ultrafiltration and ultracentrifugation exosome isolations are contaminated by free GFP and a two component fit does clearly improve the particle analyzes. To further improve the reliability of the measurements up to 3 outliers of the 30 10 second measurements were excluded from the final dataset. An outlier was defined by a value which was typically 5 to 10 fold larger or smaller than the average value. Background fluorescence was determined by corresponding non labeled samples and due to auto- fluorescence background in cell medium and fetal calf serum a minimal molecular brightness thresh hold was set in some experiments when indicated.

3.5.5 Electron microscopy (EM)

3.5.5.1 Transmission Electron Microscopy (TEM)

A 10ul sample drop was topped with a glow discharger (custom made glow discharger) treated Formvar polymer coated grid (Plano Copper G2300C, mesh size 200- 400). ECV were bound on its surface during a 20 min incubation before the grid was then passed on onto 2 additional PBS drops (incubation 2min each) and 4 water droplets (incubation 1min each) for washing and salt reduction. Subsequent the sample was exposed to 2% uranylacetat in H2H for 5min before the UA was partially removed by a filter paper (Whatman #1). The UA rest was dried on the grid for minimum 10min before it was placed in a grid holder. All samples were prepared in duplicates or triplicates and all preparation steps are done at RT. The grids were then visualized in the transmission electron microscope (Philips CM10, equipped with Veleta camera SIS) at 80kV.

3.5.5.2 Cryo-Transmission Electron Microscopy (Cryo-TEM)

A 4 ul aliquot of sample was adsorbed onto glow-discharged holey carbon coated grid (Quantifoil, Germany), blotted with Whatman filter paper and vitrified into liquid ethane at −178°C using a Vitrobot (FEI, Endhoven, Netherlands). Frozen grids were transferred onto a Philips CM200-FEG electron microscope (FEI, Endhoven, Netherlands) using a Gatan 626 cryo-holder (GATAN Inc, Pleasanton, USA). Electron micrographs were recorded at an accelerating voltage of 200 kV and a nominal magnification of 50’000x, using a low-dose system (10 e−/Å2) and

keeping the sample at −175°C. Defocus values were ranging from −2 µm to 3 µm. Micrographs were recorded at 4K × 4K CMOS camera (TVIPS, Germany).

3.5.5.3 Scanning Electron Microscopy (SEM)

Cells were grown on Thermanox coverslips (Thermo Scientifc Inc, Nunc). After a quick wash (less than 10 seconds) in fresh culture medium without protein, cells were fixed with 2 % paraformaldehyde (Electron Microscopy Science, Hatfield, USA) and 2.5 % glutaraldehyde (Electron Microscopy Science, Hatfield, USA) in 0.1 M cacodylate buffer (Sigma Aldrich), pH 7.4. Cells were rinsed in 0.1 M cacodylate buffer (3 x 5 minutes). Dehydration was performed in a graded ethanol series (30%, 50%, 70%, 90%, 95, 100% ethanol, 3 x 2 minutes each step). After dehydration, specimens were rinsed with hexamethyldisilizane (Sigma Aldrich) and dried in an oven (60°C for 2 hours). Samples were mounted on aluminum stubs by fixing the coverslip with carbon double-sided carbon tape, and sputter coated (Quorum SC7620) with gold/palladium (5-8 nm). Cells were examined with a scanning electron microscope (Versa 3D, FEI, Endhoven, Netherlands) using the ETD detector.

3.5.5.4 Atomic force microscopy (AFM) & TIRF microscopy for exosome characterization

Samples were prepared for AFM following a protocol adapted from Tian Tian, 2010 [82]. A drop of sample in buffer was placed on a glass slide in a humidity chamber for 10- 20min, so that vesicles enrich by slow water evaporation and sediment on the glass. Buffer salt and water was carefully removed with N2 flow to reduce salt crust formation.

AFM (bruker catalyst) and TIRF imaging (LeicaDMI6000, TIRF module) were performed in collaboration with Jane Hyötylä (Biozentrum Basel). In the subsequent analyses with gwyddion and Image j one image dataset from AFM and TIRF was manually overlaid (image J) since TIRF and AFM were not aligned for parallel imaging.

3.6 Exosome recipient cell interaction

3.6.1 Live cell imaging

3.6.1.1 Confocal and DIC live cell microscopy

For the combined confocal fluorescence and DIC live cell imaging cells were seeded into an 8-well m-slide (ibidi) and pre-stained prior to exosome addition as

indicated in each experiment. Cell membrane was labeled by CellMask Deep Red (dilution 1:1000 for at least 2 minutes, Life Technologies), MVB were labeled by N-rhodamine (Rh) or TopFluor-labelled (Fl) phosphatidylethanolamine (NRhPE & NFlPE). 5ul TopFuor Sphingomyelin or TopFluor Cholesterol (dissolved in Dichlormethan) was added in 1ml optiMem. After 10min incubation at 37°C cells were washed minimal 3 x with OptiMem and fresh medium was applied. NRhPE and NFlPE were dissolved in Ethanol and similar to the other lipids 5ul were added to OptiMem and then washed for imaging.
Endoplasmic reticulum and Lysosomes were labeled with ER Tracker Red (500 nM, for at least 15 minutes, Life Technologies) and LysoTracker Green (dilution 1:1000, for at least 60 minutes, Life Technologies) according to the manufactures protocol. Actin was labeled by transfection with CellLight Actin-RFP (Life Technologies) 24 hours prior to imaging. Typically, images were acquired on a confocal LSM710 microscope with Big-detector (Zeiss) with a 100x or 63x oil 1.4 NA PlanApochromat DIC objectives and temperature, gas and humidity control unit (Life Imaging Services). Differential interference contrast (DIC) was set up using the transmitting laser light of excitation as light source and the TPMT as detector. Auto fluorescence was detected by imaging unstained cells and fluorescence bleach through and cross talk was determined by imaging the samples with identical settings but reducing the appropriate laser power to zero.

3.6.1.2 Single vesicle imaging

Exosomes from CD63-emGFP/CD63-mCherry double transfected HEK293 cells were imaged either by confocal (63x Oil, NA 1.4 Plan-apochromat objective on a LSM710 microscope with Big-detector- Zeiss) or widefield (60x oil, NA 1.42 Plan Apo N objective on a DeltaVision Core microscope, Olympus IX71 stand and Photometrics CoolSNAP HQ2 CCD camera, – API) fluorescence microscopy after spotting onto coverslips. Vesicles were detected as light diffraction limited GFP or mCherry fluorescent spots of uniform size corresponding to the point spread function of the microscope (figure 5), confirming recovery of single vesicles. As a control and for evaluation of chromatic aberrations point spread functions with fluorescence 100 nm and 200nm tetraspec beads (Invitrogen) (figure 4) were imaged. Colocalization was quantified based on overlap of the point spread functions in the two fluorescent channels to derive the number of GFP (G), mCherry (R) and GFP/mCherry (RG) double positive vesicles

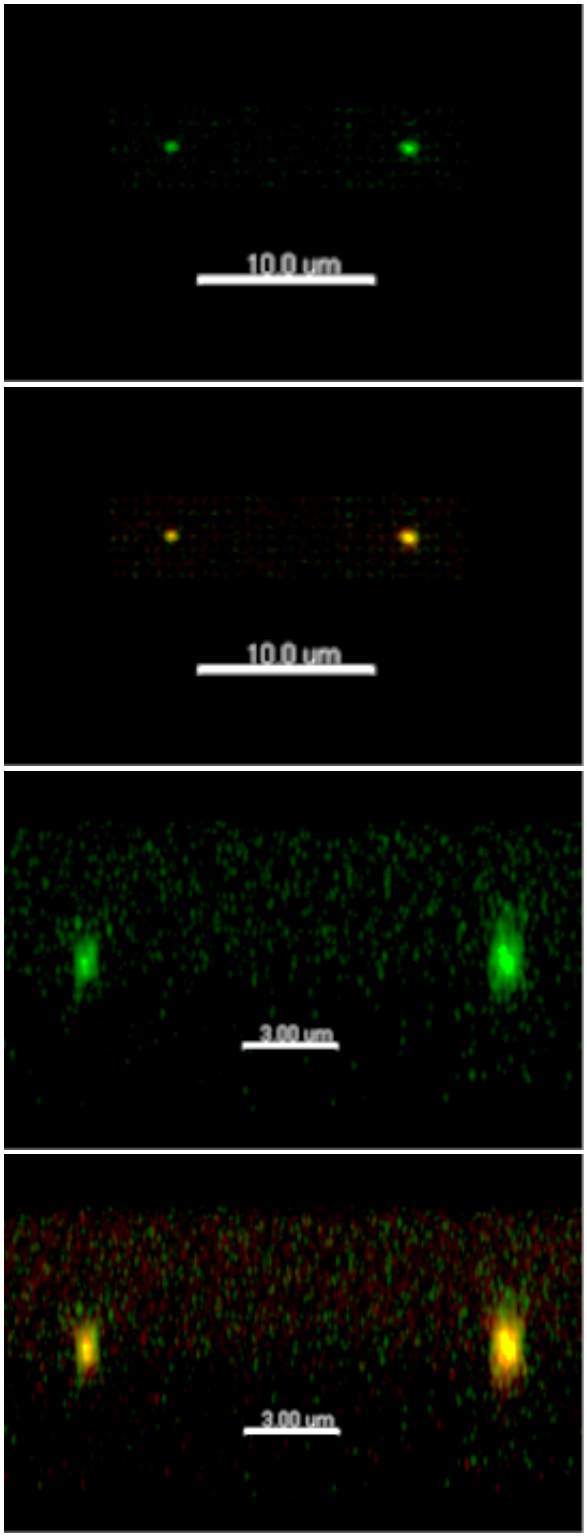

Figure 4) PSF measurement at the LSM710 (63x NA 1.4)

Determination of chromatic aberration and alignment with 100 nm and 200 nm Tetraspeck beads. Left: excitation 488, Right: excitation 488 and 561, Top XY view, bottom XZ view

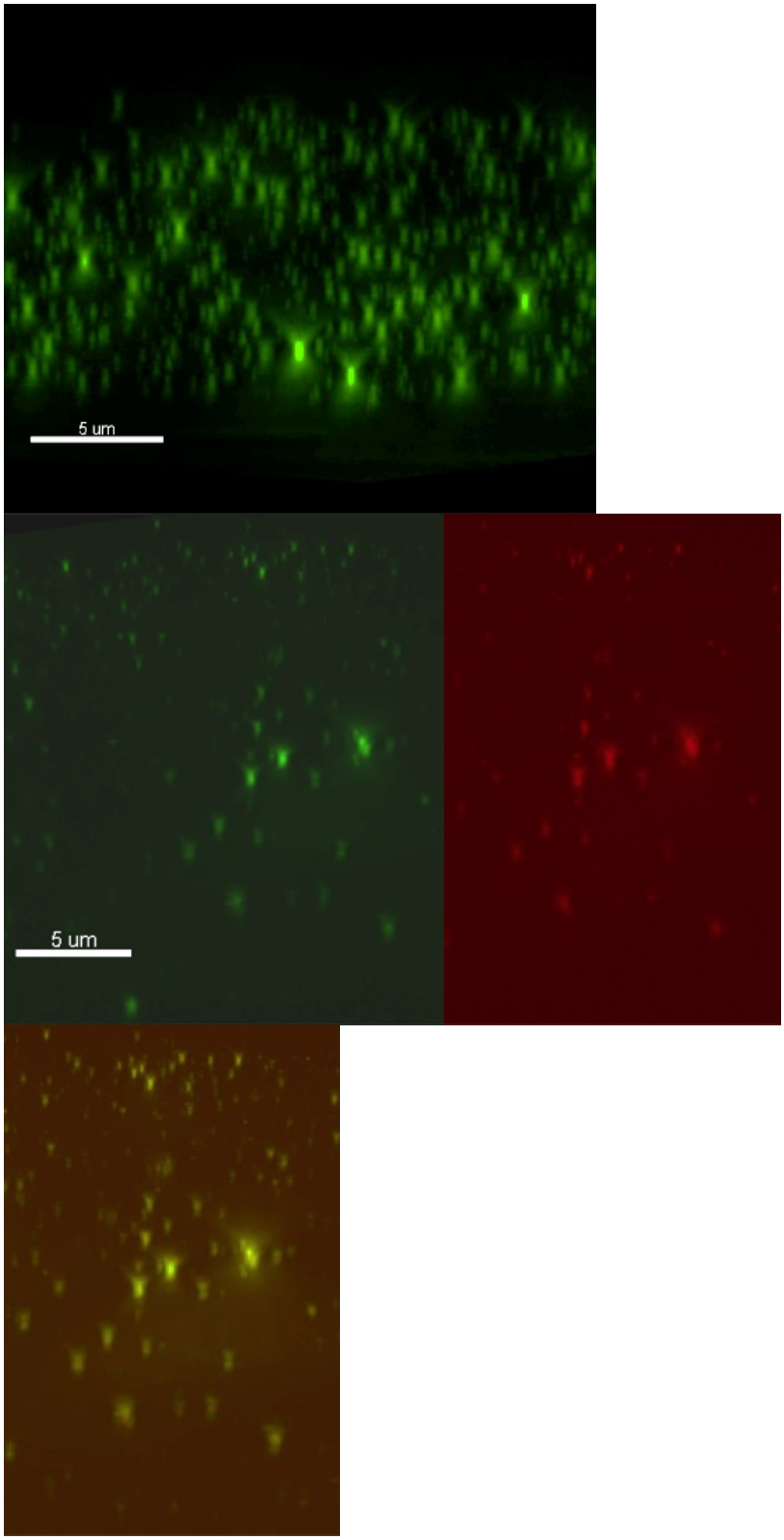

Figure 5) Imaging of fluorescent labeled exosomes on coverslip.
Top: CD63emGFP labeled exosomes, below CD63 emGFP-mCherry labeled exosomes excitation 488nm, 651nm and overlay. All Exosomes appear as PSF similar to the 100 nm and 200 nm calibration beads.

3.6.1.3 TIRF live cell microscopy

For live cell TIRF imaging, human fibroblasts were transiently transduced with Adeno-Lifeact-mCherry and seeded onto line substrates or 2D substrates prepared as described in [102] 4 hours prior to acquisition. TIRF microscopy (Roper Scientific) was performed with a Nikon TI Eclipse inverted stand equipped with a PlanApo 60x TIRF Objective, a Photometrics Evolve EMCCD camera, 491 nm and 561 solid-state laser diodes and was controlled using Metamorph imaging software. Typically fife cell positions per experiment were defined and subsequently imaged within 20-30 sec adding up to a 20 to 60 min time lapse. Fluorescent exosomes were quantified and characterized by FCS and typically added 5-10 minutes prior to image acquisition unless specified otherwise.

3.6.2 Image analysis

Confocal image stacks time series, confocal image plane time series and TIRF time lapse data were imaged with frame rates and time frames as indicated. Particles tracking and trajectory analysis was performed with the Imaris x64 (Bitplane) Particle Tracking Analysis module. For co-localization studies stacks were imaged with a Leica Sp5 HyD imaging setup using 60x 1.4 NA PlanApo Objective with 2 color sequential line scanning, 130 nm z-sectioning and 40 nm xy oversampling. Stacks were deconvolved with Huygens remote manager (automatic threshold) and then analyzed with the JACoP plugin [114] for Fiji [115].

3.6.3 Screening

In preparation of exosome uptake screenings relevant parameters were determined in collaboration with Justin Hean and Dominic Trojer. Since several popular fixation methods, e.g. PFA, quench the activity of GFP, in a first step a panel of various fixatives was assessed for their capacity to preserve GFP fluorescence and adequately fix cells to the plate surface. Penfix (Thermo Scientific) turned out to preserved GFP fluorescence well (almost comparable to live cells) and in parallel keeps levels of background fluorescence low. In result penfix, with the best signal to noise ratio was used for all screening experiments as follows: recipient cells were washed with PBS 5x and fixed for 20 minutes at room temperature after incubation in 96 well plates (ibidi). The fixative volume in presence of 1 ug/ml Hoechst (Life Technologies) and 0.02 % (v/v) CellMask Deep Red (Life Technologies) was typically 50% of the media that the cells were cultured. After fixing, cells were washed 5x with PBS and then stored in PBS. Subsequent imaging was performed on the Operetta (Perkin Elmer), using the 40x or 20x wide objective. Harmony software was used to determine overall GFP intensity per well and Mean GFP spots per cell per well. The assay was additionally scaled down from the 96well to a 384 well format. Dose response of exosome

uptake as well as time response of exosome uptake was then characterized in both formats. The typical procedure was performed as followed: 1500 Huh7 cells were seeded per well into a Greiner 384 well plate. Cells were cultured in 30 ul per well in 10% FCS DMEM. After 4 to 6 h the Huh7 cells had settled and were co-incubated with exosomes at pM concentrations as indicated for 20 hours (in triplicate). Where necessary, volumes were adjusted to maintain the 30 ul of media. Cells were fixed and stained as previously described using PenFix. Cells were stained with CellMask Deep Red plasma membrane stain and Hoeschst, in doing so the Operetta software could assign perimeters and nuclei to individual cells. Washing and fixing were done in an automated fashion at this point. It is documented in the literature that cellular confluency affects uptake of viruses, thus effects of cell confluency were investigated for exosome uptake. Huh7 cells were seeded in the 96 well plate at 0, 1000, 2000, 3000, 4000, 6000, 8000, 10 000, 12 000, 15 000 cells per well and left to establish overnight. Similarly, in the 394 well dish, cells were seeded at 0, 500, 1000, 1500, 2000 and 2500 cell per well. After 24 h exosomes were added to the cells at a final concentration of 10 pM per well. Cells were washed, stained, fixed and analyzed as previously described.

3.7 Lipid nanoparticle formulations

5'-Cy3 labeled siRNA [116] was mixed in a 1:5 ratio with unlabeled siRNA and formulated as described in detail in [117] . Briefly, the LNPs were formed by mixing equal volumes of lipid solution dissolved in ethanol with siRNA dissolved in a citrate buffer by an impinging jet process. The lipid solution contained a cationic lipid [117] , a helper lipid (cholesterol) and a PEG lipid in a ratio of 50:46:4 at a siRNA concentration of 1 mg/ml. The LNP solution was then diafiltered with a MWCO-100 kDa membrane, sterile filtered and stored at 4°C. The vesicles typically had a diameter of ca 150 nm.

4 Manuscripts of this Thesis and Extended Results

In this section I will summarize and discuss the results obtained during this thesis, largely structured by including three manuscripts (paper I, manuscript I and II). In addition, related data which are not shown in any of the manuscripts are also detailed in this section.

4.1 Exosome reagents and methods: Toolbox generation

4.1.1 Methods for analytical characterization

In the field, the definition as well as qualitative and quantitative characterization of exosomes is based on their physicochemical properties and content. For our studies we therefore first established a variety of methods for exosome characterization, including measurements of density (i.e. by sucrose gradients), size (Dynamic Light Scattering and Nanoparticle Tracking Analysis), shape (Electron Microscopy) and single molecule fluorescence (Fluorescence Correlation Spectroscopy). In addition, RNA and protein cargo was characterized by RT-qPCR and Western blot analysis, respectively. Because of its potential informative value and straightforward sample preparation we also investigated the application of atomic force microscopy (AFM) (figure 6) coupled with TIRF (figure 7) for exosome characterization (Biocenter/University Basel, Janne Hyötylä group Roderick Lim).

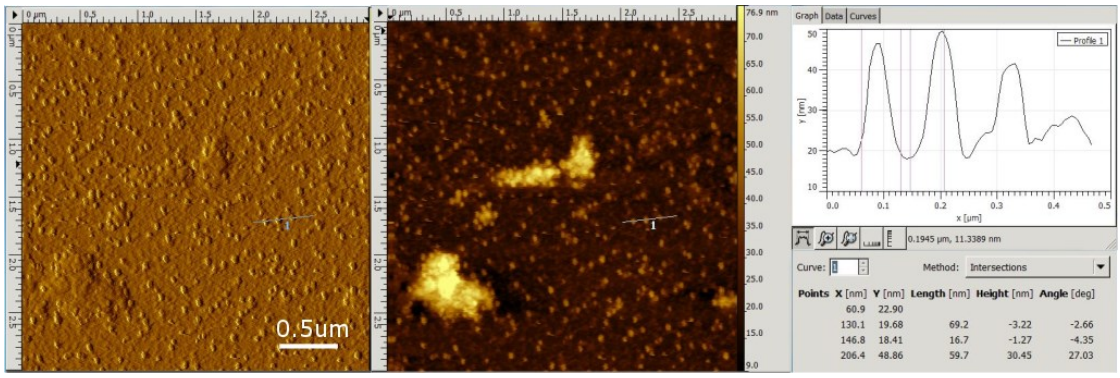

Figure 6) Exosome characterization by AFM

Extracellular vesicles isolated from Top Fluor Sphingomyelin stained HeLa cells. Left and middle image shows topographic views of an exosome sample. Bright colors in the middle image represent exsosomes as high bulges. Right image visualizes the topographic profile of the line drawn in middle image. The peak length measured on the x-axis represents the size of the vesicle (70 and 100 nm).

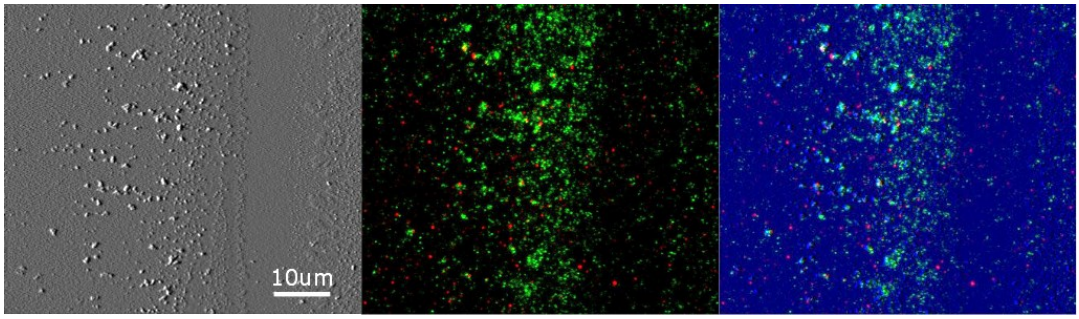

Figure 7) **Differentiation of single vesicles by combined AFM / TIRF imaging**
Proof of principle for differentiation of orthogonally labeled vesicles within the same sample. HeLa TFSM labeled exosomes were mixed with siRNA-Cy5 labeled Lipid Nanoparticles and imaged by AFM/TIRF. (A) AFM image, (B) TIRF image; (C) Overlay. Green: TFSM (exosomes). Red: Cy5 (LNP).

AFM in combination with TIRF proved to be a powerful method to discriminate individual particles and assign fluorescence directly to morphological visualization to single vesicles – an unsolved issue in the exosome field. Additionally, it allowed determination of size and shape of the vesicle with a resolution of ca 5 nm. While we conclude that this method would be a method of choice for exosome characterization, unfortunately we did not have the chance to routinely access the instrument and thus were not able to characterize all exosome samples used in this study by this technology.

An alternative technology for both, qualitative but in particular also quantitative exosome characterization is the application of single molecule techniques. Using Fluorescence Fluctuation Spectroscopy, we are able to perform absolute quantifications of particle numbers in the low nanomolar range and gather additional single particle information like hydrodynamic size and molecular brightness. In particular FCS data analysis with a two component fit strategy enables additionally an analytical separation of different subpopulations of fluorescent particles and thereby to dissect and quantify e.g. small (free fluorophores, free cargo) from large (intact) vesicles or loaded fluorescent cargo within the same sample (figure 8).

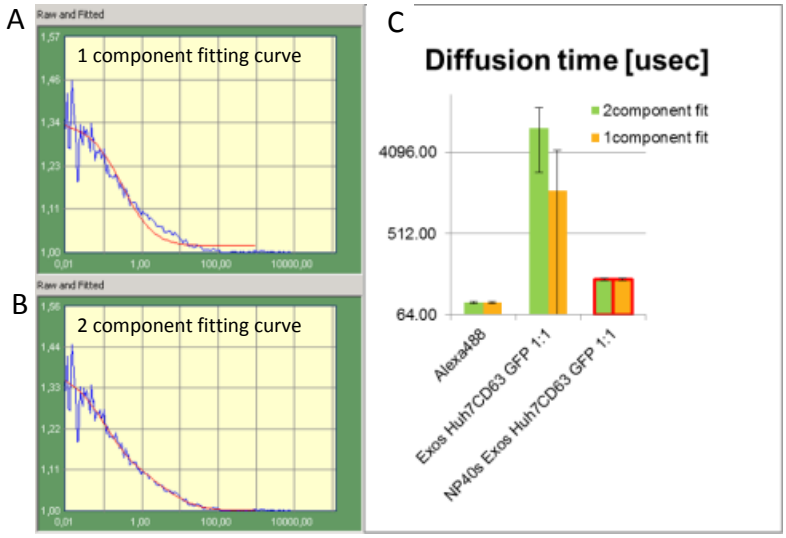

***Figure* 8*)* Exosome characterization by FCS analysis**

(A) Autocorrelation curve (blue line) overlaid with one component fitting curve (red line); (B) Autocorrelation curve (blue line) overlaid with two component fitting curve (red line); (C) Representation of a 1 and 2 component fit diffusion time (size) analysis with and without detergent treatment. Green bars represent the two component fit analyzes; orange bars represent the one component fit analyzes. The red frame marks samples treated with detergent.

This is of particular note, as there is still a gap in the exosome field for quantitative information, and most data are based on bulk protein or RNA amounts rather than particle numbers and single particle cargo concentrations. In contrast to Lightscattering or Nanoparticle tracking analyses measurements these methods are limited to fluorescently labeled particles - which can in fact be an advantage when exosome specific labels are used. This now allows quantifying exosomes directly in medium and thereby calculating absolute yields for the different isolation methods, together with additional single molecule information such as diffusion times and molecular brightness – providing information about how many fluorescent molecules per particles are present.

To determine the Influence of laser intensity on potential photobleaching of the relatively slow diffusing vesicles we measured Alexa 488 as free dye in two different concentrations as well as samples from different sucrose gradient fractions of a CD63-emGFP exosome isolation with laser intensities from 25 uW to 200 uW (figure 9a and 9b).

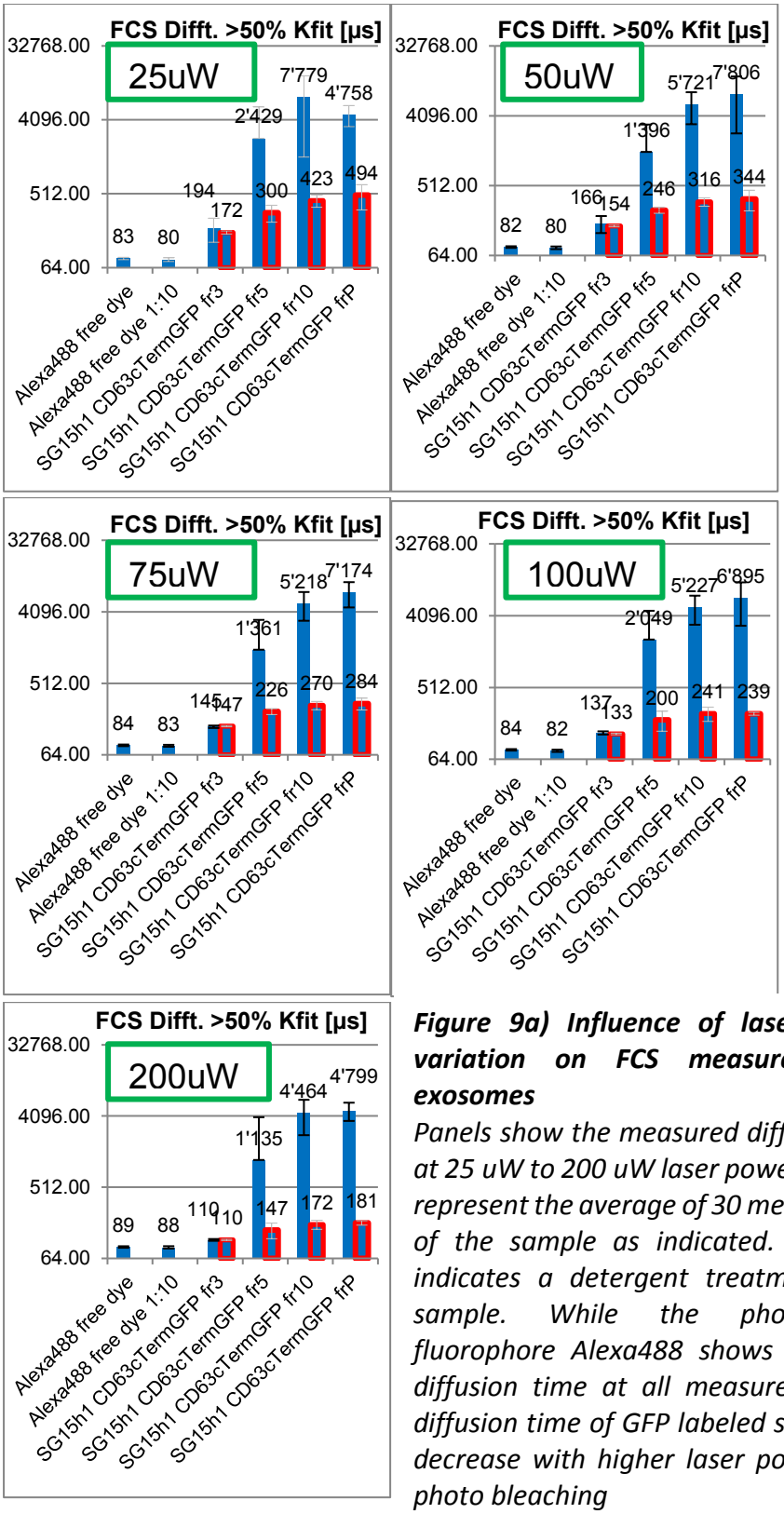

Figure 9a) Influence of laser intensity variation on FCS measurements of exosomes

Panels show the measured diffusion times at 25 uW to 200 uW laser power. Blue bars represent the average of 30 measurements of the sample as indicated. Red frame indicates a detergent treatment of the sample. While the photo stable fluorophore Alexa488 shows a constant diffusion time at all measurements, the diffusion time of GFP labeled sample does decrease with higher laser power due to photo bleaching

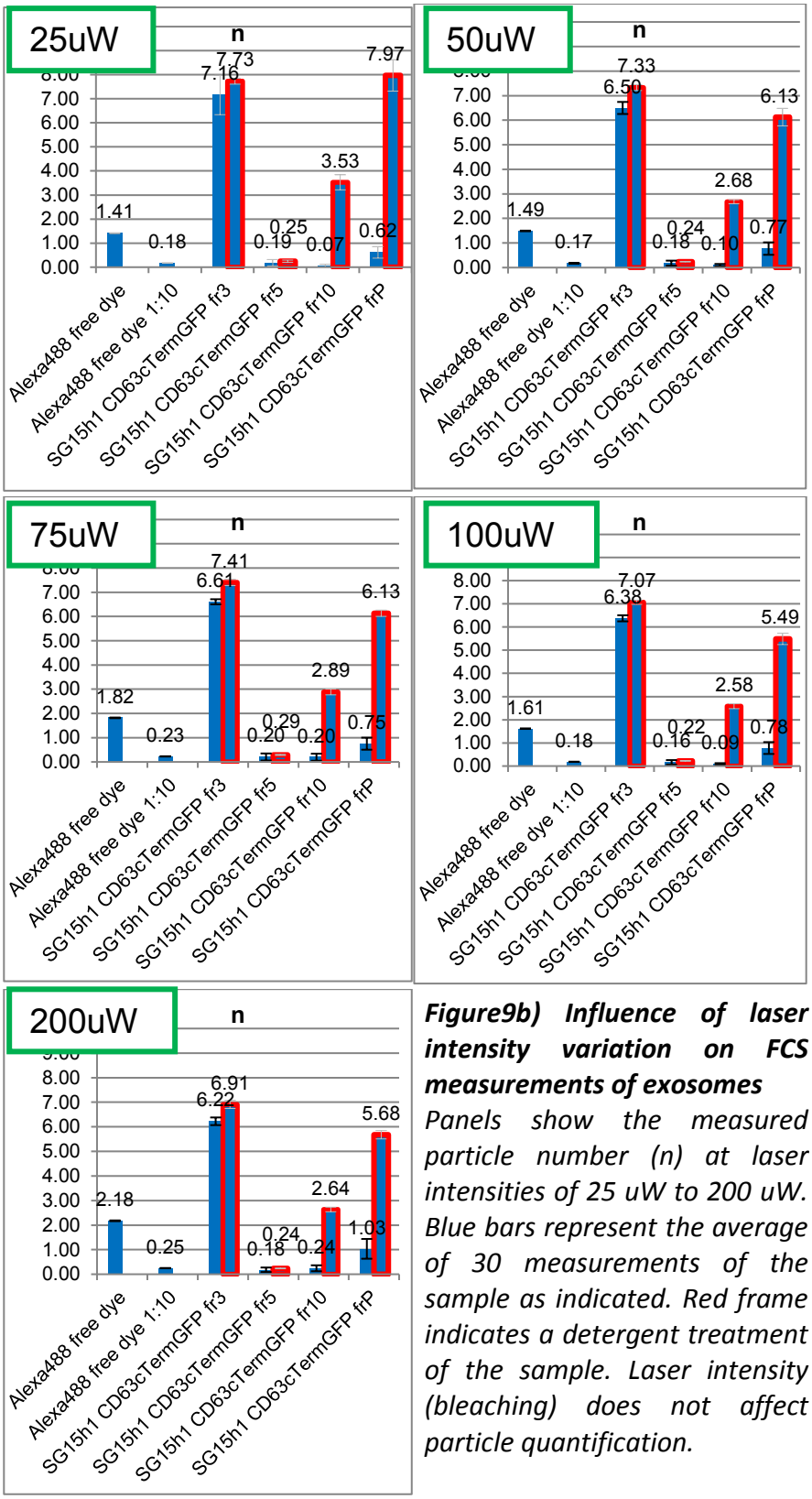

Figure9b) Influence of laser intensity variation on FCS measurements of exosomes

Panels show the measured particle number (n) at laser intensities of 25 uW to 200 uW. Blue bars represent the average of 30 measurements of the sample as indicated. Red frame indicates a detergent treatment of the sample. Laser intensity (bleaching) does not affect particle quantification.

As expected, both the molecular brightness and count rate increased with the excitation laser power, whereas at the same time the number of particles (n) did not significantly change. However, the measured diffusion time decreased with higher laser powers, which can be explained by GFP bleaching during the measurement in the confocal volume. Due to this measurement we chose 50 uW as the lowest stable laser power with decent molecular brightness of CD63-emGFP particles for all following measurements.
Additionally, we used a mild detergent mediated vesicle disruption to determine whether the analyzed particles are lipid based or possibly represent protein aggregates which typically do not dissociate under this treatment.

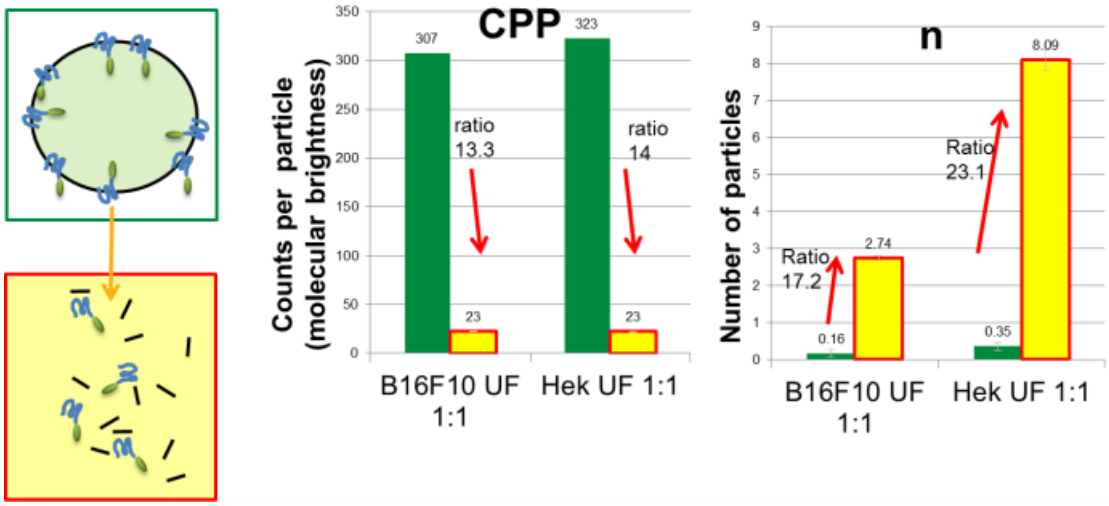

Figure 10) **Determination of number of CD63-GFP molecules per exosome by FCS**

The scheme on the left visualizes the effect of the detergent treatment of the vesicle. The vesicle carries multiple fluorophores but is recognized as one particle. By vesicle disruption CD63-emGFP molecules are separated and diffuse as single fluorophores. The middle bar graph shows the effect of vesicle disruption on the molecular brightness (CPP) in two different exosome samples. The intact particle (green bar) is much brighter than the single fluorophore (yellow bar). Red frames indicate detergent treatment. The right bar graph shows the effect of vesicle disruption on the particle number (n) in two different exosome samples. The particle number increases with detergent disruption. The ratio of the particle numbers before and after disruption represents the average number fluorophores per particle.

Exosomes showed a ca 5 to 20 times higher average molecular brightness than the detergent treated species. In parallel with the detergent treatment the number of fluorescent particles inceased in a similar ratio. This effect can be explained by an dissosiation of vesicles carrying multiple fluorescent molecules. Additionally, the population of fluorescent particles within the sample became more homogenous upon detergent dissosiation and showed translational diffusion times perfectly in line with free CD63-emGFP as measured in

independent controls. The ratio of particle numbers of detergent treated and non treated sample represents an average of the number of fluorescent molecules per exosome. Due to possible bleaching and quenching effects the number of particle measurements appeared more reliable than the molecular brightness data.

4.1.2 Tools for studying cell uptake & trafficking

4.1.2.1 Labeling

Specific fluorescent exosome labeling is the method of choice for studying inter- and intra-cellular particle trafficking. The size of 20 to 150 nm particles is too small for standard diffraction limited bright field microscopy but is clearly in the scope of fluorescent microscopy methods like confocal and TIRF life cell imaging.

Table 6 Exosome labeling strategies

Labeling strategy	Labeling of Exosomes by labeling parent cells	labeling of Exosomes post isolation
Labeling method	MVB targeting lipid dyes transfection of fluorescent exosome marker constructs	lipophilic dyes non selective labeling (NHS chemistry/PL chemistry)
Advantages	specific labeling, no additional cleaning after isolation	No manipulation of parent cells, labeling of exosomes from body fluids possible, choice variety of dyes
Disadvantages	Parent cell manipulation, not all cell lines efficiently transfectable, not applicable to exosomes from body fluids	Invariably stains all vesicles, potential self aggregation, additional purification step needed.

There are two general different labeling strategies; either indirectly via labeling the parent cells or by labeling exosomes post isolation (table 6). In our hand the second strategy is not the strategy of choice since the exosome isolation protocols are not able to differentiate between different extracellular vesicle types and the issue of low yields gets worse by the necessary additional washing steps.
To gain in specificity and not label all vesicles in the medium, we decided to label exosomes by labeling the structures in the parent cells from which exosomes derive using markers which are known to be enriched in exosomes. As exosomes are highly enriched in lipid raft markers like sphingomyelin and cholesterol [98] we first established a method to label exosomes indirectly by staining parent cells with these lipids as fluorescent derivatives prior to exosome isolation and

characterization. The stained parent cells showed a strong accumulation of TopFluor Cholesterol, TopFluor Sphingomyelin and NRhPE/NFlPE in late endosomal / MVB compartments (figure 11), and released fluorescent exosomes into the medium. Based on FCS measurements, this method yielded detergent sensitive fluorescent exosomes with expected translational diffusion times (Figure 12). FCS measurements also uncovered a contamination with lipid dye micelles as well as free dye within the samples. Therefore, we decided to focus on a second strategy with labeling exosomes by fluorescent markers. For this approach we first cloned lamp2b-GFP and lamp2b-mCherry expression constructs. Since lamp2b is also a Lysosomal marker and expression levels as well as GFP brightness was relatively low, we focused on another exosome transmembrane protein, CD63 and generated an emGFP tagged expression construct by TOPO cloning into a pCDNA vector (Figure 2). This expression vector yielded high CD63-emGFP expression levels with a comparable localization to endogenous CD63 (Figure 1). As detailed in Paper I, manuscript I and II, CD63-emGFP positive particles with exosome characteristics (density, size, detergent sensitivity, protein content, shape) were then successfully isolated from medium of Hek293, Huh7 and B16F10 cells transfected with this construct. The tetraspanin CD63 has meanwhile increasingly emerged as one of the most commonly used exosome markers in the field, and we have expanded the fluorescent label versions to mCherry as well as a double labeled mCherry-emGFP fusion construct for exosome double labeling experiments (manuscript I (*Quantitative profiling of exosome parent-recipient cell pairing by high content screening using CD63-emGFP vesicle labelling)*).

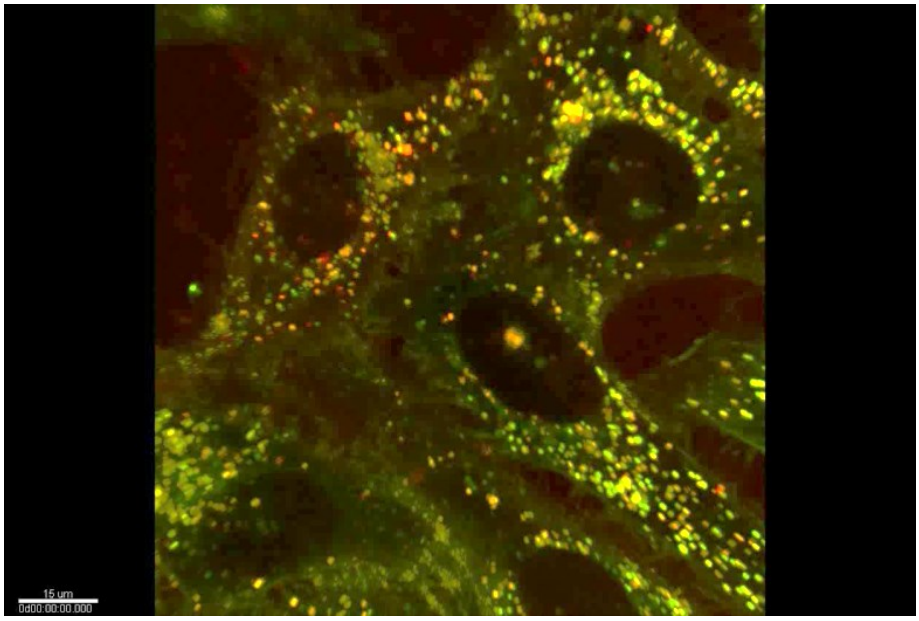

Figure 11) Parent cell labeling with lipid dyes.
HeLa cells labeled with TopFluor Sphingomyelin (green)
and NRhPE (red). (Zeiss LSM710inv. 100x 1.4NA life cell imaging)

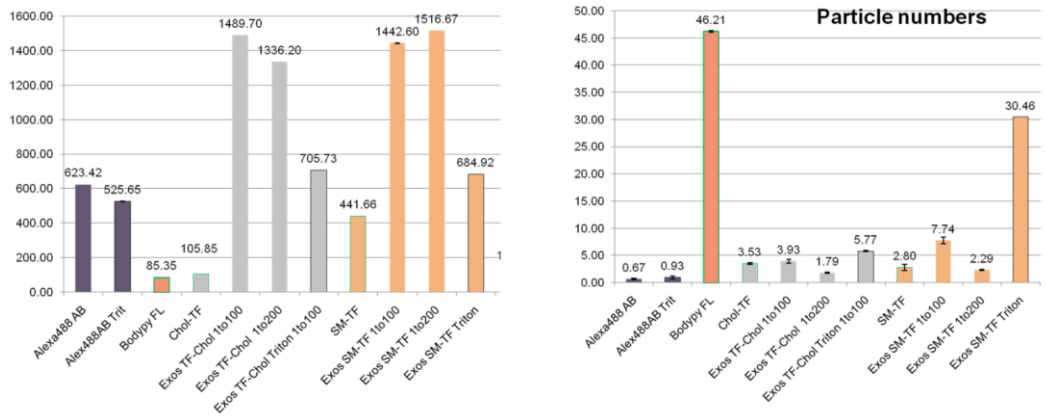

Figure 12) Lipid labeled extracellular vesicle characterization by FCS.

TopFluor Cholesterol (grey bars) as well as TopFluor Sphingomyelin (orange bars) labeled extracellular vesicles were isolated and analyzed. Both vesicle types have similar translational diffusion times and are detergent sensitive.

4.2 Exosome isolation (extended results to Paper I- *Ultrafiltration with size-exclusion liquid chromatography for high yield isolation of extracellular vesicles preserving intact biophysical and functional properties*)

In order to study exosomes uptake characteristics, it is essential to have an isolation process which results in functional, highly purified and decently concentrated vesicles at sufficient quantities. Since cells release many different vesicles with similar and overlapping properties exosome isolation turned out to be a challenging task, although different methods had been published before. We therefore first set out to benchmark the most popular isolation processes used in the exosome field, such as differential ultracentrifugation, sucrose gradients, precipitation methods, as well as particle size separation methods in light of their satisfactory recovery of exosomes for functional rather than analytical studies.

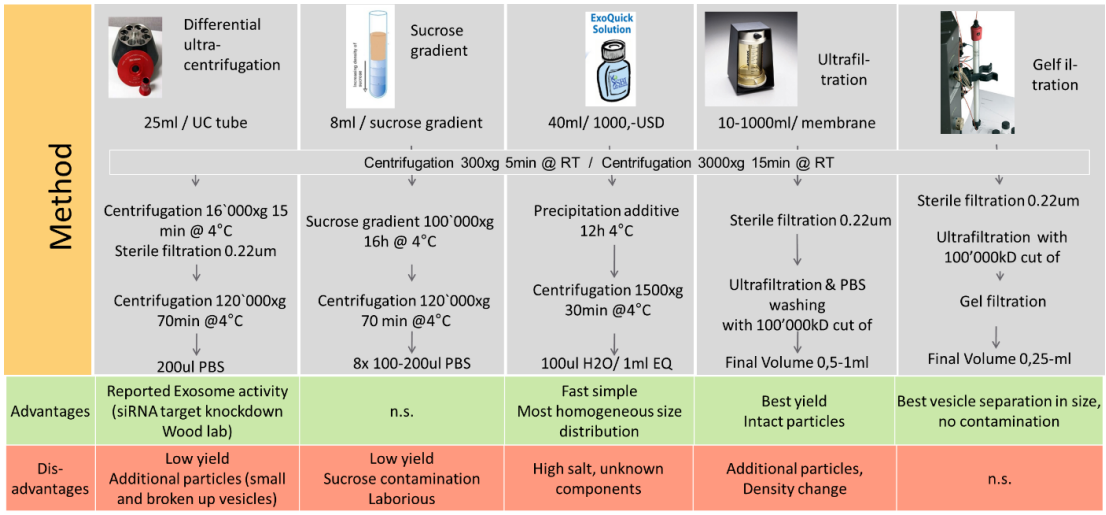

Figure 13) **Benchmarking of different exosome isolation techniques**

The conclusions from this extensive effort are summarized in figure 13. Each isolation method proved to have its advantages and limitations. The sucrose isolation method has the advantage to separate exosomes and subpopulations from the bulk medium by density and efficiently eliminate potential protein complexes and contaminations, however is laborious and of limited yield and reproducibility. An exosome isolation kit called ExoQuick generated the highest yield compared to other isolation methods but has the drawback to leave unknown components and a high salt content in the sample which likely interferes with testing exosome activity upon administration to cells. TEM imaging with negative stain confirmed that sucrose gradient isolated exosomes showed a "cup shape" as described in the literature. Also ExoQuick isolated exosomes were more homogeneous in size than SG isolated exosomes, which corresponds to lightscattering measurements (figure 14).

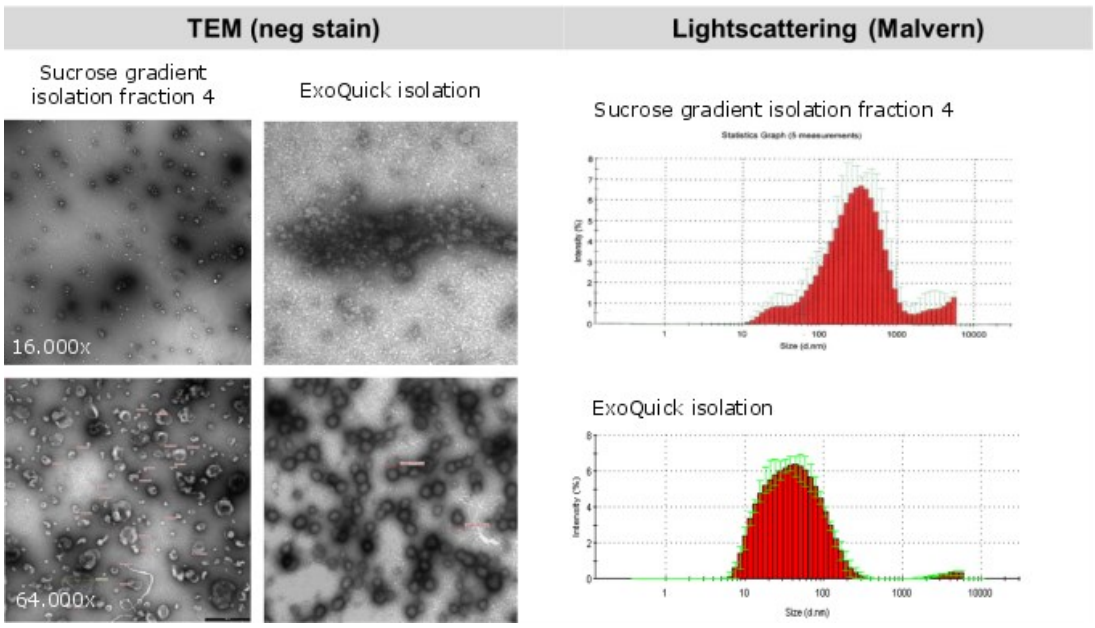

Figure 14) **Exosome size characterization by TEM and DLS**

Left panels show TEM images of EV isolated by sucrose gradient (middle fraction) and *ExoQuick*. Right panels show DLS measurements from the same exosome isolation batches.

Ultracentrifugation is one of the most common methods in the field, with evidence for recovering exosomes with functional activity as e.g. demonstrated by work from the laboratory of Matthew Wood (Oxford) [21]. However, depending on the protocol/centrifugation steps it has a low yield of particles or purity. In particular, high forces of ultracentrifugation might damage the particles, promote vesicle aggregation (Paper I (*Ultrafiltration with size-exclusion liquid chromatography for high yield isolation of extracellular vesicles preserving intact biophysical and functional properties*) and manuscript I (*Quantitative profiling of exosome parent-recipient cell pairing by high content screening using CD63-emGFP vesicle labelling*)) and potentially change their physiological properties. Most current protocols likely bring a bias in isolated vesicle subpopulations or even introduce additional species such as salts or polymers, which is a major drawback of commercial precipitation based exosome isolation kits. As a result of the heterogeneity of isolated exosome samples and their complex composition, an unambiguous quantification is still lacking in most studies. These issues may be less relevant in studies of exosome biogenesis and their release from parent cells, or their use as biomarkers which mostly relies on analytical characterization and does not normally require the vesicles to survive the isolation intact. For the purpose of the study in this work however, they pose a considerable issue for investigating the transfer and function of exosomes and their cargoes in recipient cells. To analyze this potential issue a first thoroughly comparison of UC and UF isolation was done.

Therefor parent HEK 293T cells were transfected with our working horse expression construct for a CD63-emEGFP fusion protein. The isolation of CD63-EGFP positive material was confirmed by Western blot and Nanoparticle Tracking (NTA-Nanosight) analysis. Briefly, 300 ml Medium (OptiMem) conditioned for 48 hours post CD63-EGFP transfection was cleared from cell debris by successive centrifugation for 3 min at 300 x g and 15 min at 3,000 x g, pre filtered through a 0.22 μm filter and subjected to either Ultrafiltration or Ultracentrifugation for Exosome isolation. Samples were analyzed by FCS in several serial dilutions with and without detergent treatment (NP40s at 1 % v/v) for vesicle disruption. To minimize photo bleaching of slow diffusing large vesicles, low excitation intensity (50uW) was used. Due to the high heterogeneity in the sample that became apparent in the FCS analysis, there was the need to use a multi component model

for fitting the data. For this analyzis it was assumed that the two major CD63-EGFP positive components in the isolations are intact exosomes / large vesicles and a secondary subpopulation of smaller, potentially disrupted vesicles. We then analyzed all detergent treated samples with a one component fit to derive the translational diffusion time of disrupted vesicles. Disruption of vesicles by NP40s was confirmed by dynamic light scattering. In addition, measurements of Alexa488 in an exosome sample with and without NP40s confirmed that under these conditions changes in measured translational diffusion times due to viscosity and refractive index changes were negligible. As shown in figure 15A, vesicle disruption by NP40s indeed resulted in almost identical CD63-EGFP translational diffusion times in all samples, including conditioned medium. The average value from these measurements was then defined as the translational diffusion time of the putative small, disrupted particles in a two-component fit of the detergent free samples. This allowed to fit the data with significantly improved Chi^2 and delivered a reasonably homogeneous second population with translational diffusion times corresponding to a hydrodynamic radius in the range of ca 80-100 nm (figure 15A). In this experiment the vesicle concentration in the medium was high allowing to perform comparative measurements also directly in conditioned medium (post 0.22 um filtration). This side by side comparison allowed to determine absolute recoveries of exosome isolations. To a more robust determination of concentrations, uncoupled from potentially different ranges of recovered vesicle sizes and molecular brightness, we disrupted the vesicles with NP40s and compared the absolute concentrations of CD63-EGFP molecules in each fraction. Ultrafiltration recovered ca 25 % of the CD63-EGFP molecules from the conditioned medium, which was ca 2.5-fold higher than the recovery by ultracentrifugation (figure 15B). Similar fold differences were obtained in other side by side isolations. In addition, this analysis revealed that both methods typically delivered a high fraction of large vesicles with both methods. Given that the UC supernatant showed a reduced fraction of large vesicles (figure 15C) we hypothesized that this might indicate vesicle disruption or fusion during the centrifugation. In fact, the slight increase in translational diffusion time of large vesicles after ultracentrifugation as compared to their τ_{diff} in medium would be consistent with aggregation or fusion enforced due to the centrifugation forces. We therefore performed additional experiments with two different labeled vesicles to get a clear answer on this question (confer manuscript I (Quantitative profiling of exosome parent-recipient cell pairing by high content screening using CD63-emGFP vesicle labeling.)). Altogether, these data argue that ultrafiltration not only provides higher yields of exosomes but also better preserves their physicochemical properties.

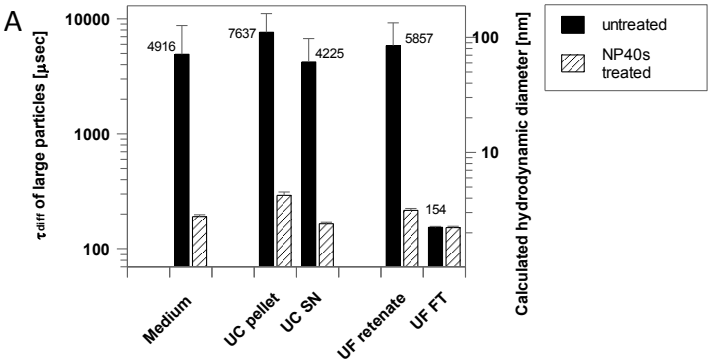
A
10000
1000
100
τdiff of large particles [µsec]
4916
7637
4225
5857
154
100
10
Calculated hydrodynamic diameter [nm]
untreated
NP40s treated
Medium
UC pellet
UC SN
UF retenate
UF FT

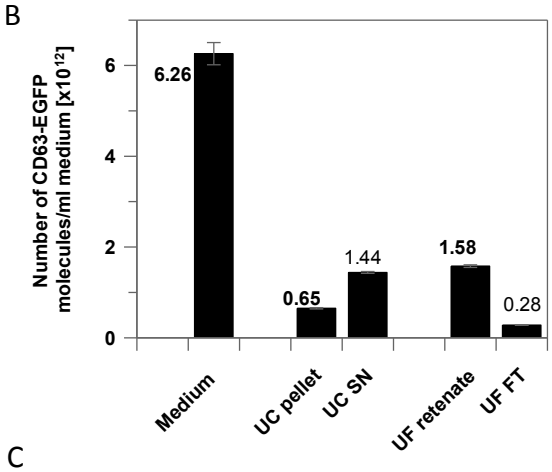
B
Number of CD63-EGFP molecules/ml medium [x10 12]
6
4
2
0
6.26
0.65
1.44
1.58
0.28
Medium
UC pellet
UC SN
UF retenate
UF FT

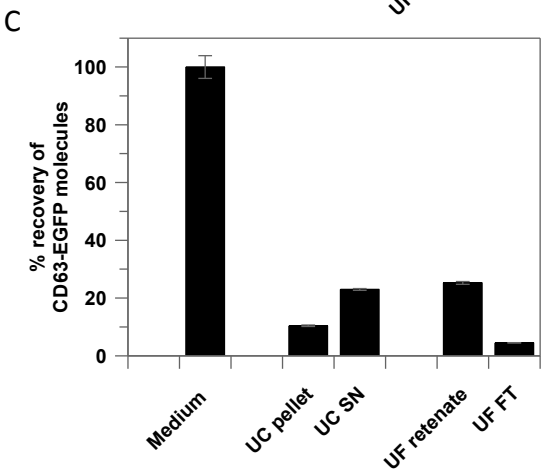
C
% recovery of CD63-EGFP molecules
100
80
60
40
20
0
Medium
UC pellet
UC SN
UF retenate
UF FT

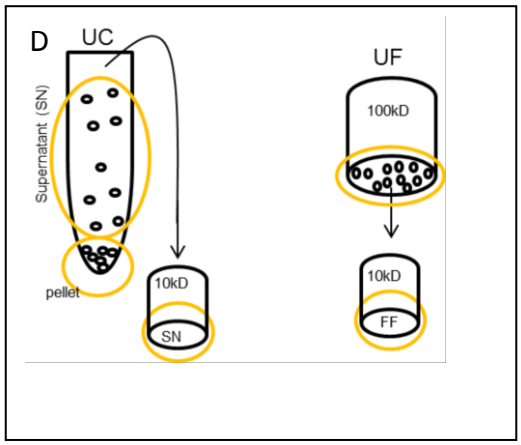
D
UC
Supernatant (SN)
pellet
10kD
SN
UF
100kD
10kD
FF

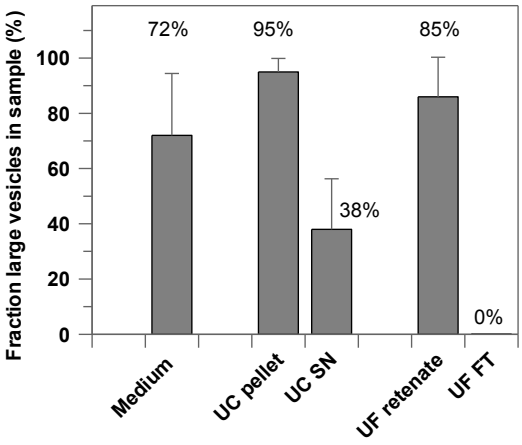
Fraction large vesicles in sample (%)
100
80
60
40
20
0
72%
95%
38%
85%
0%
Medium
UC pellet
UC SN
UF retenate
UF FT

Figure 15) **Quantification and characterization of Exosomes from ultrafiltration and ultracentrifugation isolations by Fluorescence Correlation Spectroscopy**:
CD63-EGFP positive vesicles were analyzed by FCS in extracellular vesicle samples isolated from transfected HEK293T cells by UC versus UF, as well as directly in conditioned medium (post 0.22 um filtration). UC pellet: Exosome pellet from UC, resuspended in PBS. UC SN: supernatant from ultracentrifugation, concentrated on a 10 MWCO filter. UF: Exosome sample from UF retentate. UF FT: Flowthrough from UF, concentrated on a 10kD MWCO filter.
(A) Translational diffusion times for large vesicles are shown without (black bars) and with (shaded bars) NP40s treatment to disrupt vesicles. Translational diffusion times (left axis) were converted into hydrodynamic diameters (right axis) based on extrapolation of the measured τ_{diff} for Alexa488 and the reported hydrodynamic radius of 5.8 Å (Nathanel et al). (B) Absolute concentrations of HEK293T CD63-GFP molecules upon vesicle disruption by NP40s quantified by FCS in 48 h cultured medium and yields from UC pellet, UC supernatant, UF isolate and UF flowthrough. All values were corrected for dilution factors. (C) Fraction of large CD63-EGFP positive vesicles. All samples show a high integrity of recovered Exosomes with the exception of the supernatant from UC. (D) Scheme of workflow for sample preparation (SN= supernatant, FF= flowthrough).

Based on these results there was a need to establish a new isolation method and we decided to use a mild enrichment of particles in medium using ultrafiltration. Interestingly, it turned out that a similar protocol was being independently established in the lab of Samuel Al Andaloussi at the same time, with largely identical conclusions. We therefore characterized and advanced this method in a collaborative effort. The final protocol includes an additional gel filtration step to reduce the non-vesicular protein background to a minimum, and allows to handle large volumes of medium under mild and isotonic conditions. The combined ultrafiltration / size-exclusion liquid chromatography (UF-GF) exosome isolation protocol, and its side by side comparison to UC exosome isolation was reported in Paper I (Ultrafiltration with size-exclusion liquid chromatography for high yield isolation of extracellular vesicles preserving intact biophysical and functional properties). This isolation method is now our state of the art exosome isolation method. However it is still unclear whether the withdrawal of serum or using pre-spun medium for generating conditioned medium, which is necessary to avoid contamination by exosomes contained in fetal bovine serum, might cause the cells to release exosomes of different composition than under fed conditions. This question has been subsequently addressed by Samir Andaloussi and Matthew Wood and coworkers [118].

Nanomedicine: Nanotechnology, Biology, and Medicine
11 (2015) 879–883

Short Communication

nanomedicine
Nanotechnology, Biology, and Medicine

nanomedjournal.com

Ultrafiltration with size-exclusion liquid chromatography for high yield isolation of extracellular vesicles preserving intact biophysical and functional properties

Joel Z. Nordin, M.D.[a, 1], Yi Lee, BSc[b, 1], Pieter Vader, PhD[b], Imre Mäger, PhD[b, c], Henrik J. Johansson, PhD[d], Wolf Heusermann, PhD[e], Oscar P.B. Wiklander, M.D.[a], Mattias Hällbrink, PhD[f], Yiqi Seow, DPhil[g], Jarred J. Bultema, PhD[h], Jonathan Gilthorpe, PhD[i], Tim Davies, MSc[j], Paul J. Fairchild, PhD[j], Susanne Gabrielsson, PhD[h], Nicole C. Meisner-Kober, PhD[e], Janne Lehtiö, PhD[d], C.I. Edvard Smith, M.D., PhD[a],Matthew J.A. Wood, M.D., DPhil[b,⁎], Samir EL Andaloussi, PhD[a, b,⁎⁎]

[a]*Department of Laboratory Medicine, Karolinska Institutet, Stockholm, Sweden*
[b]*Department of Physiology, Anatomy and Genetics, University of Oxford, Oxford, United Kingdom*
[c]*Institute of Technology, University of Tartu, Tartu, Estonia*
[d]*Cancer Proteomics Mass Spectrometry, Science for Life Laboratory, Department of Oncology-Pathology, Karolinska Institutet, Stockholm, Sweden*
[e]*Novartis Institutes for Biomedical Research, Basel, Switzerland*
[f]*Department of Neurochemistry, Stockholm University, Stockholm, Sweden*
[g]*Molecular Engineering Laboratory, Proteos, Agency for Science, Technology and Research (A*STAR), Singapore*
[h]*Department of Medicine Solna, Translational Immunology Unit, Karolinska Institutet and University Hospital, Stockholm, Sweden*
[i]*Umeå Centre for Molecular Medicine, Umeå University, Umeå, Sweden*
[j]*Sir William Dunn School of Pathology, University of Oxford, Oxford, United Kingdom*

Received 19 November 2014; accepted 4 January 2015

Abstract

Extracellular vesicles (EVs) are natural nanoparticles that mediate intercellular transfer of RNA and proteins and are of great medical interest; serving as novel biomarkers and potential therapeutic agents. However, there is little consensus on the most appropriate method to isolate high-yield and high-purity EVs from

various biological fluids. Here, we describe a systematic comparison between two protocols for EV purification: ultrafiltration with subsequent liquid chromatography (UF-LC) and differential ultracentrifugation (UC). A significantly higher EV yield resulted from UF-LC as compared to UC, without affecting vesicle protein composition. Importantly, we provide novel evidence that, in contrast to UC-purified EVs, the biophysical properties of UF-LC-purified EVs are preserved, leading to a different in vivo biodistribution, with less accumulation in lungs. Finally, we show that UF-LC is scalable and adaptable for EV isolation from complex media types such as stem cell media, which is of huge significance for future clinical applications involving EVs.

Statements of funding: The project was funded by the Swedish Research Council (VR-Med) and Swedish Cancer society. SEA holds a research fellowship from the Swedish Society of Medical Research (SSMF). SG holds a position from the Swedish Heart-Lung Foundation. JN and OW are both recipients of Karolinska Institutet MD/PhD grants. YL is funded by the Agency for Science, Technology and Research (A*STAR), Singapore. IM is supported by a Postdoctoral MOBILITAS Fellowship of the Estonian Science Foundation and by the EU IMI (Innovative Medicines Initiative) project COMPACT (Collaboration on the optimisation of macromolecular pharmaceutical access to cellular targets). PJF and TD are supported by the Regenerative Medicine Initiative of the Britain-Israel Research and Academic Exchange Partnership (BIRAX).

Competing financial interests: The authors declare no competing financial interests.

Author contributions: JN, YL, IM, MH, PV, OW, WH, ACS, AD, JB, MJW and SEA designed and performed the experiments and wrote the manuscript. HJ and JL performed the proteomics experiments and data analysis. YQ, IM, PV, NM, JB, JG, TD, PJF, SG, MJW and SEA contributed to the experimental design and correction of the manuscript.

*Correspondence to: M. JA Wood, Department of Physiology, Anatomy and Genetics, University of Oxford, Oxford, United Kingdom.

**Correspondence to: S. El Andaloussi, Department of Laboratory Medicine, Karolinska Institutet, Huddinge, Sweden.

E-mail addresses: matthew.wood@dpag.ox.ac.uk (M.J.A. Wood), Samir.El-Andaloussi@ki.se (S.E.L. Andaloussi).

[1]These authors contributed equally to the manuscript.

http://dx.doi.org/10.1016/j.nano.2015.01.003

Please cite this article as: Nordin JZ, et al, Ultrafiltration with size-exclusion liquid chromatography for high yield isolation of extracellular vesicles preserving intact biophysical and functional properties. *Nanomedicine: NBM* 2015;11:879-883, http://dx.doi.org/10.1016/j.nano.2015.01.003

From the Clinical Editor: Recent evidence suggests extracellular vesicles (EVs) as another route of cellular communication. These EVs may be utilized for future therapeutics. In this article, the authors compared ultrafiltration with size-exclusion liquid chromatography (UF-LC) and ultra- centrifugation (UC) for EV recovery.

Key words: Biophysical properties; extracellular vesicles; size-exclusion liquid chromatography; ultracentrifugation; ultrafiltration

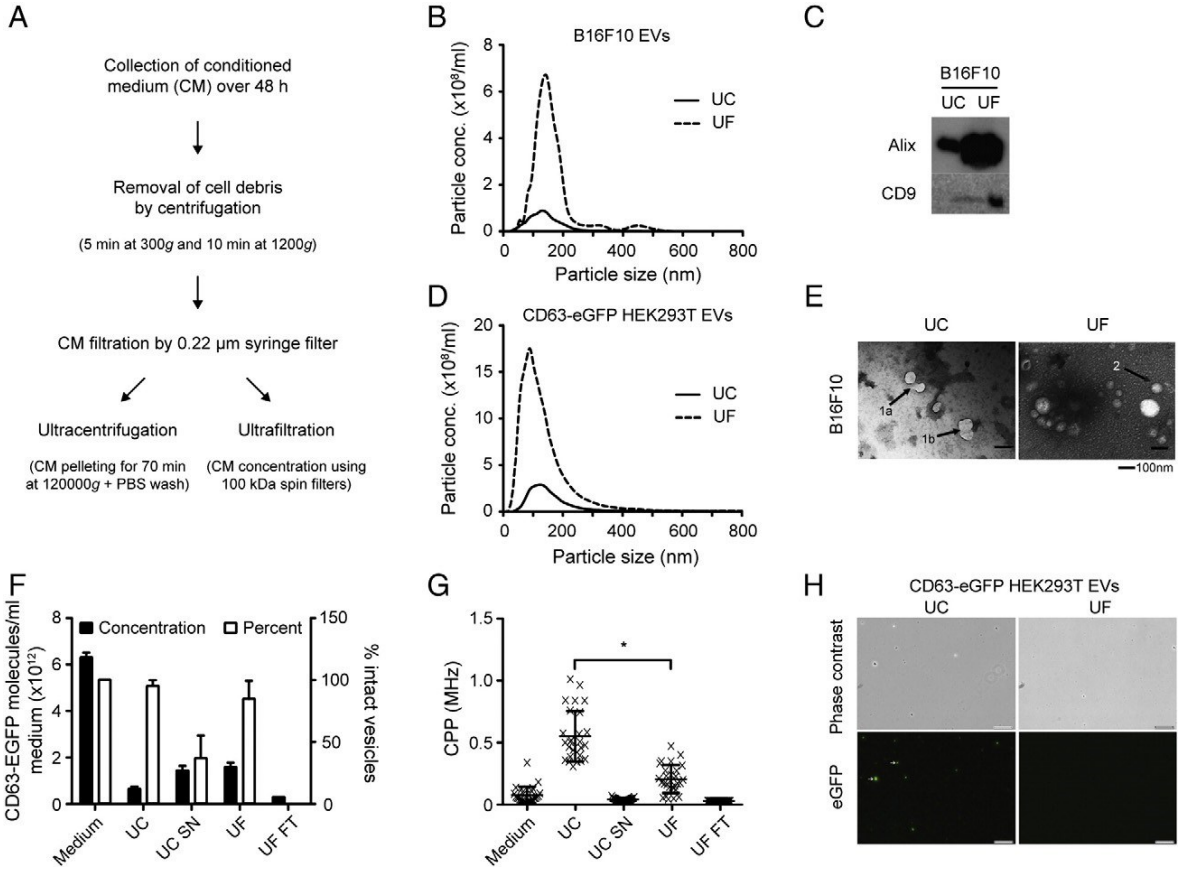

Figure 1. Ultrafiltration allows efficient isolation of intact EVs. (A) Chart outlining UF and UC protocols. (B) NTA of UF and UC-purified EVs. (C) WB of UF and UC-purified EVs. (D) NTA (fluorescence mode) of UF and UC-purified eGFP-positive EVs. (E) TEM of UF and UC-purified EVs. Arrows 1a:
fragmentation, 1b: fusion and 2: intact. (F) Absolute concentrations of CD63-eGFP molecules (left y-axis) and percentage of intact vesicles (right y-axis) according to FCS (SN=supernatant, FT=flow-through). (G) Molecular brightness for each particle (counts per particle) (CPP) (n=3). *Indicates pb0.05, results represent mean+s.d. (H) Fluorescence microscopy of CD63-eGFP-positive EVs.

Intercellular communication, via paracrine factors, is essential for survival of all multicellular organisms. Recent evidence suggests another route of cellular communication: extracellular vesicles (EVs), comprising of nano-sized exosomes, microve- sicles and apoptotic bodies.[1] Due to their ability to convey information through RNA and proteins, EVs can influence both physiological[2] and pathophysiology processes.[3,4] Moreover, EVs from mesenchymal stem cells have been exploited for regeneration of injured tissues.[5–7] Hence, EVs are emerging as disease biomarkers and nanotherapeutics.[8]

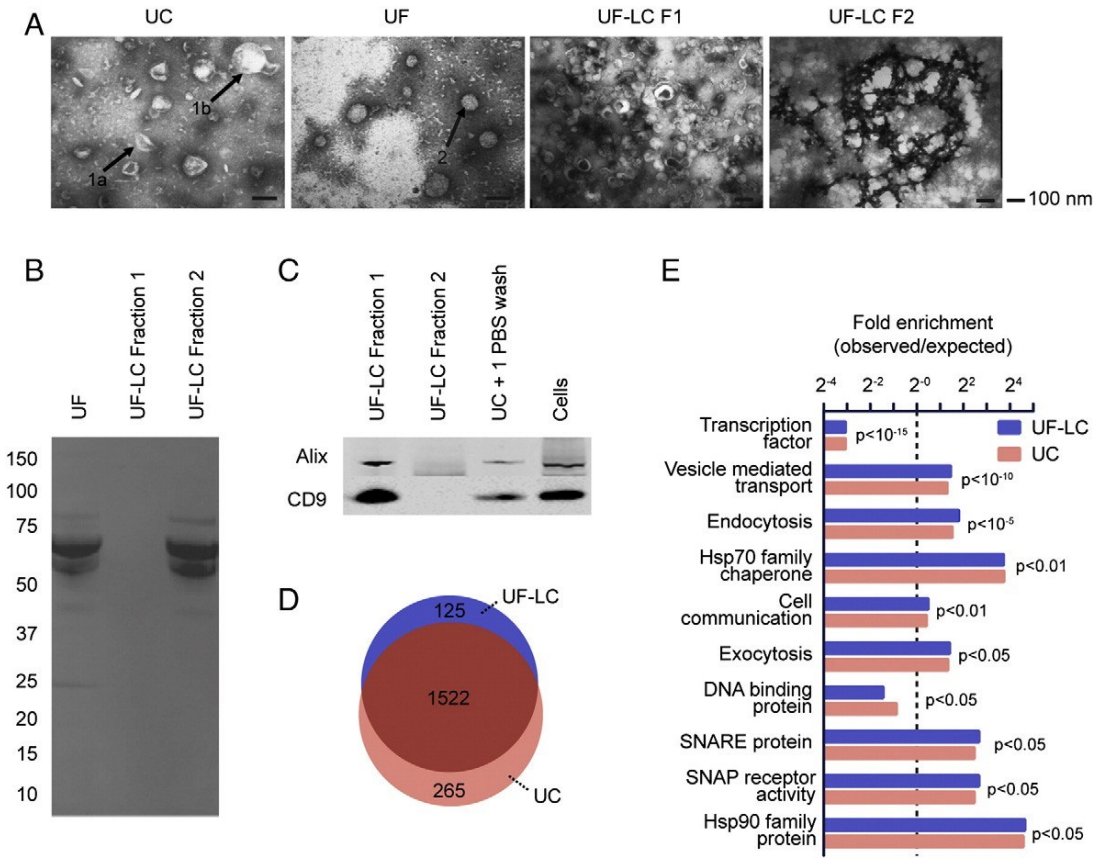

Despite progress in EV research, the challenge of purifying biologically intact EVs remains. Differential ultracentrifugation (UC)[9] is the classical protocol for EV isolation. However, problems with UC include low and operator-dependent yields.[10] Alternative strategies like immuno-affinity capture,[11] polymer- based precipitation[12] and microfluidics[13] also present shortcom- ings, e.g. vesicle disruption and co-purification of non-vesicular proteins.[10] Deriving an EV isolation method that enables high recovery of functional EVs in a scalable fashion is therefore essential for EV research.

Figure 2. Size-exclusion chromatography separates EVs from contaminants. (A) TEM of UF-LC fraction 1 shows intact EVs, whereas fraction 2 contains protein aggregates. (B) Total protein staining of UF and UF-LC fractions. (C) WB of UF-LC and UC-purified EVs. (D) Venn diagram depicting protein overlap for UF-LC and UC-purified EVs. (E) Gene ontology (GO) enrichment terms for UF-LC and UC-purified EV proteomes.

Table1
Protein/vesicle ratio of UC and UF-LC-purified EVs.

Protein/vesicle ratio (x10^{-15} g/particle)	N2a OptiMEM	N2a Prespun	iPSCs
UC	0.25	0.25	0.70
UF-LC	0.074	0.059	0.55

Here, we present a systematic comparison study between a robust EV purification method, ultrafiltration with size-exclusion liquid chromatography (UF-LC), adapted from previous studies,[14–16] and UC. We show that UF-LC permits higher EV recovery with intact biophysical properties.

Methods

EVs were isolated by either UF or UC; UF samples were subsequently loaded on a Sephacryl column for size-exclusion fractionation. EV properties were evaluated using molecular (western blotting (WB), nanoparticle tracking analysis (NTA), LC/ MS/MS) and biophysical (transmission electron microscopy (TEM), fluorescence microscopy, fluorescence correlation spectroscopy (FCS), total internal reflection fluorescence microscopy (TIRF) and DiR-imaging) analyses (see supplementary data for details).

Results

UF-LC allows high-yield isolation of biophysically intact EVs

OptiMEM conditioned medium was processed by UC or UF (Figure 1, A). According to NTA, more particles with similar size distribution were recovered after UF than after UC. Correspondingly, levels of vesicle markers (Alix and CD9) were higher in UF than UC samples. This finding was consistent across different cell lines and with CD63-eGFP labeled EVs (Figure 1, B-D and Supplementary figure S1A).

TEM revealed EVs with rounded and cup-shaped morphol- ogy in both samples. Occasionally, UC-purified EVs appeared disrupted or fused (Figure 1, E), an observation not seen with UF-purified EVs. FCS was employed for more quantitative analysis of EV integrity. In FCS, EV hydrodynamic radius, concentration and changes in biophysical properties (e.g. fusion or fragmentation) were determined by measuring diffusion and intensity of CD63-eGFP positive EVs. From these readings, 25% of the total CD63-eGFP molecules were recovered using UF, 2.5-fold more than using UC, with larger EV radius for UC.

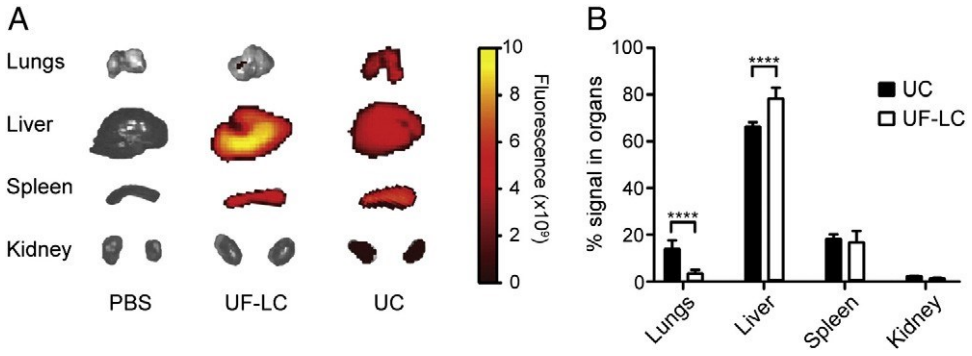

Figure 3. Biodistribution of UF-LC-purified EVs. (A) Representative IVIS images of organs from Balb/c mice 24 h post injection of DiR-labeled EVs. (B) Biodistribution of UC and UF-LC DiR-labeled EVs. ****Indicates pb0.0001% in comparison to the same organ in the corresponding group (n=5), results represent mean+s.d.

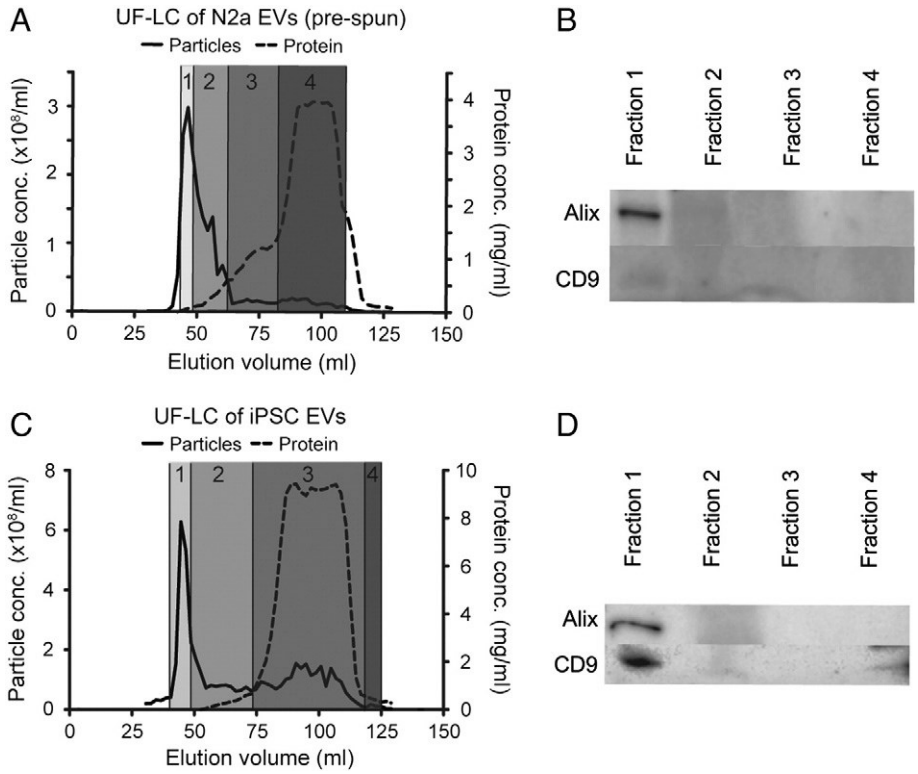

Figure 4. UF-LC EV isolation from complex media types. Graph showing the concentration of particles (x108/ml) (left y-axis) and protein concentration (mg/ml) (right y-axis) across the eluted volume after UF-LC for (A) N2a pre-spun conditioned media and (C) iPSC conditioned media. WB of (B) N2a and (D) iPSC EVs.

The brightness of individual particles (number of CD63-eGFP molecules per vesicle) was higher in UC than UF, suggesting vesicle fusion. Further, disintegration with NP-40 decreased the diameter of CD63-eGFP-positive material to 2 nm for both UC and UF-purified EVs, the putative size of free CD63-eGFP.[17] After UC, only 10% of total vesicles were recovered in the pellet; while in the supernatant, only 38% of the vesicles were intact while the

remaining 62% of the eGFP-positive material was 2 nm. This is indicative of vesicle disruption, since disrupted vesicles release their CD63-eGFP into the supernatant as free CD63-eGFP (Figure 1, *F-G* and Supplementary figure S1C). Moreover, fluorescence microscopy of EVs in suspension revealed aggregates only in UC samples (Figure 1, *H*). Since protein complexes were co-isolated using UF (Supple- mentary figure S2A-C), size-exclusion LC was used to fractionate OptiMEM conditioned media. Two distinct fractions were detected (Supplementary figure S2D-E), with vesicles and non-vesicular proteins found exclusively in fraction 1 and fraction 2, respectively (Figure 2, *A-B*). UF-LC presented with consistently high EV recovery rates (70% ±19%), along with higher EV marker expression as compared to UC samples (Figure 2, *C* and Supplementary figure S2F-G). LC/MS/MS of EVs purified by both methods presented a good correlation in overall protein expression and gene ontology annotations (Figure 2, *D-E*, Supplementary figure S3A-E and Supplementary Table S1), although the protein/vesicle ratio was lower in UF-LC than for UC-purified EVs (Table 1). TIRF imaging further corroborated the presence of aggregates/fusion of EVs only in UC samples (Supplementary figure S4A-B).

UF-LC-purified EVs demonstrate different in vivo biodistribution compared to UC-purified EVs

Based on the distinct differences observed in EV integrity, we speculated that this would influence EV biodistribution. DiR-labeled EVs were injected intravenously and mice were
imaged 24 h later. UC-purified EVs showed a 4.6 times (p0.0001)
stronger signal in lungs compared to UF-LC-purified EVs (Figure 3, *A-B*) while the reverse was seen in the liver.

UF-LC can be extended to complex biological fluids

After subjecting conditioned pre-spun and stem cell media to UF-LC, EV markers were again solely detected in fraction 1, which corresponds to the peak of particles (Figure 4, *A-F* and Supplementary figure S5A-D). Moreover, UF-LC samples consistently had a lower protein/vesicle ratio than UC samples (Table 1).

Discussion

Research in EVs has recently received increasing attention, however, one major roadblock is the lack of a scalable technique permitting efficient purification of EVs. Here we report the first systematic comparison study comparing both biochemical and biophysical aspects of UF-LC and UC-purified EVs. NTA, WB and state-of-the-art LC/MS/MS demonstrated that UF-LC generated EVs with the same proteome as UC. Furthermore, our protein/vesicle ratio was consistently lower in UF-LC than UC samples, suggesting higher EV purity.[18] TEM, FCS, TIRF

and fluorescence microscopy data suggest that EVs fuse, disrupt and aggregate during the UC isolation process, an aspect that is circumvented with UF-LC. We postulate that these large EV aggregates account for the accumulation in the lungs in our *in vivo* experiments. Another finding from this study is that UF-LC can be adapted for EV isolation from stem cell media. We believe that using UF-LC for EV isolation will allow researchers to venture into new avenues aimed at unraveling EV biological functions.

Supplementary data

Details of materials and methods

Cell culture

NSC-34, a fusion of motor neuron enriched embryonic mouse spinal cord with mouse neuroblastoma, Neuro2a (N2a), a mouse neuroblastoma, B16F10, a mouse melanoma and human embryonic kidney (HEK293T) cells were cultured at 37°C with 5% CO_2 in complete media comprised of Dulbecco's Modified Eagle Medium (DMEM), supplemented with 10% fetal bovine serum (FBS), and penicillin/streptomycin (P/S, 5000 µg/ml) (all from Life Technologies, Carlsbad, CA, USA). Mouse induced pluripotent stem cells (iPSCs) were cultured on 0.1% gelatin coated plates at 37°C with 5% CO_2 in complete stem cell media comprised of DMEM (Lonza, Basel, Switzerland) supplemented with 15% knockout serum-replacement, 2mM L-glutamine, 1 mM sodium pyruvate, 0.1mM non-essential amino acids (all from Life Technologies), 50 µg/ml P/S, 0.2mM 2-mercaptoethanol (Sigma, St Louis, MO, USA) and 10^6 units of mouse leukaemia inhibitory factor (mLIF, ESGRO®, Merck Millipore, Billerica, MA, USA). For EV isolation, media were changed 24 h after seeding to either OptiMEM (Life Technologies), pre-spun media or to fresh stem cell media for iPSCs. Pre-spun media is DMEM supplemented with 10% FBS that had been pre-spun at 120,000*g* for 70 min prior to making up the vesicle devoid media. All media were supplemented with P/S. Conditioned media was then collected for EV isolation 48 h after incubation. For large-scale experiments, conditioned media collected from multiple flasks were pooled prior to isolation of EVs.

Transfection of HEK293T cells

$6x10^6$ cells were seeded one day prior to transfection in a 15 cm culture dish in complete media. Transfection of the CD63-EGFP plasmid was done using polyethyleneimine (PEI, Sigma) at a 1:4 pDNA: PEI ratio. Briefly, 25 µg of plasmid and 100 µg of PEI were diluted in 500 µl of OptiMEM in separate tubes. After 5min of incubation at room temperature (RT), the pDNA and PEI solutions were combined and incubated for a further 30 min at RT to form the DNA/PEI complexes. The complexes were then added dropwise to cells. After 4 h, the cell growth media containing the complexes was removed; the cells were washed with phosphate buffer saline (PBS, Life Technologies) and fresh OptiMEM, supplemented with P/S antibiotics was added on the cells. After 48 h of incubation, the conditioned media was collected for EV isolation.

Ultracentrifugation (UC) for isolation of EVs

The EV isolation method by UC was adapted from Théry et al(1). Briefly, supernatants collected were subjected to two low speed spins, 300*g* for 5 min followed by 1200*g* for 10 min to get rid of cell debris and larger particles. The supernatant was subsequently filtered through a 0.22 µm syringe filter (Merck Millipore) before the final ultracentrifugation step at 120,000*g* for 70 min. The EV pellet was resuspended in PBS and subjected to an additional PBS wash at 120,000*g* for 70 min.

Ultrafiltration (UF) for isolation of EVs

The UF protocol, as shown in figure 1a, involves the same initial low-speed spins as that of the UC protocol. Instead of a high-speed ultracentrifugation at the final step, the cell culture supernatants were spun at 3,500*g* for 15 min in 100-kDa molecular weight cut-off

(MWCO) Amicon spin filters (Merck Millipore). PBS was then added onto the filters and spun to wash the samples.

Size-exclusion liquid chromatography fractionation of UF samples (UF-LC) from cell culture medias

UF samples were loaded onto a S-400 column (GE Healthcare, Uppsala, Sweden), on an ÄKTA prime (GE healthcare) equipped with a UV 280nm flow cell. Each individual fraction was collected based on the UV absorbance as indicated in supplementary figures. For all cell culture samples, 2ml fractions were pooled and concentrated using a 10-kDa MWCO Amicon Ultra spin filter (Merck Millipore).

Western blotting (WB)

WB was performed using either the Bio-Rad® Mini-PROTEAN® Tetra cell (Bio-Rad, Hercules, CA, USA) or the iBlot® system (Invitrogen, Life Technologies) according to the manufacturer's instructions. To cross-compare the yield of EVs, we proceeded to load equal volumes of the re-suspended EV pellet or filtrate on the gel.

For the Bio-Rad system, 15 µl of EV samples with 15 µl of 2X Laemilli sample buffer (Bio-Rad) containing 5% β-mercaptoethanol (Sigma) were mixed and heated at 100°C for 10 min. Samples were then loaded in a 1.5 mm, 10% Tris/Glycine SDS-polyacrylamide gel and ran at 170 V for 60-70 min in running buffer, until the dye front reached the bottom of the tank. Proteins on the gel were then transferred to a polyvinylidine fluoride (PVDF) membrane (Merck Millipore) at 100 V for 60-70 min in transfer buffer containing 20% methanol. Membranes were then incubated in blocking buffer (5% fat-free milk in Tris buffer saline with 0.1% Tween-20 (TBS-T) for 60 min at room temperature (RT) with gentle shaking.

For the iBlot® system, 30 µl of sample was mixed with a sample buffer, containing 0.5 M ditiothreitol (DTT), 0.4 M sodium carbonate (Na_2CO_3), 8% SDS and 10% glycerol, and heated at 65 °C for 5 min. Samples were then loaded in a NuPAGE® Novex® 4-12% Bis-Tris Gel and ran at 120 V in running buffer until the dye front reached the bottom of the gel. The proteins on the gel were transferred to an iBlot nitrocellulose membrane (Invitrogen, Life Technologies) for 7 min with the iBlot system. Membranes were stained with Ponceau S dye that was later washed away with PBS before blocking with Odyssey blocking buffer for 60 min at RT with gentle shaking (LI-COR, Lincoln, NE, USA).

After the blocking step, the membrane was incubated with freshly prepared primary antibody solution (anti-CD9 and anti-PDC6I (Alix), both at 1:1,000 dilution from Abcam, Cambridge UK) overnight at 4°C or 2 h at RT. Membranes were washed three times, 10 min each using washing buffer (TBS-T) with vigorous shaking before adding the secondary antibody solution (anti-mouse IgG DyLight-800 at 1:10,000 dilution if detecting Alix; anti-rabbit IgG DyLight-800 at 1:10,000 dilution for detecting CD9 (LI-COR)) and incubated for 1 h at RT. After the secondary antibody incubation, membranes were washed three times, 10 min each and visualised by scanning both 700- and 800-nm channels on the LI-COR Odyssey CLx infrared imaging system. For subsequent probing of other proteins on the same membrane, the membrane was washed three times, 10 min each before re-incubation with the next primary antibody.

Nanoparticle tracking analysis (NTA)

For particle size determination, NTA was performed with a NanoSight NS500 instrument (Malvern Ltd, Worchestershire, UK) equipped with the NTA 2.3 analytical software. For

all our recordings, we used a camera level of 13 or 15 and automatic function for all post-acquisition settings: blur and minimum expected particle size, except in the detection threshold where we fixed it at 5. Samples were thawed on ice and diluted in PBS between 1:500 to 1:20,000 to achieve a particle count of between 2 x 10^8 and 2 x 10^9 per mL. Once the dilution of the sample was determined, sample was loaded in the sample chamber and the camera focus was adjusted to make the particles appear as sharp dots of light. Using the *script control* function, we recorded five 30 or 60 s videos for each sample; incorporating a sample advance and 5 s delay between each recording. For GFP positive EVs the same set up was used with one minor alteration, which was that the sample was under constant flow in the sample chamber not to bleach the GFP signal. These measurements were then analysed using the *batch process* function and results were exported to Microsoft Excel for further analysis.

Quantification of proteins and RNA in EVs

Protein quantities in EVs were quantified using the microBCA assay kit (Thermo Scientific, Waltham, MA, USA) and levels of RNA were measured using the Quant-iT™ RiboGreen® RNA assay kit (Life Technologies), according to the manufacturer's instructions.

Transmission Electron Microscopy

5µl of EV suspension was diluted 1:1 with PBS and added on formvar-carbon coated electron microscopy grids (Agar Scientific, Elektron Technology UK Ltd, Essex, UK) for 20 min. The grid was blotted with filter paper and 15 µl of 2% uranyl acetate (UA, Sigma) was added on the grid for 1 min. Next, UA was removed and 15 µl of distilled water was added for 1 min. The water droplet was then removed and the grid was left to air dry for 15 min. The grids were then visualized in the transmission electron microscope (JEM-1010, JEOL Ltd, Tokyo, Japan).

Fluorescence microscopy

CD63-EGFP positive EVs were generated as described above. The particles were quantified by NTA and the UF-LC and UC samples were diluted to the same concentration of particles/ml. Before any measurements, the EVs were re-suspended with a 27G needle. The samples were positioned on a microscope slide and covered with a coverslip and analysed Microscopy was performed using Olympus IX-81 inverted microscope (Olympus America, Center Valley PA, USA) equipped with 20X objective. The following fluorescence filter-set (Chroma Technology Corp., Bellows Falls, VT, USA) was used, with the central wavelength and bandwidth of the excitation and emission filters as indicated: GFP (Ex. 470/40 nm; Em. 525/50 nm)

Liquid chromatography tandem mass spectrometry (LC-MS/MS) of EVs

EVs from UC and UF-LC were concentrated by speedvac and lysed with 1% SDS, 25 mM HEPES, 1 mM DTT. Lysates were heated to 95°C for 5 min followed by sonication for 1 min and centrifugation at 14,000*g* for 15 min. The supernatant was mixed with 1 mM DTT, 8 M urea, 25 mM HEPES, pH 7.6 and transferred to a 10-kDa cut-off centrifugation filtering unit (Pall, Nanosep®, Port Washington, NY, USA), and centrifuged at 14,000*g* for 15 min, followed by an addition of the 8 M urea buffer and centrifugation again. Proteins were alkylated by 50 mM iodoacetamide (IAA) in 8 M urea, 25 mM HEPES for 10 min, The proteins were then centrifuged at 14, 000*g* for 15 min followed by 2 more additions and centrifugations with 8 M urea, 25 mM HEPES. Trypsin (Promega, Madison, WI, USA) in 250 mM urea, 50 mM HEPES was added to the cell lysate at a ratio of 1:50 trypsin:protein and incubated overnight at 37°C. The filter units were centrifuged at 14,000*g* for 15 min followed by another centrifugation with MQ and the flow-through was collected. Peptides were cleaned by a strata-X-C-cartridge (Phenomenex, Torrence, CA, USA).

Before analysis on the Q Exactive (Thermo Fischer Scientific), peptides were separated using an Agilent 1200 nano-LC system. Samples were trapped on a Zorbax 300SB-C18, and separated on a NTCC-360/100-5-153 (Nikkyo Technos., Ltd) column using a gradient of A (3% ACN, 0.1% FA) and B (95% ACN, 0.1% FA), ranging from 7% to 40% B in 240 min with a flow of 0.4 µl/min. The Q Exactive was operated in a data dependent manner, selecting top 5 precursors for fragmentation by HCD. The survey scan was performed at 70,000 resolutions from 300-1700 *m/z,* using lock mass at *m/z* 445.120025, with a max injection time of 100 ms and target of 1×10^6 ions. For generation of HCD fragmentation spectra, a max ion injection time of 500 ms and AGC of 1×10^5 were used before fragmentation at 30% normalized collision energy, 17,500 resolution. Precursors were isolated with a width of 2 *m/z* and put on the exclusion list for 70 s. Single and unassigned charge states were rejected from precursor selection.

Proteome discoverer 1.3 with sequest-percolator was used for protein identification. Precursor mass tolerance was set to 10 ppm and for fragments to 0.02 Da. Oxidized methionine and was set as dynamic modification, and carbamidomethylation as static modification. Spectra were matched to a combined *mus musculus* and *bos taurus* ensembl 72 database, and results were filtered to 1% FDR. Identifications in bos taurus was considered to originate from FBS and removed. GO term enrichment analysis was done using Panther(2).

Fluorescence correlation spectroscopy (FCS)

In FCS, EV hydrodynamic radius, concentration and changes in biophysical properties (e.g. fusion or fragmentation) were determined by measuring diffusion and intensity of CD63-eGFP positive EVs from HEK293T cells. FCS was performed on a Clarina II Reader (Evotec Technologies, Perkin Elmer, Waltham, MA, USA) with 488 nm argon ion laser excitation at 50 µW to minimize photo bleaching, a 40x water emersion 1.15 N.A. objective (UAPO Olympus), a 488/633 nm major dichroic mirror in the excitation path and a HQ535/50m filter in the emission path. In-focus light was collected through a 50 µm pinhole using a SPCM-AQR-13FC avalanche photodiode (Perkin-Elmer Optoelectronics). The confocal volume was calculated in approximation according to(3) using the measured diffusional correlation time τ_{diff} of fluorescent Alexa488 free dye standard, the known translational diffusion coefficient of Alexa488 (Molecular probes; D = 280 $\mu m^2/s$) and the axis ratio fitted from calibration measurements.

HEK293T and N2A cells were plated in 15 cm dishes and transfected at 50% confluency with CD63-EGFP using Lipofectamine 2000 (Life Technologies) in DMEM supplemented with 10% FBS. After 4 h, cells were washed and medium was replaced with OptiMEM and cultivated for further 48 h. Conditioned medium was subjected to either UC or UF purification as described in Fig. 2a. The conditioned medium (post 0.22 µm), UF retentate, UF flow-through (FT), UC pellet and post-UC supernatant was re-suspended in PBS supplemented with EDTA free Complete Protease inhibitor (Roche, Basel, Switzerland) and analyzed by FCS. For each sample, several dilutions were made and measured in a 96-well glass bottom plate (Whatman, GE Healthcare) with 30 repetitive measurements of 10 s each. NP-40S at 1% v/v (Cambridge Bioscience, Cambridge, UK) was used to induce vesicle disruption. Disruption of vesicles was confirmed by dynamic light scattering. Autocorrelation curves were fitted with a one- or two-component two-dimensional diffusion model(4, 5) to extract translational diffusion times, particle numbers and molecular brightness's. For a two-component two-dimensional diffusion model we made the assumption that the two major CD63-EGFP positive components in the isolations are intact EVs/large vesicles and a secondary subpopulation of smaller, potentially disrupted

vesicles. We then analyzed all detergent treated samples with a one component fit to derive the translational diffusion time of disrupted vesicles. Alexa488 measurements in an EV sample with and without NP40s confirmed that under these conditions changes in measured translational diffusion times due to viscosity and refractive index changes were negligible (data not shown). Vesicle disruption by NP40s indeed resulted in almost identical CD63-EGFP translational diffusion times in all samples, including conditioned medium. The average value from these measurements was then defined as the translational diffusion time of the putative small, disrupted particles in a two-component fit of the detergent free samples. This allowed to fit the data with significantly improved Chi^2 and delivered a reasonably homogeneous second population with translational diffusion times corresponding to a hydrodynamic radius in the range of ca. 70-100 nm. Data from one experiment representative of at least three independent experiments are shown. Error bars represent Standard deviations from the 30 FCS measurements.

Total internal reflection fluorescence microscopy (TIRF)

TIRF microscopy experiments were performed on a Zeiss Laser TIRF 3 system using a 100x objective. Glass inserts (P35G-1.5-14-C) were from MatTek Ashland, MA, USA. TIRF angle was set at 70 degrees (depth of penetration = 86 nm) Experiments was performed at 37°C. Before assaying the EVs were mixed with *FAST* DiO™ Solid; $DiO\Delta^{9,12}\text{-}C_{18}(3)$, ClO_4 (3,3'-Dilinoleyloxacarbocyanine Perchlorate) (Life Technologies). Images were recorded after a brief refocusing.

EV biodistribution in mice

Conditioned cell supernatants were filtered through a 0.22 µm syringe filter and incubated with 1µM DiR (1,1'-Dioctadecyl-3,3,3',3'-Tetramethylindotricarbocyanine Iodide) (Invitrogen, Life Technologies). The conditioned media with DiR was then ultracentrifuged at 120,000*g* for 70 min (UC) or concentrated with a 100-kDa MWCO Amicon Ultra spin filter (UF) (Merck Millipore). The UC pellet was re-suspended and spun again in PBS to purify away-unbound DiR and UF samples LC fractionated as described above. Purified EVs were quantified with NTA and equal amounts of particles from both UC and UF-LC preparations were injected in the tail vein of Balb/c mice (n=5). 24 h post injection, the organs were harvested and subjected to imaging in the In Vivo Imaging System (IVIS) Spectrum (Caliper, CA, USA). The IVIS was set to record the fluorescence for 2 seconds (excitation 710, emission 760) and the data obtained was then analysed with the IVIS software. All animal experiments conducted were approved by The Swedish Local Board for Laboratory Animals. The experiments were performed in accordance with the ethical permission and designed to minimize the suffering and pain of the animals.

Statistics

Statistical analyses of the data were performed using Prism 6.0 (GraphPad Software Inc.) by using the nonparametric Krusckal Wallis test followed by the Sidak post-test for the bio-distribution data (Figure 3B). A One-way Anova followed by the Dunn's post-test was applied to the molecular brightness data (Figure 1G). All error bars used in this report are mean + s.d.

Supplementary figure legends

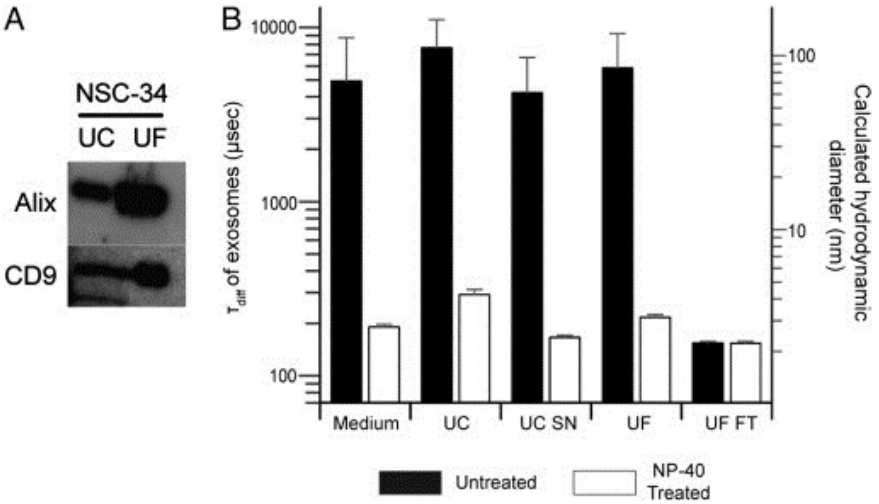

Supplementary figure S1. WB of vesicle markers and FCS of CD63-eGFP labeled EVs. (A) WB of Alix and CD9 of EVs from NSC-34 conditioned media. (B) Translational diffusion times (τ_{diff}) (left y-axis) and the hydrodynamic diameters (right y-axis) of vesicles from UC, UF, post-UC supernatant (UC SN) and post-UF flow-through (UF-FT) are shown, with (white bars) and without (black bars) NP-40 treatment. The hydrodynamic diameter was calculated based on extrapolation of the measured τ_{diff} for Alexa488 and the reported hydrodynamic radius of 5.8 Å(6). Based on these measurements, UC-purified EVs were shown to have a larger average vesicle radius than UF. This is most likely due to the fusion/aggregation of vesicles during the UC process, corroborating with EM results in Figure 1E. The difference in radius (UC versus UF) was lost upon NP-40 detergent treatment. NP-40 treatment disrupts membranes and the observation with decreased vesicle diameter post-treatment confirmed that all FCS measurements were done on membrane vesicles, as opposed to aggregated CD63-EGFP molecules. Here, NP-40 treatment decreased the hydrodynamic radius of UC and UF vesicles to around 2 nm, which is in accordance with the putative size of free CD63-EGFP(7), hence confirming the disruption of the vesicles and the release of free CD63-EGFP.

A

B16F10	Mode (nm)	Concentration		
		Particle (10^9/ml)	Protein (ug/ul)	RNA (ng/ul)
UC	134.8	41.6	0.3	6.5
UF	140.7	258.1	5.9	31.5
Fold diff.	-	6.2	19.7	4.7

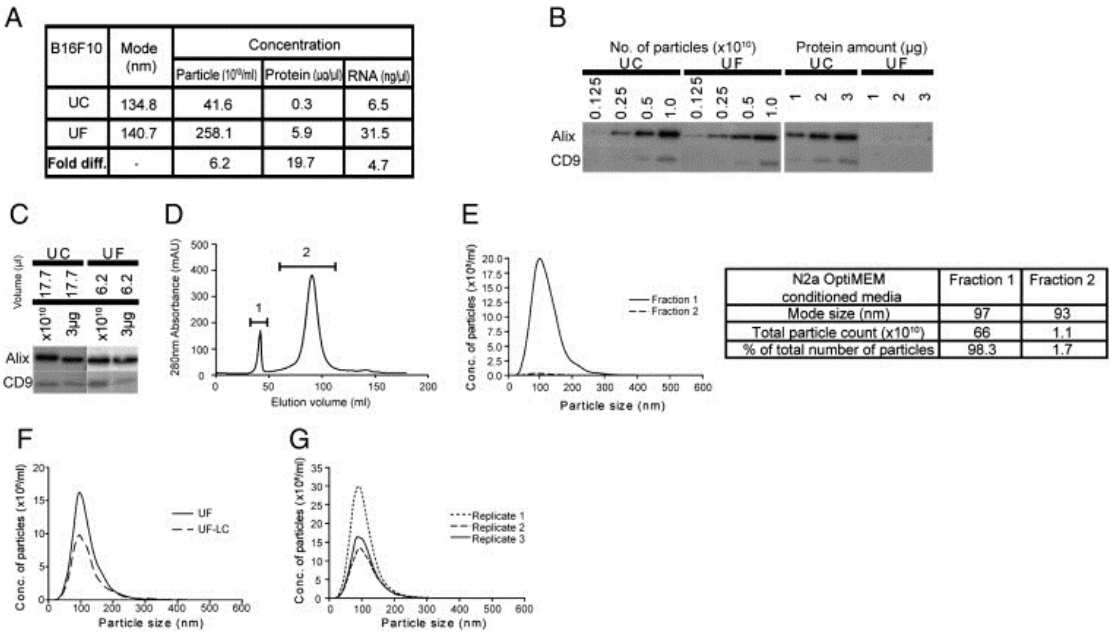

N2a OptiMEM conditioned media	Fraction 1	Fraction 2
Mode size (nm)	97	93
Total particle count (x10^{10})	66	1.1
% of total number of particles	98.3	1.7

Supplementary figure S2. UF-LC permits high-yield isolation of intact EVs with good recovery and little non-vesicular protein contamination.

(A) Table comparing the mode size, particle concentration, protein concentration and RNA concentration of particles isolated from B16F10 cells. Both particle and RNA concentration are around 6-fold higher with UF than in UC samples. However, this is not correspondingly seen with protein concentrations (20-fold difference). (B) To investigate this discrepancy, WB was done comparing the expression of vesicle markers (Alix and CD9) between UC and UF samples when loading the same amount of particles (left panel) or the same amount of protein (right panel). 4 different amounts of particles were tested: 0.125 $x10^{10}$, 0.25 $x10^{10}$, 0.5 $x10^{10}$ and 1.0 $x10^{10}$ of the same sample quantified by NTA. When loading the same amount of particles the intensity of both Alix and CD9 bands appear to be similar for the UC and UF samples. In contrast, when an equal amount of total protein (1, 2 and 3µg) was loaded, based on the microBCA measurements, the intensity of both Alix and CD9 were much higher for the UC compared to the UF samples. This suggests that the protein quantification is highly overestimated in measuring the EV yield of UF samples, and indicates that a huge majority of the proteins detected in the UF sample did not originate from the vesicles but is mostly from the presence of protein aggregates trapped in the spin filters. (C) To work out the extent of overestimation, we loaded the same volume of UF samples and recalculated the protein quantification to match with the number of particles. Our data shows that $1.0x10^{10}$ particles from the UF samples correspond to 35µg of protein. From the UC samples, the same volume of EVs: $1.0x10^{10}$ particles correspond to 3µg of protein. Hence, under the assumption that all particles contain the same amount of protein and that there is no large difference in the particles isolated from UC or UF as seen by the mode size in NTA and western blot markers in (B), we propose that the protein quantification of UF samples to be about 10 to 11-fold overestimated. Therefore, using the protein concentration as a gauge of vesicle yield after UF purification (or with any other similar precipitation methodology) is highly not recommended as any protein contamination can largely skew the quantification. (D) LC chromatograph showing two distinct peaks as measured by UV 280; collections from these two peaks were pooled to derive two fractions; fraction 1 and 2 (Lines represent approximately the collected volume for fraction 1 and 2). (E) NTA graph showing that 98% of the total number of particles detected after UF-LC was eluted in fraction 1. The particles in fraction 1 have a mode size of slightly less than 100 nm, which is in accordance with the reported size of EVs. (F) NTA graph showing that the size distribution of EVs isolated post-LC is similar to UF. Also, the recovery of EVs post-LC is maintained at 69%. (G) NTA of UF-LC fraction 1 from three individual purifications. The mode size in all three replicates is consistently around 90-100 nm with minimal particles larger than 200 nm, indicating that the methodology is reproducible.

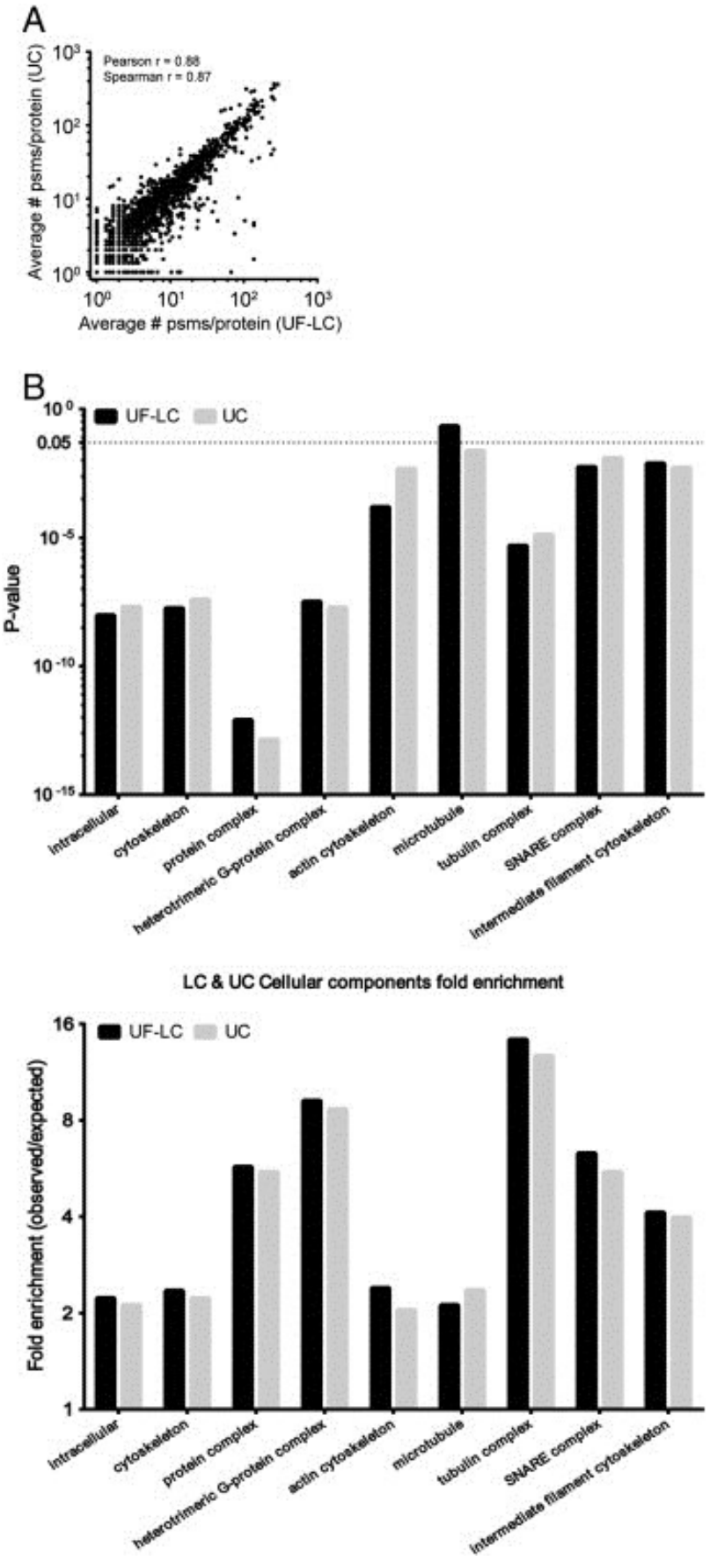
A
Pearson r = 0.88
Spearman r = 0.87
Average # psms/protein (UC)
Average # psms/protein (UF-LC)
B
UF-LC
UC
P-value
intracellular
cytoskeleton
protein complex
heterotrimeric G-protein complex
actin cytoskeleton
microtubule
tubulin complex
SNARE complex
intermediate filament cytoskeleton
LC & UC Cellular components fold enrichment
Fold enrichment (observed/expected)

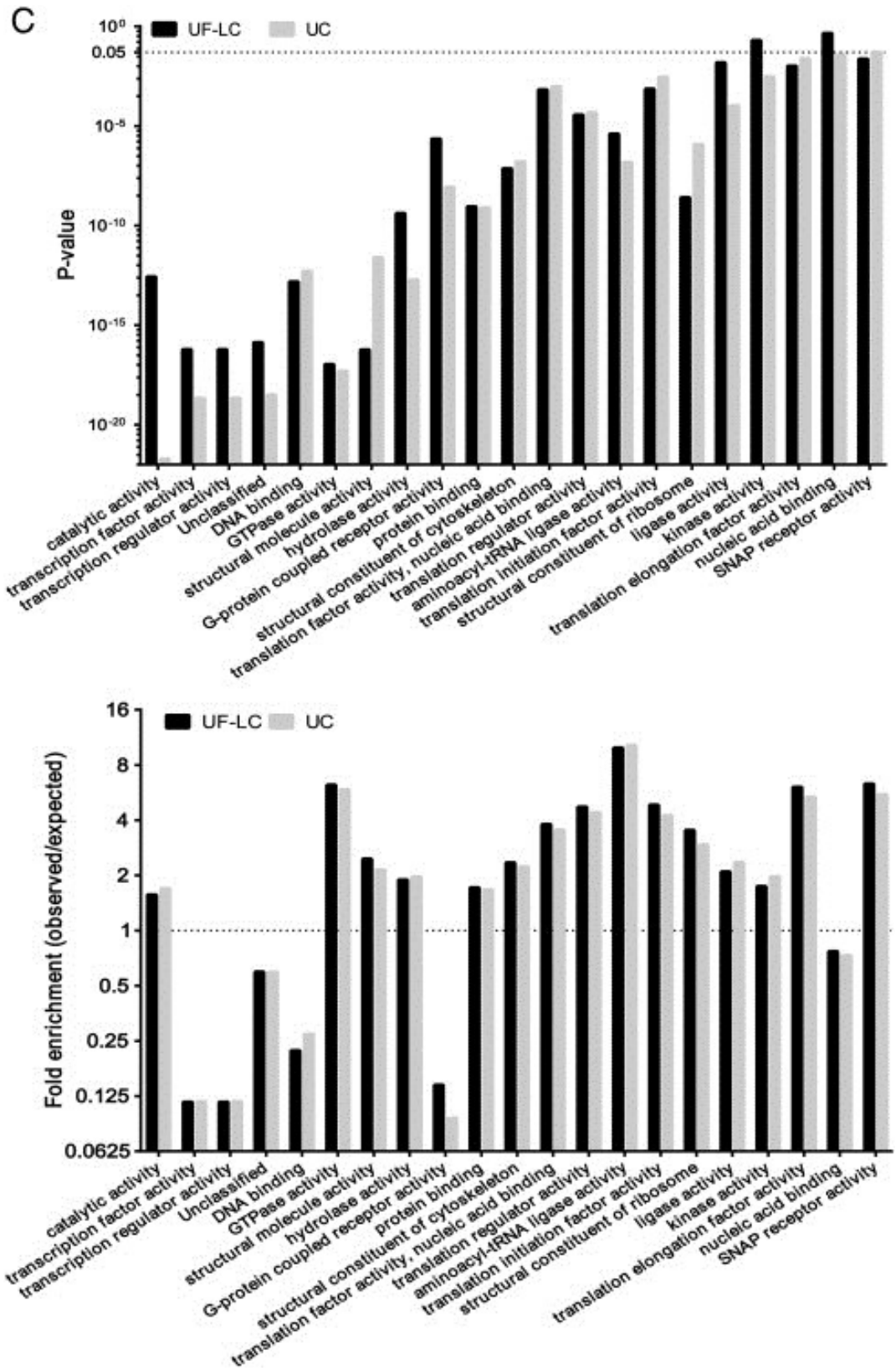
C
UF-LC
UC
P-value
10^0
0.05
10^-5
10^-10
10^-15
10^-20
catalytic activity
transcription factor activity
transcription regulator activity
Unclassified
DNA binding
GTPase activity
structural molecule activity
hydrolase activity
G-protein coupled receptor activity
protein binding
structural constituent of cytoskeleton
translation factor activity, nucleic acid binding
translation regulator activity
aminoacyl-tRNA ligase activity
translation initiation factor activity
structural constituent of ribosome
ligase activity
kinase activity
translation elongation factor activity
nucleic acid binding
SNAP receptor activity
UF-LC
UC
Fold enrichment (observed/expected)
16
8
4
2
1
0.5
0.25
0.125
0.0625
catalytic activity
transcription factor activity
transcription regulator activity
Unclassified
DNA binding
GTPase activity
structural molecule activity
hydrolase activity
G-protein coupled receptor activity
protein binding
structural constituent of cytoskeleton
translation factor activity, nucleic acid binding
translation regulator activity
aminoacyl-tRNA ligase activity
translation initiation factor activity
structural constituent of ribosome
ligase activity
kinase activity
translation elongation factor activity
nucleic acid binding
SNAP receptor activity

D

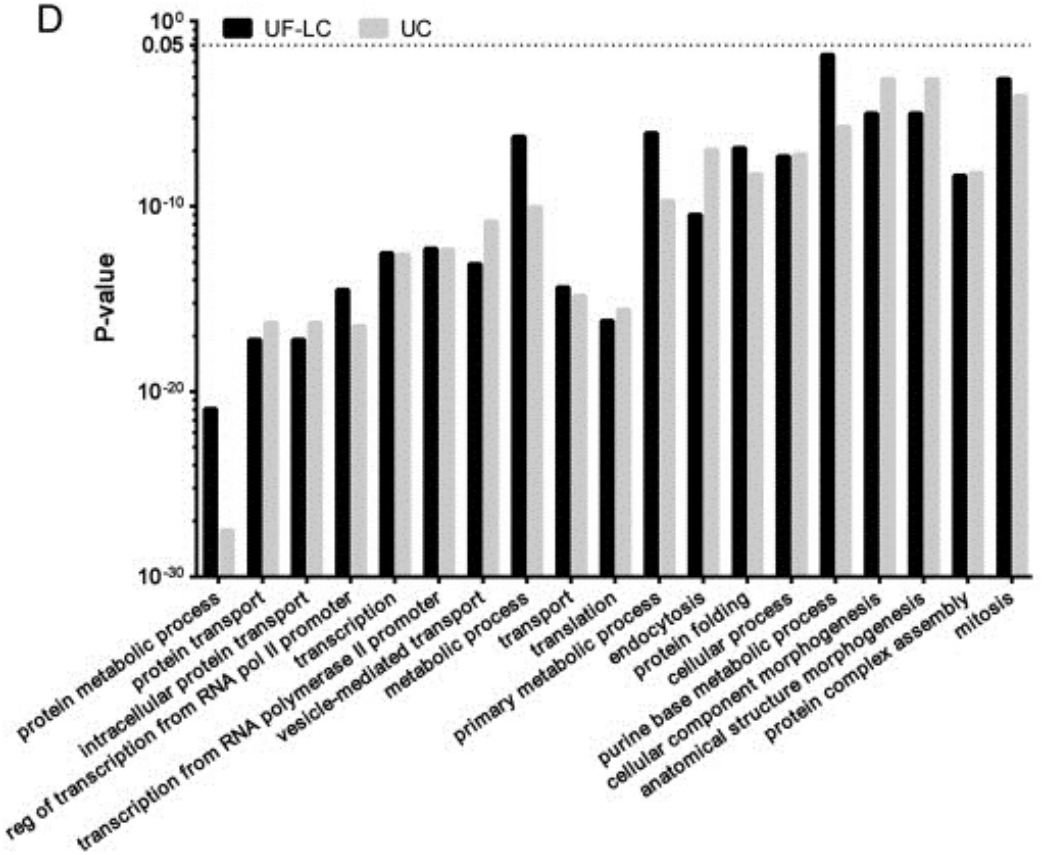
UF-LC
UC
P-value
10^0
0.05
10^-10
10^-20
10^-30
protein metabolic process
protein transport
intracellular protein transport
reg of transcription from RNA pol II promoter
transcription
transcription from RNA polymerase II promoter
vesicle-mediated transport
metabolic process
transport
translation
primary metabolic process
endocytosis
protein folding
cellular process
purine base metabolic process
cellular component morphogenesis
anatomical structure morphogenesis
protein complex assembly
mitosis

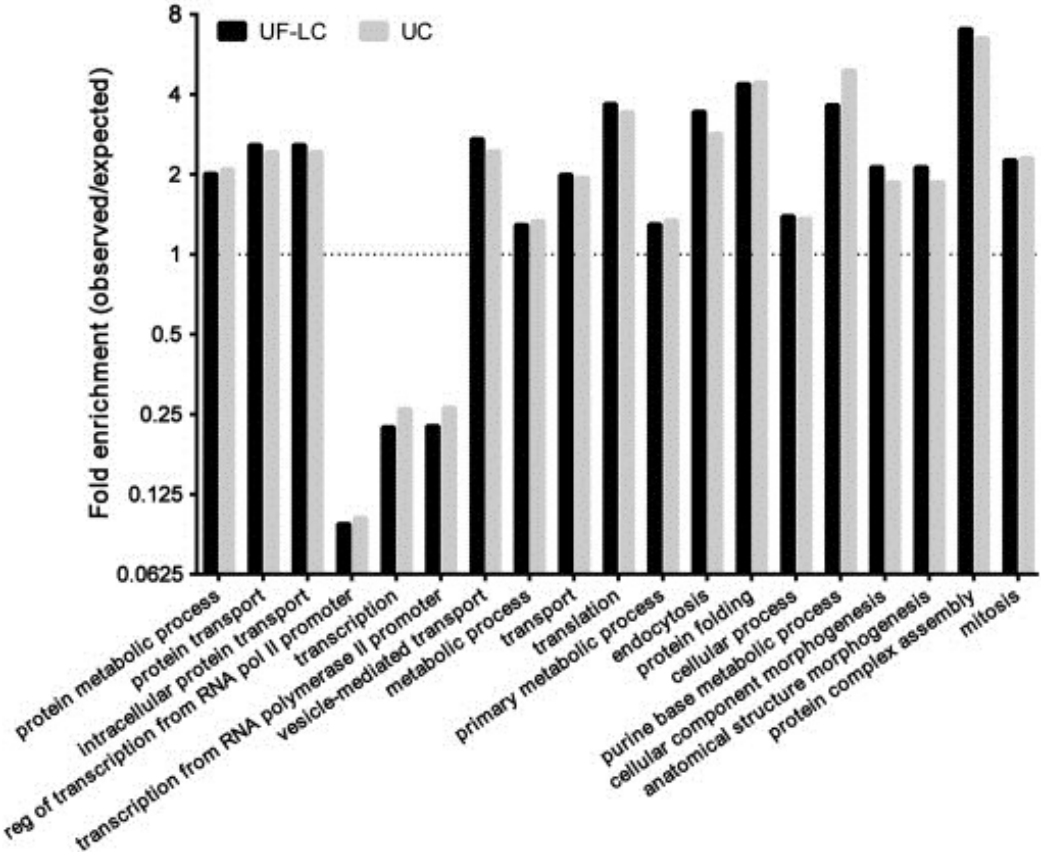
UF-LC
UC
Fold enrichment (observed/expected)
8
4
2
1
0.5
0.25
0.125
0.0625
protein metabolic process
protein transport
intracellular protein transport
reg of transcription from RNA pol II promoter
transcription
transcription from RNA polymerase II promoter
vesicle-mediated transport
metabolic process
transport
translation
primary metabolic process
endocytosis
protein folding
cellular process
purine base metabolic process
cellular component morphogenesis
anatomical structure morphogenesis
protein complex assembly
mitosis

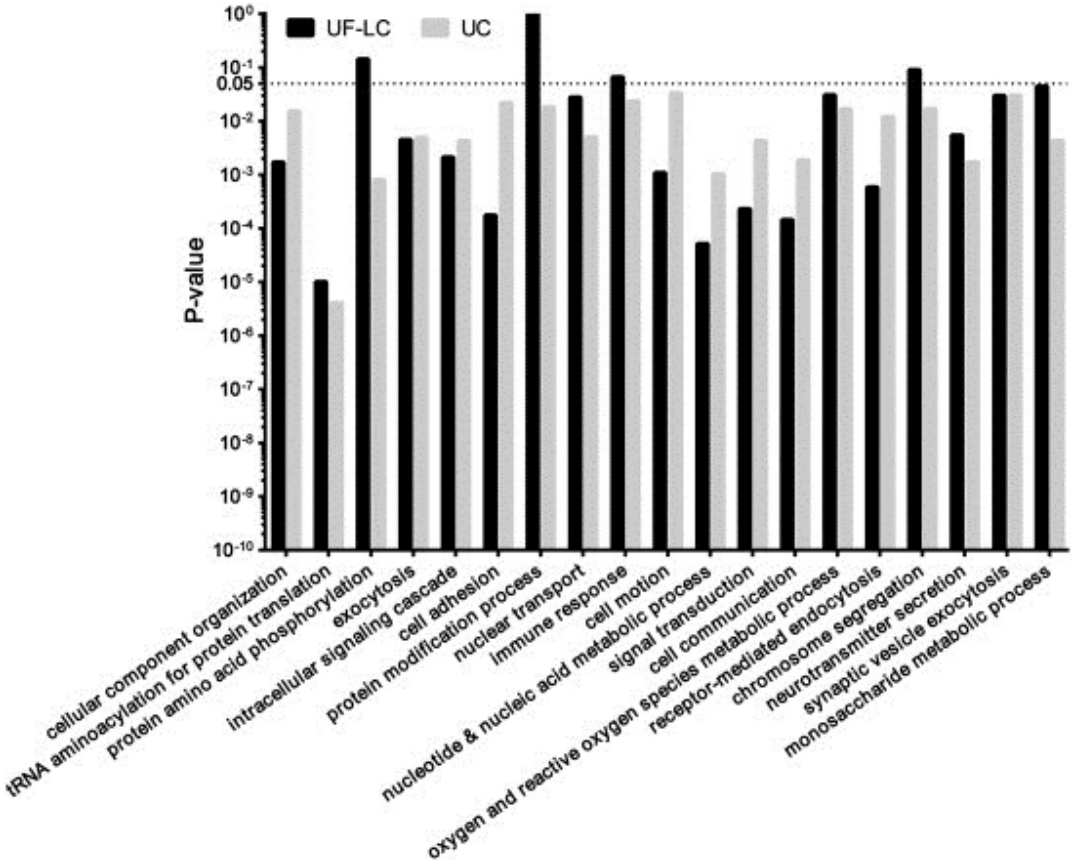
UF-LC
UC
P-value
10^{0}
10^{-1}
0.05
10^{-2}
10^{-3}
10^{-4}
10^{-5}
10^{-6}
10^{-7}
10^{-8}
10^{-9}
10^{-10}
cellular component organization
tRNA aminoacylation for protein translation
protein amino acid phosphorylation
exocytosis
intracellular signaling cascade
cell adhesion
protein modification process
nuclear transport
immune response
cell motion
nucleotide & nucleic acid metabolic process
signal transduction
cell communication
oxygen and reactive oxygen species metabolic process
receptor-mediated endocytosis
chromosome segregation
neurotransmitter secretion
synaptic vesicle exocytosis
monosaccharide metabolic process

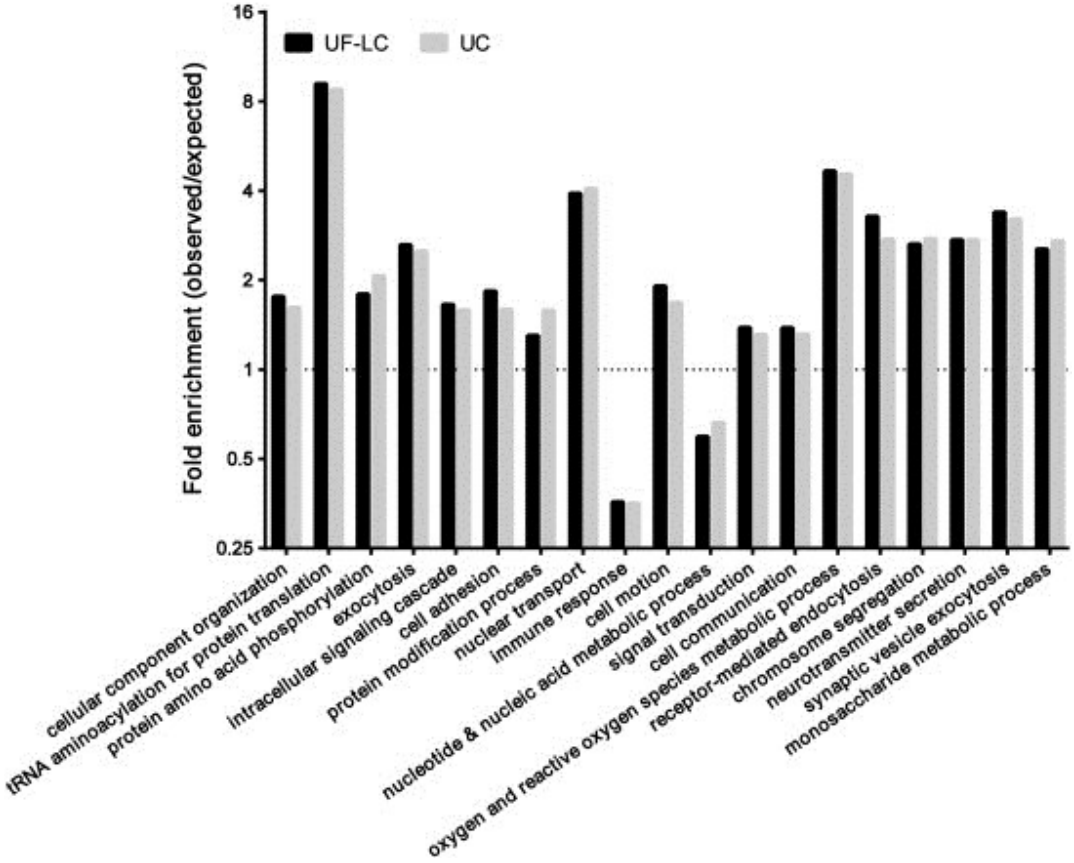
UF-LC
UC
Fold enrichment (observed/expected)
16
8
4
2
1
0.5
0.25
cellular component organization
tRNA aminoacylation for protein translation
protein amino acid phosphorylation
exocytosis
intracellular signaling cascade
cell adhesion
protein modification process
nuclear transport
immune response
cell motion
nucleotide & nucleic acid metabolic process
signal transduction
cell communication
oxygen and reactive oxygen species metabolic process
receptor-mediated endocytosis
chromosome segregation
neurotransmitter secretion
synaptic vesicle exocytosis
monosaccharide metabolic process

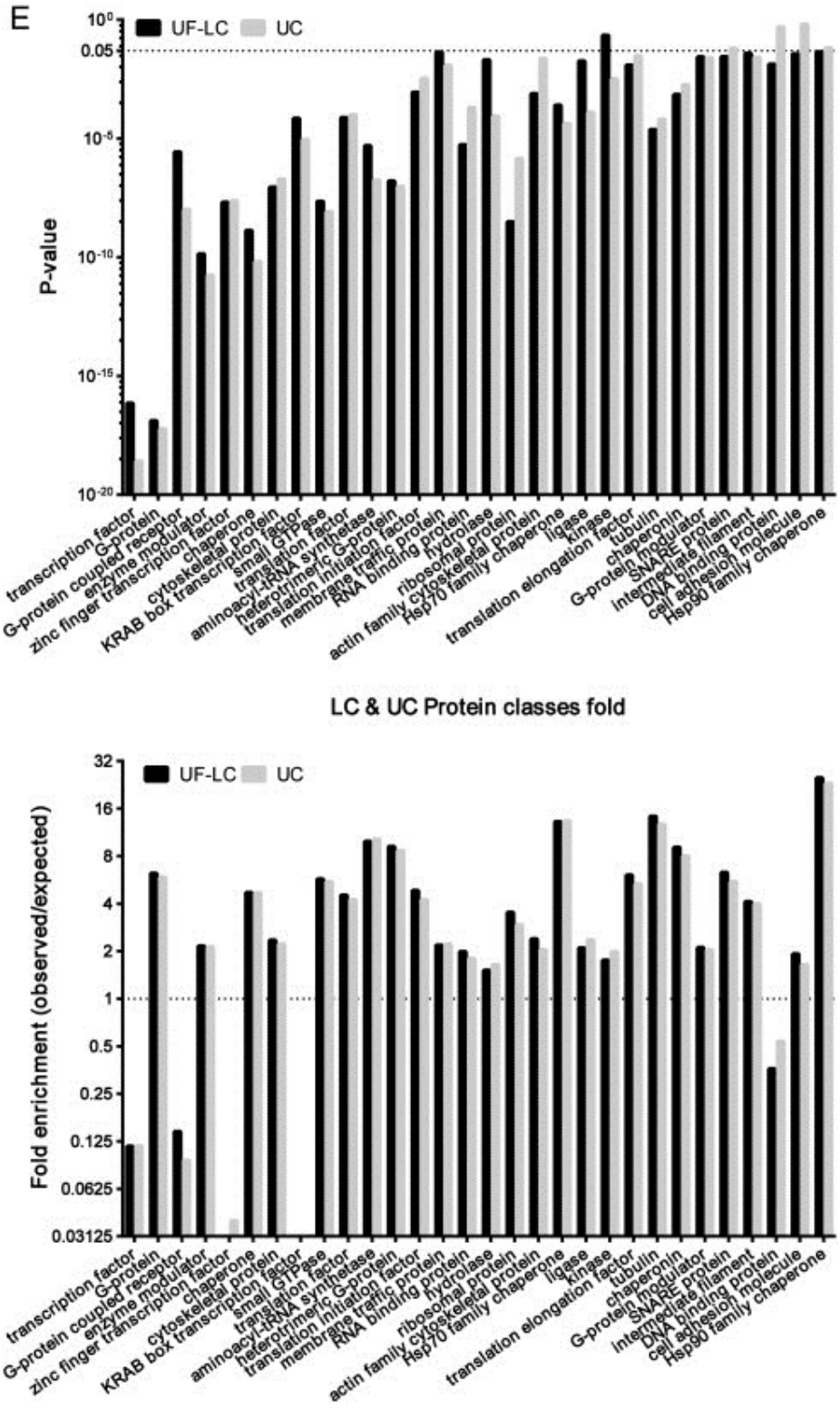

Supplementary figure S3. Correlation and complete GO enrichment (p-value and fold enrichment) for UC and UF-LC EVs derived from N2a cells.

(A) Correlation of protein abundance between UC and UF-LC preparations. All data is presented in the following groups: (B) cellular components, (C) molecular functions, (D) biological processes and (E) panther protein classes showing both UC (black bar) and UF-LC (grey bar) samples

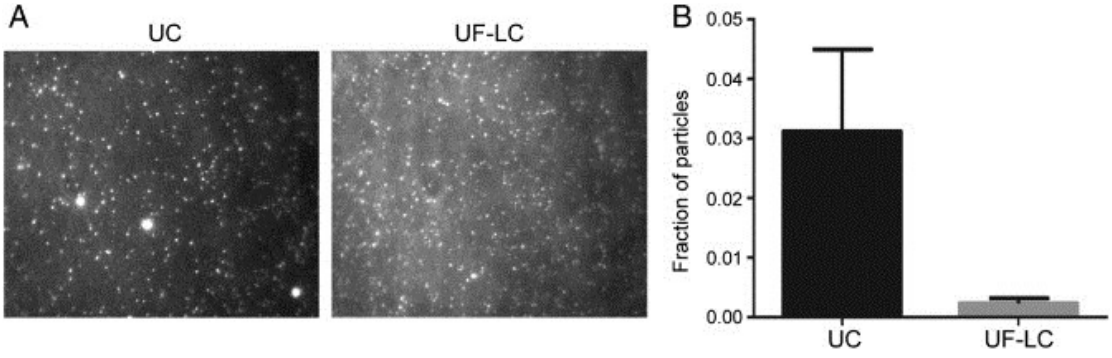

Supplementary figure S4. TIRF imaging of UC and UF-LC EVs derived from N2a cells

(A) Representative TIRF images of *FAST* DiO™ stained EVs from UC and UF-LC preparations. (B) Graph showing fraction of particles with an area 2 SD above the mean size of particles in UC (black bar) and UF-LC (grey bar) -purified EVs. Each bar represents the results (mean+/-s.d.) of three random image fields from three experiments.

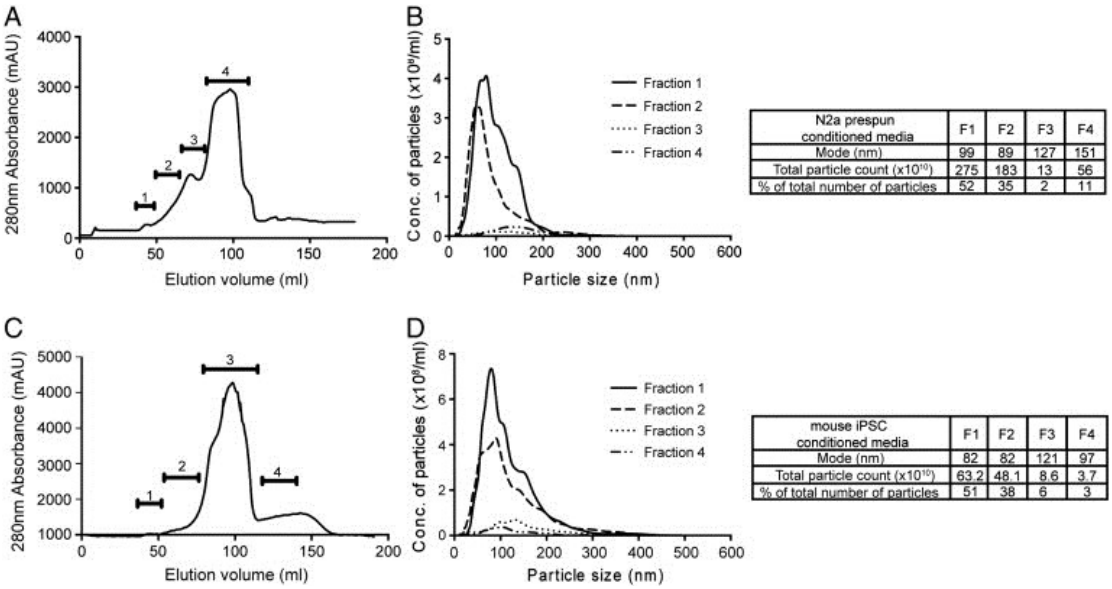

N2a prespun conditioned media	F1	F2	F3	F4
Mode (nm)	99	89	127	151
Total particle count (x10^{10})	275	183	13	56
% of total number of particles	52	35	2	11

mouse iPSC conditioned media	F1	F2	F3	F4
Mode (nm)	82	82	121	97
Total particle count (x10^{10})	63.2	48.1	8.6	3.7
% of total number of particles	51	38	6	3

Supplementary figure S5. UF-LC data for complex media sources (N2a pre-spun conditioned media and mouse iPSCs media)

LC 280nm chromatograph of conditioned pre-spun media from N2a cells (A) and conditioned stem cell media from iPSCs (C). For N2a, a total of 3 peaks were detected while a total of 2 peaks were detected for iPSCs. Collections across the eluate were pooled as indicated by the bars on the chromatograph and analysed by WB and NTA. (B) Based on NTA, the majority of the total number of particles for N2a prespun samples was eluted in fraction 1, where the mode size is around 99 nm. (D) For iPSCs, the majority of the total number of particles was eluted in fraction 1, where the mode size is around 82nm.

Supplementary table

Supplementary Table S1

Table showing all the proteins found in all 3 replicates for both UC and UF-LC. Proteins ranked according to number of Peptide spectrum matches (PSMs).
Legend: UC=Ultracentrifugation and UF-LC=Ultrafiltration with subsequent Liquid Chromatography purification. R=replicate.

References

1. Keller S, Ridinger J, Rupp AK, Janssen JW, Altevogt P. Body fluid derived exosomes as a novel template for clinical diagnostics. *J Transl Med* 2011;9:86-94.
2. Ela S, Mager I, Breakefield XO, Wood MJ. Extracellular vesicles: biology and emerging therapeutic opportunities. *Nat Rev Drug Discov* 2013;12(5):347-57.
3. Peinado H, Aleckovic M, Lavotshkin S, Matei I, Costa-Silva B, Moreno- Bueno G, et al. Melanoma exosomes educate bone marrow progenitor cells toward a pro-metastatic phenotype through MET. *Nat Med* 2012;18(6):883-91.
4. Bellingham SA, Guo BB, Coleman BM, Hill AF. Exosomes: vehicles for the transfer of toxic proteins associated with neurodegenerative diseases? *Front Physiol* 2012;3:1-12 [124].
5. Lai RC, Chen TS, Lim SK. Mesenchymal stem cell exosome: a novel stem cell-based therapy for cardiovascular disease. *Regen Med* 2011;6(4):481-92.
6. Timmers L, Lim SK, Hoefer IE, Arslan F, Lai RC, van Oorschot AA, et al. Human mesenchymal stem cell-conditioned medium improves cardiac function following myocardial infarction. *Stem Cell Res* 2011;6(3):206-14.
7. Gatti S, Bruno S, Deregibus MC, Sordi A, Cantaluppi V, Tetta C, et al. Microvesicles derived from human adult mesenchymal stem cells protect against ischaemia-reperfusion-induced acute and chronic kidney injury. *Nephrol Dial Transplant* 2011;26(5):1474-83.
8. Lee Y, El Andaloussi S, Wood MJ. Exosomes and microvesicles: extracellular vesicles for genetic information transfer and gene therapy. *Hum Mol Genet* 2012;21(R1):R125-34.
9. Thery C, Amigorena S, Raposo G, Clayton A. Isolation and characterization of exosomes from cell culture supernatants and biological fluids. *Curr Protoc Cell Biol* 2006;30(3.22):3.22.1-3.22.29.
10. Momen-Heravi F, Balaj L, Alian S, Mantel PY, Halleck AE, Trachtenberg AJ, et al. *Current methods for the isolation of extracellular vesicles. Biol Chem* 2013;394(10):1253-62.
11. Tauro BJ, Greening DW, Mathias RA, Ji H, Mathivanan S, Scott AM, et al. *Comparison of ultracentrifugation, density gradient separation, and immunoaffinity capture methods for isolating human colon cancer cell line LIM1863-derived exosomes. Methods* 2012;56(2):293-304.
12. Alvarez ML, Khosroheidari M, Kanchi Ravi R, DiStefano JK. *Com- parison of protein, microRNA, and mRNA yields using different methods of urinary exosome isolation for the discovery of kidney disease biomarkers. Kidney Int* 2012;82(9):1024-32.
13. Chen C, Skog J, Hsu CH, Lessard RT, Balaj L, Wurdinger T, et al. *Microfluidic isolation and transcriptome analysis of serum microve- sicles. Lab Chip* 2010;10(4):505-11.
14. Arslan F, Lai RC, Smeets MB, Akeroyd L, Choo A, Aguor EN, et al. *Mesenchymal stem cell-derived exosomes increase ATP levels, decrease oxidative stress and activate PI3K/Akt pathway to enhance myocardial viability and prevent adverse remodeling after myocardial ischemia/ reperfusion injury. Stem Cell Res* 2013;10(3):301-12.
15. Gercel-Taylor C, Atay S, Tullis RH, Kesimer M, Taylor DD. *Nano- particle analysis of circulating cell-derived vesicles in ovarian cancer patients. Anal Biochem* 2012;428(1):44-53.
16. Böing AN, van der Pol E, Grootemaat AE, Coumans FAW, Sturk A, Nieuwland R. *Single-step isolation of extracellular vesicles by size- exclusion chromatography. J Extracell Vesicles* 2014;3:23430.
17. Hink MA, Griep RA, Borst JW, van Hoek A, Eppink MH, Schots A, et al. *Structural dynamics of green fluorescent protein alone and fused with a single chain Fv protein. J Biol Chem* 2000;275(23):17556-60.
18. Webber J, Clayton A. *How pure are your vesicles? J Extracell Vesicles* 2013;2:19861.

4.3 Manuscript I (Quantitative profiling of exosome parent-recipient cell pairing by high content screening using CD63-emGFP vesicle labeling)

Exosomes are recognized as delivery vehicles and a role in the immune system, cancer cell environment manipulation [119] [7], miRNA delivery and even metastatic niche formation [22] [120] has been shown. These and other examples indicate that exosomes have the potential to target cells, tissues or organs in a highly specific manner. A systematic investigation though is still lacking most likely due to the unspecific and unreproducible quantification methods like total protein content or lipid dyes as described earlier. In manuscript I (Quantitative profiling of exosome parent-recipient cell pairing by high content screening using CD63-emGFP vesicle labeling.) we describe the highly specific fluorescent exosome labeling with a CD63-emGFP marker. We extensively characterize labeled and unlabeled exosome vesicles and show that there are no relevant differences in density, morphology and protein content detectable. With this labeling strategy, the sensitive quantification method and the above described gentle isolation method we finally had the required enabling technologies in our hands to quantitatively profile exosome uptake efficiencies. In this manuscript (manuscript I (Quantitative profiling of exosome parent-recipient cell pairing by high content screening using CD63-emGFP vesicle labeling)) we then identified preferences in cell pairing by screening across a panel of parent and recipient cells.

CD63-emGFP as a marker for exosome cell uptake quantification at the single vesicle level by high content screening

Heusermann W[1, 2,*], Hean J[1, 3], Trojer D[1], vonBueren S[1], Graff-Meyer A[4], Genoud C[4], Steib E[1], Voshol H[1], EL Andaloussi S[5], Wood MJ[3], Meisner-Kober NC[1,*]

[1]Novartis Institutes for Biomedical Research, CH-4000 Basel, Switzerland

[2]current: Imaging Core Facility, Biozentrum, University of Basel, CH-4056 Basel, Switzerland

[3]Department of Physiology, Anatomy and Genetics, University of Oxford, Oxford OX1 3QX, UK

[4]Friedrich-Miescher Institute for Biomedical Research, CH-4000 Basel, Switzerland

[5] Karolinska Institutet, Department of Laboratory Medicine, SE-141 86 Huddinge, Sweden

*Corresponding authors: wolf.heusermann@unibas.ch, nicole.meisner-kober@novartis.com

Abstract. Cellular communication by exosomes is thought to be highly efficient but quantitative characterization of their interaction with recipient cells is lacking. Such studies demand for a labelling strategy that allows to specifically and quantitatively trace exosomes on the background of co-purifying extracellular vesicles and particles, while minimizing alterations of the vesicle physicochemical properties. Here we provide extensive characterization of exosome labelling by emerald GFP (emGFP) tagged CD63. Overexpression in parent cells yields fluorescent exosomes that carry 10-30 CD63-emGFP molecules per vesicle. In addition, a second species of free emGFP, truncated from CD63 is released into the extracellular space which is co-purified by ultrafiltration but largely removed by gel filtration. Based on sedimentation density fractionation, size exclusion chromatography, fluorescence correlation spectroscopy, cryo-electron microscopy and proteomics we demonstrate that neither the parent cell transfection, CD63-emGFP overexpression nor UF-GF isolation significantly compromise measured physicochemical integrity of the vesicles, including their density, size, protein cargo repertoire as well as morphology. Quantitative single vesicle imaging further reveals that ultrafiltration recovers single, intact vesicles whereas ultracentrifugation gives rise to a fraction of vesicle fusion and/or aggregation. Using these extensively characterized vesicles we further describe a high content screening assay allowing to quantify exosome cell uptake with high statistical power and at the single cell level. As a direct application of this assay we provide the first quantitative profiling of exosome uptake across an array or parent-recipient cell pairs to reveal preferences in exosome internalization by different cell types.

Keywords
Exosomes; Extracellular vesicles; Microvesicles; Exosome labelling; Fluorescence correlation spectroscopy; CD63-GFP; Exosome uptake; High content screening; Tissue targeting.

Introduction

Cell to cell communication by exosomes is gaining increasing traction in basic cell biology research, biomarker discovery and therapeutic drug delivery alike. Thus there is high demand for an increased understanding of how exosomes interact with recipient cells. Furthermore, a quantitative characterization is still lacking. Fluorescence imaging is a method of choice to monitor exosome uptake dynamics and efficiency, but demands for fluorescence labelling of the vesicles. The main issues to address are a selective labelling of exosomes on the background of other

extracellular vesicles and particles, with minimal perturbation of their physicochemical and biological properties. The two general approaches can be classified into post-isolation labelling versus modification of the parent cells, whereas the fluorescence can be introduced via exosome cargo, lipids or protein markers. A relatively straightforward approach is to stain exosomes post isolation with lipophilic carbocyanine dyes such as DiI, DiO or DiD. These compounds are lipid-like molecules with fluorescent head groups and long aliphatic tails capable of inserting into the vesicle membranes. Alternative lipid stains that might be used are FM4-64, R18, CFSE, PKH-26 [1], PKH-67 [2], as well as Top Fluor Sphingomyelin or Top Fluor Cholesterol (Heusermann et al, unpublished data). Employing lipophilic carbocyanine dyes is experimentally straightforward and allows for the use of synthetic fluorophores with optimal photophysical properties as well as flexibility over the entire spectral range. This strategy has meanwhile become of widespread use for fluorescence microscopy based studies of exosomes [2]–[6]. The major drawback of lipophilic tracers however is that they are not exosome specific and indiscriminately stain all vesicles and lipid particles contained within the sample. Additionally, the integration of non-natural lipids may alter the physicochemical properties of the exosome membrane and thereby affect their functionality. To complicate matters, additional washing and ultracentrifugation steps needed to remove unincorporated tracers may introduce further bias (and yield issues). Thus, careful optimisation of labelling ratios as well as monitoring changes of exosome size and zeta potential may be required to allow for the least perturbing conditions. Another difficulty is that in salt-containing buffers or media most of these lipid stains rapidly form micelles or aggregates themselves. Since these lipid aggregates and micelles can have similar physicochemical properties as exosomes they can lead to erroneous results, and their efficient removal may require stringent purification conditions.

The expression of fluorescent protein (FP) tagged exosome surface markers in parent cells therefore appears as a more specific and less invasive strategy, and first examples have been presented in recent studies [7], [8]. However, the selectivity of such markers for visualization of exosomes within complex samples of extracellular particles are a critical issue. In addition, it remains unclear whether a non-physiological overexpression of FP-tagged exosome markers within the parent cells may influence exosome biogenesis, release as well as their composition due to cell stress or simply altered surface marker abundance. Therefore, a careful characterization of labelled versus unlabelled exosomes is warranted. Here we provide an extensive quantitative and qualitative characterization of exosomes labelled via CD63-emGFP overexpression in parent cells to address specificity of labelling as well as potential perturbation of vesicle properties. Using fluorescence correlation spectroscopy, we quantitatively

characterize the vesicles at the single vesicle / single molecule level and monitor exosome release over time. Using these extensively characterized vesicles we further report a high content screening assay to quantify exosome uptake with high statistical power which we apply to quantitatively profile exosome parent - recipient cell pairing preferences across a panel of primary cells and cell lines.

Results

Exosome labelling by CD63-emGFP. To retain the natural function of CD63 in signal transduction or integrin complexation, emGFP was fused to the N-terminus of CD63 (Supplementary Figure 1a), thereby oriented to the luminal side of the exosome membrane (Figure 1a). CD63-emGFP was transiently overexpressed in HEK293 cells or Huh7 cells using lipofection for 5 hours. Following extensive washing, exosome free medium (OptiMEM) was added and conditioned for 48 hours. To confirm the presence of CD63-emGFP in exosomes we first tested for co-fractionation of emGFP fluorescence with exosome markers based on density using a sucrose sedimentation gradient (Figure 1b), as well as based on size using gel filtration chromatography (Figure 1c). Exosomes have been widely established to float at 33-39 % (w/v) sucrose (corresponding to 1.14-1.17 g/mL). Of note, all previous studies using sucrose density gradients have analyzed the vesicles following at least one initial ultracentrifugation or ultrafiltration step, to the best of our knowledge. To analyze the vesicles without any prior concentration or ultracentrifugation steps we established conditions for fractionating conditioned medium directly onto a sucrose gradient. Our data for the first time confirm that also native exosomes, analyzed directly from medium, sediment at a density of 32-40 % (1.13-1.18 g/mL) sucrose as assessed by Western blotting analysis for the exosomal marker proteins Alix and Tsg101 as well as by Nanoparticle Tracking Analysis (Supplementary Figure 1b). CD63 was not detected in the gradients from unconcentrated medium, most likely due to the poor antibody sensitivity. Exosomes from CD63-emGFP transfected HEK293 cells (Figure 1b) sedimented at a similar density as exosomes from untransfected cells. Fluorescence correlation spectroscopy (FCS) analysis in all fractions further confirmed the enrichment of emGFP positive particles with translational diffusion times (tdiff) of 2-10 ms, corresponding to a vesicle size of ca 50-120 nm, co-fractionating with Alix (Figure 1b).

To isolate CD63-emGFP vesicles in as native state as possible, we followed a successive ultrafiltration-gel filtration (UF-GF) protocol recently established by us and others [9]. Briefly, after removal of cell debris and filtration on a 0.22 um filter, conditioned medium was concentrated by ultrafiltration on a 100 kDa MWCO

filter and further fractionated on a size exclusion chromatography column (Superdex-200, Figure 1c). Consistent with our previous description of exosome isolation by GF [9], the UV chromatogram revealed two major peaks, one corresponding to the expected elution volume of vesicles (ca 1 MDa, Supplementary Figure 1c) and one peak at ca 82 kDa most likely comprising residual serum albumin and other serum proteins, as supported by Bradford protein quantification (Supplementary Figure 1d, upper panel). In line with the first peak comprising vesicles and the second peak comprising non-vesicular protein complexes, the ratio of 254/280 absorption was also markedly different with Abs_{254}:Abs_{280} ~ 1.3 in peak 1, and Abs_{254}: Abs_{280}~ 2 in peak2 (Supplementary Figure 1d, bottom panel). Pooled samples of 4 fractions each (omitting one fraction between pools) were analyzed by Western blotting. The exosomal marker proteins Alix and Tsg101 eluted in a relatively sharp peak close to the void volume, as expected based on the upper size separation limit of the column at 600 kDa (exclusion limit 1.3 MDa). The still widely used exosomal marker Lamp2b also co-eluted with the vesicles however showed a broad elution profile with two apparent maxima, suggesting its association with a different vesicle population. The emGFP fluorescence peaked with the exosomal markers, as well as with the CD63-emGFP fusion protein detected by anti-GFP western blotting. A second major GFP fluorescent peak was observed eluting at ca 26.8 kDa (Supplementary Figure 1c) and comprising emGFP truncated from CD63 according to Western blotting (Figure 1c).

Quantitative characterization of CD63-emGFP labeling at the single vesicle level.
To further characterize the emGFP positive species within these two major peaks at the single molecule / single vesicle level, we analyzed all fractions by FCS (Figure 2a). Fractions of peak 1 comprised a relatively heterogeneous population of emGFP fluorescent, large particles with translational diffusion times ranging from ca 2-10 ms (mean of ca 4 ms), corresponding to ca 50-120 nm in size (mean of ca 100 nm). A similar heterogeneity was observed in molecular brightness, ranging from ca 80 kHz to 1000 kHz per particle (mean of ca 250 kHz per particle). Treatment with the detergent NP40s resulted in a uniform population of molecules with a translational diffusion time of 300 us, corresponding to the expected t_{diff} of CD63-emGFP (based on extrapolation from data measured for free emGFP, t_{diff} = 160 us, data not shown). These data confirm a physical association of CD63-emGFP with ca 100 nm sized vesicles. Consistently, NP40s treatment also resulted in a drop of the molecular brightness of these species yielding a homogeneous population of molecules with similar brightness as measured for free, monomeric emGFP (ca 18 kHz, data not shown). The number of emGFP molecules independently diffusing through the confocal volume was in

turn increased upon vesicle disruption by NP40s. Together, these data reveal the presence of multiple CD63-emGFP molecules per vesicle, ranging between ca 10 to 30 molecules for individual vesicles (Figure 2a, bottom). The second major eluting GFP peak in contrast comprised molecules of relatively homogeneous translation diffusion times and molecular brightness, insensitive to NP40s treatment and consistent with the size and brightness expected for monomeric GFP. This is in line with the Western blotting results in Figure 1c and corroborates that this second species contains mainly non-vesicular, truncated GFP. Similar data were obtained for Huh7 and B16 exosomes (Supplementary Figure 2a and b, and data not shown). The fractions comprising exosomal markers and GFP positive vesicles were pooled after gel filtration and are henceforth referred to as UF-GF enriched exosomes.

Since FCS allowed to specifically quantify CD63-emGFP vesicles within heterogeneous samples, we reasoned it might be a straightforward method to monitor the release of CD63 positive vesicles. As the sensitivity in the nanomolar range was not sufficient for reliable quantification directly in medium, we enriched the conditioned medium by ultrafiltration (100 kDa MWCO) and then quantified the amounts of CD63-emGFP vesicle released at different time points by FCS. Using a 2-component fit with a diffusion time of free, non-vesicular GFP set to the measured value of 160 us allowed to specifically determine the concentration of GFP positive vesicles within the heterogenous samples (Figure 2b). The total number of vesicles per ml of conditioned medium as determined by NTA increased over time, whereas the release of fluorescent vesicles was delayed by several hours, most likely reflecting the onset of expression the transfected CD63-emGFP. The relative fraction of CD63-emGFP vesicles was highest after 16 hours and reached up to an apparent 80 % of all vesicles. While both, fluorescent and total vesicles numbers further increased over time, the relative fraction of fluorescent vesicles declined, which might be due to the reporter plasmid being diluted out with cell division, and/or an increased contribution of other types of vesicles being released at later time points.

CD63-emGFP labelling results in minimal vesicle perturbation. In addition to their unchanged size and density, we next assessed the morphological integrity of exosomes from CD63-emGFP transfected parent cells. UF-GF enriched exosome samples with and without fluorescent markers were analyzed by cryo-electron microscopy (cryo-EM). In both conditions the samples contained a similar repertoire of predominantly double membrane enclosed, perfectly round, protein-coated vesicles with homogeneous structure and size of ca 50-140 nm in diameter (Figure 3a and Supplementary Figure 3a). Finally, we aimed to determine whether CD63-emGFP parent cell transfection might result in

significant changes of the exosome protein content. UF-GF enriched exosomes from CD63-emGFP transfected versus untransfected HEK293 cells were analyzed by MS-proteomics (Supplementary Table 1), which confirmed a high abundance of several canonical exosome markers (Figure 3b). Importantly, the proteome of HEK293 CD63-emGFP vesicles closed matched that of untransfected cells. Among the top 350 proteins, GFP was essentially the only different cargo (Figure 3c and Supplementary Table 1).

UF-GF isolation yields single, intact vesicles. It has been an open question in the field whether certain isolation protocols might cause aggregation or fusion of the vesicles, which would compromise any studies of exosome uptake or function. To address this, we generated separate samples of CD63-emGFP and CD63-mCherry labelled exosomes from independently transfected HEK293 cells, and then mixed the two conditioned media prior to purification by UF-GF or a standard ultracentrifugation (UC) protocol [9]. Diluted vesicle samples were spotted onto a coverslip and imaged by confocal microscopy. Vesicles were detected as light diffraction limited GFP or mCherry fluorescent spots of uniform size, corresponding to the point spread function of the microscope. Following UF-GF, no double positive spots were detected, demonstrating that the exosomes remained intact and disperse after UF-GF purification, as well as confirming the detection of single vesicles (Figure 4a and Supplementary Figure 4a). In contrast, ultracentrifugation (UC) yielded a small population of double positive, slightly larger spots, revealing a certain degree of vesicle fusion and/or aggregation during the purification (Figure 4b and Supplementary Figure 4b) that furthermore varied between experiments. As positive controls, exosomes labelled with a CD63-emGFP-mCherry fusion protein were predominantly detected as double positive spots (Figure 4c and Supplementary Figure 4c). Controls with exosomes from either CD63-emGFP or CD63-mCherry transfected cells were performed as well and confirmed exclusive detection in the correct channels (data not shown). These data directly demonstrate that CD63-emGFP labelled, UF-GF isolated exosomes remain and can be detected as single vesicles by confocal microscopy, whereas caution may be taken with UC isolation.

Quantitative profiling of exosome uptake across a panel of parent - recipient cell pairs using high content screening. While gel filtration largely removed the extracellular non-vesicular GFP, residual amounts were still present in the exosomal fractions recovered by UF-GF according to Western blotting (Figure 1c) and FCS. We therefore wanted to exclude any potential artefacts in studying cell uptake of CD63-emGFP exosomes due to residual non-vesicular GFP and compared uptake of both species into HEK293 cells side by side using matched concentrations based on FCS analysis. While CD63-emGFP exosomes were taken

up well, virtually no uptake of free GFP was detected by high resolution confocal microscopy (Figure 5a). We next tested the cell uptake of CD63-emGFP exosomes by directly adding conditioned medium to recipient cells. To quantify the exosome uptake over time the confocal images from live cell experiments were analyzed in Cell Profiler. Exosome internalization was most robustly quantified based on the number of fluorescent spots per cell. A low but significant level of internalized fluorescence was detected which increased over time (Figure 5b, left panel). Also the percentage of transfected cells increased over time and reached up to at least 90 % of positive cells within 15 hours (Figure 5b, right panel and Figure 5c). Interestingly, exosomes from UF enriched samples showed remarkably identical uptake efficiency as compared to vesicles from direct addition of conditioned medium (Figure 5b). At the low, subpicomolar concentrations used in order to match those of CD63-emGFP exosomes within conditioned medium, no saturation was detected up to 15 hours.

We next set up a quantitative high content screening assay for exosome uptake in a 384well format. For practical reasons we focused on Huh7 recipient cells for the assay development. Cells were fixed at various time points following CD63-emGFP exosome addition, and imaged on an automated plate imaging station (Operetta, Perkin Elmer). Internalized GFP fluorescence was quantified based on the number of intracellular GFP fluorescent vesicles per cell using automated image analysis (Harmony, Perkin Elmer). At low picomolar concentrations of exosomes, uptake saturated with time (Figure 5d). Consistent with the imaging data in Figure 5a, also in the HCS assay the uptake detected for non-vesicular emGFP was negligible, even at increased concentrations of free GFP to match the number of fluorophores rather than vesicles.

Using this assay, we next set out to assess quantitative differences in exosome uptake across a panel of parent cell - recipient cell pairs. CD63-emGFP labelled exosomes were isolated from HEK293, Huh7 and B16 cells and analyzed by FCS to confirm a similar brightness of the vesicles (Supplementary Figure 2 and data not shown). Uptake was then tested side by side across a panel of recipient cell lines and primary cells (HEK293, B16, Huh7, HeLa, human primary fibroblasts, human primary keratinocytes, human endothelial cells and human iPS derived neurons). Based on the data in Figure 5d exosomes were added at increasing concentrations (1-18 pM of CD63-emGFP vesicles) for 8 hours, and uptake was quantified using the automated plate imaging assay described above (Figure 6a). Relative uptake efficiency was scored semi-quantitatively based on the level of internalized GFP at the highest concentration, as well as the EC50. As summarized in Table 1 and illustrated in Figure 6b, exosomes from all three parent lines were taken up well into a variety of recipient lines. In most recipient cells we only observed minor

uptake differences between exosomes from different parent cells. However, in Huh7 cells there was a major difference with Huh7 exosomes being taken up with ca 4-fold reduced efficiency than B16 and HEK293 exosomes. An even more striking difference was observed between different recipient lines. Some cell lines, including B16 melanoma cells and primary human keratinocytes, even appeared to be resistant to exosome uptake, at least for the exosome types used in this study. Even after increasing the exosome concentration ~10,000 fold (200 nM instead of 18 pM), no uptake of HEK exosomes was detectable in keratinocytes (Supplementary Figure 5). These data support a highly specific mechanism for exosome cell uptake and suggest that preferential cell-cell pairing exists.

Discussion

To quantitatively study the interaction of exosomes with recipient cells a labelling strategy is needed that allows to specifically trace exosomes on the background of co-purifying ectosomes, apoptotic bodies and other types of extracellular vesicles and particles [10], while minimizing alterations of the vesicle physicochemical properties. CD63 is a tetraspanin glycoprotein that has been recognized as a relatively ubiquitous marker present in extracellular vesicles, with growing evidence for selective enrichment in exosomes [10]–[13]. While first examples of using CD63 reporters for fluorescent labelling of exosomes have been reported [7], [13] and exosome labelling kits based on FP tagged CD63 reporters have now even become commercially available, a thorough characterization of these vesicles is still lacking. Here we use labelling through emerald GFP (emGFP)-tagged CD63 and provide an extensive characterization of the fluorescent vesicles. Overexpression of our construct in parent cells yields vesicles with typically 10-30 CD63-emGFP molecules per vesicle that are sensitive to detergent treatment, whereas a second species of free emGFP, truncated from CD63 is released into the extracellular space and co-purified by ultrafiltration but largely removed by gel filtration.

Since CD63-emGFP vesicles showed a size, sedimentation density and morphology consistent with that of exosomes, co-fractionated with Alix and Tsg101 on sucrose gradients as well as gel filtration, and were enriched together with Alix, CD81, CD9, Tsg101 and CD63 as determined by proteomics, we conclude that CD63-emGFP vesicles are predominantly exosomes. Based on a comparative characterization of vesicles from transfected and untransfected cells by sedimentation density fractionation, size exclusion chromatography, fluorescence correlation spectroscopy, cryo-EM and proteomics, our results demonstrate that neither the parent cell transfection, CD63-emGFP overexpression nor UF-GF isolation significantly compromise measured

physicochemical integrity of the vesicles, including their density, size, morphology and, importantly, proteome. Consistent with previous data [9], single vesicle imaging now provide direct evidence that UF-GF recovers single vesicles, whereas UC gives rise to a variable extent of vesicle aggregation/fusion. We therefore recommend UF-GF as a preferred method whenever isolating exosomes for functional studies. Furthermore, we demonstrate the power of FCS for exosome quantification. This provides a significant advance towards commonly used quantification based on total protein or Nanoparticle Tracking. The first is subject to large variation depending on the isolation method, and does not give any information on exosome or even vesicle concentrations. The latter detects all vesicles within the sample that share a similar size. In contrast, FCS enables the quantification of concentration and size of CD63 positive vesicles specifically within complex samples. In addition, single vesicle parameters such as the number of fluorophores per vesicle can be derived. Finally, our data also unravel that when using FP tagged exosome reporters care must be taken with assigning the total fluorescence signal to vesicles, since a significant fraction of non-vesicular GFP is recovered from conditioned medium - at least for CD63.

Previous quantification of exosome uptake has largely been based on FACS [1], [14]–[16], which does however not discriminate between truly internalized vesicles and vesicles simply adhering to the cell surface. We here report the first HCS assay to quantify exosome uptake with high statistical power and medium throughput using automated confocal plate imaging. We are using this assay to provide a first systematic and quantitative profiling of exosome uptake efficiency across a panel of parent - recipient pairs. At large, cells either did or did not take up the three exosome types used in this study. While most cell types tested showed significant uptake of HEK293, Huh7 as well as B16 exosomes that saturated with time and dose, human primary keratinocytes and B16 melanoma cells appeared virtually resistant to uptake of these exosomes. It is conceivable that this might in part be due to the lack of cognate receptors and that these cells might take up exosomes from other cell types that were not included in this small pilot study. In particular the deficiency of B16 cells to take up B16-derived exosomes was nonetheless surprising and it will be interesting to study whether these cells may take up exosomes only under specific conditions such as hypoxia. Interestingly however, also Huh7 cells showed a significantly reduced uptake of Huh7 derived exosomes. This may suggest that the fluorescent vesicles generally compete with autocrine reuptake of unlabelled exosomes constantly released from the recipient cells. Alternatively, a true lack of allo-exosome uptake would suggest that exosomes are primarily targeted to home to different cell and tissue types rather than a function in auto- and paracrine signalling - at least for B16 and Huh7 exosomes. In either case these data support the model that highly specific

receptor-ligand interactions between exosomes and recipient cells determine parent-recipient cell pairing. We anticipate that the described assay will be valuable for the community to grow our systematic and quantitative characterization of exosome cell/tissue targeting, as well as provide a starting point for interrogating exosome function by high throughput biology such as through genetic and small molecule screens.

Figure 1

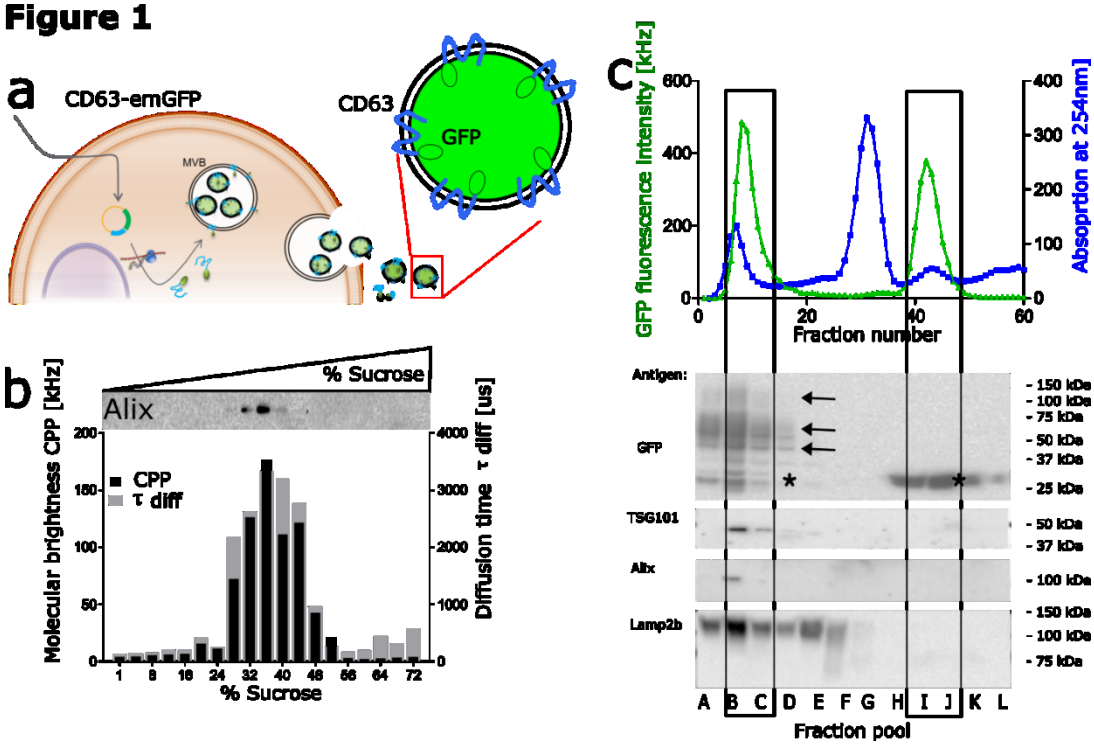

Figure 1. Native isolation of CD63-emGFP labeled exosomes by successive ultrafiltration and gel filtration. (a) Exosome labeling by transfection of parent cells. **(b)** Sucrose gradient fractionation of conditioned medium from CD63-emGFP transfected HEK293 cells without prior ultracentrifugation**.** X-axis: measured sucrose concentrations in collected fractions. GFP fluorescent particles of ca 50-120 nm diameter (measured by FCS) co-fractionate with the exosomal marker Alix, peaking at ca 32-36 % sucrose. **(c)** Following UF on a 100 kDa MWCO membrane, enriched medium was loaded onto a Superdex200 column for size exclusion chromatography, with continuous UV detection (blue line). The total GFP fluorescence count rate was measured in each of the 60 fractions by FCS (upper panel, green line). Western blots against different exosomal markers were performed after pooling of 4 fractions each into samples A-L as indicated, omitting one fraction in between pools. CD63-emGFP fusion protein bands (multiple glycosylated isoforms) versus truncated GFP bands detected on an anti-GFP western blot are indicated by arrows and asterisks, respectively.

Figure 2

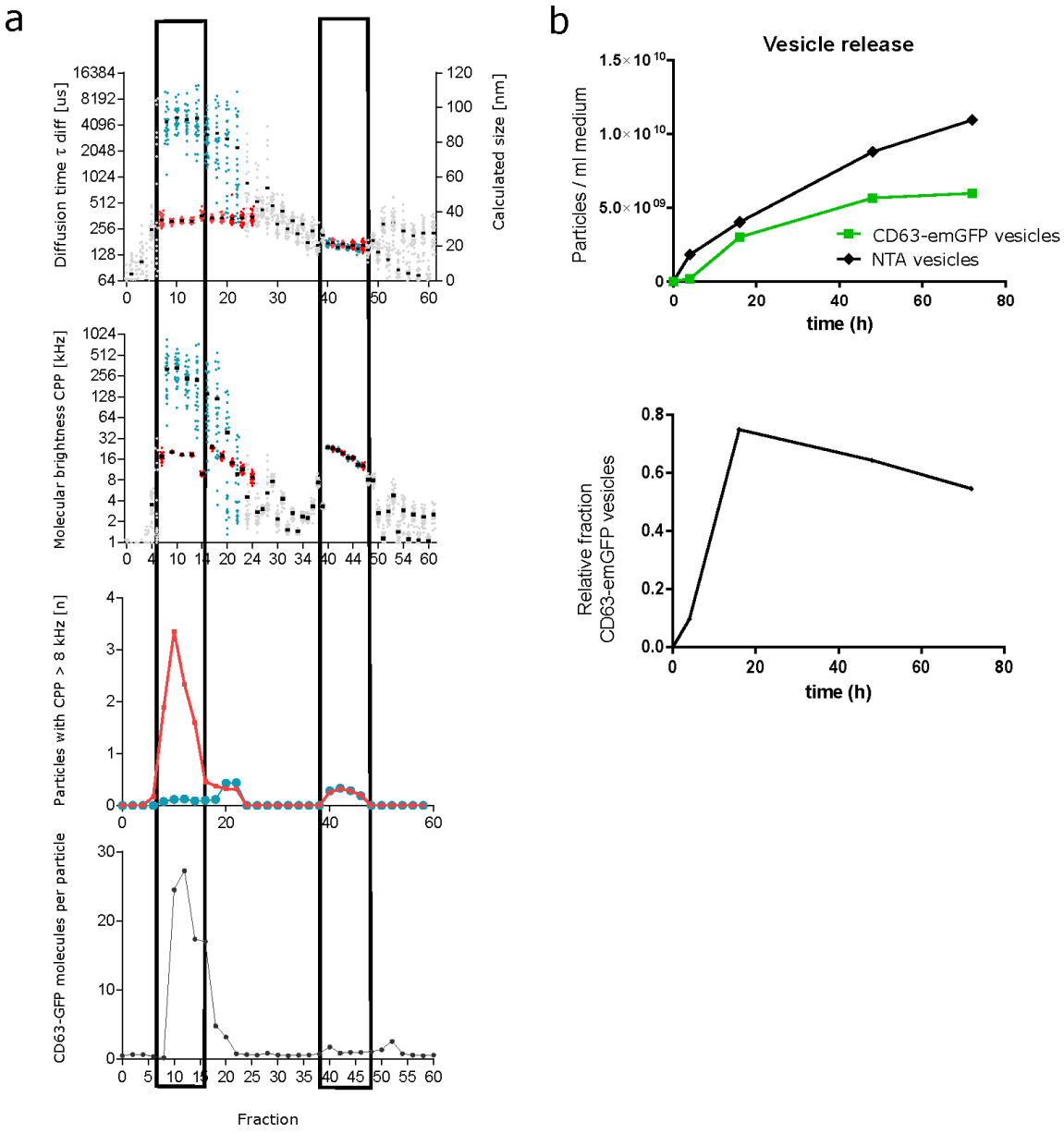

Figure 2. Single molecule characterization of CD63-emGFP labelled UF-GF isolated exosomes. (a) Individual fractions from gel filtration of HEK293 CD63-emGFP exosomes in Figure 1c were analyzed by FCS with (red data points) and without (blue data points) vesicle disruption by the detergent NP40S. The translational diffusion time (t_{diff}, upper panel), molecular brightness (CPP, second panel) as well as absolute number of fluorescent molecules within the confocal volume (n, third panel) are depicted across the fraction number from the gel filtration. The ratio of freely diffusing GFP fluorescent particles before and after NP40S treatment (third panel) yields the average number of CD63-emGFP molecules per particle (bottom panel). Frames indicate fractions comprising the two main fluorescent populations. The first peak comprises a relatively

heterogeneous population of emGFP fluorescent, large particles with tdiff ranging from ca 2-10 ms (mean of ca 4 ms), corresponding to ca 50-120 nm in size (mean of ca 90 nm). A similar heterogeneity was observed in molecular brightness CPP, ranging from ca 80 kHz to 1'000 kHz per particle (mean of ca 250 kHz). Treatment with the detergent NP40S resulted in a uniform population of molecules with a tdiff of ca. 300 us and CPP of 20 kHz, corresponding to the expected values for free CD63-emGFP (based on extrapolation from data measured for free monomeric emGFP, t-diff = 160 us, CPP = 18 kHz). The number of emGFP molecules independently diffusing through the confocal volume in turn increased upon vesicle disruption by NP40S. The second major eluting GFP peak comprises molecules of relatively homogeneous t-diff and CPP, insensitive to NP40S treatment and consistent with the size and brightness expected for monomeric GFP. **(b)** Time course of CD63-emGFP vesicle release. The concentration of CD63-emGFP positive vesicles in UF enriched samples from HEK293 cells recovered was determined by FCS, the total number of vesicles between 70-140 nm in size was determined by NTA (upper panel). Time points represent hours of conditioning, starting 5 hours after transfection. The ratio of fluorescent and total vesicle numbers is shown in the bottom panel.

Figure 3

a

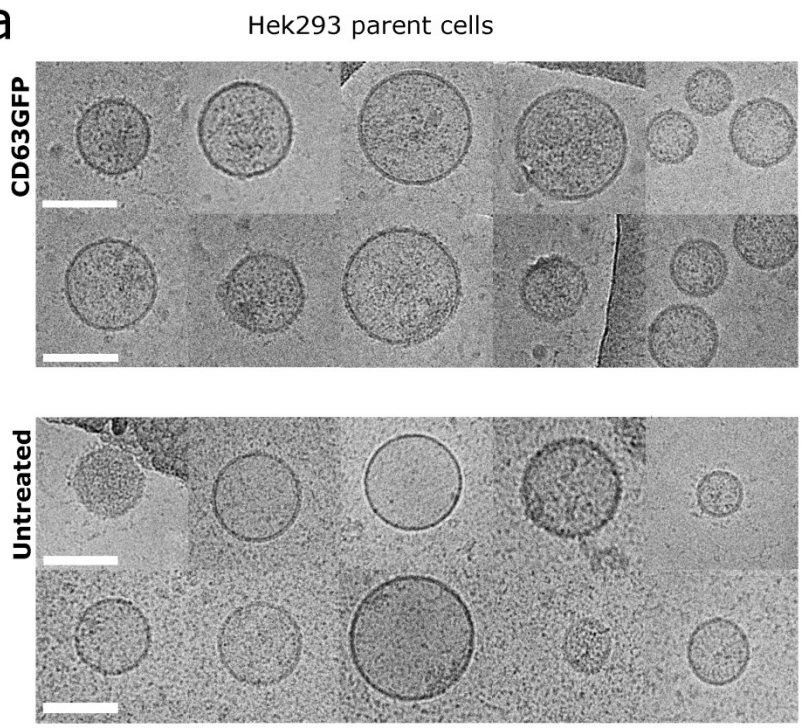

b

Marker	untreated	CD63 GFP
Alix/PDCD6IP	*47*	*30*
CD81	*23*	*15*
CD9	*11*	*10*
TSG101	*9*	*2*
CD63	*5*	*8*
GFP	*0*	*32*

c

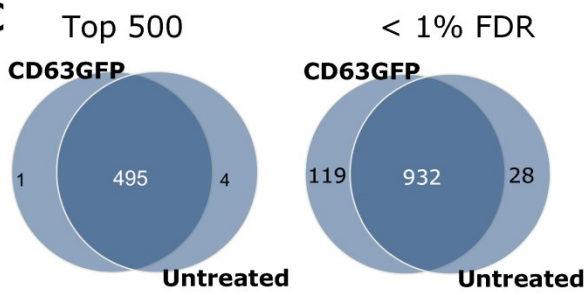

Figure 3. Morphology and proteome of extracellular microvesicles recovered from CD63-emGFP transfected and untransfected HEK293 cells. (a) Cryo-EM analysis of UF-GF isolated CD63-emGFP versus native exosomes (representative images). Scaling bar: 100 nm. **(b)** LC-MS proteomics of native versus CD63-emGFP HEK293 exosomes. Spectral counts for a subset of proteins from the list in Supplementary Table 1 are shown. **(c)** Venn diagram comparing the top 500 proteins, ranked by total spectral count (left panel), or all proteins detected at a < 1 % FDR (right panel). Of the 1079 identified proteins with 2 unique peptides in at least one of the samples, 86 % (932) were identified in both samples, 119 were unique to the emGFP-CD63 and 28 unique to the untransfected cells.

Figure 4

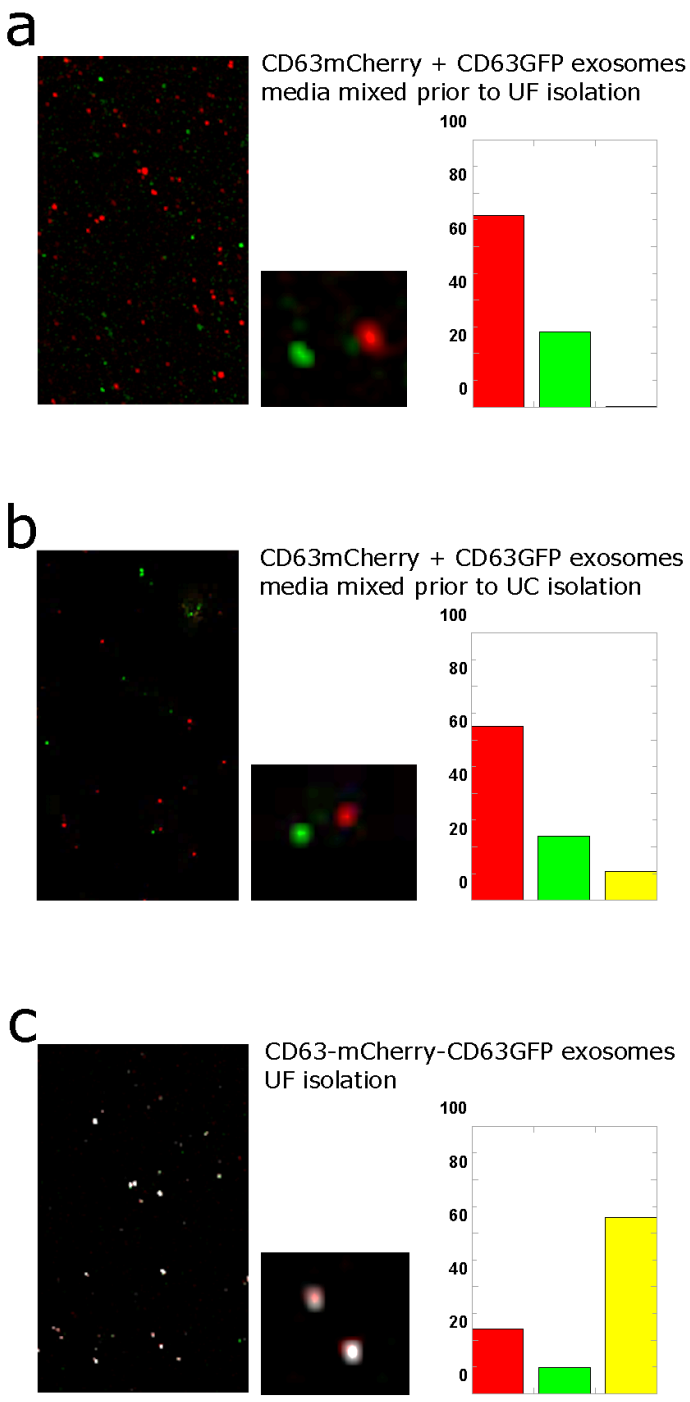

Figure 4. Single vesicle imaging of exosomes isolated by UF-GF or UC. Conditioned media from HEK293 cells transfected with either CD63-mCherry or CD63-emGFP were mixed prior to exosome isolation by ultrafiltration (UF) or ultracentrifugation (UC). Exosomes were imaged by confocal fluorescence microscopy after spotting onto coverslips. Vesicles were detected as light diffraction limited GFP or mCherry fluorescent spots of uniform size,

corresponding to the point spread function of the microscope. Colocalization was quantified based on overlap of the point spread functions in the two fluorescent channels to derive the number of GFP (G), mCherry (R) and GFP/mCherry (RG) double positive vesicles. Following UF-GF, almost no double positive spots were detected, demonstrating that the exosomes remained intact and disperse after **(a)** UF-GF purification, as well as confirming the detection of single vesicles. **(b)** In contrast, ultracentrifugation (UC) yielded a subpopulation of double positive, slightly larger spots, revealing a certain degree of vesicle fusion and/or aggregation during the purification. **(c)** As controls, UF-GF isolated vesicles from cells transfected with a CD63-emGFP-mCherry fusion protein were predominantly detected as double positive spots. Data for individually isolated CD63-emGFP or CD63-mCherry exosomes are not shown and confirmed exclusive detection in one color only.

Figure 5

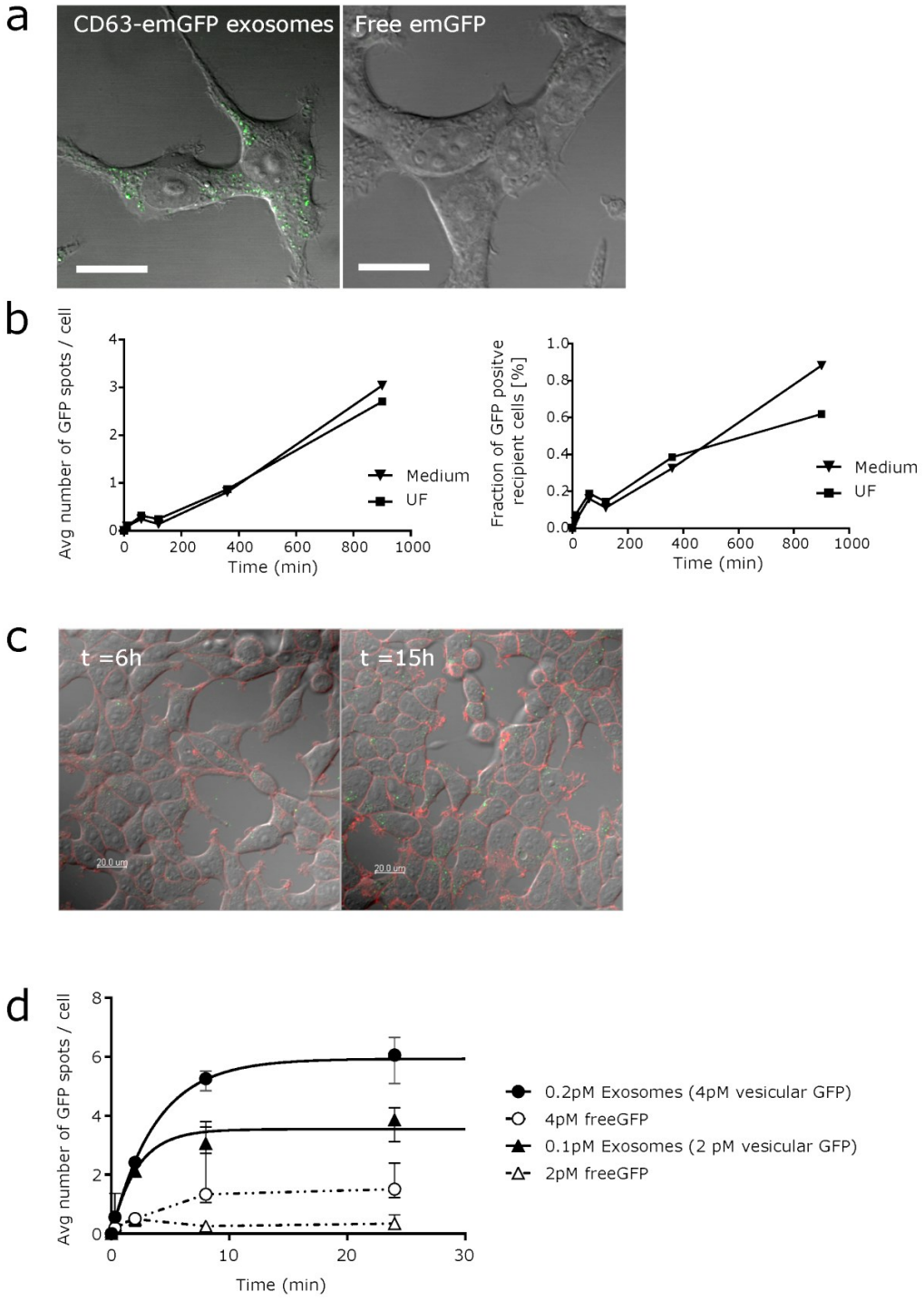
a
CD63-emGFP exosomes
Free emGFP
b
Avg number of GFP spots / cell
Time (min)
Medium
UF
Fraction of GFP posive recipient cells [%]
Time (min)
Medium
UF
c
t =6h
t =15h
d
Avg number of GFP spots / cell
Time (min)
0.2pM Exosomes (4pM vesicular GFP)
4pM freeGFP
0.1pM Exosomes (2 pM vesicular GFP)
2pM freeGFP

Figure 5. Quantification of exosome cell uptake by HCS. (a) Live cell imaging of HEK293 cells after 24 hour incubation with 10 nM of either CD63-emGFP vesicles (left panel) or non-vesicular GFP truncated from CD63 (right panel). Scaling bar: 20 um. **(b)** Quantification of HEK293 CD63-emGFP exosome uptake time course into HEK293 cells using a 96-well automated high content screening assay. Recipient cells were incubated with CD63-emGFP exosomes either by addition of conditioned medium of UF enriched samples at matched concentrations, and fixed at various time points up to 15 hours. Whole wells were then imaged on an automated confocal plate imaging station (Operetta, Perkin Elmer) and internalized GFP fluorescence was quantified based on the number of intracellular GFP fluorescent vesicles per cell using automated image analysis (left panel). Single cell data of (b) were analyzed to quantify the fraction of exosome targeted cells (right panel) **(c)** Confocal images illustrating the uptake of UF enriched CD63-emGFP HEK293 exosomes into HEK293 cells after 15 hours (green: GFP; red: Cell Mask DeepRed) **(d)** Time course of uptake of UF-GF enriched CD63-emGFP exosomes into Huh7 cells in 384well format. Non-vesicular GFP was recovered from the gel filtration (Figure 1, peak 2) and uptake was tested at fluorophore matched concentrations based on FCS quantification. All data represent averages and standard deviations from 3 biological replicates, with at least 1000 cells analysed per sample.

Figure 6

a

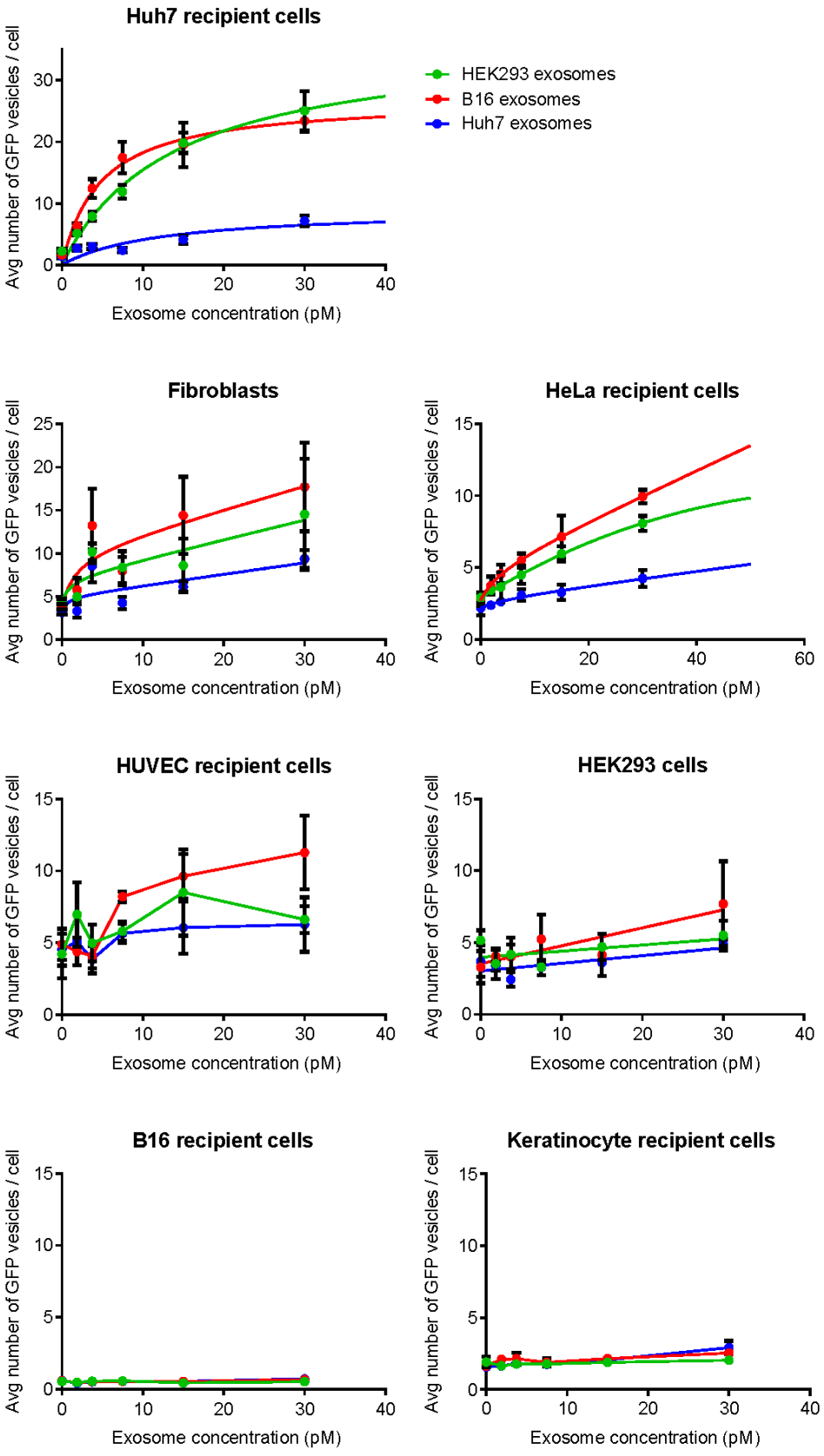
Huh7 recipient cells
HEK293 exosomes
B16 exosomes
Huh7 exosomes
Avg number of GFP vesicles / cell
Exosome concentration (pM)
Fibroblasts
HeLa recipient cells
HUVEC recipient cells
HEK293 cells
B16 recipient cells
Keratinocyte recipient cells

Figure 6

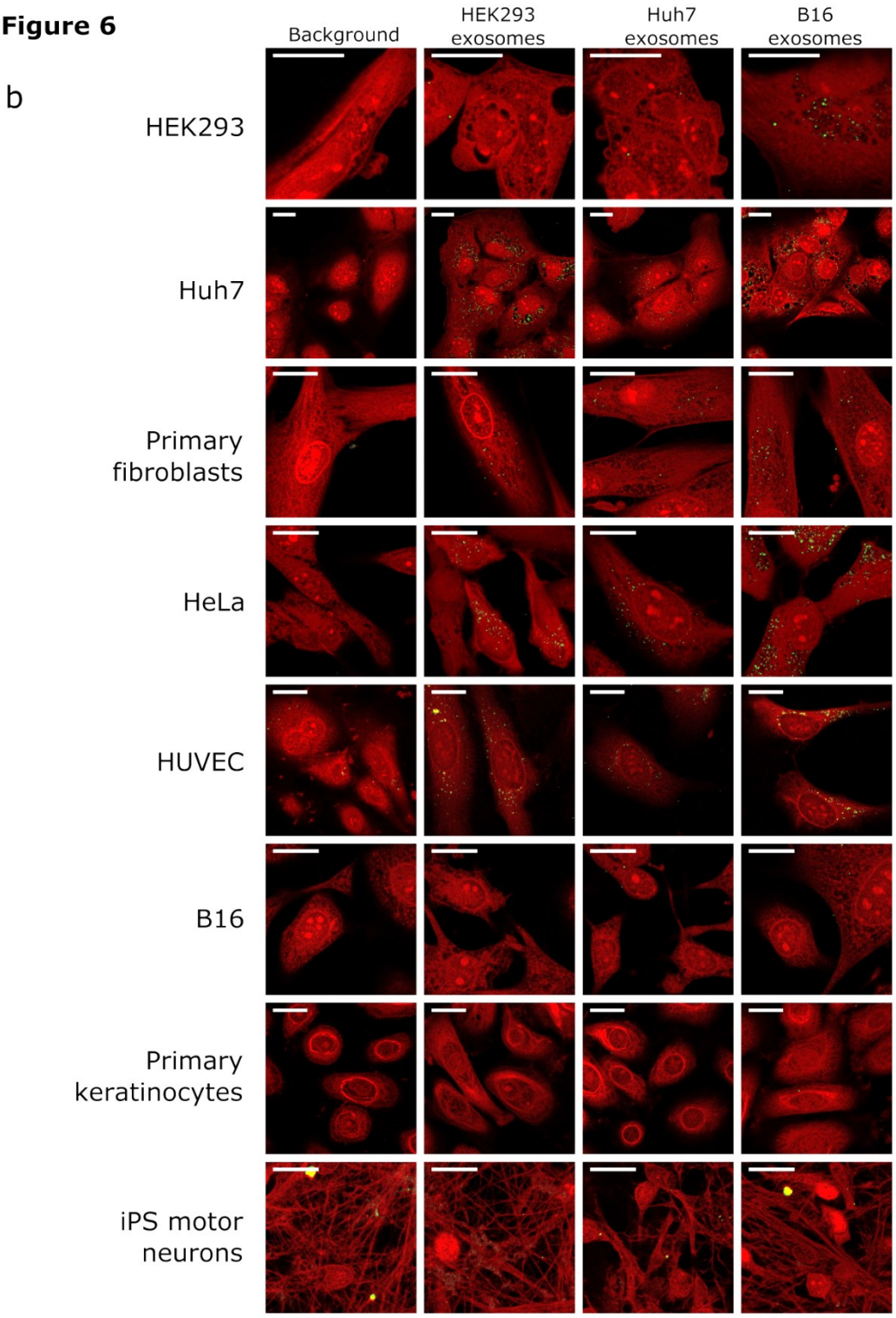

Figure 6. Profiling of exosome uptake efficiency across an array of parent and recipient lines. UF-GF isolated CD63-emGFP exosomes from HEK293, Huh7 and B16 cells were added to a variety of recipient lines in 384well format in a dose response assay (1-18 pM) and uptake was quantified after 8 hours by whole well automated fluorescent imaging. At least 5'000 cells were analyzed per sample. Error bars represent standard deviations from three biological replicates. **(b)**

Confocal images of cells incubated without (background) or with exosomes at 18 pM for different combinations of exosome parent and recipient lines as indicated (green: CD63-emGFP signal; red: CellMask Deep Red; Scaling bar: 20 um; Zeiss LSM710 inverted confocal microscope). Notably, no uptake was detected in iPS derived motor neuron cultures, however the cell morphology and 3D-network complicated the automated quantification as well as visual evaluation of truly internalized signal, and we can thus not rule out low levels of uptake.

Table1

a

	CD63GFP labeled exosomes- parent cell line		
Recipient cell line	Hek293	Huh7	B16
Huh7	++++	++	+++++
Primary fibroblasts	++++	+++	+++++
HeLa	+++	++	++++
HUVEC	++	++	+++
Hek293	+	+	+
B16	-	-	-
Keratinocytes	-	-	-
iPS motor neurons	(+/-)	(+/-)	(+/-)
HCT116	n.d.	++	n.d.
iPS cortical neurons	-	n.d.	n.d

Table 1. Scoring of exosome parent - recipient cell pairing. UF-GF isolated CD63-emGFP exosomes from HEK293, Huh7 and B16 cells were added to a variety of recipient lines in a dose response assay (1-18 pM, 3 biological replicates) and uptake was quantified after 8 hours by whole well automated fluorescent imaging (Figure 6). Relative uptake efficiency was scored based on both, the level of internalized GFP at the highest dose, as well as the EC50.

Supplementary Figure 1

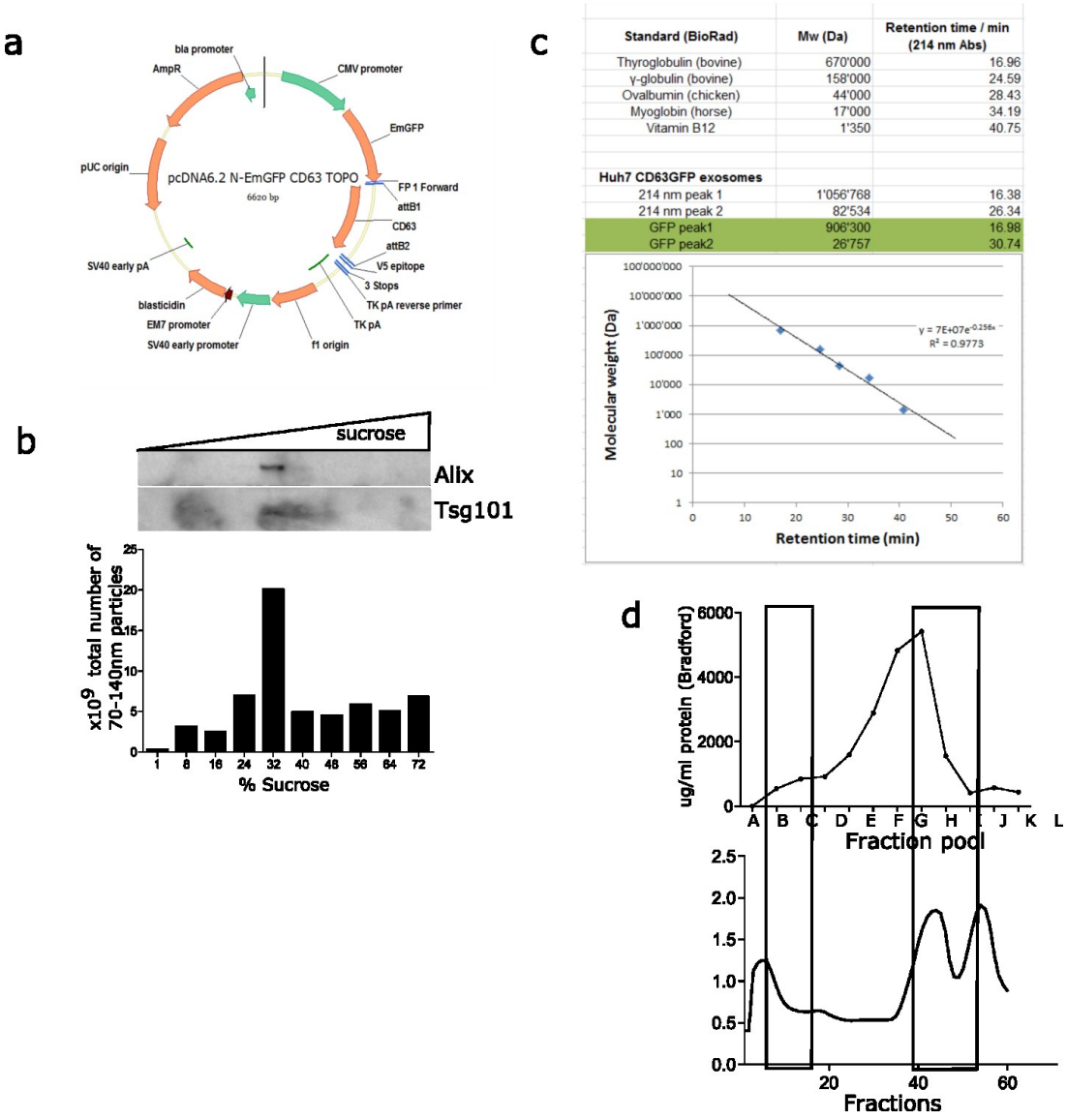

Supplementary Figure 1. Supplementary data of CD63-emGFP exosome characterization. (a) Map of the CD63-emGFP expression vector. **(b)** Conditioned medium from untransfected HEK293 cells was directly fractionated on a sucrose sedimentation gradient without any prior ultracentrifugation step**.** X-axis shows measured sucrose concentrations in the collected fractions. Particles with a size of 70-140 nm (as measured by NTA) co-fractionate with the exosome markers Alix and Tsg101, peaking at ca 32-36 % sucrose. **(c)** Retention time analysis of gel filtration of exosome samples using a size standard. Upper size separation limit of the column: 600 kDa. Exclusion limit: 1.3 MDa. **(d)** Fractions from gel filtration of CD63-emGFP HEK293 exosomes shown in Figure 1c were analyzed for total protein concentration by a Bradford assay (upper panel). The ratio between the 254/280 traces is shown in the lower panel.

Supplementary Figure 2

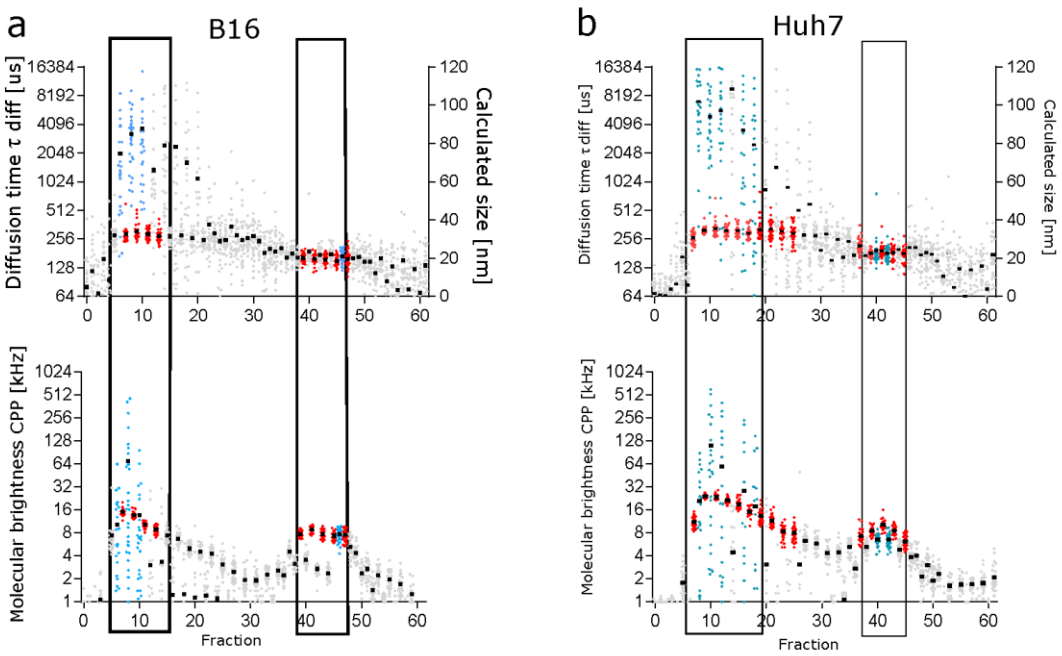

Supplementary Figure 2. Single molecule characterization of CD63-emGFP labeled UF-GF isolated exosomes. Individual fractions from gel filtration of B16 CD63-emGFP exosomes and Huh7 CD63-emGFP were analyzed by FCS with (red data points) and without (blue data points) vesicle disruption by the detergent NP40S. The translational diffusion time (t_{diff}, upper panel) and molecular brightness (CPP, second panel) are depicted across the fraction number from the GF. Frames indicate fractions comprising the two main fluorescent populations. **(a)** B16 medium isolation: The first peak comprises a relatively heterogeneous population of emGFP fluorescent, large particles with t_{diff} ranging from ca 2-10 ms (mean of ca 3.5 ms), corresponding to ca 50-120 nm in size (mean of ca 80 nm). A similar heterogeneity was observed in molecular brightness CPP, ranging from ca 9 kHz to 500 kHz per particle (mean of ca 70 kHz). **(b)** Huh7 medium isolation: The first peak comprises a relatively heterogeneous population of emGFP fluorescent, large particles with tdiff ranging from ca 2-10 ms (mean of ca 4.8 ms), corresponding to ca 50-120 nm in size (mean of ca 100 nm). A similar heterogeneity was observed in molecular brightness CPP, ranging from ca 9 kHz to 270 kHz per particle (mean of ca 110 kHz). In both samples the treatment with the detergent NP40S resulted in a uniform population of molecules with a tdiff of ca. 300 us and CPP of 9-15 kHz (B16) or 15-24 kHz (Huh7), corresponding to the expected values for free CD63-emGFP (based on extrapolation from data measured for free monomeric emGFP, t_{diff} = ca 160 us, CPP = 8-10 kHz). The

second major eluting GFP peak comprises molecules of relatively homogeneous t_{diff} and CPP, insensitive to NP40S treatment and consistent with the size and brightness expected for monomeric GFP.

Supplementary Figure 3

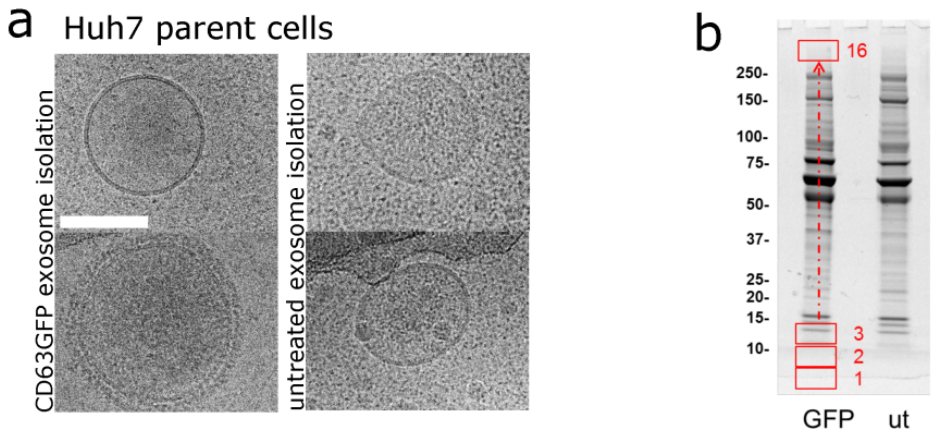

Supplementary Figure 3. Comparison of exosomes from CD63-emGFP transfected and untransfected parent cells. (a) Cryo-EM analysis of UF-GF isolated CD63-emGFP versus native Huh7 exosomes (representative images). Scaling bar: 100 nm. **(b)** SDS PAGE (Colloidal Coomassie Blue stain) of exosome samples used for LC-MS proteomics in Figure 3 and Supplementary Table 1. The 16 gel slices for in gel digestion are indicated by red boxes.

Supplementary Figure 4

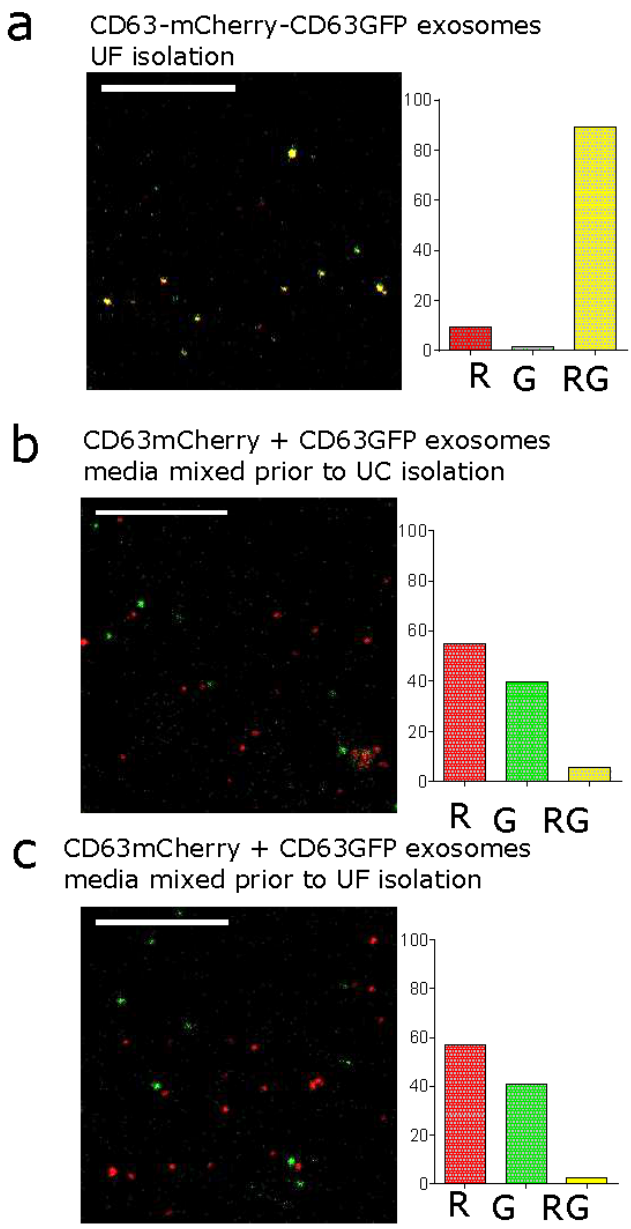

Supplementary Figure 4. Single vesicle imaging. The data in Figure 4 are shown with a more stringent threshold to limit the analysis to the 100 brightest vesicles.

Supplementary Figure 5

a

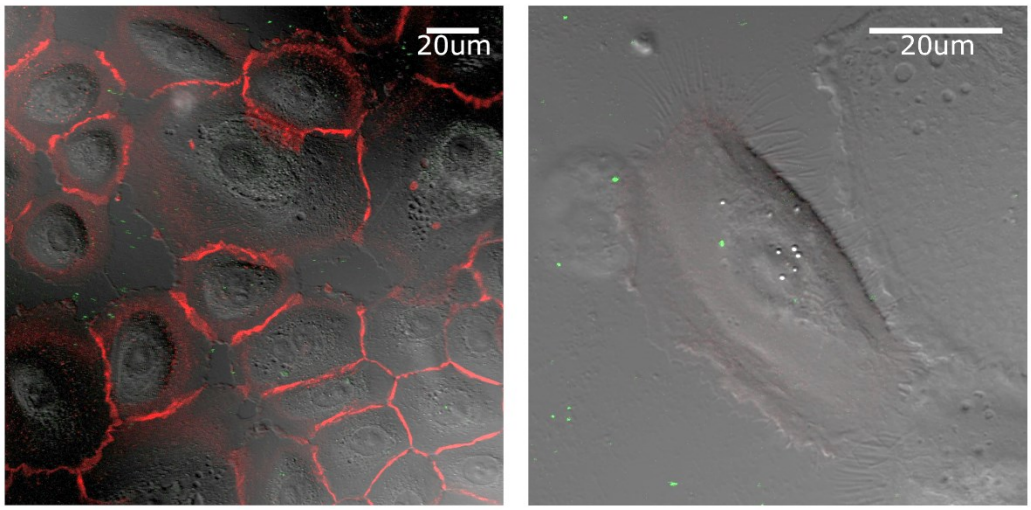

b

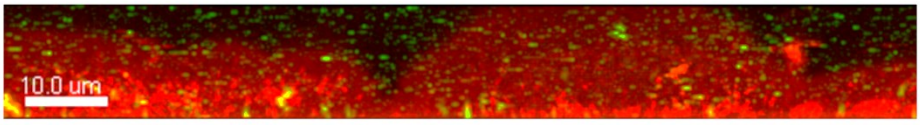

Supplementary Figure 5. Lack of HEK293 exosome uptake in human primary keratinocytes. (a) Confocal live cell image (fluorescence and DIC overlay) of human primary keratinocytes 100 minutes (left panel) and 13 hours (right panel) after incubation with HEK293 CD63-emGFP exosomes (green) at 200 nM, demonstrating lack of uptake even at high exosome concentrations. An x-z orthoview of the image in the left panel of (a) is shown in **(b)**, visualizing the high concentration of exosomes floating in the medium. CellMask Deep Red is shown in red.

Supplementary Table 1. MS-proteomics analysis of UF-GF enriched exosomes from CD63-emGFP transfected versus non-transfected HEK293 cells. Spectral counts are listed for all proteins detected at a < 1% FDR. Among the top 350 proteins, GFP was the only difference.

Materials and Methods

Parent cells. Human hepatocellular carcinoma cells (Huh7, ATCC), human embryonic kidney cells (HEK293T, ATCC), and a mouse melanoma cell line (B16F10, ATCC) were cultured in complete media comprised of Dulbecco's Modified Eagle Medium (DMEM, Life Technologies), supplemented with 10 % fetal bovine serum (FBS, Cellgro) and penicillin/streptomycin (5 mg/ml, Cellgro). All cells were cultured at 37°C with 5 % CO_2. For fluorescent exosome labeling, the full length coding sequence of human CD63 isoform A (RefSeq NM_001257390.1) was TOPO cloned into the pcDNA 6.2 N-emGFP vector (Promega) to result in an N-terminal fusion of emGFP to CD63. pcDNA 6.2 N-mCherry-CD63 and N-mCherry-emGFP-CD63 vectors were then subcloned by replacing the emGFP CDS in between the Ava I sites by gene synthesized inserts (Solvias) comprising the CDS of either mCherry or an emGFP-mCherry fusion. For exosome isolation, 5-8 x 10^6 HEK293, 4-5 x 10^6 Huh7 or 4-5 x 10^6 B16 cells were seeded in a 15 cm culture dish with complete media and transfected with CD63 expression constructs the next day. Cell transfection was done in complete medium using Lipofectamine2000 (Life Technologies; 1 mg DNA/2.2 ml LF2000) following the manufacturer's instructions. After 4 hours, cells were washed and medium was replaced by OptiMEM. Conditioned media were collected after 48 hours if not indicated otherwise for exosome isolation. Typically, 100-200 ml of conditioned medium (pooled from multiple dishes) was used in most experiments.

Exosome isolation.

Exosome isolation via UF/GF was essentially performed as described elsewhere [9]. Briefly, conditioned medium was pre-cleared of cell debris and larger particles by consecutive centrifugation at 300 *g* for 5 minutes followed by 3'000 *g* for 10 minutes, as well as filtration over a 0.22 mm filter. Typically, 100-200 ml of the pre-cleared conditioned medium was then concentrated to a volume of 0.5-1 ml on an AMICON ultrafiltration device using a 100-kDa MWCO membrane (Millipore). Enriched medium was then loaded onto a Superdex200 column (GE Healthcare) connected to an ÄKTA prime FPLC instrument (GE healthcare) equipped with a UV flow cell. Gel filtration was performed at 4°C using sterile filtered 50 mM Tris-buffer (flow rate 0.5 ml/min). Ninety-six individual fractions of 200 ml each were collected. NTA and FCS was performed directly in all fractions. For Western blotting, fractions were pooled (4 fractions each, omitting one fraction in between pools) and further concentrated to a volume of 30 ml on an Amicon 10-kDa MWCO spin columns (Millipore). UC isolation for the experiment in Figure 4 was performed following the protocol specified in [9].

Sucrose gradients.

Ten 350 ml fractions with increasing sucrose density (8-80 %) were overlaid via freezing between each step and topped with 12 ml conditioned, pre-cleared medium. The gradient was centrifuged for 65 hours at 120'000 *g* at 4°C and fractions were collected by snap freezing the gradient on dry ice and slicing into 10 or 20 fractions from the bottom. The sucrose concentration in each fraction was then determined by refractive index measurements.

Western Blotting.

Aliquots of sucrose gradient fractions or pooled and spin column concentrated gel filtration fractions were heated in SDS sample buffer for 10 minutes at 70°C and electrophoresed on 4-12 % NuPage gels (Life Technologies). Proteins were transferred to Protran nitrocellulose membranes (Whatman) using a SD Transblot system (BioRad) and blocked for 1 hour in PBS with 5 % (w/v) milk powder (BioRad) at RT prior to primary antibody incubation either for 2 hours in blocking buffer at RT or overnight at 4°C. Immune complexes were visualized using HRP-conjugated secondary antibodies (Santa Cruz) on a Biorad XRS system. Antibodies: PDC6I/Alix (ab117600, Abcam, 1/500 dilution), Tsg101 (ab83, Abcam, 1/500 dilution); Lamp2b (ab25631, Abcam, 1/500 dilution); GFP (ab290, Abcam, 1/1000 dilution).

Fluorescence Correlation Spectroscopy (FCS).

Exosome quantification and characterization via FCS was essentially performed as described elsewhere [9]. Briefly, samples were measured on a Clarina II Reader (Evotec Technologies) with 488 nm argon ion laser excitation, a 40x water immersion 1.15 N.A. objective (UAPO Olympus), 50 mm pinhole and a SPCM-AQR-13FC avalanche photodiode (Perkin-Elmer Optoelectronics). The confocal volume was calculated in approximation according to [17] using the measured diffusional correlation time tdiff of free dye (Alexa488, Life Technologies), the known translational diffusion coefficient of Alexa488 (Molecular Probes; D = 280 mm^2/s) and the axis ratio fitted from calibration measurements. For each sample, several dilutions were made and measured in a 96-well glass bottom plate (Whatman) with 30 repetitive measurements of 10 seconds each. NP-40S at 1% v/v (Biosciences) was used to induce vesicle disruption for determination of detergent sensitivity and quantification of CD63-emGFP molecules per exosome. Data from one experiment representative of at least three independent experiments are shown. Error bars represent standard deviations from the 30 FCS measurements.

Cryo-Transmission Electron Microscopy (Cryo-TEM).

A 4 μl aliquot of sample was adsorbed onto glow-discharged holey carbon coated grid (Quantifoil, Germany), blotted with Whatman filter paper and vitrified into liquid ethane at −178°C using a Vitrobot (FEI, Endhoven, Netherlands). Frozen grids were transferred onto a Philips CM200-FEG electron microscope (FEI, Endhoven, Netherlands) using a Gatan 626 cryo-holder (GATAN Inc, Pleasanton, USA). Electron micrographs were recorded at an accelerating voltage of 200 kV and a nominal magnification of 50'000x, using a low-dose system (10 e−/Å2) and keeping the sample at −175°C. Defocus values were ranging from −2 μm to 3 μm. Micrographs were recorded at 4K × 4K CMOS camera (TVIPS, Germany).

Single vesicle imaging.

Exosomes from CD63-emGFP/CD63-mCherry double transfected HEK293 cells were imaged by confocal fluorescence microscopy after spotting onto coverslips. Vesicles were detected as light diffraction limited GFP or mCherry fluorescent spots of uniform size corresponding to the point spread function of the microscope, confirming recovery of single vesicles. Co-localization was quantified based on overlap of the point spread functions in the two fluorescent channels to derive the number of GFP (G), mCherry (R) and GFP/mCherry (RG) double positive vesicles.

Nanoparticle Tracking Analysis (NTA).

Label-free particle size and concentration determination was performed on a LM NTA instrument (NanoSight). With a camera gain of 500, full detection range and 90 second recordings all camera settings as well as analyses parameters (detection threshold of 2, minimum expected particle size of 50 nm, fixed minimal track length of 4) where kept constant throughout all measurements. For quantitative analysis of particle size distribution and concentration, a dilution row of samples between 1:100 to 1:10'000 was analyzed to hit the dynamic range of the instrument (1 - 4 x 108 particles/ml).

MS-Proteomics.

UF-GF isolated exosomes were separated by SDS-PAGE on a NuPAGE 4-12 % (Life Technologies) gel and stained with a Colloidal Coomassie stain (Sigma). Sixteen equal sized slices were excised from each of the gel lanes (Supplementary Figure 3b). In-gel digestion and subsequent identification by liquid chromatography coupled with tandem mass spectrometry was performed as described [18], with the exception that a mix of Trypsin and Endopeptidase Lys-C (Promega) was used instead of trypsin alone. Database searches were done with Mascot (version 2.4, Matrix Science) against the UniProt database (release of April 2013) concatenated with a reversed version and supplemented with known contaminants (such as

trypsin, BSA and commonly used tags). Protein identifications were validated and summarized in Scaffold (version 4.0.3, Proteome Software Inc.), setting the protein identification threshold at a 1 % false discovery rate (FDR) in the reversed database. At these settings peptide FDR was 0.05 %. The resulting protein list is provided as Supplementary Table 1. Keratin contaminants were removed and are listed separately. Trypsin and Lys-C were also removed from the list. Total spectral count is provided as a semi-quantitative measure, as well as the number of unique peptides for each protein (Supplementary Table 1). The spectral count is shown without correction for the total number of assigned spectra in each sample (24'626 for GFP-CD63 and 21'234 for the untransfected sample).

Recipient cells.

Human primary fibroblasts from a healthy donor (Life Technologies, #C-013-5C) were grown in MEM (Life Technologies) supplemented with 15 % fetal bovine serum and penicillin/streptomycin (5000 mg/ml, Cellgro) in 0.1% gelatine (Sigma Aldrich) coated T150 flasks. Human hepatocellular carcinoma cells (Huh7, ATCC), human embryonic kidney cells (HEK293T, ATCC), and a mouse melanoma cell line (B16F10, ATCC) were cultured in complete media comprised of Dulbecco's Modified Eagle Medium (DMEM, Life Technologies), supplemented with 10 % fetal bovine serum (FBS, Cellgro) and penicillin/streptomycin (5 mg/ml, Cellgro). All cells were cultured at 37°C with 5 % CO_2. For exosome exosome uptake screening assay, these cell lines were either plated in 96-well or 384-well uclear plates (ibidi) at a density of 60 %. Human primary keratinocyte progenitors (CELLnTEC Advanced Cell Systems AG, Bern, Switzerland) were kindly provided by Gabi Schutzius (Novartis Basel) and cultured in Epithelial Culture Medium (CELLnTEC Advanced Cell Systems AG) under sub-confluent culture conditions to prevent differentiation. For the exosome uptake assay cells at passage 6 were detached with Accutase (CELLnTEC Advanced Cell Systems AG), and plated 48 hours prior to exosome addition at a density of 20'000 cells per 96-well. Human iPS cells from a healthy donor (Coriell) were kindly provided by Claudia Merk (Novartis Basel) and differentiated into motor neurons following a protocol adapted from[19], [20] , plated in Matrigel coated 96-well plates (ibidi) and cultivated for 3 weeks prior to exosome uptake studies. HUVEC primary human endothelial cells (Promocell) were kindly provided by Giorgia Jurisic (Novartis Basel) cultivated in Endothelial Cell Growth Medium (Promocell) and plated in 96-well plates (ibidi) coated with Collagen (50 mg/ml, PureCol™ Advanced BioMatrix). HEK293 cells (ATCC), B16-F10 cells (ATCC), Huh7 cells (HSRRB) and HeLa cells (ATCC) were cultivated in DMEM (Life Technologies) supplemented with 10 % fetal bovine serum and 1x L-Glutamine 200 mM (100X; Life Technologies) and penicillin/streptomycin (Life Technologies) and plated in 96-

well plates (ibidi) at a cell density of 40-60 % confluency one day prior to exosome addition.

Confocal live cell microscopy.

For the combined confocal fluorescence and DIC live cell imaging cells were seeded into an 8-well m-slide (ibidi) and pre-stained prior to exosome addition as indicated in each experiment; Cell membrane: CellMask Deep Red (dilution 1:1000 for at least 2 minutes, Life Technologies);

Images were acquired on a confocal LSM710 microscope with Big-detector (Zeiss) with a 100x or 63x oil 1.4 NA PlanApochromat DIC objectives and temperature, gas and humidity control unit (Life Imaging Services). Differential interference contrast (DIC) was set up using the transmitting laser light of excitation as light source and the TPMT as detector.

Automated imaging assay for exosome uptake.

Cells were seeded into a 96-well Ibidi plate and incubated with exosomes as indicated in each experiment. Cells were fixed for 20 minutes at room temperature with PenFix (Thermo Scientific) in presence of 1 mg/ml Hoechst (Life Technologies) and 0.02 % (v/v) CellMask Deep Red (Life Technologies). Following extensive washing with PBS, wells were imaged on an automated confocal plate scanning instrument (Operetta, Perkin Elmer) at 40x magnification. Image analysis was done using the Harmony software, by first identifying the nuclei (Hoechst), defining the cell boundaries (CellMask Deep Red) and finally quantifying the number of GFP spots per cell. At least 5,000 cells were analyzed by condition. Data are shown from one representative experiment from at least three independent experiments, and represent averages with error bars indicating standard deviations from three independent samples.

References

[1] C. A. Franzen, P. E. Simms, A. F. Van Huis, K. E. Foreman, P. C. Kuo, and G. N. Gupta, "Characterization of uptake and internalization of exosomes by bladder cancer cells.," *Biomed Res. Int.*, vol. 2014, p. 619829, Jan. 2014.

[2] A. E. Morelli, A. T. Larregina, W. J. Shufesky, M. L. G. Sullivan, D. B. Stolz, G. D. Papworth, A. F. Zahorchak, A. J. Logar, Z. Wang, S. C. Watkins, L. D. Falo, and A. W. Thomson, "Endocytosis, intracellular sorting, and processing of exosomes by dendritic cells.," *Blood*, vol. 104, no. 10, pp. 3257–66, Nov. 2004.

[3] A. Suetsugu, K. Honma, S. Saji, H. Moriwaki, T. Ochiya, and R. M. Hoffman, "Imaging exosome transfer from breast cancer cells to stroma at metastatic sites in orthotopic nude-mouse models.," *Adv. Drug Deliv. Rev.*, vol. 65, no. 3, pp. 383–90, Mar. 2013.

[4] T. Tian, Y. Wang, H. Wang, Z. Zhu, and Z. Xiao, "Visualizing of the cellular uptake and intracellular trafficking of exosomes by live-cell microscopy.," *J. Cell. Biochem.*, vol. 111, no. 2, pp. 488–96, Oct. 2010.

[5] D. Feng, W.-L. Zhao, Y.-Y. Ye, X.-C. Bai, R.-Q. Liu, L.-F. Chang, Q. Zhou, and S.-F. Sui, "Cellular internalization of exosomes occurs through phagocytosis.," *Traffic*, vol. 11, no. 5, pp. 675–87, May 2010.

[6] M. Chiba, M. Kimura, and S. Asari, "Exosomes secreted from human colorectal cancer cell lines contain mRNAs, microRNAs and natural antisense RNAs, that can transfer into the human hepatoma HepG2 and lung cancer A549 cell lines.," *Oncol. Rep.*, vol. 28, no. 5, pp. 1551–8, Nov. 2012.

[7] M. Mittelbrunn, C. Gutiérrez-Vázquez, C. Villarroya-Beltri, S. González, F. Sánchez-Cabo, M. Á. González, A. Bernad, and F. Sánchez-Madrid, "Unidirectional transfer of microRNA-loaded exosomes from T cells to antigen-presenting cells.," *Nat. Commun.*, vol. 2, p. 282, Jan. 2011.

[8] M. Fabbri, A. Paone, F. Calore, R. Galli, E. Gaudio, R. Santhanam, F. Lovat, P. Fadda, C. Mao, G. J. Nuovo, N. Zanesi, M. Crawford, G. H. Ozer, D. Wernicke, H. Alder, M. A. Caligiuri, P. Nana-Sinkam, D. Perrotti, et al., "MicroRNAs bind to Toll-like receptors to induce prometastatic inflammatory response.," *Proc. Natl. Acad. Sci. U. S. A.*, vol. 109, no. 31, pp. E2110–6, Jul. 2012.

[9] J. Z. Nordin, Y. Lee, P. Vader, I. Mäger, H. J. Johansson, W. Heusermann, O. P. B. Wiklander, M. Hällbrink, Y. Seow, J. J. Bultema, J. Gilthorpe, T. Davies, P. J. Fairchild, S. Gabrielsson, N. C. Meisner-Kober, J. Lehtiö, C. I. E. Smith, M. J. A. Wood, et al., "Ultrafiltration with size-exclusion liquid chromatography for high yield isolation of extracellular vesicles preserving intact biophysical and functional properties.," *Nanomedicine*, pp. 1–5, Feb. 2015.

[10] C. Thery, S. Amigorena, G. Raposo, A. Clayton, and C. Théry, "Isolation and characterization of exosomes from cell culture supernatants and biological fluids.," *Curr. Protoc. Cell Biol.*, vol. Chapter 3, p. Unit 3.22, Apr. 2006.

[11] J. M. Escola, M. J. Kleijmeer, W. Stoorvogel, J. M. Griffith, O. Yoshie, and H. J. Geuze, "Selective enrichment of tetraspan proteins on the internal vesicles of multivesicular endosomes and on exosomes secreted by human B-lymphocytes.," *J. Biol. Chem.*, vol. 273, no. 32, pp. 20121–7, Aug. 1998.

[12] H. F. Heijnen, A. E. Schiel, R. Fijnheer, H. J. Geuze, and J. J. Sixma, "Activated platelets release two types of membrane vesicles: microvesicles by surface shedding and exosomes derived from exocytosis of multivesicular bodies and alpha-granules.," *Blood*, vol. 94, no. 11, pp. 3791–9, Dec. 1999.

[13] R. Xu, D. W. Greening, A. Rai, H. Ji, and R. J. Simpson, "Highly-purified exosomes and shed microvesicles isolated from the human colon cancer cell line LIM1863 by sequential centrifugal ultrafiltration are biochemically and functionally distinct.," *Methods*, Apr. 2015.

[14] K. J. Svensson, H. C. Christianson, A. Wittrup, E. Bourseau-Guilmain, E. Lindqvist, L. M. Svensson, M. Mörgelin, and M. Belting, "Exosome uptake depends on ERK1/2-heat shock protein 27 signaling and lipid Raft-mediated endocytosis negatively regulated by caveolin-1.," *J. Biol. Chem.*, vol. 288, no. 24, pp. 17713–24, Jun. 2013.

[15] C. Lässer, M. Eldh, and J. Lötvall, "Isolation and characterization of RNA-containing exosomes.," *J. Vis. Exp.*, no. 59, p. e3037, Jan. 2012.

[16] A. F. Orozco and D. E. Lewis, "Flow cytometric analysis of circulating microparticles in plasma.," *Cytometry. A*, vol. 77, no. 6, pp. 502–14, Jun. 2010.

[17] S. El-Andaloussi, Y. Lee, S. Lakhal-Littleton, J. Li, Y. Seow, C. Gardiner, L. Alvarez-Erviti, I. L. Sargent, and M. J. A. Wood, "Exosome-mediated delivery of siRNA in vitro and in vivo.," *Nat. Protoc.*, vol. 7, no. 12, pp. 2112–26, Dec. 2012.

[18] M. J. Culbertson, J. T. B. Williams, W. W. L. Cheng, D. A. Stults, E. R. Wiebracht, J. J. Kasianowicz, and D. L. Burden, "Numerical fluorescence correlation spectroscopy for the analysis of molecular dynamics under nonstandard conditions.," *Anal. Chem.*, vol. 79, no. 11, pp. 4031–9, Jun. 2007.

[19] C. Michaloglou, W. Lehmann, T. Martin, C. Delaunay, A. Hueber, L. Barys, H. Niu, E. Billy, M. Wartmann, M. Ito, C. J. Wilson, M. E. Digan, A. Bauer, H. Voshol, G. Christofori, W. R. Sellers, F. Hofmann, and T. Schmelzle, "The Tyrosine Phosphatase PTPN14 Is a Negative Regulator of YAP Activity," *PLoS One*, vol. 8, no. 4, p. e61916, Apr. 2013.

[20] F. P. Di Giorgio, G. L. Boulting, S. Bobrowicz, and K. C. Eggan, "Human embryonic stem cell-derived motor neurons are sensitive to the toxic effect of glial cells carrying an ALS-causing mutation.," *Cell Stem Cell*, vol. 3, no. 6, pp. 637–48, Dec. 2008.

[21] G. L. Boulting, E. Kiskinis, G. F. Croft, M. W. Amoroso, D. H. Oakley, B. J. Wainger, D. J. Williams, D. J. Kahler, M. Yamaki, L. Davidow, C. T. Rodolfa, J. T. Dimos, S. Mikkilineni, A. B. MacDermott, C. J. Woolf, C. E. Henderson, H. Wichterle, and K. Eggan, "A functionally characterized test set of human induced pluripotent stem cells.," *Nat. Biotechnol.*, vol. 29, no. 3, pp. 279–86, Mar. 2011.

4.4 Manuscript II (Exosomes surf on filopodia to enter cells at endocytic hot spots, and shuttle with endosomes to scan the endoplasmic reticulum – a highway to the cell)

Finally, we focused on quantitative and mechanistic characterization of exosome mediated cell uptake and uncovered a new analogy to some viruses by high resolution imaging and single vesicle dye tracing in live cells. We discovered that exosomes enter cells as single vesicles within minutes of addition, and are actively recruited to the cell body by surfing on filopodia, as well as via filopodial grabbing and pulling. In 98% of events, exosomes enter cells at the filopodia base, regions of active actin remodeling and considered endocytic hot spots. Following internalization, exosomes enter and shuttle with endocytic vesicles and scan along the ER before they end up in lysosomes. Exosomes have been shown to carry specific and active miRNA cargo. This indicates that exosomes may not only target cells specifically but additionally deliver their miRNA cargo directly to the site of RNA silencing (paper II). This model could explain how a rare miRNA communication vehicle nonetheless does have an impact in cell behavior by a direct delivery to the site of action at the ER. However, mechanisms of exosome cargo release remain to be investigated.

Exosomes surf on filopodia to enter cells at endocytic hot spots, and shuttle with endosomes to scan the endoplasmic reticulum – a highway to the cell.

Heusermann W[1, 2,*], Hean J[1, 3], Trojer D[1], vonBueren S[1], Graff-Meyer A[4], Genoud C[4], Martin K[5], Voshol H[1], Morrissey DV[6, 7], EL Andaloussi S[3,8],
Wood MJ[3], Meisner-Kober NC[1,*]

[1]Novartis Institutes for Biomedical Research, CH-4000 Basel, Switzerland

[2]current: Imaging Core Facility, Biozentrum, University of Basel, CH-4056 Basel, Switzerland

[3] Department of Physiology, Anatomy and Genetics, University of Oxford, Oxford OX1 3QX, UK

[4]Friedrich-Miescher Institute for Biomedical Research, CH-4000 Basel, Switzerland

[5]Department of Biomedicine, University of Basel, CH-4058 Basel, Switzerland

[6]Novartis Institutes for Biomedical Research, Cambridge, MA-02139, United States

[7]current: Intellia Therapeutics, Inc., Cambridge, MA-02139, United States

[8] Karolinska Institutet, Department of Laboratory Medicine, SE-141 86 Huddinge, Sweden

*Corresponding authors: wolf.heusermann@unibas.ch, nicole.meisner-kober@novartis.com

Abstract. Exosomes are nanovesicles released by virtually all cells which act as intercellular messengers by transfer of protein, lipid and RNA cargo. Their quantitative efficiency, routes of cell uptake and subcellular fate within recipient cells remain elusive. We quantitatively characterize exosome cell uptake which saturates with dose and time and reaches near 100 % 'transduction' efficiency at picomolar concentrations. Highly reminiscent of pathogenic bacteria and viruses, exosomes are recruited as single vesicles to the cell body by surfing on filopodia, as well as filopodia grabbing and pulling motions to reach endocytic hot spots at the filopodial base. Following internalization, exosomes shuttle with endocytic vesicles to scan the endoplasmic reticulum before being sorted into the lysosome as their final intracellular destination. Our data quantify and explain the efficiency of exosome internalization by recipient cells, establish a new parallel between exosome and virus host cell interaction and suggest unanticipated routes of subcellular cargo delivery.

Introduction. Exosomes are extracellular vesicles that mediate cell-to-cell communication (Colombo et al., 2014), sometimes at a distance (Hood et al., 2011) and even between organisms (Corrigan et al., 2014; Twu et al., 2013). They modulate recipient cell gene expression and physiology by induction of cell signaling as well as intercellular transfer of protein, lipid and RNA cargo (Ratajczak et al., 2006; Valadi et al., 2007). They also have clinical significance due to their potential use as biomarkers (Properzi et al., 2013) or next generation therapeutics (Alvarez-Erviti et al., 2011; Kordelas et al., 2014). Hence there is need for a better understanding of how these vesicles target and enter recipient cells. The current model postulates exosome uptake via energy-dependent, receptor-mediated endocytosis (Svensson et al., 2013; Tian et al., 2013) or macropinocytosis (Fitzner et al., 2011; Tian et al., 2014). However, there are opposing models proposing direct fusion with the plasma membrane (Conde et al., 2005; Parolini et al., 2009) or phagocytosis (Feng et al., 2010). It remains to be seen whether different entry routes reflect cell specialization or conditions, or whether multiple entry routes co-exist in the same cell. Further, the subcellular fate of exosomes within recipient cells and in particular their mechanisms of cargo release remain largely enigmatic. Here we report by single vesicle dye tracing in live cells that exosomes enter cells primarily via filopodia to sort into endocytic vesicle circuits that are targeted to scan the endoplasmic reticulum (ER) before being directed to the lysosome.

Results and Discussion.

Exosomes are efficiently taken up as single vesicles. Exosomes were labeled by transient transfection of HEK293 parent cells with CD63-emGFP and/or CD63-mCherry and isolated by ultrafiltration-gel filtration (Nordin et al., 2015). An extensive characterization of these vesicles is described elsewhere (Heusermann et al., 2015) confirming selective exosome labeling with minimal perturbation of physicochemical properties and cargo loading. Exosome concentrations were determined by fluorescence correlation spectroscopy (FCS) to enable quantification at the single vesicle level. To quantify exosome cell uptake over a statistically significant number of cells, we set up a high content screening assay on a plate scanning microscope with automated image analysis. To avoid any major cell line bias, we selected cells based on a systematic profiling of parent – recipient cell pairing preferences (Heusermann et al., 2015) and focused on uptake of HEK293 exosomes primarily in human primary fibroblasts, as well as Huh7 and HEK293 recipient cells for selected experiments. Exosome uptake levels were similar for different cell densities when confluency was low, but declined with cell density beyond an estimated threshold of ~60 % confluency (Suppl.Fig.1a). Uptake was time and dose dependent (Fig.1a and c, left panels), targeting up to 95 % of Huh7 cells at 30 pM exosomes within less than 6 hours (Fig.1a and c right panels and Suppl.Fig.1b). The saturating characteristics indicate that specific molecular interactions are involved in mediating exosome uptake. Similar data were obtained for human primary fibroblasts (Fig.1b).

We next studied exosome uptake dynamics at the single cell level using confocal live cell imaging. Since exosomes share several physicochemical properties with liposomal delivery vehicles including their size and lipid composition, we compared the uptake dynamics of CD63-emGFP fluorescently labeled exosomes with a representative cationic lipid nanoparticle formulation with encapsulated Cy3 labeled siRNA. Similar vesicle concentrations were independently applied to Huh7 cells and time lapse confocal microscopy movies were recorded at different confocal planes. Liposomes accumulated into islands at the cell surface that became larger over time, with only a minor fraction being endocytosed within the first few hours (Suppl.Fig.1c and Suppl.Movies 1 and 2). In contrast, exosomes appeared to enter cells as single vesicles within minutes of addition without accumulation at the cell surface (Suppl.Fig.1d). We therefore next monitored uptake of CD63-emGFP/CD63-mCherry double labeled UF-GF isolated vesicles (Fig.1d) using single particle tracking (SPT), which confirmed that exosomes entered cells as single vesicles in virtually all recorded cell entry events (Fig.1e). Analyzing trajectories from 1600 internalized exosomes showed that the observation time of double labeled vesicles was statistically not shorter than that

for the single labeled vesicles (Fig.1f), demonstrating that no separation of the two labels occurred, at least within the time of max 20 minutes that we were able to trace single particles. These data indicate that vesicles remain intact during and after cell entry and rule out a plasma membrane fusion, at least under the conditions studied.

Exosome uptake is clustered into filopodia active regions. To trace a statistically significant number of single exosomes throughout cell entry, we recorded 5-60 minute live cell movies of CD63-emGFP labeled HEK293 exosomes following their addition to either human primary fibroblasts (Fig.2a, and Suppl.Movies 3 and 4), HEK293 (Suppl.Fig.1e and g) or Huh7 recipient cells (Suppl.Fig.1f and h) with confocal and TIRF microscopy. Fig.2a shows the cumulative trajectories of single exosomes followed over an 80 minute time frame (dragon tail visualization). Rather than being randomly distributed across the cell, exosome residency clustered into hotspot areas. This was not a consequence of intracellular segregation since cell entry events also clustered into the same regions. Interestingly, these uptake hotspots were near the tips of cortical actin bundles (Fig.2a, left panel) and coincided with filopodia and lamellipodia active regions (Fig.2a, right panel and Suppl.Fig.1e-h). To uncouple the localization of filopodia from the lamellipodium we used human primary fibroblasts grown on a line substrate (Martin et al., 2014). The cell body and filopodia were visualized by adenoviral expression of actin-RFP. As had been demonstrated before, cells became highly polarized and showed persistent migration in one direction, with a defined lamellipodium at the front end, filopodia distributed across the lateral regions of the cell surface and retraction fibers at the back end (Fig.2b). Uptake of CD63-emGFP HEK293 exosomes was monitored by TIRF microscopy to focus at the bottom 200 nm layer where filopodia are typically localized. Uptake through the lamellipodium of the migrating cell should result in a time-space correlation, as exemplified for podosome positions which re-form at the front end over time (Fig.2d, right panel). In contrast, exosome cell entry trajectories were uncoupled in space and time from the lamellipodium. Instead they redistributed, together with filopodia, to the lateral regions (Fig.2c and Fig.2d left panel). This pointed to a possible direct involvement of filopodia in exosome uptake.

Exosome recruitment and cell entry is facilitated by filopodia surfing, grabbing, and pulling. Filopodia are cellular protrusions formed by actin filaments that constantly scan the environment and thus interact with substrate and ligands (Bornschlögl, 2013; Mattila and Lappalainen, 2008). Their highly dynamic movement increases the effective surface area of a cell and facilitates interaction with extracellular ligands. Moreover, the filopodial base is an area of active actin remodeling and thus a hotspot for endocytosis (Lehmann et al., 2005; Mattila and

Lappalainen, 2008). The possibility of exosomes entering cells via filopodia is thus plausible. In fact previous reports revealed that filopodia facilitate efficient cell entry of certain pathogens including enveloped viral particles (Lehmann et al., 2005; Zamudio-Meza et al., 2009). Indeed we observed a prominent occurrence of direct contact of exosomes with filopodia by confocal fluorescence microscopy, which was almost mirror imaged in scanning electron microscopy images (Fig.3a). We next used high resolution live cell imaging with detection of both fluorescence as well as differential interference contrast (DIC) to monitor dynamics of exosomes simultaneously with filopodia and other light diffracting, fine structures. This revealed different types of filopodia-facilitated exosome recruitment. Exosomes moved along filopodia and retraction fibers towards the cell body (Fig.3b, Suppl.Fig.4a-e and Suppl.movies 5 and 6) – in striking analogy to a process previously introduced as filopodia surfing in studies of viral uptake (Lehmann et al., 2005). We also documented examples where exosomes associated with tunneling nanotubes and moved back and forth along fibers connecting two cells (Suppl.Fig.2f and g). Individual exosomes surfed on filopodia with relatively constant speed in the range of 0.1-0.3 □0.3 ividual exosomes surfed on filopodia with relatively constant speed in the range of 0.1ack and forth along fibers connecting two cells (6027225", "abs(Lidke et al., 2005) or MLV particles (Lehmann et al., 2005) and suggests a movement with F-actin retrograde flow (Bornschlögl, 2013; Sheetz et al., 1989; Forscher and Smith, 1988; Mitchison and Kirschner, 1988). Analyzing trajectories of 100 individual exosome filopodia surfing events from 13 live cell movies recorded in 6 independent experiments, we found in at least 90 % of the cases that the exosomes moved towards the cell body immediately after filopodial contact. In rare cases however, we documented an initial short movement in the opposite direction, followed by a transient stalling and redirection towards the cell body (Suppl.Fig.2j-k) – another parallel to previously published data for viral particles (Lehmann et al., 2005). Once redirected towards the cell, exosomes again moved with relatively constant speed matching that of F-actin retrograde flow. Together these characteristics indicate that after exosome attachment, additional molecular interactions or receptor recruitment might be required to trigger an eventual coupling with F-actin retrograde flow, rather than directly hitchhiking onto a running conveyor belt. In analogy it has been demonstrated that systematic retrograde transport of EGF receptors present in filopodia is triggered upon binding of EGF and activation of the receptor tyrosine kinase (Lidke et al., 2005). Likewise, extensive studies of filopodia surfing with artificial beads have identified receptors of the integrin and CAM protein receptor families to couple with the filopodial actin filament. Intriguingly, both had previously been implicated as receptors involved in exosome uptake (Morelli et al., 2004; Rana and Zöller, 2011).

In addition to filopodia surfing, two further modes of filopodia-mediated exosome recruitment were observed: contractile filopodia bound exosomes at their tips and pulled them actively to the cell surface (Fig.3c, Suppl.Fig.2h and Suppl.Movie 7), whereas laterally moving filopodia fished exosomes from the medium and actively hinged the vesicles to the cell body (Fig.3d, Suppl.Fig.2i, and Suppl.Movie 8). Further, our movies documented examples demonstrating that all three modes of filopodia interaction can also result in exosome cell entry (Fig.2 and 3, Suppl. Fig.2, and Suppl.Movie 4. Next to quantify the overall contribution of filopodia recruitment for exosome internalization in an unbiased manner, 394 individual exosome cell entry trajectories from several independent experiments were classified based on filopodia and non-filopodia mediated uptake as illustrated in Fig.4. Strikingly, over 98 % of all exosome entry events occurred at the base of filopodia and retraction fibers (Fig.4a). In approximately one third of these cases we were able to indeed document filopodia mediated exosome recruitment prior to cell entry. This number might be an underestimate due to the technical limitation of visualizing these small and highly dynamic structures over a sufficiently long time frame. The predominant mode of exosome filopodia interaction resulting in confirmed cell entry was surfing, detected in ~25 % of all analyzed cell entry trajectories (Fig.4b and d). Filopodia pulling and grabbing were only detected in ~3 % and 1 % of all cases, respectively. However, due to the rapid dynamics in 3D space of laterally moving filopodia as well as the shorter length of contractile filopodia, numbers of pulling and grabbing events might be underrepresented.

Since filopodia mediated exosome uptake implies dependence on actin polymerization, we tested the effect of Cytochalasin D on the dynamics of exosome recipient cell interaction. Time lapse imaging showed no major loss of exosome cell binding but an inhibition of directed and rapid movement as well as uptake (Suppl.Fig.2l). This suggests that actin inhibition stalls exosome uptake during recruitment to the cell body and that filopodia activity is required upstream of exosome internalization. In line with these data it is intriguing to speculate that also the decrease of exosome uptake with cell confluency in Suppl.Fig.1a might be due to reduced filopodia numbers and activity. However, this effect may also be a consequence of a number of other effects under contact inhibition, such as changed endocytic rate or simply smaller accessible cell surface area.

Of note it has been demonstrated that filopodia-surfing viruses such as human papilloma virus can additionally promote an increased filopodia formation in their host cells through PI3K activation, thereby reinforcing invasion by the virus (Smith et al., 2008; Nobile et al., 2010). By analogy it has been reported that exosome treatment increases the number of tunneling nanotubes (Thayanithy et al., 2014).

It is thus conceivable that exosomes might use similar mechanisms for directly modulating filopodial activity in recipient cells for feedback control of their own uptake. Likewise it will be interesting to see how the direct interaction of exosomes with filopodia revealed in this study may relate to their recently reported modulation of cell migration (Harris et al., 2015; Salomon et al., 2013; Sung et al., 2015), and whether different types of filopodia specialize in either exosome recruitment versus cell migration.

Exosomes shuttle with endosomes to undergo a stop-and-go movement along the ER and are sorted to the lysosome. At the base of filopodia, single CD63-emGFP labeled exosomes were encapsulated into larger, CellMask Deep Red labeled endocytic vesicles and were shuttled onwards following cell entry (illustrated in Fig.4e, also apparent in Fig.4b-d and Suppl.Movie 9). Together with the continued association of exosomal CD63-emGFP and CD63-mCherry in Fig 1e and f these data imply that the vesicles either remain stable over time within the cell, or at least their membranous components remain within the same endocytic vesicle. While this does not completely rule out that exosomes might utilize mechanisms for endosomal escape, this would imply a massive dilution of exosomal cargo into the cytoplasmic volume. In fact even for liposomal delivery vehicles (Sahay et al., 2013) the concept of endosomal escape as a productive route for siRNA delivery has been challenged (Gilleron et al., 2013). Quantification of the specific activity of exosomal cargo at the level of molecular concentrations is still lacking. Basic theoretical considerations of the volume of an 80 nm sphere and the average volume requirement per RNA or protein cargo molecule imply that a single exosome cannot even carry one copy of each cargo from the large proteome and transcriptome repertoire typically found in an exosome sample. Indeed, a recent study determined experimentally that on average, at least 100 exosomal vesicles need to be sampled to cover one copy of a given miRNA (Chevillet et al., 2014). Although RNA silencing is a highly efficient process and requires only a small number of RISC loaded siRNA or miRNA molecules per cell (Stalder et al., 2013) the above numbers imply that 1000 exosomes would be required to deliver 10 copies of a miRNA into one cell. Even if specialized vesicle subpopulations exist that are enriched for certain cargo, it is conceivable that exosomes have evolved highly effective mechanisms to deliver their miRNA (and possibly mRNA) cargo directly to the site of action. We therefore hypothesized that exosomes might sort into specific endosomal trafficking circuits to reach their subcellular sites of action, and set out to further characterize intracellular trafficking of these endocytic, exosomal vesicles. Statistical analysis of 312 intracellular trajectories (Suppl.Fig.3a and b) suggested that the vesicles did not primarily proceed on straight intracellular routes, with frequent transient stalling. Consistently, the speed variation of single vesicles over time revealed a stop-and-

go movement (Fig.5a and Suppl.Fig.3c) with peak velocities reaching up to ~1 □ with peak velocities reaching up to ~1 marily proceed on straight intracelome trajectories overlaid with DIC further suggested that exosomal vesicles largely followed intracellular filamentous and mesh-like structures (Fig.5b right panel) which were identified as endoplasmic reticulum based on labeling with ER Tracker (Fig.5b left panel and Fig.5c). Moreover, the pauses in the movement of exosomal vesicles typically occurred in close proximity to or at the ER, whereas the vesicles showed fast movement between ER sites (illustrated by examples in Fig.5d, Suppl.Fig.3d-j and Suppl.Movies 8 and 10). A guided movement by the ER mesh is further in line with the lack of highly straight paths apparent in the trajectory statistics. Highly reminiscent of the recently revealed interaction between endosomal vesicles and the ER (Friedman et al., 2013), exosome-containing endosomes showed close association with ER filaments, tips, branches and cavities (Fig.5e and Suppl.Fig.3d-j). Even though both ER as well as exosomal vesicles were highly dynamic, contact events of several seconds were recorded (Suppl.Movies 8 and 10). Since live cell movies further show a transiently coordinated movement rather than random crossing of their paths, this suggests a true interaction of ER and exosome containing vesicles.

We and others have recently revealed that siRNA as well as miRNA loading into RISC, target mRNA complexation and mRNA slicing/silencing are nucleated at the rough ER membrane (Stalder et al., 2013; Li et al., 2013). In addition the ER is increasingly recognized as a nucleation site for translation in general - rather than only for secreted proteins as had long been assumed (Reid and Nicchitta, 2015; Reid et al., 2014; Jagannathan et al., 2014). A directed transport of exosomes to the ER membrane would therefore allow for an efficient entry of exosomal miRNA and mRNA cargo into the RNAi and translation machineries. Some viruses also need to reach the ER for their replication (Spooner et al., 2006), however within the cell they seem to use routes that are different from those of exosomes. For example, Hepatitis C virus (HCV), which also retracts along filopodia (Coller et al., 2009), utilizes the endosomal system for retrograde transport through the ER-Golgi intermediate compartment (ERGIC) into the ER lumen and eventual transport across the ER membrane to reach the cytosolic ER surface (Dubuisson and Cosset, 2014). In contrast we show that exosomes shuttle with endosomal vesicles that are directed to, scan along and transiently interact with the ER. Since such ER scanning vesicles were recently identified as Rab5 and Rab7 positive endosomes (Lehmann et al., 2005), we finally wanted to assess an eventual sorting of exosomes to compartments of the late endosome. We quantified the co-localization of CD63-mCherry exosomes with LysoTracker Green based on (Bolte and Cordelières, 2006). Pearson's and Mander's coefficients both confirmed a partial co-localization of exosomes with lysosomes, increasing over time up to ~50-60 % after 48 hours in fibroblasts (Suppl.Fig.3k and l).

Our data demonstrate that exosomes *(i)* enter cells as individual vesicles within minutes upon addition, *(ii)* show no accumulation at the cell surface but rather a seemingly 'barrierless' cell penetration with *(iii)* a majority of detectable cell contact events leading to internalization, resulting in *(iv)* over 95 % of cells being targeted within only a few hours and (v) reaching saturation at low picomolar concentrations. We therefore conclude that exosome cell uptake is highly efficient. Since these characteristics are highly reminiscent of effective pathogen infection rather than lipid or liposomal delivery vehicles we propose to use the term 'transduction' rather than 'transfection' for exosome recipient cell targeting. The filopodia-facilitated exosome recruitment to endocytic hotspots revealed in this study provides a plausible explanation for the efficient cell entry of exosomes and adds another layer to their previously noted convergence with viral pathways (Wurdinger et al., 2012). Based on our data we propose a new physiological function of filopodia as highways for cell entry of exosomes which are hijacked by viruses and other pathogens. At the base of filopodia however, exosomes sort into endosomal trafficking circuits that appear to diverge from known viral trafficking routes, whereas we uncover that the ER plays a major role in intracellular exosome fate. The molecular details of how exosomes interact with filopodia, as well as whether and how exosomal cargo may be released, or functionally displayed at the ER across the endosomal (and exosomal) double lipid membranes will be important questions for future studies.

Figure 1

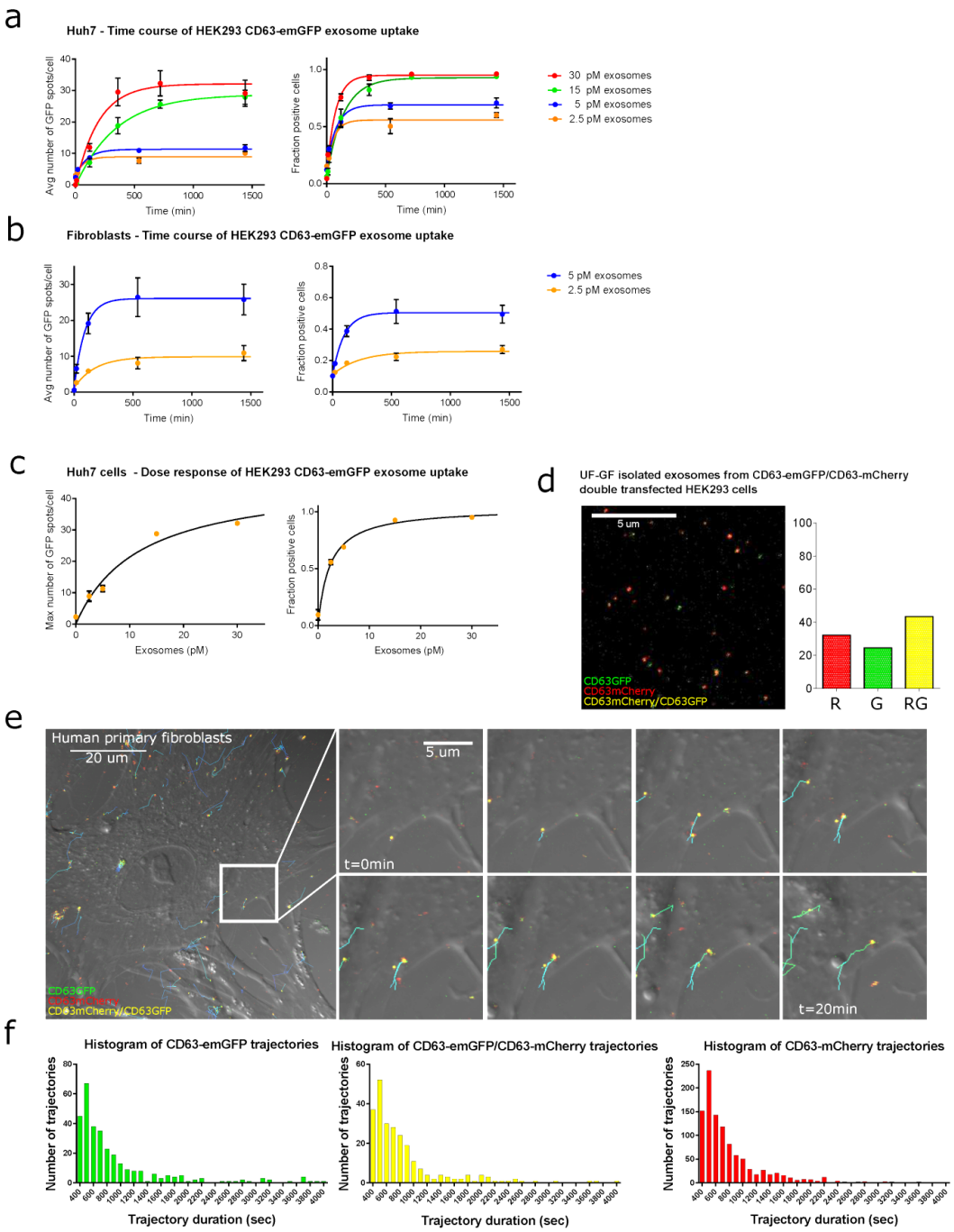

Figure 1. Quantitative exosome cell uptake dynamics.

(a-c) HEK293 CD63-emGFP exosome uptake using quantitative high content screening. **(d)** Exosomes from CD63-emGFP/CD63-mCherry double transfected HEK293 cells were imaged by confocal fluorescence microscopy after spotting onto coverslips. Vesicles were detected as light diffraction limited GFP or mCherry fluorescent spots of uniform size corresponding to the point spread function of the microscope, confirming recovery of single vesicles. The number of GFP (G), mCherry (R) and GFP/mCherry (RG) double positive vesicles was derived based on

co-localization quantification. **(e)**Single particle tracing of CD63-emGFP/CD63-mCherry HEK293 exosome uptake in primary human fibroblasts (confocal live cell imaging, 50 s/z-stack) and **(f)** Frequency distribution of the duration of 1'600 individual SPT trajectories of exosomes detected either in the GFP, mCherry or coloc channel.

Figure 2

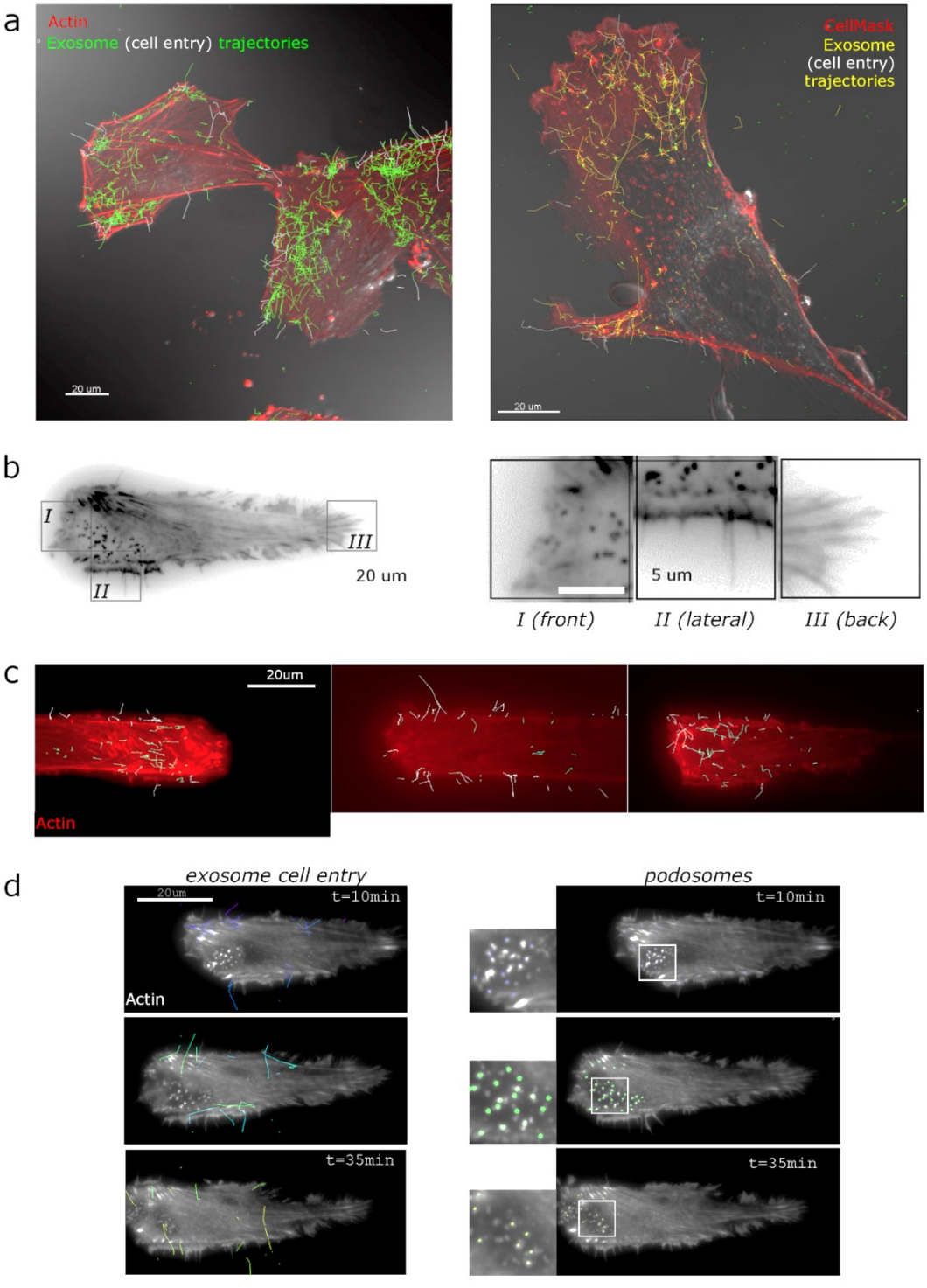

Figure 2. Exosome uptake is clustered into filopodia active regions. **(a)** SPT of exosome uptake dynamics by confocal live cell imaging of actin (left panel) or plasma membrane labeled (right panel) human primary fibroblasts. Exosomes at 100 pM; 50 s/frame. **(b)** TIRF live cell microscopy of stable actin-RFP expressing human fibroblasts (black) grown on line substrates. **(c)** Exosome uptake dynamics in fibroblasts on line substrates with single vesicle trajectories from TIRF live cell movies (2 frames/min). SPT trajectories documenting cell uptake events are highlighted in white, intracellular vesicle trajectories in green or yellow. The spatial distribution of cell entry events in the migrating cell is shown in **(d)** with trajectories pseudocolored for absolute time within the movie (left panel). In contrast to the lack of time-space correlation for exosome entry, podosomes remain at the front end over time (right panel).

Figure 3

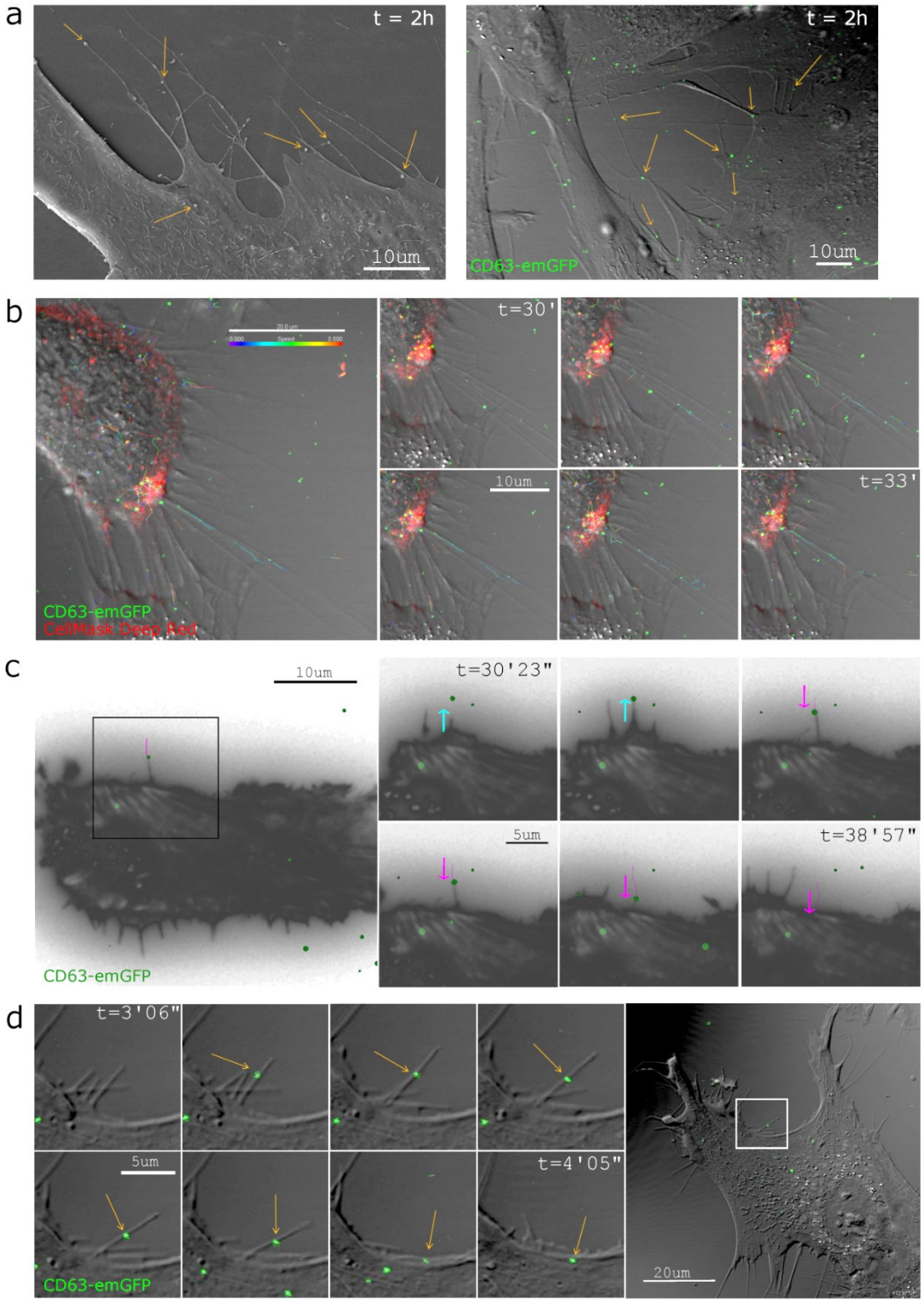

Figure 3. Exosome cell entry is facilitated by filopodia surfing, grabbing and pulling. Representative examples from human primary fibroblasts incubated with HEK293 CD63-emGFP exosomes (green). Time points represent absolute times after addition of 100 pM exosomes. **(a)** SEM (left panel) or live cell DIC/confocal fluorescence microscopy (right panel) visualization of apparent contacts of

nanovesicles/exosomes with filopodia (arrows). **(b)** Exosome surfing on filopodia documented by live cell DIC/confocal fluorescence microscopy (Suppl. movie 5, 12 frames/min). Vesicle trajectories are color coded for speed as indicated (0-0.5 um/sec). **(c)** Exosome pulling by filopodia documented by TIRF live cell microscopy of actin-RFP (black) expressing human fibroblasts grown on a line substrate (2 frames/min). Successive filopodia outreach and pulling movements are indicated by blue and pink arrows, respectively. Exosome trajectory in pink. **(d)** Grabbing of exosomes by filopodia by live cell DIC/confocal fluorescence microscopy. Additional examples are shown in Suppl.Fig.4.

.

Figure 4

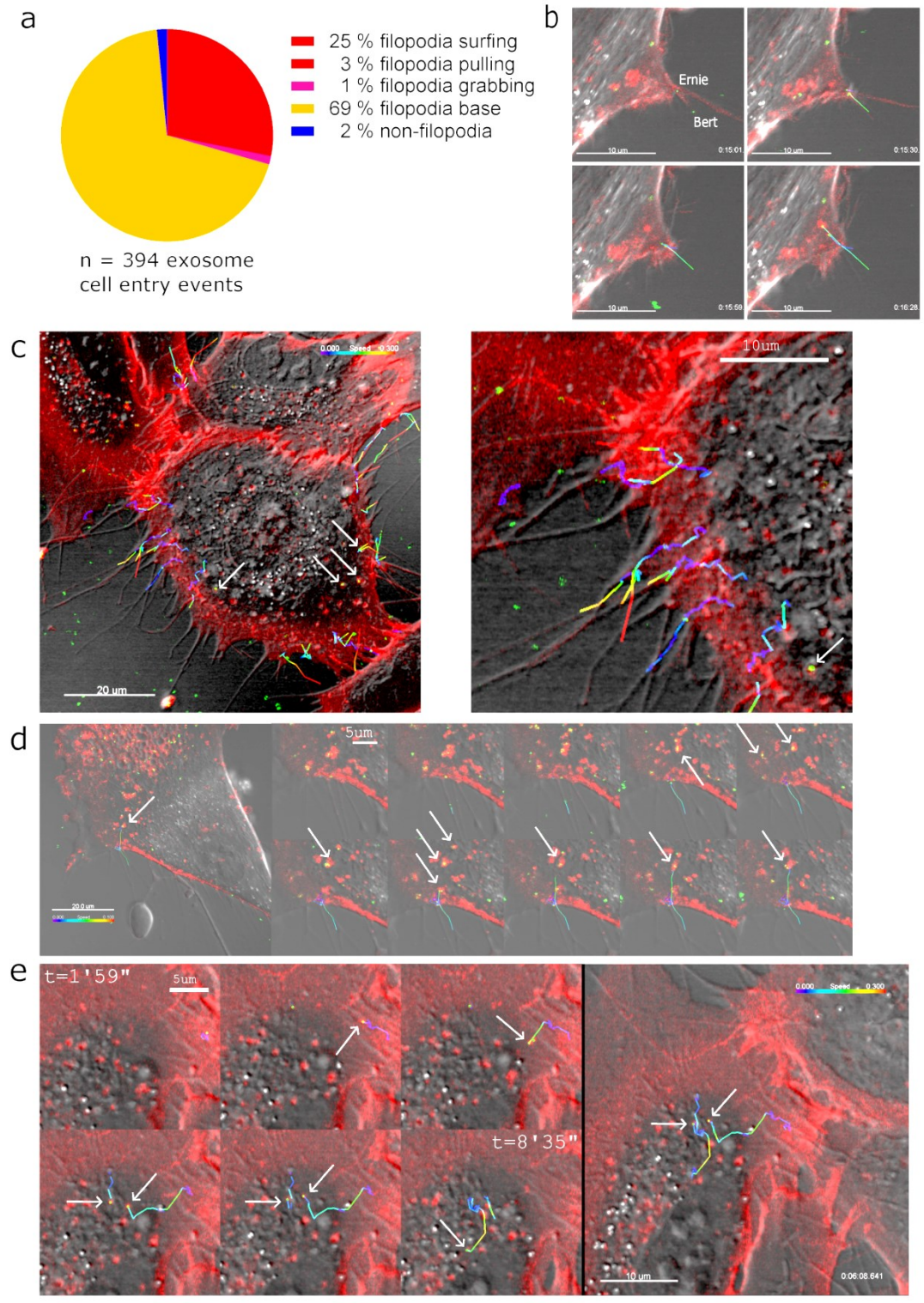

Figure 4. Exosomes are taken up at the filopodia base and shuttle with endosomes. (a) 394 individual HEK293 CD63-emGFP exosome cell entry events in human primary fibroblasts documented by DIC/confocal fluorescence or TIRF microscopy (Suppl.Movies 4, 5, 6) were classified as indicated. **(b)** 'Ernie' and

'Bert' represent typical examples for exosomes classified as either filopodia surfing or entering at the filopodia base, respectively. Further examples of exosome cell entry following filopodia surfing are shown in **(c)** and **(d)**. Examples for exosome cell entry following filopodia pulling or grabbing are shown in Suppl Fig.4h-i. Representative examples of exosomes entering plasma membrane derived endocytic vesicles are highlighted in **(e)**. All images represent single frames from DIC/confocal fluorescence live cell movies. Red: plasma membrane labelling (CellMask Deep Red), green: CD63-emGFP exosomes. Exosome trajectories color coded for speed.

Figure 5

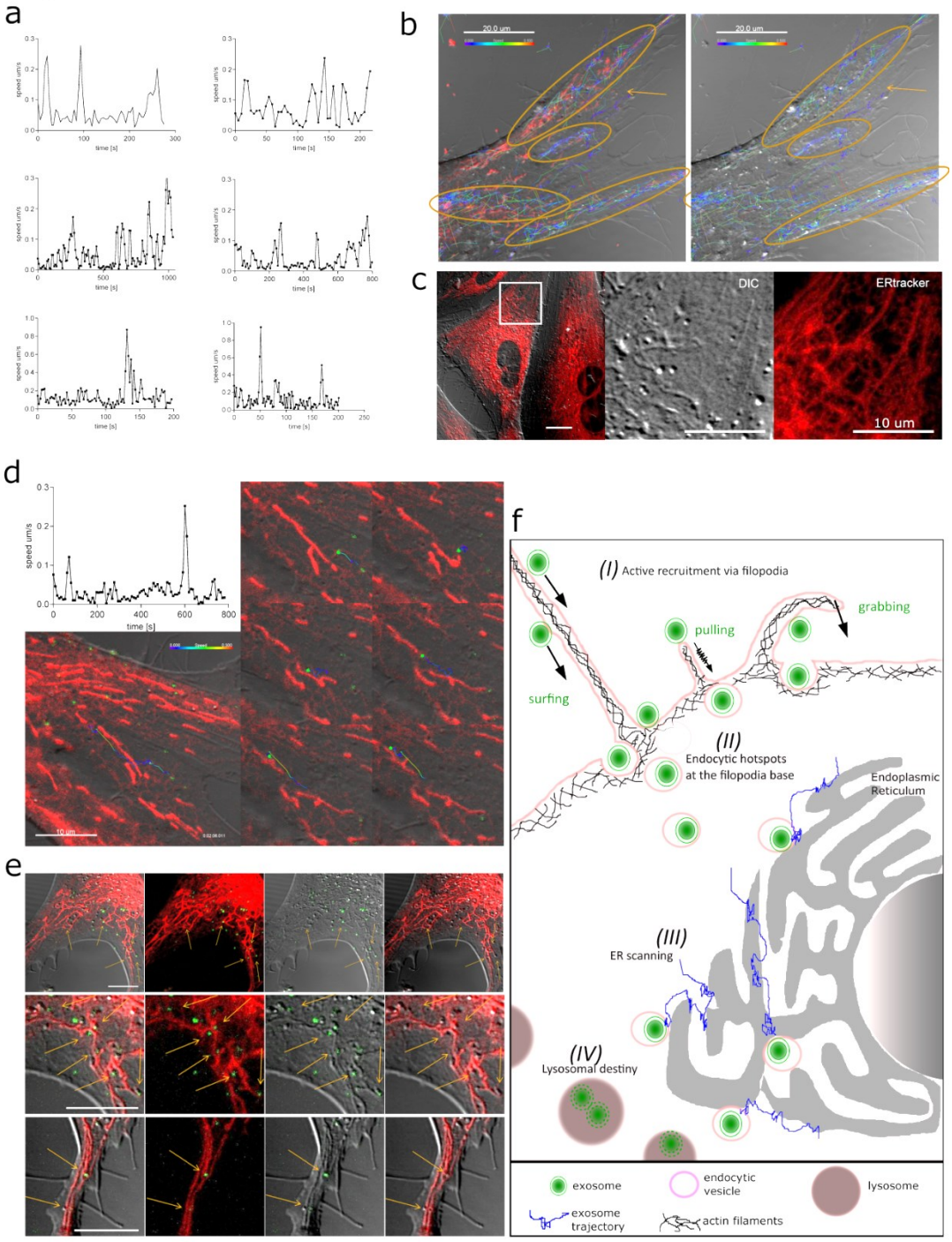

Figure 5. Internalized exosomes undergo a stop-and-go movement along the ER. **(a)** Examples for intracellular speed traces of HEK293 CD63-emGFP exosomes in human primary fibroblasts from confocal live cell movies (Suppl.movie 8). **(b)** Cumulative intracellular exosome trajectories color coded for exosome speed (0-0.5 um/s) in an overlay of DIC with confocal fluorescence images, with and without visualization of ER tracker (red). **(c)** A close up view of the overlay, showing the ER tracker fluorescence and DIC image side by side. **(d)**

Representative exosome trajectory with stop-and-go movement along the ER, color coded by speed (0-0.3 um/s). The corresponding speed trace is shown in the upper left panel. **(e)** Overlay of DIC with confocal fluorescence images taken 150 minutes post exosome addition show exosomes localizing closely to ER filaments, tips, cavities and branches (arrows). Green: CD63-emGFP exosomes; Red: ER Tracker; Scaling bars: 10 um. **(f)** Exosomes from the medium are actively recruited to the cell body via different modes of filopodia activity (surfing, pulling, grabbing) to reach endocytic hotspots at the filopodia base, where they are internalized as intact vesicles into endosomes. Within the cell, exosome containing vesicles undergo a stop-and-go movement scanning the endoplasmic reticulum, before being finally directed to the lysosome.

.

Materials and Methods

Parent cells. Human embryonic kidney cells (HEK293, ATCC) were cultured in complete media comprised of Dulbecco's Modified Eagle Medium (DMEM, Life Technologies), supplemented with 10 % fetal bovine serum (FBS, Cellgro) and penicillin/streptomycin (5 mg/ml, Cellgro) at 37°C with 5 % CO_2. For fluorescent exosome labeling, the full length coding sequence of human CD63 isoform A (RefSeq NM_001257390.1) was TOPO cloned into the pcDNA 6.2 N-emGFP vector (Promega) to result in an N-terminal fusion of emGFP to CD63. pcDNA 6.2 N-mCherry-CD63 and N-mCherry-emGFP-CD63 vectors were then subcloned by replacing the emGFP CDS in between the Ava I sites by gene synthesized inserts (Solvias) comprising the CDS of either mCherry or an emGFP-mCherry fusion. For exosome isolation, 5-8 x 10^6 HEK293 cells were seeded in a 15 cm culture dish with complete media and transfected with CD63 expression constructs the next day. Cell transfection was done in complete medium using Lipofectamine2000 (Life Technologies; 1 ug DNA/2.2 ul LF2000) following the manufacturer's instructions. After 4 hours, cells were washed and medium was replaced by OptiMEM. Conditioned media were collected after 48 hours for exosome isolation. Typically, 100-200 ml of conditioned medium (pooled from multiple dishes) was used in most experiments.

Recipient cells. Human primary fibroblasts from a healthy donor (Life Technologies, #C-013-5C) were grown in MEM (Life Technologies) supplemented with 15 % fetal bovine serum and penicillin/streptomycin (5 ug/ml, Cellgro) in 0.1 % gelatine (Sigma Aldrich) coated T150 flasks. For exosome uptake experiments, cells were either plated in 8-well slides (ibidi) at a density of 40-60 % (confocal and DIC live cell imaging experiments) or 96-well plates (ibidi) at a density of 60 % (exosome uptake high content screening assay). Transient expression of Adeno-Lifeact-mCherry in human fibroblast cells was obtained by adenoviral

transduction, and cells were seeded onto line substrates or 2D substrates (Fibronectin coated coverslips) at least 6 hours prior to TIRF life cell imaging. Line substrate microfabrication was performed as described elsewhere (Martin et al., 2014). Huh7 cells (HSRRB) and HEK293 cells (ATCC) were cultivated in DMEM (Life Technologies) supplemented with 10 % fetal bovine serum and 1x L-Glutamine 200 mM (Life Technologies) and penicillin/streptomycin (Life Technologies) and plated in 96-well plates (ibidi) at a cell density of 40-60 % confluency one day prior to exosome addition.

Exosome isolation. Exosome isolation via UF/GF was essentially performed as described elsewhere (Nordin et al., 2015). Briefly, conditioned medium was pre-cleared of cell debris and larger particles by consecutive centrifugation at 300 *g* for 5 minutes followed by 3'000 *g* for 10 minutes, as well as filtration over a 0.22 um filter. Typically, 100-200 ml of the pre-cleared conditioned medium was then concentrated to a volume of 0.5-1 ml on an AMICON ultrafiltration device using a 100-kDa MWCO membrane (Millipore). Enriched medium was then loaded onto a Superdex200 column (GE Healthcare) connected to an ÄKTA prime FPLC instrument (GE healthcare) equipped with a UV flow cell. Gel filtration was performed at 4°C using sterile filtered 50 mM Tris-buffer (flow rate 0.5 ml/min). Ninety-six individual fractions of 200 ul each were collected. NTA and FCS was performed directly in all fractions. For Western blotting, fractions were pooled (4 fractions each, omitting one fraction in between pools) and further concentrated to a volume of 30 ul on an Amicon 10-kDa MWCO spin columns (Millipore).

Fluorescence Correlation Spectroscopy (FCS). Exosome quantification and characterization via FCS was essentially performed as described elsewhere (Nordin et al., 2015). Briefly, samples were measured on a Clarina II Reader (Evotec Technologies) with 488 nm argon ion laser excitation, a 40x water immersion 1.15 N.A. objective (UAPO Olympus), 50 □m pinhole and a SPCM-AQR-13FC avalanche photodiode (Perkin-Elmer Optoelectronics). The confocal volume was calculated in approximation according to (Culbertson et al., 2007) using the measured diffusional correlation time t_{diff} of free dye (Alexa488, Life Technologies), the known translational diffusion coefficient of Alexa488 (Molecular Probes; D = 280 um^2/s) and the axis ratio fitted from calibration measurements. For each sample, several dilutions were made and measured in a 96-well glass bottom plate (Whatman) with 30 repetitive measurements of 10 seconds each. NP-40S at 1 % v/v (Biosciences) was used to induce vesicle disruption for determination of detergent sensitivity and quantification of CD63-emGFP molecules per exosome.

Single vesicle imaging. Exosomes from CD63-emGFP/CD63-mCherry double transfected HEK293 cells were imaged by confocal fluorescence microscopy after spotting onto coverslips. Colocalization was quantified based on overlap of the point spread functions in the two fluorescent channels to derive the number of GFP (G), mCherry (R) and GFP/mCherry (RG) double positive vesicles.

Scanning Electron Microscopy (SEM). Cells were grown on Thermanox coverslips (Thermo Scientifc Inc, Nunc). After a quick wash (less than 10 seconds) in fresh culture medium without protein, cells were fixed with 2 % paraformaldehyde (Electron Microscopy Science, Hatfield, USA) and 2.5 % glutaraldehyde (Electron Microscopy Science, Hatfield, USA) in 0.1 M cacodylate buffer (Sigma Aldrich), pH 7.4. Cells were rinsed in 0.1 M cacodylate buffer (3 x 5 minutes). Dehydration was performed in a graded ethanol series (30, 50, 70, 90, 95, 100 % ethanol, 3 x 2 minutes each step). After dehydration, specimens were rinsed with hexamethyldisilizane (Sigma Aldrich) and dried in an oven (60°C for 2 hours). Samples were mounted on aluminum stubs by fixing the coverslip with carbon double-sided carbon tape, and sputter coated (Quorum SC7620) with gold/palladium (5-8 nm). Cells were examined with a scanning electron microscope (Versa 3D, FEI, Endhoven, Netherlands) using the ETD detector.

Nanoparticle Tracking Analysis (NTA). Label-free particle size and concentration determination was performed on a LM NTA instrument (NanoSight). With a camera gain of 500, full detection range and 90 second recordings all camera settings as well as analyses parameters (detection threshold of 2, minimum expected particle size of 50 nm, fixed minimal track length of 4) where kept constant throughout all measurements. For quantitative analysis of particle size distribution and concentration, a dilution row of samples between 1:100 to 1:10'000 was analyzed to hit the dynamic range of the instrument (1 - 4 x 10^8 particles/ml).

Automated imaging assay for exosome uptake. Cells were seeded into a 96-well ibidi plate and incubated with exosomes as indicated in each experiment. Cells were fixed for 20 minutes at room temperature with PenFix (Thermo Scientific) in presence of 1 □g/ml Hoechst (Life Technologies) and 0.02 % (v/v) CellMask Deep Red (Life Technologies). Following extensive washing with PBS, wells were imaged on an automated confocal plate scanning instrument (Operetta, Perkin Elmer) at 40x magnification. Image analysis was done using the Harmony software, by first identifying the nuclei (Hoechst), defining the cell boundaries (CellMask Deep Red) and finally quantifying the number of GFP spots per cell. At least 5,000 cells were analyzed by condition. Data are shown from one representative experiment from

at least three independent experiments, and represent averages with error bars indicating standard deviations from three independent samples.

Confocal, TIRF and DIC live cell microscopy. For combined confocal fluorescence and DIC live cell imaging cells were seeded into an 8-well m-slide (ibidi) and pre-stained prior to exosome addition as indicated in each experiment; Cell membrane: CellMask Deep Red (dilution 1:1000 for at least 2 minutes, Life Technologies); MVB: N-rhodamine-labelled phosphatidylethanolamine (NRhPE) (2.5 uM, for at least 60 minutes; Avanti Polar Lipids); Endoplasmic reticulum: ER Tracker Red (500 nM, for at least 15 minutes, Life Technologies); Lysosomes: LysoTracker Green (dilution 1:1000, for at least 60 minutes, Life Technologies). Actin was labeled by transfection with CellLight Actin-RFP (Life Technologies) 24 hours prior to imaging. Images were acquired on a confocal LSM710 microscope with Big-detector (Zeiss) with a 100x or 63x oil 1.4 NA PlanApochromat DIC objective and temperature, gas and humidity control unit (Life Imaging Services, Basel, Switzerland). Differential interference contrast (DIC) was set up using the transmission of the excitation laser as a light source and the TPMT as detector.
For live cell TIRF imaging, human fibroblasts were transiently transduced with Adeno-Lifeact-mCherry and seeded onto line substrates or 2D substrates prepared as described in (Martin et al., 2014) 4 hours prior to acquisition. TIRF microscopy (Roper Scientific) was performed with a Nikon TI Eclipse inverted stand equipped with a PlanApo 60x TIRF Objective, a Photometrics Evolve EMCCD camera, 491 nm and 561 solid-state laser diodes and was controlled using Metamorph imaging software. Fluorescent exosomes were quantified and characterized by FCS and typically added 5-10 minutes prior to image acquisition unless specified otherwise.

Image analysis. Confocal image stacks time series, confocal image plane time series and TIRF time lapse data were imaged with frame rates and time frames as indicated. Particles tracking and trajectory analysis was performed with the Imaris x64 (Bitplane) Particle Tracking Analysis module. Unless specified otherwise, SPT trajectories are shown as dragontail visualization with a max of 20 frames. Speeds were derived from relative exosome displacement between two frames. For co-localization studies stacks were imaged with a Leica Sp5 HyD imaging setup using 60x 1.4 NA PlanApo Objective with 2 color sequential line scanning, 130 nm z-sectioning and 40 nm xy oversampling. Stacks were deconvolved with Huygens remote manager (automatic threshold) and then analysed with the JACoP plugin (Bolte and Cordelières, 2006) for Fiji (Rasband).

Lipid nanoparticle formulations. 5'-Cy3 labeled siRNA (Stalder et al., 2013) was mixed in a 1:5 ratio with unlabeled siRNA and formulated as described in detail in (Baryza et al., 2014). Briefly, the LNPs were formed by mixing equal volumes of

lipid solution dissolved in ethanol with siRNA dissolved in a citrate buffer by an impinging jet process. The lipid solution contained a cationic lipid (Baryza et al., 2014) , a helper lipid (cholesterol) and a PEG lipid in a ratio of 50:46:4 at a siRNA concentration of 1 mg/ml. The LNP solution was then diafiltered with a MWCO-100 kDa membrane, sterile filtered and stored at 4°C. The vesicles typically had a diameter of ca 150 nm.

Acknowledgements. We thank Jeremy Baryza and Keith Bowman (NIBR Cambridge) for providing LNP encapsulated siRNA, and Rene Hemming (NIBR Basel) for guidance in setting up the gel filtration. We further thank Nancy Hynes and Helge Grosshans (FMI Basel) for continued feedback on the study, and Helge Grosshans for feedback on the manuscript. SELA is supported by the Swedish Research Council (VR-Med and EuroNanoMedII) and the Swedish Society of Medical Research (SSMF).

Abbreviations. DIC: Differential interference contrast. CAM: Cell adhesion molecule. EGF: epidermal growth factor. ER: endoplasmatic reticulum. FCS: Fluorescence Correlation Spectroscopy. GFP: Green fluorescent protein. emGFP: Emerald GFP. HIV: Human immunodeficiency virus. HCV: Hepatitis C virus. LNP: Lipid nanoparticle. MLV: murine leukemia virus. MS: Mass spectrometry. MWCO: molecular weight cut off. NTA: Nanoparticle Tracking Analysis. PEG: Polyethylene glycol. PI3K: Phosphoinositide-3-kinase. RFP: Red fluorescent protein. SEM: Scanning Electron Microscopy. SPT: single particle

Supporting online material. This manuscript contains three Supplementary Figures, and ten Supplementary videos.

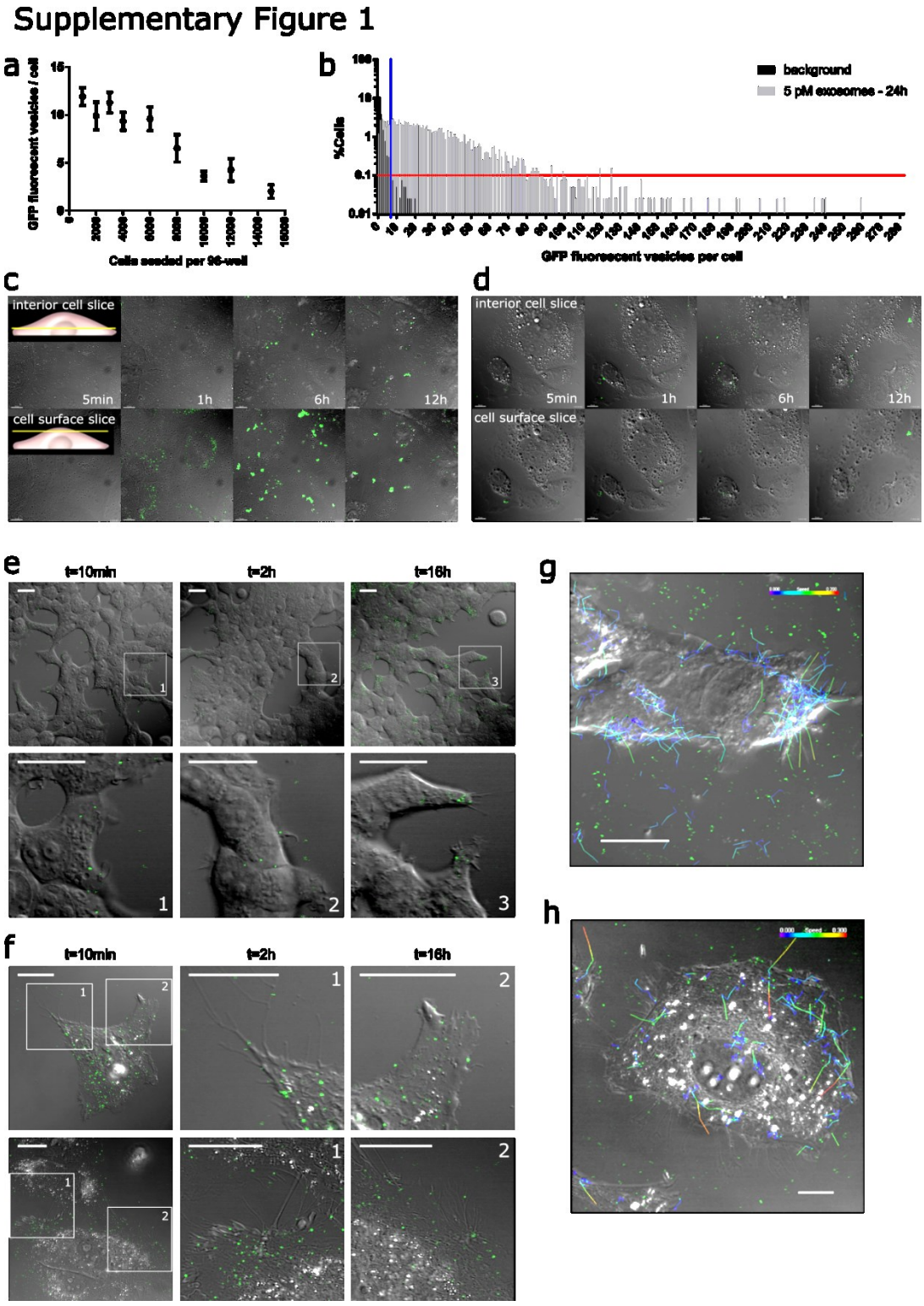

Supplementary Figure 1. Supplementary data to quantification of CD63-emGFP uptake. (a) HEK293 CD63-emGFP exosome uptake into Huh7 cells was quantified as a function of cell density using the same 96-well automated high content screening assay as in Fig.1. Number of cells plated per 96-well (0.143 cm^2) is shown on the x-axis. Exosome uptake was quantified 20 hours post addition of 10 pM CD63-emGFP exosomes based on the number of GFP vesicles per cell. At least

5’000 cells were analyzed per condition. Error bars represent standard deviations from three biological replicates. **(b)** Single cell analysis of data in Fig.1a-c. To illustrate the determination of the fraction of positive cells, the single cell histograms are shown for the examples of untreated Huh7 cells (dark grey bars) and Huh7 cells treated for 24 hours with CD63-emGFP HEK293 exosomes at 5 pM (light grey bars). The background fluorescence in the untreated cells was used to define a threshold fluorescence signal (red line) for positive cells based on a 90 % confidence for true negative assignment in the untreated cells. In the example shown, all cells at the right side of the blue line were counted as positive. Panels **(c)** and **(d)** show a side by side comparison of exosome versus lipid nanoparticle uptake. Huh7 cells were exposed to (d) 0.5 nM CD63-emGFP HEK293 exosomes or (c) a lipid nanoparticle formulated Cy3-labeled siRNA (SSB19, (Stalder et al., 2013)) at similar vesicle concentrations (200 nM siRNA, 20 % labeled siRNA, ca 1000 siRNA molecules per liposome) and uptake was monitored by combined DIC with confocal fluorescence live cell microscopy. Z-stacks were taken every 10 minutes over 12 hours. Images of individual time points from the movies are shown for two confocal planes corresponding to the cell surface (top rows) or the cell interior (bottom rows). Scaling bars: 10 um. Additional examples for exosome uptake clustering in filopodia active regions (Fig.2) are shown for **(e)** HEK293 recipient cells or **(f)** Huh7 recipient cells. Images were taken by combined DIC with confocal fluorescence live cell microscopy at time points post exosome addition (200 pM) as indicated. White rectangles highlight areas shown in close up views (as indicated by numbers). GFP fluorescence is pseudocolored in green. Scaling bars: 20 um. Panels **(g)** and **(h)** show uptake dynamics from corresponding live cell movies for HEK293 recipient cells and Huh7 recipient cells, respectively. Single exosome trajectories from 30 minutes live cell movies (starting 90 minutes post addition of exosomes at 200 pM; 20 s/frame) are illustrated in a dragontail visualization (max 20 frames) with pseudocoloring for exosome speed as indicated.

Supplementary Figure 2

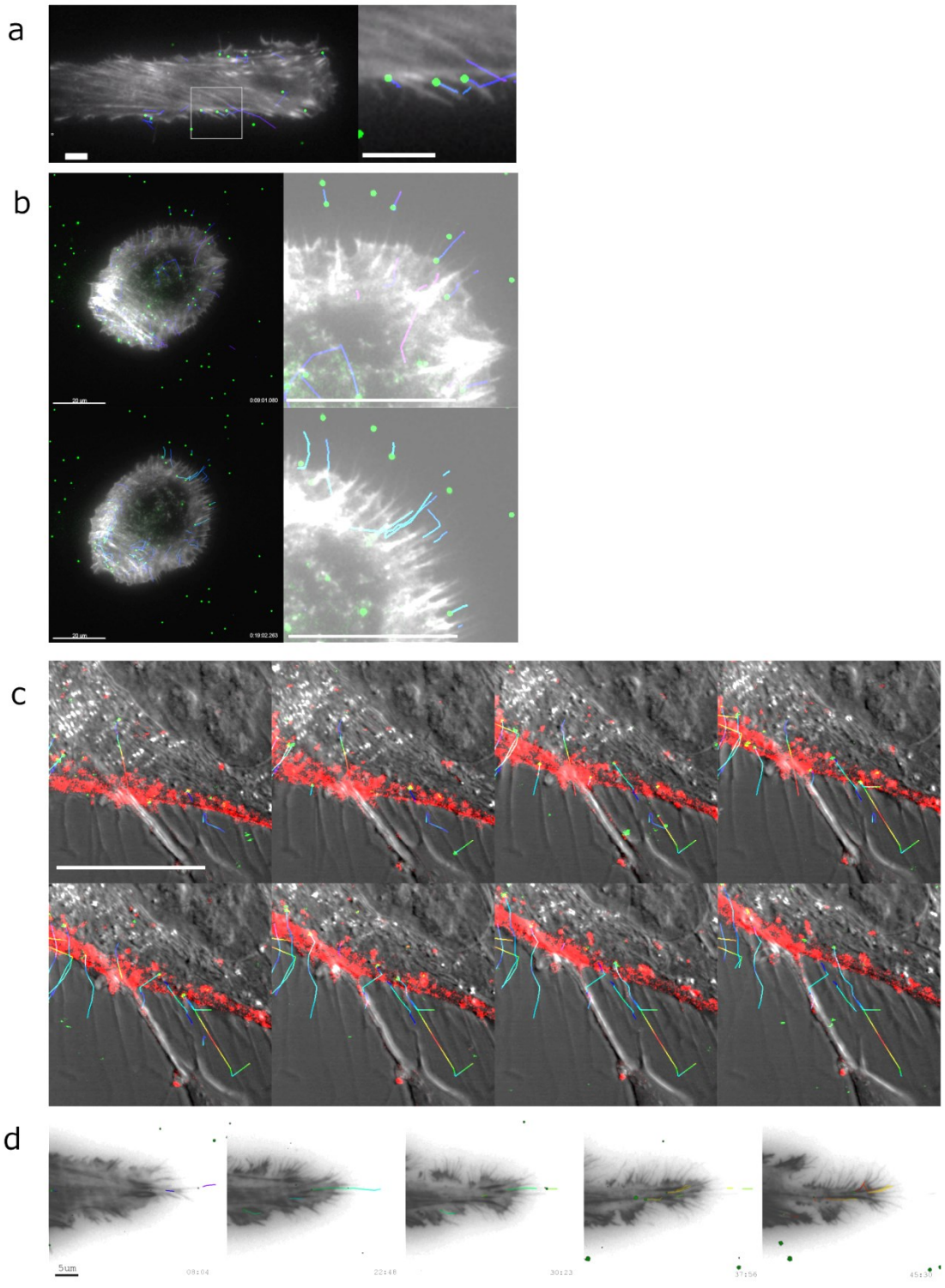

Supplementary Figure 2

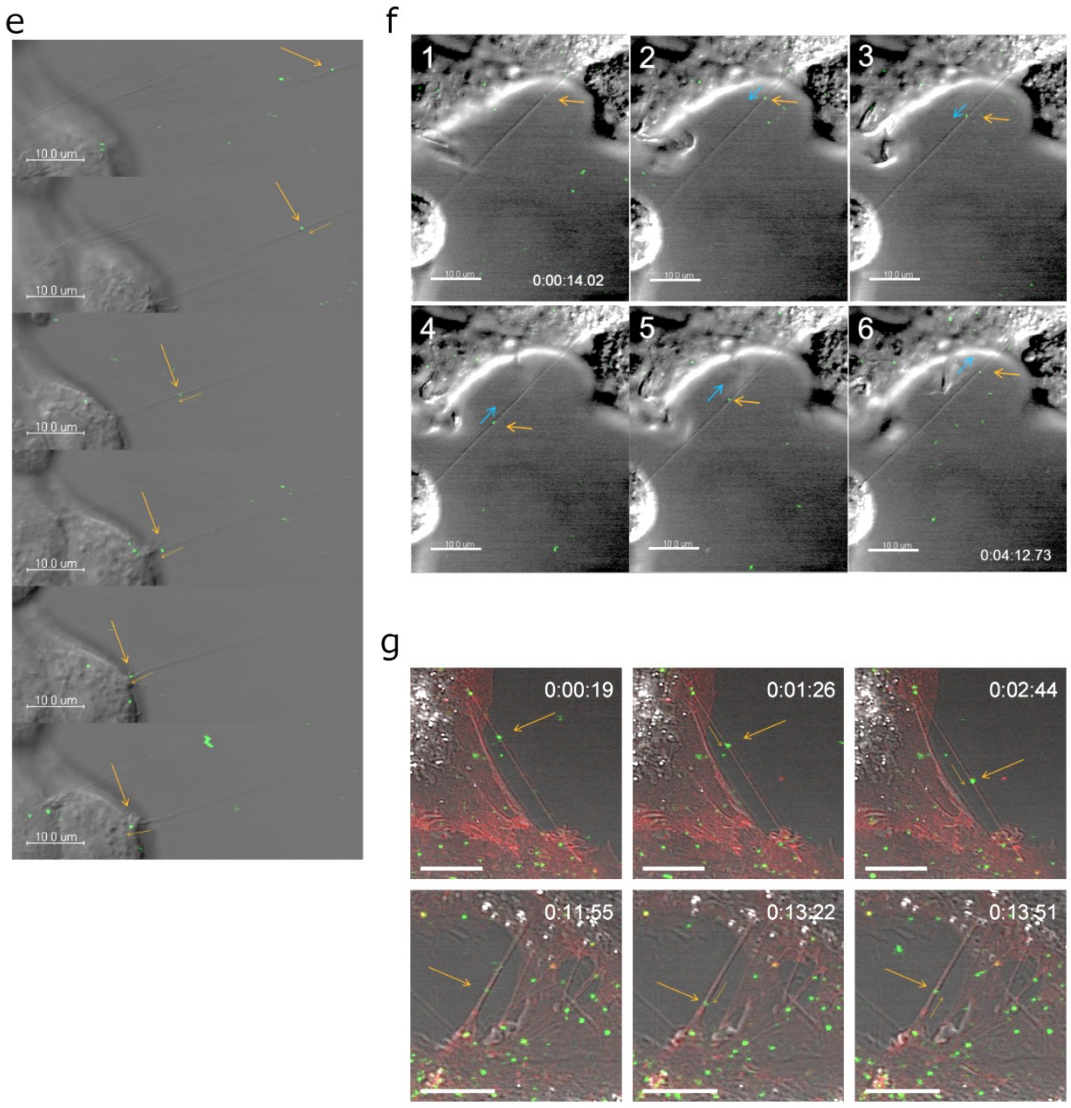

Supplementary Figure 2

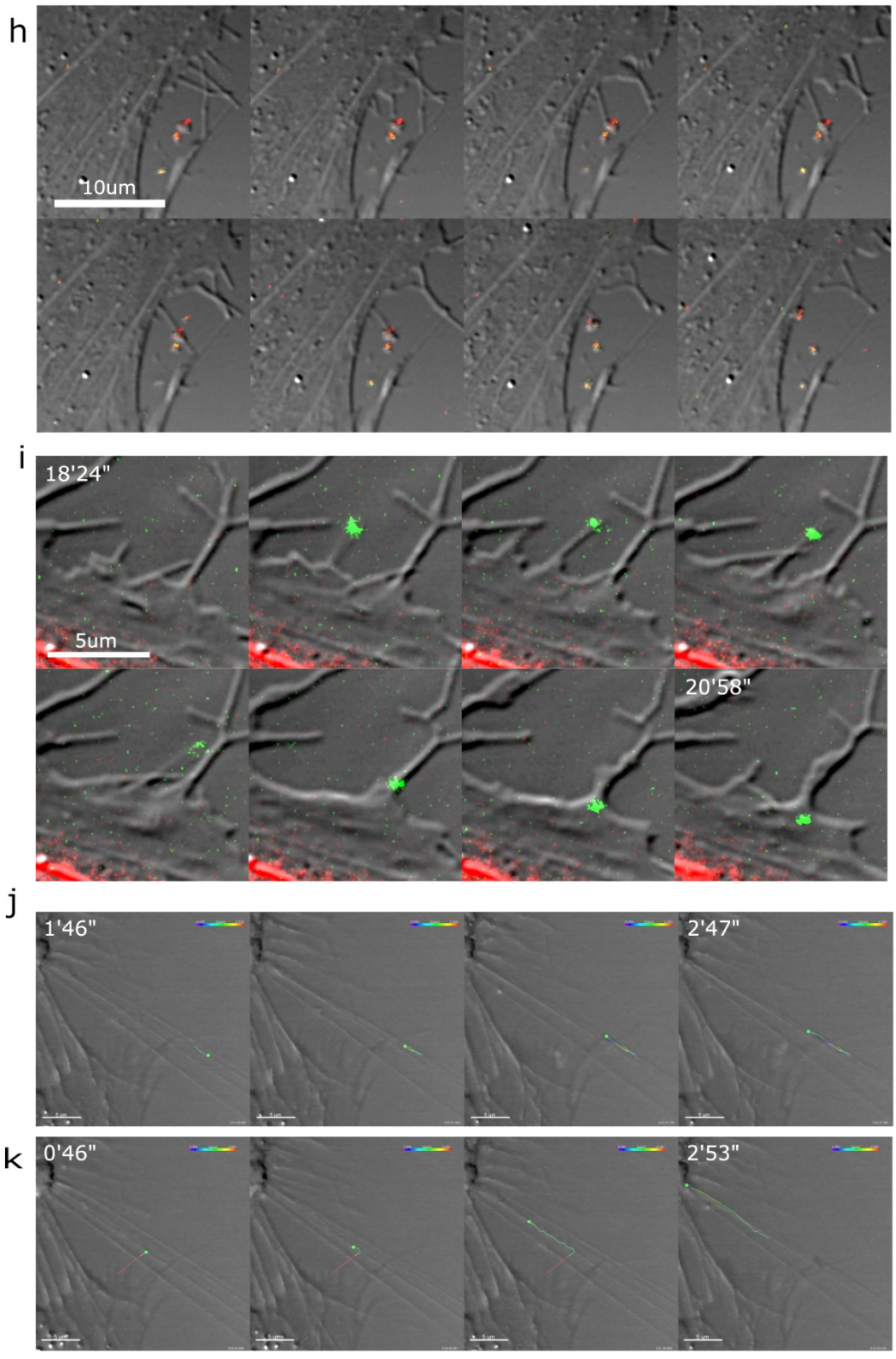

Supplementary Figure 2

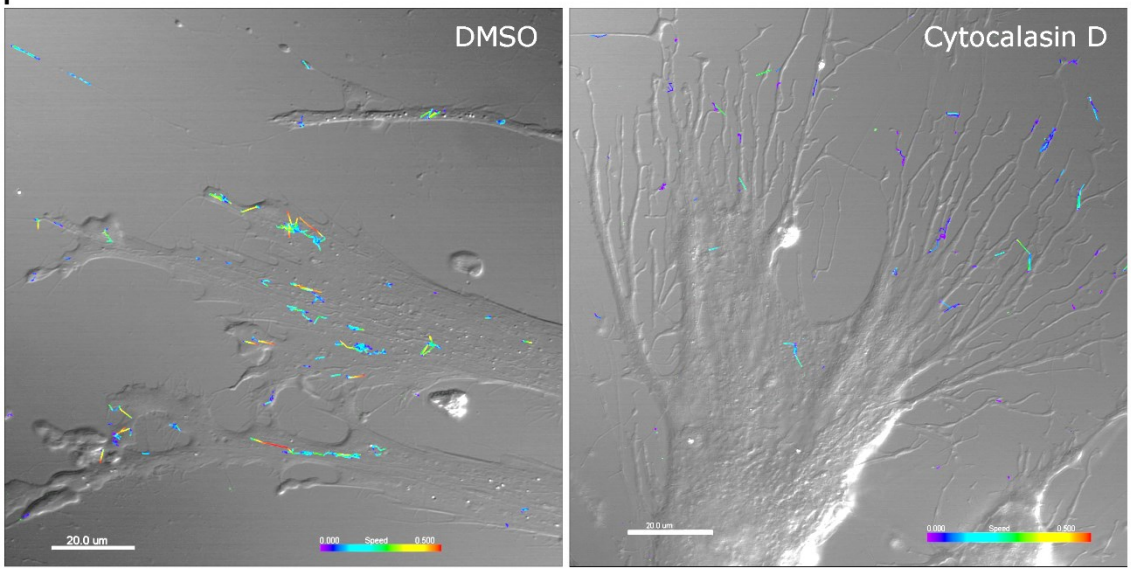

Supplementary Figure 2. Exosome filopodia surfing, grabbing and pulling. Additional examples to Fig.3 illustrating CD63-emGFP HEK293 exosomes (green) surfing on filopodia **(a-e)** or tunneling nanotubes **(f and g)**, exosome recruitment by filopodia pulling **(h)** or grabbing **(i).** Individual images from time lapse movies are shown at selected time points as indicated. Exosome trajectories are shown in a dragontail visualization (max 20 frames), pseudocolored for speed as indicated. (a): human primary fibroblasts stably expressing actin-RFP (white) grown on a line substrate, imaged by TIRF live cell microscopy. Scaling bars: 5 um; (b): human primary fibroblasts stably expressing actin-RFP (white) grown on a 2D-substrate, imaged by TIRF live cell microscopy. Scaling bars: 20 um; (c): human primary fibroblasts labeled with CellMask Deep Red (red) imaged by combined DIC with confocal fluorescence live cell microscopy. Scaling bars: 20 um; (d): human primary fibroblasts stably expressing actin-RFP (black) grown on a line substrate, imaged by TIRF live cell microscopy. Scaling bars: 5 um; (e) and (f): HEK293 cells imaged by combined DIC with confocal fluorescence live cell microscopy. Scaling bars: 10 um; (g): Huh7 cells stained with CellMask Deep Red (red) imaged by combined DIC with confocal fluorescence live cell microscopy. Scaling bar: 10 um; (h) and (i): human primary fibroblasts imaged by combined DIC with confocal fluorescence live cell microscopy. Scaling bars: 5 um. Examples illustrating different types of exosome movement on filopodia are shown in **(j)** and **(k)**. Typically, exosomes were directed towards the cell body immediately after apparent contact with the filopodium, and migrated with relatively constant speed (j). In rare cases, this was preceded by an initial short movement in the opposite direction, followed by a stalling and redirection towards the cell body

(k). **(I)** Cytochalasin D inhibition of exosome uptake. CD63-emGFP HEK293 exosomes (10 pM) were added to human primary fibroblasts pretreated with DMSO (left panel) or Cytochalasin D (50 uM for 20 minutes, right panel). Uptake was monitored by combined DIC with confocal fluorescence live cell imaging. Exosome trajectories are shown in a dragontail visualization, pseudocolored for exosome speed as indicated. Scaling bar: 20 um.

Supplementary Figure 3

a

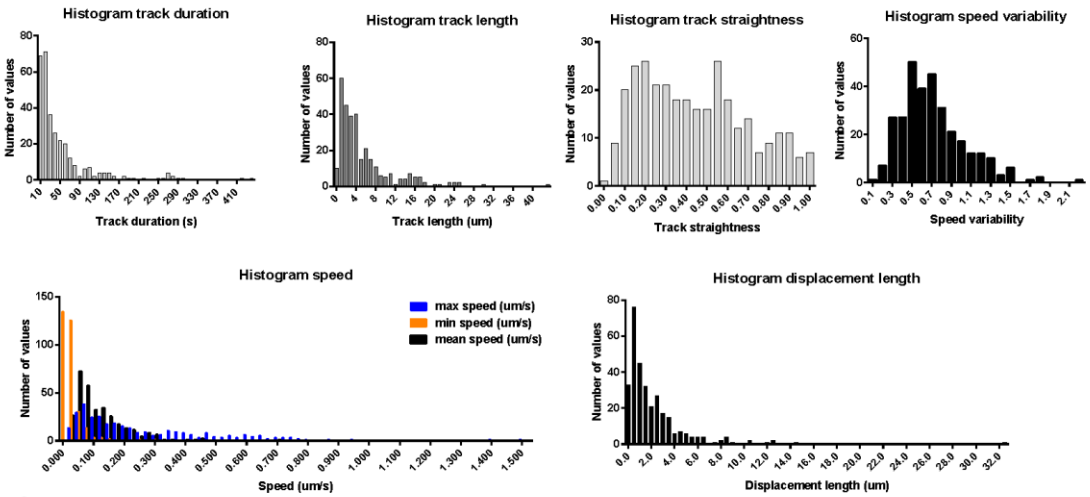

b

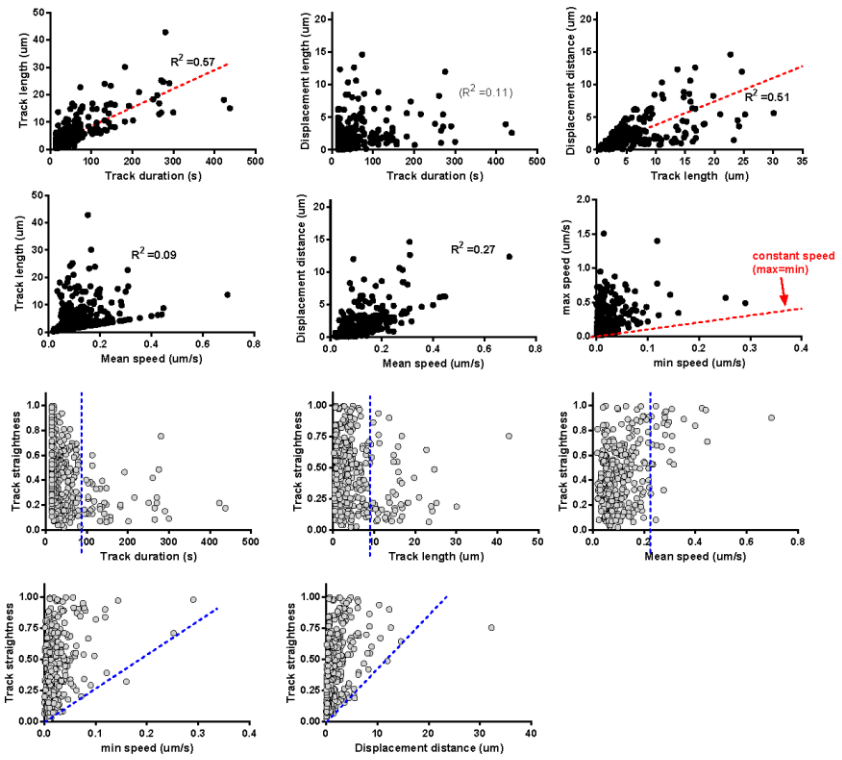

Supplementary Figure 3

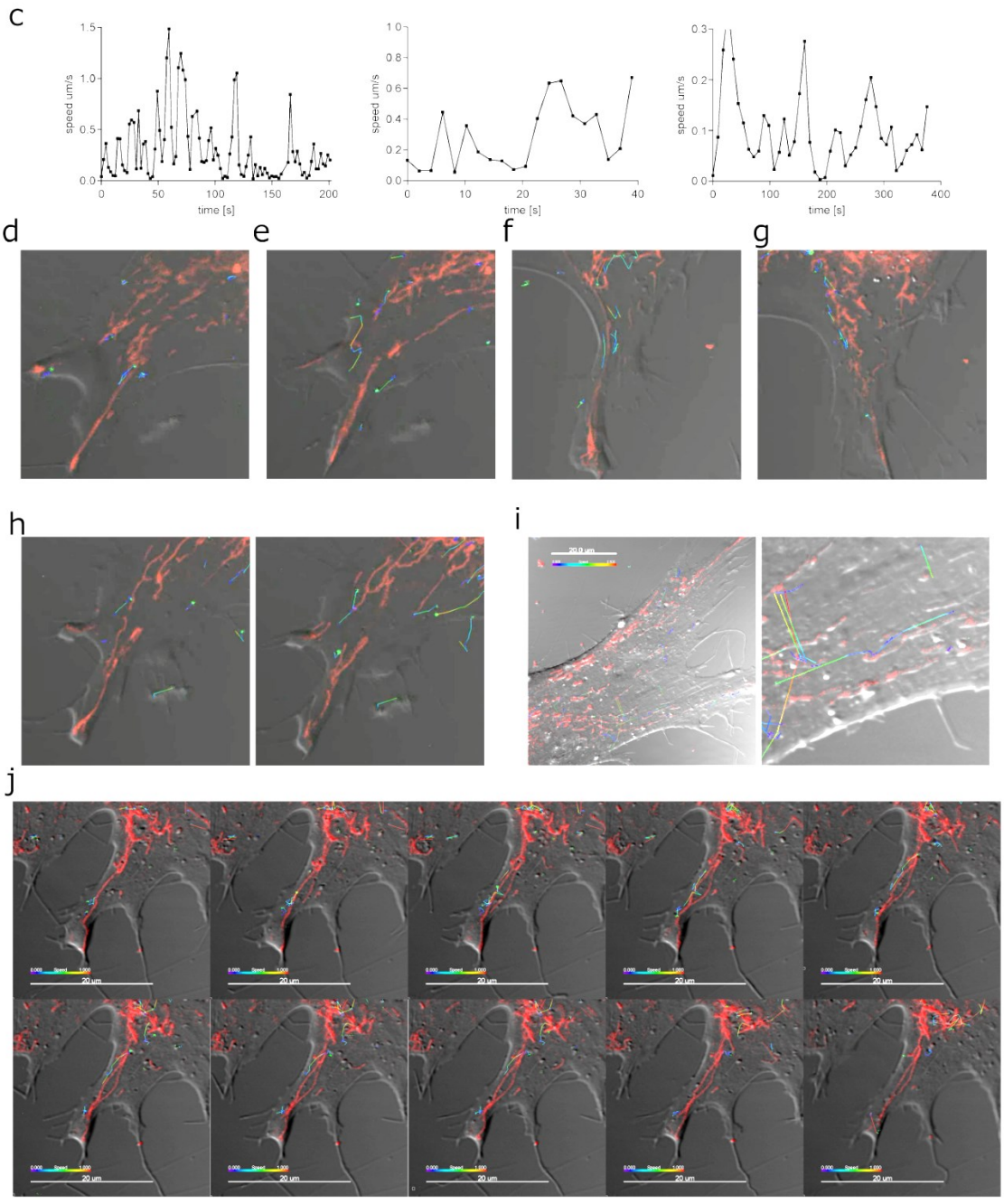

Supplementary Figure 3

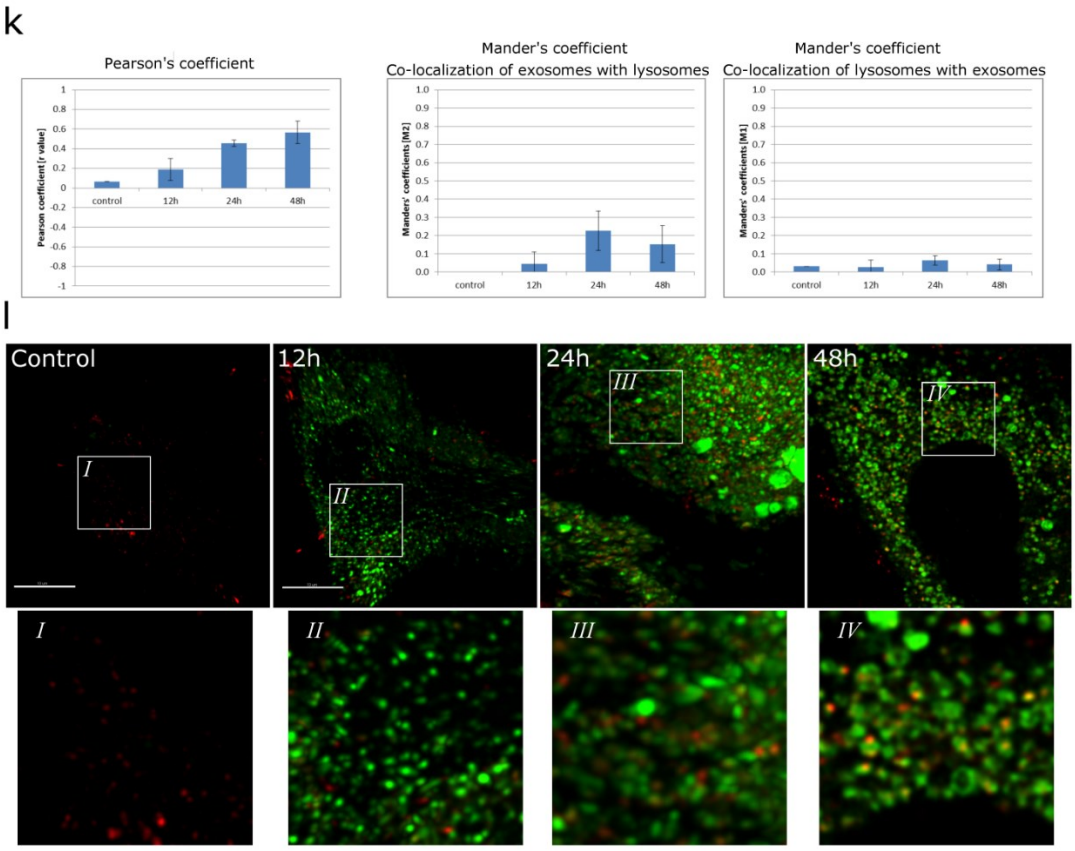

Supplementary Figure 3. Characterization of intracellular exosome fate. Intracellular trajectories of a total of 312 single HEK CD63-emGFP exosomes in fibroblasts from a 75-minute movie (5 s/frame) were analyzed for different motion parameters. The frequency distributions of individual exosome trajectory parameters are shown in **(a)**. x-y scatter plots showing the relation between different parameters for each individual vesicle are shown in **(b)**. Fifty percent of the vesicles were traced for 20 to 50 seconds, with a median total trajectory length of 3.5 um. Trajectory length showed a good correlation with the time a vesicle was observed. The wide distribution of the maximum speed with no apparent upper cut off confirms that our frame rate is sufficient to trace the majority of intracellular movements. More than 80 % of the vesicles showed a minimum speed of close to zero suggesting that transient stalling was a common characteristic. Seventy-five percent of the vesicles showed an at least 5-fold higher maximum than minimum speed, with a mean of 30-fold. Together these characteristics argue for a stop-and-go movement. The displacement length was significantly shorter than the absolute trajectory length, demonstrating that the vesicles did not primarily proceed on straight intracellular routes. This can also be seen in the histogram of track straightness. A 2D correlation analysis for each individual vesicle suggested that straight tracks are under-represented in trajectories of long duration or length, and over-represented in the population of

fast vesicles. In addition, vesicles moving on straight tracks showed larger displacements. Track length: total length of trajectory. Displacement distance: absolute distance of particle displacement within duration of trajectory. Track straightness: relative measure for track straightness with 0 representing random diffusion and 1 representing a straight line. Linear regression analysis with regression coefficient (R) as indicated. **(c)** Additional examples for intracellular speed traces of HEK293 CD63-emGFP exosomes in human primary fibroblasts from confocal live cell movies. Data points represent speeds derived from relative exosome displacement between two frames. **(d-j)** Additional examples for exosome trajectories with stop-and-go movement along the ER: CD63-emGFP exosomes in green, ER tracker in red, dragontail visualization (max 20 frames) color coded by speed as indicated. **(k)** Co-localization of CD63-mCherry exosomes with lysosomes increases over time. Human primary fibroblasts, stained with LysoTracker (green) were imaged by confocal live cell microscopy 12, 24 and 48 hours upon addition of HEK293 CD63-mCherry exosomes (red). High resolution z-stacks with oversampling (x-y: 40 nm; z: 130 nm) were recorded of perinuclear regions. Stacks were deconvolved by Huygen's remote manager and co-localization was quantified using JaCoP (Fiji) to derive Pearson's coefficients (left panel) and Mander's coefficients (middle and right panels). M1: green in red. M2: red in green. Projections of the deconvolved z-stacks are shown in **(l)**. Scaling bars: 10 um

Supplementary Movies.
The exosome concentration in all movies was 100 pM unless specified otherwise.

Supplementary movies 1 and 2: Lipid nanoparticle formulations accumulate at the cell surface. Cationic lipid nanoparticle formulation (1nM) with encapsulated Cy3 labelled siRNA (200 nM, green) were added to Huh7 cells and 2 min post addition uptake was monitored over 12 h with by live cell confocal imaging with optical sections and DIC transmitted light channel. Alexa647 labeled Transferrin (red) was additionally applied to monitor endosomal uptake. Movie 1 shows an upper optical section representing the cell surface and movie 2 shows an optical section representing the interior of the cell.

Supplementary movie 3: Exosome uptake in human primary fibroblasts is clustered into filopodia active regions. CD63-emGFP labeled HEK293 exosome (green) uptake was monitored over 80 min in Actin-RFP (red) labeled human primary fibroblasts. Exosome trajectories (dragontail) are shown with color coding for absolute time to visualize the progressive distribution of the intracellular movement and the cellular entry points of the exosomes.

Supplementary movie 4: Exosomes are endocytosed in human primary fibroblasts at filopodia active regions. CD63-emGFP labeled HEK293 exosome (green) uptake was monitored over 28 min in CellMask deep red (red) labeled human primary fibroblasts by live cell confocal imaging with optical sections and DIC transmitted light channel. Movie shows speed color coded exosome tracks (dragontail) to visualize the intracellular movement and entry points. CellMask labels the plasma membrane and gets internalized with endocytic vesicles.

Supplementary movies 5 and 6. Exosome surf on filopodia of human primary fibroblasts. CD63-emGFP labeled HEK293 exosome (green) movement along filopodia of CellMask Deep Red (red) labeled primary fibroblasts or was monitored for 8 minutes by live cell confocal imaging and DIC transmitted light channel with a frame rate of 5 s/f 1 h after transduction (Supplementary movie 5). Surfing along F-actin labeled primary fibroblast filopodia (white) and uptake of CD63-emGFP labeled HEK293 exosome (green) was tracked for 1 h by live cell TIRF imaging with a frame rate of 30 s/f 2h after transduction (Supplementary movie 6). Trajectories are color coded by speed as indicated.

Supplementary movie 7: Fibroblast pulls exosome to cell surface. CD63-emGFP labeled HEK293 exosome (green) were added to F-actin (black) labeled primary fibroblasts grown on a line substrate. The movie starts 60 min after exosome addition and documents the scenery for 20 min by live cell TIRF imaging with a frame rate of 10 s/f.

Supplementary movies 8: Exosomes scan along the ER. CD63-GFP labeled HEK293 exosomes (green) were tracked and ER movement is monitored for 75 min in human primary fibroblasts with a framerate of 5 sec/f by live cell confocal and DIC transmitted light channel imaging. The movie starts 150 min after exosome addition. Exosome trajectories are visualized as dragontails (dragontail of 4 images) with color coding for speed as indicated.

Supplementary movie 9: Exosome uptake in human primary fibroblast recipient cells. CD63-emGFP labeled HEK293 exosome (green) are taken up in CellMask deep red (red) labeled primary fibroblast. Time lapse movie was recorded for 10 minutes by live cell confocal optical section imaging and DIC transmitted light channel with a frame rate of 9 s/f, starting 5 min upon exosome addition.

Supplementary movie 10: Intracellular exosome movement. The movement of CD63-mCherry labeled HEK293 exosomes (red) in human primary fibroblasts was monitored for 5 min with a framerate of 1.5 s/f by live cell confocal and DIC

transmitted light channel imaging. The movie starts 165 min after transduction. The DIC channel visualizes the movement of intracellular vesicles, ER membrane and the outline of the cell with filopodia. The fluorescently labeled exosomes move within these larger vesicles and scan along the ER.

Supplementary movies 8 and 10 demonstrates the motion of fluorescently labeled exosomes within larger DIC, contrast rich, intracellular vesicles that scan along the ER, which is visualized as membraneous web either in the DIC or confocal fluorescence channel (ER Tracker red) as indicated.

Literature

Alvarez-Erviti, L., Y. Seow, H. Yin, C. Betts, S. Lakhal, and M.J.A. Wood. 2011. Delivery of siRNA to the mouse brain by systemic injection of targeted exosomes. *Nat. Biotechnol.* 29:341–5. doi:10.1038/nbt.1807.

Baryza, J., K. Bowman, A. Geall, T. Labonte, C. Lee, C. Vargeese, L. West, and J. Zhao. 2014. Lipids, lipid compositions, and methods of using them. *US 2014/0309277 A1*. 191.

Bolte, S., and F.P. Cordelières. 2006. A guided tour into subcellular colocalization analysis in light microscopy. *J. Microsc.* 224:213–32. doi:10.1111/j.1365-2818.2006.01706.x.

Bornschlögl, T. 2013. How filopodia pull: what we know about the mechanics and dynamics of filopodia. *Cytoskeleton*. 70:590–603. doi:10.1002/cm.21130.

Chevillet, J.R., Q. Kang, I.K. Ruf, H. a Briggs, L.N. Vojtech, S.M. Hughes, H.H. Cheng, J.D. Arroyo, E.K. Meredith, E.N. Gallichotte, E.L. Pogosova-Agadjanyan, C. Morrissey, D.L. Stirewalt, F. Hladik, E.Y. Yu, C.S. Higano, and M. Tewari. 2014. Quantitative and stoichiometric analysis of the microRNA content of exosomes. *Proc. Natl. Acad. Sci. U. S. A.* 111. doi:10.1073/pnas.1408301111.

Coller, K.E., K.L. Berger, N.S. Heaton, J.D. Cooper, R. Yoon, and G. Randall. 2009. RNA interference and single particle tracking analysis of hepatitis C virus endocytosis. *PLoS Pathog.* 5:e1000702. doi:10.1371/journal.ppat.1000702.

Colombo, M., G. Raposo, and C. Théry. 2014. Biogenesis, Secretion, and Intercellular Interactions of Exosomes and Other Extracellular Vesicles. *Annu. Rev. Cell Dev. Biol.* 30:255–289. doi:10.1146/annurev-cellbio-101512-122326.

Conde, I. del, C. Shrimpton, P. Thiagarajan, and J. López. 2005. Tissue-factor–bearing microvesicles arise from lipid rafts and fuse with activated platelets to initiate coagulation. *Blood*. 106:1604–1612. doi:10.1182/blood-2004-03-1095.Supported.

Corrigan, L., S. Redhai, A. Leiblich, S.-J. Fan, S.M.W. Perera, R. Patel, C. Gandy, S.M. Wainwright, J.F. Morris, F. Hamdy, D.C.I. Goberdhan, and C. Wilson. 2014. BMP-regulated exosomes from Drosophila male reproductive glands reprogram female behavior. *J. Cell Biol.* 206:671–88. doi:10.1083/jcb.201401072.

Culbertson, M.J., J.T.B. Williams, W.W.L. Cheng, D.A. Stults, E.R. Wiebracht, J.J. Kasianowicz, and D.L. Burden. 2007. Numerical fluorescence correlation spectroscopy for the analysis of molecular dynamics under nonstandard conditions. *Anal. Chem.* 79:4031–9. doi:10.1021/ac062013m.

Dubuisson, J., and F.-L. Cosset. 2014. Virology and cell biology of the hepatitis C virus life cycle--an update. *J. Hepatol.* 61:S3–S13. doi:10.1016/j.jhep.2014.06.031.

Feng, D., W.-L. Zhao, Y.-Y. Ye, X.-C. Bai, R.-Q. Liu, L.-F. Chang, Q. Zhou, and S.-F. Sui. 2010. Cellular internalization of exosomes occurs through phagocytosis. *Traffic*. 11:675–87. doi:10.1111/j.1600-0854.2010.01041.x.

Fitzner, D., M. Schnaars, D. van Rossum, G. Krishnamoorthy, P. Dibaj, M. Bakhti, T. Regen, U.-K. Hanisch, and M. Simons. 2011. Selective transfer of exosomes from oligodendrocytes to microglia by macropinocytosis. *J. Cell Sci.* 124:447–58. doi:10.1242/jcs.074088.

Forscher, P., and S.J. Smith. 1988. Actions of cytochalasins on the organization of actin filaments and microtubules in a neuronal growth cone. *J. Cell Biol.* 107:1505–16.

Friedman, J.R., J.R. Dibenedetto, M. West, A.A. Rowland, and G.K. Voeltz. 2013. Endoplasmic reticulum-endosome contact increases as endosomes traffic and mature. *Mol. Biol. Cell*. 24:1030–40. doi:10.1091/mbc.E12-10-0733.

Gilleron, J., W. Querbes, A. Zeigerer, A. Borodovsky, G. Marsico, U. Schubert, K. Manygoats, S. Seifert, C. Andree, M. Stöter, H. Epstein-Barash, L. Zhang, V. Koteliansky, K. Fitzgerald, E. Fava, M. Bickle, Y. Kalaidzidis, A. Akinc, M. Maier, and M. Zerial. 2013. Image-based analysis of lipid nanoparticle-mediated siRNA delivery, intracellular trafficking and endosomal escape. *Nat. Biotechnol.* 31:638–46. doi:10.1038/nbt.2612.

Harris, D.A., S.H. Patel, M. Gucek, A. Hendrix, W. Westbroek, and J.W. Taraska. 2015. Exosomes Released from Breast Cancer Carcinomas Stimulate Cell Movement. *PLoS One*. 10:e0117495. doi:10.1371/journal.pone.0117495.

Heusermann, W., Hean J., Trojer D., VonBueren S., Graff-Meyer A, Genoud C., Voshol H., EL Andaloussi S., Wood M. and Meisner-Kober N. 2015. CD63-emGFP as a marker for quantification of exosome cell uptake at the single vesicle level by high content screening. *Manuscript Submitted.*

Hood, J.L., R.S. San, and S.A. Wickline. 2011. Exosomes Released by Melanoma Cells Prepare Sentinel Lymph Nodes for Tumor Metastasis. *Cancer Res.* 71:3792–3801. doi:10.1158/0008-5472.CAN-10-4455.
Jagannathan, S., D. Reid, A. Cox, and C. Nicchitta. 2014. De novo translation initiation on membrane-bound ribosomes as a mechanism for localization of cytosolic protein mRNAs to the endoplasmic reticulum. *RNA*. 10.1261/rna.045526.114. doi:10.1261/rna.045526.114.
Kordelas, L., V. Rebmann, A.-K. Ludwig, S. Radtke, J. Ruesing, T.R. Doeppner, M. Epple, P.A. Horn, D.W. Beelen, and B. Giebel. 2014. MSC-derived exosomes: a novel tool to treat therapy-refractory graft-versus-host disease. *Leukemia*. 28:970–3. doi:10.1038/leu.2014.41.
Lehmann, M.J., N.M. Sherer, C.B. Marks, M. Pypaert, and W. Mothes. 2005. Actin- and myosin-driven movement of viruses along filopodia precedes their entry into cells. *J. Cell Biol.* 170:317–25. doi:10.1083/jcb.200503059.
Li, S., L. Liu, X. Zhuang, Y. Yu, X. Liu, X. Cui, L. Ji, Z. Pan, X. Cao, B. Mo, F. Zhang, N. Raikhel, L. Jiang, and X. Chen. 2013. MicroRNAs inhibit the translation of target mRNAs on the endoplasmic reticulum in Arabidopsis. *Cell*. 153:562–74. doi:10.1016/j.cell.2013.04.005.
Lidke, D.S., K. a Lidke, B. Rieger, T.M. Jovin, and D.J. Arndt-Jovin. 2005. Reaching out for signals: filopodia sense EGF and respond by directed retrograde transport of activated receptors. *J. Cell Biol.* 170:619–26. doi:10.1083/jcb.200503140.
Martin, K., M. Vilela, N.L. Jeon, G. Danuser, and O. Pertz. 2014. A growth factor-induced, spatially organizing cytoskeletal module enables rapid and persistent fibroblast migration. *Dev. Cell*. 30:701–16. doi:10.1016/j.devcel.2014.07.022.
Mattila, P.K., and P. Lappalainen. 2008. Filopodia: molecular architecture and cellular functions. *Nat. Rev. Mol. Cell Biol.* 9:446–54. doi:10.1038/nrm2406.
Mitchison, T., and M. Kirschner. 1988. Cytoskeletal dynamics and nerve growth. *Neuron.* 1:761–72.
Morelli, A.E., A.T. Larregina, W.J. Shufesky, M.L.G. Sullivan, D.B. Stolz, G.D. Papworth, A.F. Zahorchak, A.J. Logar, Z. Wang, S.C. Watkins, L.D. Falo, and A.W. Thomson. 2004. Endocytosis, intracellular sorting, and processing of exosomes by dendritic cells. *Blood.* 104:3257–66. doi:10.1182/blood-2004-03-0824.
Nobile, C., D. Rudnicka, M. Hasan, N. Aulner, F. Porrot, C. Machu, O. Renaud, M.-C. Prévost, C. Hivroz, O. Schwartz, and N. Sol-Foulon. 2010. HIV-1 Nef inhibits ruffles, induces filopodia, and modulates migration of infected lymphocytes. *J. Virol.* 84:2282–93. doi:10.1128/JVI.02230-09.
Nordin, J.Z., Y. Lee, P. Vader, I. Mäger, H.J. Johansson, W. Heusermann, O.P.B. Wiklander, M. Hällbrink, Y. Seow, J.J. Bultema, J. Gilthorpe, T. Davies, P.J. Fairchild, S. Gabrielsson, N.C. Meisner-Kober, J. Lehtiö, C.I.E. Smith, M.J.A. Wood, and S.E.L. Andaloussi. 2015. Ultrafiltration with size-exclusion liquid chromatography for high yield isolation of extracellular vesicles preserving intact biophysical and functional properties. *Nanomedicine*. 1–5. doi:10.1016/j.nano.2015.01.003.
Parolini, I., C. Federici, C. Raggi, L. Lugini, S. Palleschi, A. De Milito, C. Coscia, E. Iessi, M. Logozzi, A. Molinari, M. Colone, M. Tatti, M. Sargiacomo, and S. Fais. 2009. Microenvironmental pH is a key factor for exosome traffic in tumor cells. *J. Biol. Chem.* 284:34211–22. doi:10.1074/jbc.M109.041152.
Properzi, F., M. Logozzi, and S. Fais. 2013. Exosomes: the future of biomarkers in medicine. *Biomark. Med.* 7:769–78. doi:10.2217/bmm.13.63.
Rana, S., and M. Zöller. 2011. Exosome target cell selection and the importance of exosomal tetraspanins: a hypothesis. *Biochem. Soc. Trans.* 39:559–62. doi:10.1042/BST0390559.
Rasband, W.S. ImageJ, U. S. National Institutes of Health, Bethesda, Maryland, USA, http://imagej.nih.gov/ij/.
Ratajczak, J., M. Wysoczynski, F. Hayek, a Janowska-Wieczorek, and M.Z. Ratajczak. 2006. Membrane-derived microvesicles: important and underappreciated mediators of cell-to-cell communication. *Leukemia*. 20:1487–95. doi:10.1038/sj.leu.2404296.
Reid, D.W., Q. Chen, A.S.-L. Tay, S. Shenolikar, and C.V. Nicchitta. 2014. The Unfolded Protein Response Triggers Selective mRNA Release from the Endoplasmic Reticulum. *Cell*. 158:1362–1374. doi:10.1016/j.cell.2014.08.012.
Reid, D.W., and C. V Nicchitta. 2015. Diversity and selectivity in mRNA translation on the endoplasmic reticulum. *Nat. Rev. Neurosci.* 16:221–231. doi:10.1038/nrm3958.
Sahay, G., W. Querbes, C. Alabi, A. Eltoukhy, S. Sarkar, C. Zurenko, E. Karagiannis, K. Love, D. Chen, R. Zoncu, Y. Buganim, A. Schroeder, R. Langer, and D.G. Anderson. 2013. Efficiency of siRNA delivery by lipid nanoparticles is limited by endocytic recycling. *Nat. Biotechnol.* 31:653–8. doi:10.1038/nbt.2614.
Salomon, C., J. Ryan, L. Sobrevia, M. Kobayashi, K. Ashman, M. Mitchell, and G.E. Rice. 2013. Exosomal signaling during hypoxia mediates microvascular endothelial cell migration and vasculogenesis. *PLoS One*. 8:e68451. doi:10.1371/journal.pone.0068451.
Sheetz, M.P., S. Turney, H. Qian, and E.L. Elson. 1989. Nanometre-level analysis demonstrates that lipid flow does not drive membrane glycoprotein movements. *Nature*. 340:284–8. doi:10.1038/340284a0.
Smith, J.L., S.K. Campos, A. Wandinger-Ness, and M. a Ozbun. 2008. Caveolin-1-dependent infectious entry of human papillomavirus type 31 in human keratinocytes proceeds to the endosomal pathway for pH-dependent uncoating. *J. Virol.* 82:9505–12. doi:10.1128/JVI.01014-08.
Spooner, R.A., D.C. Smith, A.J. Easton, L.M. Roberts, and J.M. Lord. 2006. Retrograde transport pathways utilised by viruses and protein toxins. *Virol. J.* 3:26. doi:10.1186/1743-422X-3-26.
Stalder, L., W. Heusermann, L. Sokol, D. Trojer, J. Wirz, J. Hean, A. Fritzsche, F. Aeschimann, V. Pfanzagl, P. Basselet, J. Weiler, M. Hintersteiner, D. V Morrissey, and N.C. Meisner-Kober. 2013. The rough endoplasmatic reticulum is a central nucleation site of siRNA-mediated RNA silencing. *EMBO J.* 32:1115–27. doi:10.1038/emboj.2013.52.
Sung, B.H., T. Ketova, D. Hoshino, A. Zijlstra, and A.M. Weaver. 2015. Directional cell movement through tissues is controlled by exosome secretion. *Nat. Commun.* 6:7164. doi:10.1038/ncomms8164.
Svensson, K.J., H.C. Christianson, A. Wittrup, E. Bourseau-Guilmain, E. Lindqvist, L.M. Svensson, M. Mörgelin, and M. Belting. 2013. Exosome uptake depends on ERK1/2-heat shock protein 27 signaling and lipid Raft-mediated endocytosis negatively regulated by caveolin-1. *J. Biol. Chem.* 288:17713–24. doi:10.1074/jbc.M112.445403.
Thayanithy, V., V. Babatunde, E.L. Dickson, P. Wong, S. Oh, X. Ke, A. Barlas, S. Fujisawa, Y. Romin, A.L. Moreira, R.J. Downey, C.J. Steer, S. Subramanian, K. Manova-Todorova, M. a. S.S. Moore, and E. Lou.

2014. Tumor exosomes induce tunneling nanotubes in lipid raft-enriched regions of human mesothelioma cells. *Exp. Cell Res.* 323:178–188. doi:10.1016/j.yexcr.2014.01.014.
Tian, T., Y.-L. Zhu, F.-H. Hu, Y.-Y. Wang, N.-P. Huang, and Z.-D. Xiao. 2013. Dynamics of exosome internalization and trafficking. *J. Cell. Physiol.* 228:1487–95. doi:10.1002/jcp.24304.
Tian, T., Y.-L. Zhu, Y.-Y. Zhou, G.-F. Liang, Y.-Y. Wang, F.-H. Hu, and Z.-D. Xiao. 2014. Exosome uptake through clathrin-mediated endocytosis and macropinocytosis and mediating miR-21 delivery. *J. Biol. Chem.* 289:22258–67. doi:10.1074/jbc.M114.588046.
Twu, O., N. de Miguel, G. Lustig, G.C. Stevens, A.A. Vashisht, J.A. Wohlschlegel, and P.J. Johnson. 2013. Trichomonas vaginalis exosomes deliver cargo to host cells and mediate host:parasite interactions. *PLoS Pathog.* 9:e1003482. doi:10.1371/journal.ppat.1003482.
Valadi, H., K. Ekström, A. Bossios, M. Sjöstrand, J.J. Lee, and J.O. Lötvall. 2007. Exosome-mediated transfer of mRNAs and microRNAs is a novel mechanism of genetic exchange between cells. *Nat. Cell Biol.* 9:654–9. doi:10.1038/ncb1596.
Wurdinger, T., N.N. Gatson, L. Balaj, B. Kaur, X.O. Breakefield, and D.M. Pegtel. 2012. Extracellular vesicles and their convergence with viral pathways. *Adv. Virol.* 2012:767694. doi:10.1155/2012/767694.
Zamudio-Meza, H., A. Castillo-Alvarez, C. González-Bonilla, and I. Meza. 2009. Cross-talk between Rac1 and Cdc42 GTPases regulates formation of filopodia required for dengue virus type-2 entry into HMEC-1 cells. *J. Gen. Virol.* 90:2902–11. doi:10.1099/vir.0.014159-0.

5 Conclusions and Future Perspectives

In the course of this thesis we have established a toolbox of reagents and methods for isolation, labeling and characterization of exosomes. Benchmarking different isolation methods revealed significant shortcomings of state of the art protocols in providing sufficient yields, purity and vesicle integrity to enable functional exosome studies. Addressing these issues, we established a new gentle and scalable protocol based on a combination of ultrafiltration and gel filtration and compared this method with sequential ultracentrifugation, the gold standard isolation method in the field. Using single vesicle detection techniques, we report for the first time a characterization of vesicle integrity following different purification protocols. The main advantages of the new isolation method include a significant increase in yield, reproducibility and purity while preserving physicochemical properties and biological composition. We next established a strategy for fluorescent exosome labeling by transiently expressing fluorescent MVB and exosome marker proteins in the parent cells and extensively characterized labeled exosomes in comparison to unlabeled exosomes. We further adapted the sensitive single molecule fluorescence fluctuation correlation spectroscopy (FCS) method for quantitative exosome characterization. At the same time FCS allowed a discrimination of vesicular and nonvesicular fluorescent populations within the same sample. These experiments revealed that a number of GFP and mCherry tagged endomembrane proteins (including CD63, Lamp2, Alix, and Ago2) end up in the medium as freely diffusing proteins in surprisingly high concentrations, whereas FCS allows to specifically determine the concentration of vesicular particles within the same sample. By taking advantage of detergent induced vesicle disruption we further quantify the number of fluorescent molecules per exosome at the single vesicle level. Our preferred expression construct resulted in fluorescent exosomes with 10-30 CD63-emGFP molecules per vesicle, thereby enabling monitoring the dynamics of single exosomes by live cell imaging. This part of the work set the stage for a quantitative investigation of the dynamics and routes of exosome uptake.

Using these tools, we set up a high content screening assay to quantify exosome uptake by automated imaging, and apply this assay to report a first systematic and quantitative profiling of exosome parent - recipient pairing. It should now be straightforward to extend this small pilot to a more extensive array of cell types and conditions, which would provide a resource of general value for the cell communication field. In particular this information may guide studies of exosome tissue homing in vivo. Experiments in this direction seem to be quite straightforward based on the toolbox, methods and data contributed by this work. Fluorescence labeled exosomes of different flavor (different parent cell

origins, different vesicle subpopulations or even engineered vesicles with different extravesicular ligands) may be administered to mice for analyzing tissue homing by microscopy of histological sections or even whole organ imaging with a serial two-photon tomography technique (eg. Tissue Visions), whereas it will be interesting to assess for a correlation with in vitro cell targeting preferences.
Likewise the finding that certain cell types (human primary keratinocytes as well as B16 mouse melanoma cells) turned out to be refractory for exosome uptake has some interesting implications; It would be worthwhile to screen more extensively for potential exosome sources that might be taken up into these cells. Such highly specific pairing would provide new clues to molecular mechanisms and receptor-ligand interactions both necessary and sufficient for exosome cell targeting, e.g. by differential proteomic profiling of the cognate and inert exosomes. Alternatively, should these cells indeed confirm to be refractory to exosome uptake in general, it would be of high interest to elucidate why. From a practical perspective such exosome uptake inert cells would provide valuable tools for gain of function assays to identify exosome receptors. The high content exosome screening assay described in this work may directly enable the systematic search for exosome uptake receptors as well as modulators. shRNA or CRISPR based exosome uptake inhibition or enhancer screens would allow to systematically dissect the major players in exosome cell uptake. For a more targeted study, a more comprehensive comparison of exosome and viral particle literature might be a good place to start for a list of candidate receptors. Likewise, the HCS assay now enables small molecule screens to identify tool compounds for further exosome research. Finally, the fact that B16 melanoma cells were refractory even to uptake of their own exosomes sheds interesting new light on the role of exosomes in tumorigenesis and may suggest that such cells have specialized in unidirectional exosomal communication.

In the main part of this work we characterized the cell uptake dynamics of exosomes at the single vesicle and single cell level to reveal characteristics that parallel those of some viruses. We demonstrate that exosome uptake saturates with dose and time to reach near 100 % ‘transduction’ efficiency at picomolar concentrations and that exosome uptake is largely mediated by active recruitment and surfing on filopodia to reach endocytic hotspots for their internalization at the filopodia base. While this provides a cell biological explanation for the, virus-like, high efficiency of exosomes in recipient cell targeting, a great concern in a read out based on pure cell internalization is that we are following the average, bulk behavior of the vesicles without knowing anything about whether this population is reflective of the functional uptake route that leads to functional activity. One can look to the HIV field, where the majority of HIV particles taken up by the cell are trafficked to lysosomes and

degraded, without ever leading to a productive infection, whereas only a very minor fraction of cell- virion interactions leads to productive infection of the cell. A similar lesson in this regard was learned in siRNA delivery field, where liposomal delivery vehicles have for years been optimized primarily optimized for general target cell delivery and endosomal escape, which now turns out to be completely unrelated to the pool of siRNA responsible for activity. Consistent with this notion, previous work from our laboratory (Stalder et al. 2013) (Paper II in the appendix), revealed that, while the bulk of liposome delivered siRNA delivered gets degraded in Lysosomes only a few molecules are sufficient for effective target mRNA knockdown if trafficked to the site of action- the ER.
An emerging issue in the exosome field is the notion that miRNAs are of much lower abundance in exosomes than anticipated, with an estimate of ca 1 copy per 100 vesicles. This questions whether at physiological exosome concentrations it is ever possible to achieve effective miRNA concentrations within recipient cells, unless their uptake route is highly effective in delivering directly to the subcellular target site [121]. Interestingly in this work we revealed that exosomes licensed through the flilopodia pathway enter into endocytic vesicles destined to directly home to the ER – the site of RISC loading [122]. Again clues might be provided by viruses which replicate at this organelle.

The work within this thesis unravels yet another facet of exosome biology converging with virus biology. This is in line with an increasing notion of viruses having potentially hijacked mechanisms that originally evolved for exosome function, ranging from biogenesis, release, and recipient cell interaction. Therefore it is conceivable that we may in turn take advantage of decades of research in the virology field to enhance our understanding of exosomes. This faces however the challenge that viral mechanisms are highly divergent, making it difficult to prioritize candidate strains. The filopodia mediated uptake route revealed in this work now shortlists those viruses and pathogens that are known to also surf on filopodia. Intriguingly HIV, one such virus, has previously been noted to share a number of similarities in intracellular pathways and some overlap in host derived proteins to exosomes. Consistently it was reported that exosomes compete with HIV for virus entry into endocytic compartments [123]. At the same time, there is also emerging evidence for cross regulation between exosomes and HIV; exosomes isolated from semen but not from blood were recently shown to have anti HIV-infectious properties. In turn, the exosome pathway can also contribute to pro-viral activity, such as by using exosomes as Trojan horses to escape from the immune system [124]. Further research in convergence and parallels between exosomes and in particular HIV would therefore be warranted. Apart from HIV, also other pathogens are able to subvert the exosome pathway. In particular the use of exosomes by pathogens for hide and seek from the

immune system seems to be a prevalent theme. miRNAs secreted by Epstein Barr virus (EBV)-infected cells are transferred by exosomes and act in uninfected recipient cells [31]. Also prions are being distributed by exosomes [19] [125] and many different parasitic diseases are connected to exosomes or the exosomal pathway in a pro or anti pathogenic manner (reviewed in [54]).

The ultimate goal of this work in translating the learnings of highly efficient exosome delivery towards a synthetic delivery vehicle will now require to revisit strategies for exosome cargo loading in light of the results from this work. Since our data suggest that cargo might be subject to highly controlled release mechanisms at sites such as the ER this implies that it is likely crucial to mimic endogenous cargo loading. Of note it is still unclear whether miRNA and RISC are residing within the lumen or instead are being embedded within the inner or outer leavelet of the vesicle membrane – a question imperative to answer for effective exosome based therapeutic strategies.

Finally, in the course of this project we also stumbled over two independent additional hints which are under further investigation at the moment, and which are not detailed in this thesis. Based on an observation of autophagy receptors and cargo (LC3, p62, FIP200) being present in exosomes a follow up project in the lab now investigates a potential connection between exosome biogenesis and the autophagy pathway. Another line of investigation in the lab now follows up on a set of data which suggest the existence of a population of vesicles deriving from the lysosome, positive for Lamp2, carrying truncated proteins and inactive in targeting other cells.

Personally I feel that this work brings together several pieces in the exosome puzzle and adds a new facet to exosome biology, I hope my input in exosome characterization and quantification on one hand and the uptake and intracellular routes on the other hand may prompt new directions in basic research of exosome biology as well as their translation into clinical applications.

6 Appendix

6.1 Paper II

The rough endoplasmatic reticulum is a central nucleation site of siRNA-mediated RNA silencing

Lukas Stalder[1,2*], Wolf Heusermann[1], Lena Sokol[1], Dominic Trojer[1], Joel Wirz[1], Justin Hean[1,3], Anja Fritzsche[1], Florian Aeschimann[1,4], Vera Pfanzagl[1], Pascal Basselet[1], Jan Weiler[1], Martin Hintersteiner[1], David V. Morrissey[5] and Nicole C. Meisner-Kober[1*]

[1] Novartis Institutes for Biomedical Research, NIBR Biologics Center, RNAi Therapeutics, Basel/Switzerland
[2] Present address: Swiss Group for Clinical Cancer Research, Bern/Switzerland
[3] Present address: University of the Witwatersrand Medical School, Johannesburg/South Africa
[3] Friedrich Miescher Institute, Basel/Switzerland
[4] Novartis Institutes for Biomedical Research, NIBR Biologics Center, RNAi Therapeutics, Cambridge MA/USA

*Corresponding authors: nicole.meisner-kober@novartis.com, lukas.stalder@sakk.ch

Keywords. small interfering RNA, microRNA, RNA silencing, siRNA localization, rough endoplasmatic reticulum, RNA interference, Argonaute 2, gene expression regulation.

Abstract

Despite of progress in mechanistic understanding of the RNA interference (RNAi) pathways, the subcellular sites of RNA silencing still remain under debate. Here we show that loading of lipid-transfected siRNAs and endogenous microRNAs (miRNA) into RISC (RNA induced silencing complexes), encounter of the target mRNA, and Ago2-mediated mRNA slicing in mammalian cells are nucleated at the rough endoplasmic reticulum (rER). Although the major RNAi pathway proteins are found in most subcellular compartments, the miRNA- and siRNA- loaded Ago2 populations co-sediment almost exclusively with the rER membranes, together with the RISC loading complex (RLC) factors Dicer, TRBP and PACT. Fractionation and membrane co-immune precipitations further confirm that siRNA-loaded Ago2 physically associates with the cytosolic side of the rER membrane. Additionally, RLC-associated double-stranded siRNA, diagnostic of RISC loading, and RISC-mediated mRNA cleavage products exclusively co-sediment with rER. Finally, we identify TRBP and PACT as key factors anchoring RISC to ER membranes in an RNA-

independent manner. Together, our findings demonstrate that the outer rER membrane is a central nucleation site of siRNA-mediated RNA silencing.

Introduction

Since the discovery of RNA interference (RNAi), the interest in small RNAs as both therapeutic targets and agents has been growing rapidly. The effective and safe delivery of small RNA therapeutics into cells still remains one of the biggest challenges, which is partially linked to the still incomplete picture of the intracellular sites of endogenous RNA silencing. Small interfering RNAs (siRNAs) and microRNAs (miRNAs) exhibit their functions once they are loaded into RNA induced silencing complexes (RISCs) (Carthew and Sontheimer, 2009). Proteins from the Argonaute (Ago) family are the core of RISC complexes, and Argonaute2 (Ago2) is the only of the four mammalian Ago proteins with the ability to slice the target mRNA by endonucleolytic cleavage (Liu *et al.*, 2004;Meister *et al.*, 2004). Although Ago2 can bind single stranded siRNAs *in vitro* (Rivas et al., 2005), endogenous loading of double stranded small RNAs is thought to require the RISC loading machinery (Liu *et al.*, 2004;Yoda *et al.*, 2010). The canonical, minimal human RISC loading complex (RLC) comprises Ago2, Dicer and TRBP (TAR binding protein) (Gregory *et al.*, 2005;MacRae *et al.*, 2008;Maniataki and Mourelatos, 2005;Noland *et al.*, 2011). This triad of proteins is capable of binding and processing dsRNA into 21-23nt siRNAs or miRNAs, loading of Ago2 and removing the passenger strand (MacRae et al., 2008). As Dicer knockout mouse embryonic stem cells (ES) – while devoid of mature miRNAs – are however proficient of siRNA-mediated gene silencing (Kanellopoulou et al., 2005), it has been suggested that this canoncial mode of RISC loading can be bypassed by other mechanisms, one of them involving the Heat shock cognate 70 (Hsc70) and Heat shock protein 90 (Hsp90) chaperones (Iki *et al.*, 2010; Iwasaki *et al.*, 2010; Johnston *et al.*, 2010; Miyoshi *et al.*, 2005; Miyoshi *et al.*, 2010). Once Ago2 is loaded with the double-stranded siRNA, only one strand (guide) is retained and the other strand (passenger) gets removed and degraded (Leuschner *et al.*, 2006;Matranga *et al.*, 2005;Miyoshi *et al.*, 2010;Rand *et al.*, 2005), which can be facilitated by a complex consisting of TRAX and translin (C3PO, component 3 promoter of RISC)(Liu *et al.*, 2009;Ye *et al.*, 2011).

The specific subcellular sites of the RISC loading, target association, and silencing steps still remain under debate. Ago2, miRNAs and target mRNAs that are targeted for translational inhibition have been found to localize to P-bodies (Jagannath and Wood, 2009; Liu *et al.*, 2005; Pillai *et al.*, 2005), and it has been suggested that miRNAs and RNAi proteins guide their target mRNAs to P-bodies (Eulalio *et al.*, 2007b; Jakymiw *et al.*, 2005; Pillai *et al.*, 2005). However,

microscopically visible P-bodies do not seem to be required for RNAi (Chu and Rana, 2006;Eulalio *et al.*, 2007b), but have been proposed to be rather a consequence than a cause of silencing (Eulalio *et al.*, 2007a; Eulalio *et al.*, 2007b). Moreover, siRNAs have been found to localize to P-bodies as double strands in an at least partially Ago2-dependent manner (Jagannath *et al.*, 2009; Jakymiw *et al.*, 2005). Other reports have demonstrated a link between RNAi and membranes (Cikaluk *et al.*, 1999; Gibbings and Voinnet, 2010; Gibbings *et al.*, 2009; Lee *et al.*, 2009; Tahbaz *et al.*, 2001; Tahbaz *et al.*, 2004). In early reports, Dicer and Ago2 have been shown to fractionate with membranes (Tahbaz et al., 2004) and to co-localize with the Golgi apparatus (Barbato *et al.*, 2007; Cikaluk *et al.*, 1999;Tahbaz *et al.*, 2001). Furthermore, disruption of the Hermansky Pudlak 1 and 4 proteins (HPS1, HPS4), which are implicated in membrane trafficking and function (Huizing et al., 2000), accelerate the loading of Ago2 with siRNAs in flies (Lee et al., 2009). Additionally it has been proposed that RISC assembly and disassembly is linked to membranes of the endo-lysosomal sytem (Gibbings *et al.*, 2010; Gibbings *et al.*, 2009; Lee *et al.*, 2009). Given that there is still no clear picture about the sites of RISC loading, target mRNA association and silencing, in this work we aimed to quantitatively and spatially follow the siRNA fate within the cell upon lipid delivery from initial uptake and subcellular redistribution to its entry into the RNAi pathway, and to identify the sites of RNAi activity.

Results

Ago2, siRNAs and miRNAs localize to a number of different compartments

To characterize the intracellular distribution of RNAi pathway proteins, exogenously added siRNAs, and endogenous miRNAs, HeLa cells were transfected by lipofection with siRNAs against SSB (Pei et al., 2010) (Sjogren syndrome antigen B), lysed after 24 hours and the post-nuclear detergent-free supernatants were fractionated on continuous density sucrose gradients (Fig. 1A). Markers for lysosomes (Lamp2), endosomes and multi vesicular bodies (MVBs; Hrs, Rab5, Tsg101) were enriched in fractions 2-3 (20-33 % sucrose), markers for Golgi (b4-GalT1) in fractions 3-5, the ER-Golgi intermediate compartment (ERGIC; p58), the endoplasmatic reticulum (ER; Calnexin) and ribosomes (RPS6) in fractions 4-7 (42-64 % sucrose), confirming the expected fractionation pattern consistent with fractionation of cytoplasmic lysates in previous studies (eg (Gibbings *et al.*, 2009; Jouannet *et al.*, 2012)). Ago2 showed a broad distribution and was present throughout fractions 3-9. Similarly, Ago1, Dicer and PACT fractionated broadly, whereas only TRBP showed evidence for a more confined localization and co–sedimented sharply with Golgi and ER marker proteins (Fig. 1A). The fractionation of the RNAi pathway proteins did not change upon the transfection of a siRNA, suggesting that a transfected siRNA does not induce a major redistribution of these proteins (Fig. S1A).

To confirm the general fractionation pattern of endogenous Ago2, we performed immune-fluorescence (IF) of Ago2 as well as the different organelle marker proteins in HeLa cells (Fig. 1B). The established high specifity of the Ago2-antibody (clone 11A9) (Rüdel et al., 2008) was validated also in our hands using a peptide comprising the antigenic epitope (Fig. S1B). Ago2 staining showed the typical diffuse punctuate pattern throughout the cytoplasm with the typical enrichment in the perinuclear region and a half-moon shaped structure (Golgi) and some individual strong foci (P-bodies). In accordance with the broad fractionation of Ago2, endogenous Ago2 also co-localized by IF partially with the ER, ERGIC, Golgi, P-bodies, and early endosomes (Fig. 1B). This intracellular distribution of endogenous Ago2 is consistent with previous publications, where Ago2 was shown to partially co-localize with Golgi (Cikaluk *et al.*, 1999; Tahbaz *et al.*, 2001), P-bodies (Jagannath *et al.*, 2009; Leung *et al.*, 2006; Liu *et al.*, 2005; Ohrt *et al.*, 2008; Pare *et al.*, 2009; Pillai *et al.*, 2005; Sen and Blau, 2005; Zeng *et al.*, 2008), or endosomes (Gibbings *et al.*, 2009; Lee *et al.*, 2009). Additionally, our data confirm the general notion that endogenous Ago2 appears to distribute differently than Ago2-GFP, which was shown to strongly accumulate in P-bodies (Jagannath *et al.*, 2009;Leung *et al.*, 2006;Liu *et al.*, 2005;Ohrt *et al.*, 2008;Sen *et al.*, 2005). Consistent with an accumulation in P-bodies, we found overexpressed Ago2-GFP enriched in the Dcp1 containing fractions (4-6) of the continuous sucrose density gradient (Fig. S1C).

As the overall Ago2 localization was not instructive about sites of RNA silencing activity, we next followed the siRNA during onset of uptake and a potential subsequent subcellular redistribution to monitor its putative entry into the RNAi pathway. HeLa cells were transfected with the SSB siRNA and a control siRNA with no target in human cells (pGL3), harvested after 1.3, 3.3, 5 and 28 h and fractionated as above. During the 5 hours transfection period, the SSB siRNA was increasingly enriched in the endo-/lysosomal fractions. After 28 hours, the cells were cleared of 75-90 % of the transfected siRNAs by secretion and/or degradation (Figs. 1C, S1D), whereas the remaining siRNA was now mostly in the non-endosomal fractions, suggesting that only 10-25 % of the transfected siRNA ever had the potential to load into RISC. In accordance with a strong accumulation and degradation of the siRNA in endosomes and lysosomes, respectively, a transfected TMR-labeled siRNA co-localized with endosomal (transferrin) and lysosomal (LysoTracker) markers in living cells and in sucrose gradients (Figs. 1D, S1E-G), suggesting that the bulk of transfected siRNA enters the cells through the endosomal system (Lu et al., 2009), and that the major fraction of the transfected siRNA is quickly targeted to lysosomes for degradation (Figs. 1D, S1E-G). Interestingly, the non-targeting pGL3 siRNA fractionated similar to the SSB siRNA, suggesting that trafficking of siRNAs is not driven by the presence of a target mRNA (Fig. S1D). Given this dramatic clearance of siRNA within the initial phase

of transfection, we reasoned that at late time points, the remaining amount of siRNA might better reflect the active population. Indeed, siRNA remaining at 28 hours fractionated in a sucrose gradient similarly as endogenous miR-16 (Fig. S1H), a representative and relatively abundant miRNA in HeLa cells, indicating that, once in the cytoplasm, siRNA is subject to similar protein interactions and trafficking events as endogenous miRNAs. However, both, miR-16 as well as the SSB siRNA were present in all Ago2 containing fractions, suggesting that even after initial clearance, the co-fractionation of RNAi factors and siRNAs or miRNAs is also not indicative to discern the active siRNA/Ago2 population.

Excess of inactive siRNA masks active population

Using Ago2 immune precipitations (IPs), we next quantified how much of the siRNA residing in the cell after the initial major clearance wave is loaded into Ago2. Ago2 IPs (Rüdel et al., 2008) were quantitatively highly reproducible (Figs. S2A-B), and importantly, showed a linear correlation between eluted Ago2 and the amount of input lysate over the relevant range of sample concentration (Fig. S2C). Also, the IP efficiency of Ago2 was independent of the sucrose concentration as confirmed for both, the continuous (Fig S2D) as well as discontinuous sucrose gradients (Fig 2E) used in this study. Additionally, to rule out that loaded siRNA might get lost during the IP procedure due to dissociation from Ago2 and to unambiguously confirm that the IP procedure allows to quantitatively determine the amount of complex, we used 5'TMR-labeled single-stranded HuR siRNA complexed to recombinant Ago2 *in vitro* as a standard to quantify siRNA recovery by RT-qPCR, which yielded a relative recovery of Ago2-siRNA complexes in the protein IP of 83 % (Fig. S2F). In addition, fluorescence anisotropy measurements confirmed that the recovered siRNA was still mostly complexed with Ago2 after native elution with the antigenic peptide (Fig S2G). This data demonstrates the stability of the complex throughout the IP procedure, consistent with the long half-life of Ago2-guide strand complexes *in vitro* (half-life of Ago2-guide strand > 20 hours, Fig.S2H) and the high stability of the complex reported previously (Martinez J, Genes Dev 2004), and altogether unambiguously confirm that the IP procedure allows to quantitatively determine Ago2 loaded siRNA within a range of +/- 20 % accuracy.

HeLa cells transfected with increasing doses of the very potent SSB siRNA reached saturation of the mRNA knockdown already at 0.25 nM transfected siRNAs, with an IC_{50} of 24±4 pM (Figs. 2A-B). In contrast, the amount of loaded guide strand in Ago2 increased almost linearly up to the highest transfected dose (6.25 nM; Figs. 2A, S2K, S2L). Consistent with observations emerging from previous *in vivo* studies (Pei et al., 2010), our data suggest that at siRNA concentrations beyond saturation of knockdown, a depot of loaded Ago2 may be formed and that the

capacity of the RISC loading machinery is not yet saturated, at least for SSB siRNA concentrations of up to 200 to 300-fold beyond the IC_{50} (Fig. 2A). Further calculations reveal that the IC_{50} of SSB mRNA knockdown is as little as 35-40 molecules of siRISC per cell (Fig. 2B). To investigate whether these low numbers of siRISC per cell required for a 50 % mRNA knock-down is a general feature of siRNAs, we performed the analogous experiments with absolute quantification for three additional siRNAs of markedly different potency (Figs S2N-P). Two siRNAs were targeting other mRNAs (GAPDH and HuR), the third siRNA ("SSB(53)") targets another site within the same mRNA (SSB) but with significantly lower overall potency. Strikingly, for all of these siRNAs we find equally low numbers at IC_{50} ranging from 10-110 siRISC molecules per cell. These data suggest that RNA silencing is in general a remarkably efficient process once the siRNA is loaded into RISC. Additionally, we quantified the fraction of Ago2-loaded siRNA in relation to total intracellular siRNA followed a hyperbolic saturation curve with increasing siRNA dose, with less than 1 % fraction bound at the IC_{50} of knockdown and saturating at ca 4 % (Figs. S2I, S2J, S2M). This behavior suggests that either compartmentalization and/or other limiting factors prevent a quantitative loading of the intracellular siRNA material into Ago2. Considering estimate accuracies of our correction for the efficiencies of all experimental steps, the precision of these numbers is subject to a variation of at most 2-3 fold, suggesting that even at maximum experimental underestimation, a major fraction of intracellular siRNA but also miRNA (see Figures 4B, S1H and S3B) is non-RISC associated, which may appear counter intuitive to the current assumption in the field. Interestingly however, a recent publication (Janas *et al.*, 2012) reports a conclusion perfectly consistent with our quantitative data. Based on an absolute quantification of Ago proteins and total miRNA copies per cell, the authors come to the conclusion that there is a 13-fold excess of miRNA over Argonaute molecules in HeLa cells, which implies that only a few percent of a given miRNA will be loaded in Ago proteins on average.

Active siRISC co–sediments with ER and Golgi membranes

Given that such a minor fraction of intracellular siRNA gets loaded into Ago2, we concluded that for localization of siRNA activity, tracing bulk siRNA with microscopy or fractionation becomes very misleading. Therefore we further refined the cell fractionation analysis of the siRNA by performing Ago2-IPs from continuous density sucrose gradients to quantify the amount of siRNA and miRNA loaded in Ago2 in each fraction. IP efficiencies were comparable across the gradient and well reproducible between independent fractionation experiments (Fig. S2D-E). Surprisingly and in contrast to the broad bulk distribution of siRNA, miRNA and RNAi pathway proteins, the Ago2 loaded SSB siRNA, miR-16 and miR-21 all eluted in a sharp peak in the Golgi and ER fractions (fractions 4-6; Fig. 3A),

suggesting that the active siRNA/miRNA population may be associated with Golgi and/or ER membranes. To get further evidence for activity of the siRNA-Ago2 complexes (siRISC) in these fractions, we next performed 5'RACE with RNA purified from each fraction to qualitatively assess the absence or presence of the cleavage product of the SSB mRNA. Consistent with the fractionation of the siRISC, a 5'RACE product was only detected in fractions 4-6 (Fig. 3B). Sequencing of the 200 bp 5'RACE PCR product confirmed that all sequenced clones contained SSB mRNA cleaved at the expected position (Fig. S3A). Additionally, we tested the distribution of the cytoplasmatic 5' to 3' exonuclease Xrn1 in the same sucrose gradient fractions (Fig. 1A). Xrn1 was present in all non-endo/lysosomal fractions and enriched in fractions 4-6. This shows that the sliced mRNA can even be detected in fractions where it can be degraded and in turn excludes the possibility that the absence of 5'RACE products in the fractions 1-3 and 7-9 was due to immediate mRNA degradation after the siRNA-mediated mRNA slicing. In summary, these experiments show that siRISC as well as the sliced mRNA do co-fractionate with Golgi and ER membranes.

Active siRISC associates to the outside of the rough ER

To investigate whether the active siRISC also physically associates with membranes, post-nuclear lysates of HeLa cells transfected with SSB siRNA were subjected to a membrane floatation assay on a discontinuous sucrose gradient (Tahbaz et al., 2004). After the centrifugation, membrane proteins of Lysosomes, Golgi and ER were enriched on the top (fraction 1 and partially 2), whereas non-membrane bound material remained in the loading zone (fractions 3-5; Fig. 4A). Consistent with a previous report (Tahbaz et al., 2004), a portion of the cytoplasmatic population of Ago2 and Dicer, but also a fraction of Ago1 and PACT floated with membranes; Interestingly, TRBP was exclusively membrane associated. While the major siRNA, miRNA as well as Ago2 amounts were found in the non-membrane fractions, loaded siRISC as well as miRISC (miR-16 and miR-21) were strongly enriched in the membrane fractions (Figs. 4B, S3B). Additionally, the SSB mRNA cleavage product floated exclusively with membranes (Fig. 4C), whereas again, Xrn1 was present in all fractions (Fig. 4A). Together, this suggested that the siRISC activity is not only co-fractionating with Golgi and ER membranes but is indeed membrane associated. To further characterize the Ago2 association with membranes, HeLa lysates were treated with RNAseA or ProteinaseK, and subsequently subjected to membrane floatation assays. RNAseA treatment did not lead to a detectable reduction of Ago2 in the membrane fraction (Fig. 4D, S3C), indicating that indirect association via the target mRNA does not play a major role for Ago2 membrane association (Fig. 4A). Additionally, given that Ago2 membrane association is independent of RNA (Fig. 4D), this rules out that Ago2 membrane association is mediated through polysomes.

Upon ProteinaseK treatment all Ago2 was lost from the membrane fraction (Fig. 4D). As controls, also Dcp1a which is not supposed to be encapsulated by membranes was fully susceptible to ProteinaseK treatment, whereas Calreticulin as an ER luminal protein was entirely protected from degradation and only detectable in the membrane fraction. In consequence and consistent with a previous report (Cikaluk et al., 1999), this data demonstrates that Ago2 associates to the cytosolic rather than the luminal side of membrane enclosed compartments.

Finally, to unambiguously corroborate the physical association of Ago2 and RISC with membranes by an additional orthogonal method and to identify the membranes Ago2 associates with, HeLa cells were treated with Nocodazole and CytochalasinD to disrupt the cytoskeleton, lysed in the absence of detergents, and an IP against Ago2 was performed to pull down the Ago2-associated membranes. Species which were indirectly immune precipitated via membranes were subsequently recovered by mild elution with an NP-40 containing buffer. IP with the anti-Ago2 antibody brought down the ER membrane marker Calnexin, but no markers of Golgi or endosomal membranes, demonstrating a specific physical association of Ago2 with the membrane of the ER (Fig. 5A). As negative control, the anti-Ago2 IP was performed already in the presence of NP-40, thereby omitting any lipid mediated interactions. Under these conditions, no Calnexin was detectable in the eluate, which confirms that the interaction of Ago2 with Calnexin is membrane mediated. As additional control, in a similar IP with mouse IgG, none of the membrane marker proteins were detectable (Fig. 5A). To confirm that, as indicated by the fractionation (Fig. 4A), not only Ago2 but also the RISC and RLC factors associate with the ER, HeLa cells were subjected to sedimentation gradients optimized for purification of ER membranes (Fig. 5B). The fractions containing the membranes of the rough ER (fractions 8-10) were pooled and used for a membrane IP specific for the ER membrane protein calnexin (Fig. S4A). Strikingly, Ago2, TRBP and Dicer were all present in the eluate from the anti-calnexin membrane IP, indicating that the factors constituting RLC and RISC associate with the rough ER membrane. Consistently, it has been shown by immune fluorescence that TRBP co-localizes with the ER (Eckmann and Jantsch, 1997), and that TRBP and Dicer co-localize predominantly in the perinuclear region in HeLa cells (Daniels *et al.*, 2009). As additional control, anti-Golgi membrane IPs were performed with the fractions containing Golgi membranes (fractions 2-4). Neither Ago2, nor Dicer, nor TRBP were enriched in the Golgi IP eluate compared to the IgG negative control IP (Fig. S4A). Altogether, these data provide strong evidence that RLC and siRISC are bound to the cytosolic surface of the rough ER membrane.

siRNA – mediated target mRNA cleavage occurs on the rER

After having found that siRNA loaded Ago2 floats with membranes, that Ago2 associates specifically with the ER membrane, and that siRNA loaded Ago2 as well as the slicing product co-fractionate with ER as well as Golgi markers, we wanted to further refine at which of these compartments siRNA mediated target cleavage occurs. HeLa cells tranfected with SSB, HuR and pGL3 siRNAs were subjected to sedimentation gradients optimized for purification of ER membranes. In these gradients, Golgi membranes were enriched in fractions 2-4, membranes of the smooth ER in fractions 5-7 and membranes of the rough ER (rER), revealed by the additional presence of the ribosomal protein RPS6, in fractions 8-10 (Fig. 5B). In agreement with the fractionation data in Fig. 1A, also after separation of Golgi from ER factions, Ago2 and Dicer indeed co-sedimented with both membranes (Cikaluk *et al.*, 1999;Tahbaz *et al.*, 2001). Interestingly, Ago1 and Ago2 were most abundant in the fractions of the rER, whereas Dicer peaked in the Golgi fractions. Consistently, Dicer had previously been observed to co-localize with Golgi and ER in rat primary neurons (Barbato et al., 2007). TRBP and PACT again showed a very confined localization and co-sedimented exclusively with the rER, in consistence with early work in *X. laevis* reporting cytoplasmic TRBP to localize to the ER and/or polysomes (Eckmann *et al.*, 1997). Again, the bulk siRNA fractionated broadly throughout the gradient (Fig. S4B). After IP of Ago2 from the fractions however, we observed two distinct pools of siRNA loaded Ago2, the major population co-sedimenting with the rER (Fig. 5C). A second, minor pool of siRISC was detected in fractions containing not only Golgi membranes but also the P-body marker Dcp1, which, in these gradients peaks together with the Golgi markers. In fact, in light of the absence of significant Golgi association as determined by Ago2 membrane IPs (Fig 5A), it appears more plausible that this second minor population of siRISC is P-body rather than Golgi associated. Interestingly, the non-targeting pGL3 siRNA loaded into Ago2 also co-sedimented predominantly with rER, identical to the targeting siRNAs (Fig. 5C, HuR and SSB), further supporting that this fractionation is independent of a target mRNA and not dependent on polysomes. We next wanted to address whether these two spatially separated siRISC pools represent functionally different complexes or complexes of different maturation state. As, *ex vivo*, both pools of immune purified Ago2 were competent of *in vitro* mRNA slicing we concluded that both complexes comprise mature siRISC (Yoda et al., 2010), i.e. slicing competent RISC with single stranded guide siRNA (Fig. S4C). As this does not necessarily imply that alike *ex vivo*, slicing indeed occurs in both compartments within the cell, we again performed 5'RACE on all fractions to detect the endogenous slicing product. Strikingly, the endogenous mRNA cleavage product co-sedimented exclusively with membranes of the rER (Fig. 5D), strongly suggesting that the site of endogenous mRNA silencing, at least for siRNA, is the rER.

Canonical RISC loading occurs at the rER

We next aimed to address whether the rER is also the site of RISC loading, or whether instead the additional, minor Golgi/P-body population of siRNA-Ago2 might account for complexes engaged in loading. The canonical RLC was proposed to comprise Ago2, Dicer and TRBP (Chendrimada *et al.*, 2007;Gregory *et al.*, 2005;MacRae *et al.*, 2008;Maniataki *et al.*, 2005;Noland *et al.*, 2011). We have shown that all three proteins float with membranes (Fig. 4A), and can be pulled down in a membrane IP with an ER membrane protein (Fig. S4A). Furthermore, TRBP does exclusively co-fractionate with the rER, and also Ago2 and Dicer partially co-fractionate with the rER (Fig. 5B). This supports that a canonical RLC may form on the rER rather than at Golgi or P-bodies where TRBP and PACT are absent. To further corroborate this hypothesis, lysates of siRNA transfected HeLa cells were subjected to a Golgi/ER gradient as in Fig. 5B. For qPCR detection sensitivity reasons of the passenger strand, we focused on the HuR siRNA rather than the SSB siRNA in these experiments. After pooling each, the Golgi/P-body fractions (2-4) as well as the rER fractions (8-10), immune precipitations for TRBP, Dicer and Ago2 were performed (Fig. 5E). In the TRBP and Dicer IPs, both guide as well as passenger strand of the HuR siRNA were detectable in the rER fractions, suggesting that TRBP and Dicer are associated with double stranded siRNA in these fractions. Consistent with the Ago2 IPs from the other gradients, Ago2 bound HuR siRNA guide strand was again detectable in both the Golgi/P-body as well as in the rER fractions, however, the Ago2 associated passenger strand was clearly enriched in the rER fraction. Moreover, despite the dramatically higher amounts of Dicer in the Golgi/P-body fractions, neither guide nor passenger strand were detectable in this pool but clearly enriched in Dicer immune precipitates from the rER fractions. Together, these data strongly suggest that the rER fractions comprise both, mature siRISC as well as full RLC associated with double stranded siRNA (and potentially single stranded siRNA as well), whereas the Golgi/P-body pool of loaded Ago2 consists to > 98 % of mature siRISC with guide strand only, as well as non-siRNA associated Dicer.

To further corroborate this conclusion, we wanted to rule out the possibility that the detected HuR sense strand in the eluates resulted from sense strand misloaded as guide rather than siRNA duplex. While bioinformatic analysis supported a high asymmetry and therefore antisense strand selectivity for the HuR siRNA (data not shown), we additionally designed a Firefly/Renilla dual luciferase reporter containing either the target site of the antisense or the sense strand in the 3' UTR, and co-transfected these plasmids together with the HuR siRNA into HeLa cells. With an IC_{50} of 0.2 nM the passenger strand was more than 1000-fold less active than the guide strand which had an IC_{50} of 0.1 pM (Figs. 5F and S4D), confirming that strand selection for this siRNA is highly biased to the antisense strand and that loading of sense strand as guide can be neglected.

Therefore we conclude that Ago2 in the rER fractions is indeed partially associated with double stranded siRNA and comprises not only mature siRISC but also complexes engaged in loading, i.e. a “pre-RISC state” (Czech and Hannon, 2011;Kawamata and Tomari, 2010). Altogether, this data suggests that also canonical RISC loading of Ago2 through Dicer and TRBP/PACT occurs at the membranes of the rER.

Membrane anchoring of RISC is dependent on TRBP and PACT

Given that TRBP and PACT did co-sediment with Golgi and ER membranes, we speculated that Ago2 might be anchored to the membranes (potentially indirectly) via TRBP and PACT. We thus depleted TRBP or PACT by RNAi (Fig. S5A), and subjected the post nuclear lysates to membrane floatation assays. The Ago2 protein levels were similar in control cells and in the cells with TRBP or PACT knock-down (Fig. S5A), but in contrast to the RNAseA treated lysates (Fig. 4D), the amount of membrane associated Ago2 was strongly reduced after TRBP depletion and completely abolished after PACT depletion (Fig. 6A). Additionally, in a membrane IP with antibodies against Ago2, the amount of co-eluted marker proteins for the ER and ribosomes were reduced when TRBP or PACT were depleted as compared to mock treated cells (Fig. S5B). Interestingly, the smaller effect of TRBP knockdown on Calnexin association with Ago2 as compared to the more dramatic effect upon PACT knockdown mirror images the efficiency of the knockdown of the two proteins. This data suggests that Ago2 associates with membranes through TBRP and PACT, most plausibly indirectly through the complex of TRBP and PACT with Dicer.

Nucleation of RISC loading and mRNA slicing at the rER membrane is important for kinetic and thermodynamic efficiency of RNAi

Results from previous publications about whether TRBP and PACT are required for siRNA-mediated RNA silencing are contradictory (Haase *et al.*, 2005;Kok *et al.*, 2007). Given that as little as 10-110 molecules of siRISC per cell are sufficient for 50 % knock-down of three different, relatively abundant mRNAs (Fig. 2B and Fig. S2N-P), but that the onset of RNAi after transfection is extremely fast, we reasoned that the sequestration of active Ago2 to membranes may be responsible for accelerating the silencing kinetics. This would imply that TRBP and/or PACT as membrane anchors may not be qualitatively required for RNAi but might rather play a main role in the quantitative efficiency and particularly the kinetics of the onset of silencing. To test this hypothesis, we transfected the SSB siRNA into TRBP/PACT RNAi depleted versus mock treated cells. Consistent with our hypothesis, the onset of SSB mRNA knockdown was clearly delayed when TRBP or PACT had been depleted (Fig. 6B). After 24 hours, also in TRBP/PACT depleted cells knockdown had caught up to reach saturation, most likely explaining why

TRBP and PACT had not been found to be essential for RNAi in earlier reports. In addition, we tested whether perturbation of directional cytoskeleton-dependent cell transport to the ER would result in a similar delay in the onset of silencing. HeLa cells were pre-treated for 2 hours with Nocodazole (5 μg/ml) prior to transfection with the SSB siRNA, and knockdown was quantified at various time points after transfection by RT-qPCR (Fig. 6C). Indeed, the onset of silencing was delayed. While this is again consistent with subcellular localization being important for the kinetic efficiency of RNAi, cytoskeleton perturbation is a rather harsh treatment which may also indirectly impair RNA silencing. We therefore hypothesized that a strategy to enhance RNAi by perturbation of anterograde transport and the resulting general accumulation and concentration of material at the ER by Brefeldin A treatment might allow addressing this question more specifically. Indeed, Brefeldin A pre-treatment (10 μg/ml) resulted in the opposite effect and accelerated and increased SSB mRNA knockdown as compared to the DMSO control (Fig. 6C). Interestingly, the IC_{50} of the SSB siRNA was additionally shifted to lower concentrations, resulting in an approximately 10-fold higher siRNA efficiency at 24 hours (Fig. S5D). Altogether these data show that nucleation of RISC loading and mRNA slicing at the ER membrane is not qualitatively essential but physiologally important for the kinetics and efficiency of this process.

Discussion

In this work we have demonstrated that Ago2 associates to the cytosolic side of the rER, that loaded and active Ago2 is mostly membrane associated, and that the slicing product as well as mature siRISC co-sediment with the rER. Additionally, also RLC bound to double-stranded siRNA is enriched at the rER. Our data therefore strongly suggests a model where canonical RISC loading of Ago2 through Dicer and TRBP/PACT, encounter of RISC with target mRNA as well as siRNA-mediated mRNA slicing all occurs primarily at the cytosolic membrane surface of the rER (Fig. 7A). Altogether these data show that the compartmentalization and thereby the nucleation of RISC loading and mRNA slicing at the ER membrane is physiologally important for the kinetics and efficiency RNAi. While genomic analysis confirms the general textbook view that stable association and translation of mRNAs at the ER correlates well with predicted motifs for protein secretion or membrane anchoring (Diehn et al., 2006), it has also been shown that most mRNAs at least transiently associate with the ER during their lifecycle (Chen *et al.*, 2011;Gerst, 2008;Lerner *et al.*, 2003). Given the high dynamics of peripheral ER, the nucleation site of siRNA-mediated silencing being on the cytosolic side of the rER membrane seems not at all incompatible with silencing of mRNAs of soluble proteins. Rather, this localization provides the ER-bound RISCs a privileged predisposition to dynamically sample over translationally active mRNAs. As an important note, based on our data we

cannot exclude that silencing would not function in other sites of the cell as well; however, from a quantitative point of view, compartmentalization of the initial steps of RNA silencing at endomembranes, and in particular at the rER is absolutely plausible given that only few molecules of active RISC per cell are sufficient to silence even relatively abundant mRNAs within less than one hour upon initial cell exposure to siRNA. Such efficiency would be thermodynamically and kinetically implausible if all partners were homogeneously distributed throughout the cytosol. As a side observation, our findings are also consistent with the site at which the hepatitis C virus (HCV) replicates using RISC components. HCV forms a replication complex in a membranous web derived from the rER, and requires both Ago2 and miR-122 for efficient replication (Jopling *et al.*, 2005;Wilson *et al.*, 2011).

Previous investigations have largely been focused on localization and tracing of overexpressed bulk RNAi pathway proteins, miRNA or siRNA. In this work we show that after lipid delivery and endosomal entry of siRNA into mammalian cells, the lion's share gets cleared within a few hours and a very small fraction (<< 0.25-0.1%) is eventually loaded into Ago2 (Fig. 7B). As the small number of active siRISC molecules per cell is masked by such a huge excess of both, nonproductive siRNA as well as additional pools of Ago2, in this work we aimed to specifically trace functional RISCs and RNAi activity, which might explain the partially different conclusions compared to previous reports (Jagannath *et al.*, 2009;Liu *et al.*, 2005;Sen *et al.*, 2005). In a previous study which used fluorescence cross correlation spectroscopy to also explicitely trace the minute fraction of siRNA-Ago2 complexes on the massive background of bulk Ago2 and siRNA (Ohrt et al., 2008), cytoplasmic siRISC showed a slow translational diffusion time either reflecting a very large complex and/or confined movement, generally supporting a (dynamic) membrane anchoring of loaded RISC. Furthermore, our findings are also fully consistent with a recent report which shows that membrane association of Ago1 in *A. thaliana* is required for miRNA activity (Brodersen et al., 2012).

After initial encounter and endonucleolytic cleavage of the target mRNA by Ago2 at the rER, the sliced mRNA (or silenced miRNP) may likely be taken up by P-bodies to facilitate the degradation of the mRNA. This would be consistent with the repeated detection of siRNA as well as Ago2 and particularly Ago2-GFP in P-bodies (Jagannath *et al.*, 2009;Leung *et al.*, 2006;Liu *et al.*, 2005;Ohrt *et al.*, 2008;Sen *et al.*, 2005), as well as the notion that P-bodies, while clearly involved in RNAi, are rather a consequence than cause of silencing. Interestingly, life cell microscopy supports a transient and dynamic association of Ago2-GFP, which is known to be primarily P-body associated, with the ER (Movie S1). Also, "consumed" RISC may dissociate from the mRNP after slicing and recycle back to the rER via the Golgi, and the second minor pool of mature siRISC which we detect in the Golgi/P-body fractions might reflect either of these possible downstream steps (Fig. 5C).

At least two studies have implicated membranes of the endo-/lysosomal system as important sites in the RNA silencing pathways in mammalian cells and flies (Gibbings *et al.*, 2010;Gibbings *et al.*, 2009;Lee *et al.*, 2009). These studies reported that GW bodies, membrane enclosed granules rich in GW182/Tnrc6, miRNAs, and Ago proteins are MVB associated. Blocking MVB turnover enhanced, whereas blocking MVB maturation inhibited miRNA mediated target mRNA silencing, indicating that MVBs and GW bodies are functionally involved in miRNA-mediated RNA silencing. As also RISC loading was enhanced upon inhibiting MVB turnover by Hps4 knock-down (Lee et al., 2009), the authors argued that MVBs might also be sites of RISC diassembly and, possibly RISC loading. However, the increased levels of loaded RISC might as well be an indirect consequence of enhanced RISC disassembly upon impaired MVB turnover, which would facilitate recycling to and *de novo* loading at another site. In light of our data it seems plausible that endo/lysosomal compartments rather play a role downstream of RISC loading. While our data shows that canonical RISC loading, initial RISC-mRNA binding and slicing happen at the rER, the siRNPs or miRNPs may then likely be sorted into different effector compartments for downstream events such as mRNA degradation in P-bodies or translational silencing in MVBs and MVB-associated GW bodies, and that consumed RISC is continuously recycled back from such effector sites to the rER as the primary nucleation site of RNAi. This model not only reconciles much of the apparently controversial evidence in the literature, but most importantly may now enable the rational design of a new generation of therapeutic siRNA delivery strategies.

Methods

Cell culture, transfections and Plasmids

HeLa cells were grown in RPMI (Invitrogen) supplemented with 10 % fetal bovine serum. For transfections, 2 x 10^5 or 1-2 x 10^6 cells were seeded into six well plates or 10 cm^2 dishes, respectively, and transfected the next day. siRNAs were transfected with Lipofectamine 2000 (Invitrogen) according to the manufacturer's protocol. For TRBP or PACT knock-downs, HeLa cells were transfected in 10 cm^2 dishes with 25 nM siRNA, and re-transfected with 25 nM siRNA 24 hours later. The cells were used for the experiments 48 – 96 hours after the first transfection. For luciferase reporters, a 1.2 kb fragment of the HuR mRNA starting at position +1 of the 3'UTR comprising the HuR siRNA binding site (position 1186 in GenBank acession number NM001419) in either sense or antisense orientation was generated by gene synthesis and cloned into the XhoI and NotI sites of psiCHECK-2 plasmids (Promega).

Luciferase assays

7000 HeLa cells/well were seeded into 96 well plates. The next day, 50 ng psi-Check2 plasmid was co-transfected with siRNA using Lipofectamine 2000 (Invitrogen) and 24 hours later renilla and firefly luciferase activities were measured using the Dual Luciferase Assay System from Promega on a GloMax®-Multi+ Microplate Multimode Reader (Promega) according to manufacturer's protocol.

siRNAs and Antibodies

The siRNAs have the following sequences:

SSB (guide: 5'- UUACAUUAAAGUCUGUUGUUU -3';
passenger 5'- ACAACAGACUUUAAUGUAAUU -3'),
HuR (guide: 5'- UUAAUUAUCUAUUCCGUACTT -3';
passenger 5'- GUACGGAAUAGAUAAUUAATT -3'),
pGL3 (guide: 5'- UCGAAGUACUCAGCGUAAGUU -3';
passenger 5'- CUUACGCUGAGUACUUCGAUU -3'),
SSB(53) (guide: 5'- CCUUUGUAAUAUGAGAAUGUU;
passenger: 5'- CAUUCUCAUAUUACAAAGGUU-3'),
GAPDH (guide: 5'- 5'GGCCAUCCACAGUCUUCUGdGdG -3';
passenger: 5'- CAGAAGACUGUGGAUGGCCdTdT-3';),
Renilla (guide: 5'- UCGAUGAACAUCUUAGGCATT -3';
passenger 5'- UGCCUAAGAUGUUCAUCGATT -3'),
YFP (guide: 5'- CUUGUCGGCCAUGAUAUAGAC -3';
passenger 5'- CUAUAUCAUGGCCGACAAGTT -3').

TMR labeled HuR siRNA was labeled via a 5'terminal amino-C6 linker at the guide strand (Eurogentec). ON-TARGETplus SMARTpool siRNAs (Dharmacon) were used to deplete TRBP (L-017430-00) or PACT (L-006426-00).

Antibodies against Ago2 (clone 11A9 or 4G8) were from Ascenion or Wako Chemicals, antibody against Ago1 (clone 4B8) was from Ascenion. Antibodies against Hrs (ab56468), Rab5 (ab18211), tsg101 (ab83), lamp2 (ab25631), calnexin (ab22595), Dcp1a (ab47811), TRBP (ab42018) were from Abcam, and antibodies against calreticulin (A301-130A), RPS6 (A300-557A), PACT (A302-016A) and Dicer (A301-936A) were from Bethyl laboratories. Antibodies against p58 (sc-66880), GM130 (sc-16268) were from Santa Cruz, antibodies against b4-GalT1 (HPA010807) were from Atlas antibodies and antibodies against SmB (S0698) were from Sigma. A rabbit antibody against dicer was described previously (Haase et al., 2005).

Immune precipitations

Magnetic protein G sepharose beads (GE Healthcare) were incubated at 4 °C with saturating amounts of antibody for 2 h or over night. Unless stated differently, 15 mg anti-Ago2 antibody was coupled to 10 µl beads in a total volume of IP buffer (0.1 % v/v Nonidet-P40, 100 u/ml RNasIn (Promega), 0.5 mM DTT, 20 mM TrisHCl 7.4, 150 mM NaCl, 1 mg/ml heparin and complete EDTA-free protease inhibitor (Roche)). For the Ago2-IP in Figure 2, 22.5 mg anti-Ago2 antibody was coupled to 20 ul beads. For whole cell extracts cells were incubated in lysis buffer (20 mM TrisHCl 7.4, 150 mM NaCl, 0.5 % v/v NP-40, 2 mM EDTA, 1 mg/ml heparin, 2.5 mM DTT, 500 u/ml RNAsin (Promega) and Complete™ EDTA-free protease inhibitor (Roche)) and centrifuged at 1000 g for 5 min. For sucrose gradient fractions, 200 µl from each fraction were incubated with lysis buffer. For the IP in Figure S2F/G, 11.25 mg anti-Ago2 antibody was coupled to 10 µl beads, then 2 µM recombinant Ago2 was together with 5 µM 3'TMR HuR guide strand. Immune precipitations were rotated head over tail for 2-4 h at 4 °C in IP buffer. Beads were washed twice with IP wash buffer (50 mM TrisHCl 7.4, 300 mM NaCl, 5 mM $MgCl_2$, 0.05 % v/v NP-40). Proteins were eluted by incubating the beads for 10 in at 70 °C in SDS loading buffer. For small RNA elution, beads were incubated for 10 min at 95 °C in elution buffer (6 mM TCEP (tris(2-carboxyethyl)phosphine), 1 mM HCl, 1 % v/v Triton X-100). For *in vitro* slicing reactions, beads were incubated for 45 min at 37 °C with 1 µM target RNA (5'-Cy3-ACCGUCUAACAACAGACUUUAAUGUAAUUGUGGAA-3') in RLC buffer (20 mM TrisHCl 7.4, 50 mM NaCl, 3 mM $MgCl_2$, 2 mM DTT, 0.5 mg/ml tRNA, 2 u/µl RNAsin (Promega)). Slicing products were separated on 15 % denaturing polyacrylamide TBE urea gels and visualized using a Pharos FX (Biorad).

For membrane IPs with post-nuclear supernatants, cells were incubated for 18 h at 37 °C with cytochalasinD (10 µM) and nocodazole (13 µM), trypsinized and washed with PBS pH 7.2 (Invitrogen), and incubated in hypotonic buffer for 10 min on ice. Cells were then lysed similar as for sucrose gradients (20 strokes, 12 µm tungsten ball). Lysates were cleared for 5 min at 500 g, and the supernatant was incubated with 15 µg antibody for 2.5 h at 4 °C in PBS pH 7.2 supplemented with Complete™ EDTA-free protease inhibitor (Roche), cytochalasinD (25 µM) and nocodazole (33 µM), and respectively 0.4 % v/v NP-40 for the control sample. 25 ul ProteinG dynabeads (Invitrogen) were blocked with 2.5 % w/v bovine serum albumine (BSA) in PBS pH 7.2, and antibody-protein complexes were captured for 30 min at 4 °C. Beads were washed three times with IP wash buffer (without Nonidet P-40), and proteins were eluted by incubating the beads for 5 min at room temperature with 0.4 % v/v Nonidet P-40 in PBS pH 7.2. For membrane IPs out of sucrose gradients, 200 µl of the fractions were used as input, and the IP was performed with 5 µg antibody in the absence of nocodazole and cytochalasinD.

Immune blotting and RT-qPCR

Whole cell lysates corresponding to 1-2 x 10^5 cells per lane or aliquots of sucrose gradient fractions or immune precipitations were heated for 10 min at 70 °C and electrophoresed on 4-12 % NuPage gels (Invitrogen). Proteins were transferred to Protran nitrocellulose membranes (Whatman) using a SD Transblot system (BioRad) and incubated with primary antibodies. Immune complexes were visualized using HRP-conjugated anti-rabbit, anti-mouse, anti-goat and anti-rat antibodies (Santa Cruz) on a Biorad XRS system.

For mRNA quantifications, total RNA was isolated using the RNeasy Plus kit (Qiagen). One Step RT-qPCR reactions were performed using 40 ng RNA, 1 mM dNTPs, 0.5 U Multiscribe reverse transcriptase (Applied Biosystems), 0.03 U FastStart Taq polymerase (Roche) in GeneAmp PCR buffer I (Applied Biosystems). Samples were heated to 50 °C for 30 min, then 95 °C for 10 min, and then cycled 40 times with 3 sec at 95 °C and 30 sec at 50 °C on a 7900HT Fast RT-qPCR System (Applied Biosystems). SSB and GAPDH mRNA were measured using Assay-on-demand reagents from Applied Biosystems (hs00427601_m1 and 4333764, respectively). For small RNA quantifications an adapted RT-qPCR protocol from (Pei et al., 2010) was used.

Sucrose sedimentation gradients

2-4 confluent 10 cm^2 dishes with HeLa cells were used for each gradient. Cells were washed with PBS pH 7.2, then incubated for 10 min at 4 °C in hypotonic buffer (HB; 10 mM Tris pH8, 10 mM KCl, 1.5 mM $MgCl_2$, 10 mM DTT, 1x complete EDTA-free protease Inhibitors (Roche), 400 u/ml RNasIn (Promega)) and then lysed with 20 strokes in a cell homogenizer (Isobiotec) using the 12 □m tungsten ball. Lysates were cleared for 5 min at 500 g, and the supernatant was loaded on top of a previously prepared continuous sucrose gradient. To generate the gradients, sucrose dissolved in HB was overlaid and frozen between each step, then the gradient was thawed over night at 4 °C to allow the formation of a continuous gradient. The gradient was centrifuged for 16 hours at 100'000 g at 4 °C in a Beckman Optima Max, and fractions were collected from the top.

Membrane floatation assays

Membrane floatation assays were essentially performed as described elsewhere (Tahbaz et al., 2004). Sucrose solutions and cell lysates were prepared as for the sucrose sedimentation gradients.

Immune cytochemistry

Immune cytochemistry was essentially performed as described elsewhere (Stalder and Muhlemann, 2009). Briefly, 0.5 – 1.5 x 10^5 HeLa cells were seeded into an □ – slide VI0.4 (Ibidi). The next day, the cells were washed with PBS, fixed

for 30 min at 37 °C in DSS-IF-buffer (PBS pH 7.2 containing 2 mM $MgCl_2$, 10 % v/v glycerol, 0.5 mM disuccinimidyl suberate (DSS, Pierce)), and subsequently washed five times with DSS-IF-buffer without DSS and permeabilized for 20 min with PBS pH 7.2 containing 0.2 % v/v Triton X-100 and 0.2 M glycine. The cells were incubated for 30 min with Signal-iT FX Signal Enhancer (Invitrogen), washed with PBS containing 0.15 % w/v BSA and incubated with primary antibodies for 1 hour at room temperature. The cells were then washed five times with PBS containing 0.15 % BSA and incubated with primary antibodies for 1 hour at room temperature and washed five times with PBS containing 0.15 % BSA. Anti-rat AlexaFluor488 (Molecular Probes) and anti-rabbit or anti-mouse AlexaFluor647 (Molecular Probes) were used as secondary antibodies, images were taken on a Zeiss LSM710 confocal microscope with a 63x W 1.2 NA objective.

Life cell imaging

HeLa cells were seeded into an 8 well -slide (Ibidi) and at 60 % confluency transfected with 12 nM 5'TMR-labeled HuR siRNA (guide strand, Eurogentec) using Lipofectamine 2000 according to manufacturer's protocol. To stain the endosomes or lysosmes, Alexa Fluor 647 labeled transferrin (2.5 M) or lysotracker green (10 M, Invitrogen) were added 30 min before the images were taken. Images were acquired on a confocal LSM710 microscope with GaAsp-detector (Zeiss) with a 100x oil 1.4 NA objective and temperature, gas and humidity control unit (Life Imaging Services) and analyzed with Imaris64 (Bitplane).

5'RACE

Total RNA was isolated from the sucrose gradient fractions with Trizol LS (Invitrogen). 5' RACE was performed with the Generacer kit (Invitrogen) according to the manufacturer's protocol. The following primers were used: RT-primer and first PCR primer (5'-GGCCAGGGGTCTCTACAAAT -3'), nested reverse (5'-AGAGTTGCATCAGTTGGGAAG -3').

Fluorescence anisotropy measurements.

Binding of HuR siRNA or miR-122 to recombinant Ago2 as well as off rates were measured with anisotropy determination by 2D-FIDA as described elsewhere (Kask *et al.*, 2000;Meisner *et al.*, 2004). For binding curves, 1 nM of 5'TMR labeled miR-122 (5'TMR-UGGAGUGUGACAAUGGUGUUUG, EuroGentec) or HuR siRNA (5'- UUAAUUAUCUAUUCCGUACTT -3') was incubated with increasing concentrations of recombinant human full length Ago2 protein for at least 15 minutes at room temperature (23 °C) in a buffer of PBS pH 7.2, 0.1 % (w/v) Pluronic F-127 (Molecular Probes), 1 mM $MgCl_2$ and 1 mM DTT. 2D-FIDA measurements and anisotropy calculations were done as described previously (Meisner *et al.*, 2004). Samples of Ago2 loaded 5'TMR HuR siRNA before and after

IP were measured under the same conditions. For off rate measurements, 1 nM of 5'TMR labeled miR-122 was incubated with hAgo2 at 2.6 ?M (corresponding to 95 % complex formation according to the affinity determination) for 10 minutes. Unlabeled competitor guide (5'phosphorylated miR-16, UAGCAGCACGUAAAUAUUGGCG, Eurogentec) was added at 10 ?M and the 2D-FIDA measurement was started, whereas the exact delay time between the addition of the competitor and the start of the measurement was taken with a chronometer. All curve fits were done by nonlinear regression in GraFit as described (Meisner *et al.*, 2004). Off rates were fitted to a pseudo first order mono-exponential decay, binding curves were fitted to the equation describing the anisotropy in dependence of 1:1 complex formation.

Data analysis

All data are representatives from at least two to three independent experiments. Unless stated otherwise, error bars represent standard deviations from at least three technical replicates of one representative biological experiment. Nonlinear curve fitting was performed using GraFit 5.0. For absolute quantification of siRNA and siRISC molecule numbers per cell, cells used per IP were counted and related to the amount of siRNA in the whole IP, which was extrapolated from the siRNA amount in the RT-qPCR reaction with calibration to an external synthetic siRNA standard. Based on the combined errors of all steps, the overall accuracy of this analysis lies within a factor of ca 2-3.

References

1. Barbato C, Ciotti MT, Serafino A, Calissano P, and Cogoni C (2007) Dicer expression and localization in post-mitotic neurons. *Brain Res,* **1175,** 17-27.
2. Brodersen P, Sakvarelidze-Achard L, Schaller H, Khafif M, Schott G, Bendahmane A, and Voinnet O (2012) Isoprenoid biosynthesis is required for miRNA function and affects membrane association of ARGONAUTE 1 in Arabidopsis. *Proc Natl Acad Sci U S A,* **109,** 1778-1783.
3. Carthew RW and Sontheimer EJ (2009) Origins and Mechanisms of miRNAs and siRNAs. *Cell,* **136,** 642-655.
4. Chen Q, Jagannathan S, Reid DW, Zheng T, and Nicchitta CV (2011) Hierarchical regulation of mRNA partitioning between the cytoplasm and the endoplasmic reticulum of mammalian cells. *Mol Biol Cell,* **22,** 2646-2658.
5. Chendrimada TP, Finn KJ, Ji X, Baillat D, Gregory RI, Liebhaber SA, Pasquinelli AE, and Shiekhattar R (2007) MicroRNA silencing through RISC recruitment of eIF6. *Nature,* **447,** 823-828.
6. Chu CY and Rana TM (2006) Translation repression in human cells by microRNA-induced gene silencing requires RCK/p54. *PLoS Biol,* **4,** e210.
7. Cikaluk DE, Tahbaz N, Hendricks LC, DiMattia GE, Hansen D, Pilgrim D, and Hobman TC (1999) GERp95, a membrane-associated protein that belongs to a family of proteins involved in stem cell differentiation. *Mol Biol Cell,* **10,** 3357-3372.
8. Czech B and Hannon GJ (2011) Small RNA sorting: matchmaking for Argonautes. *Nat Rev Genet,* **12,** 19-31.
9. Daniels SM, Melendez-Pena CE, Scarborough RJ, Daher A, Christensen HS, El FM, Purcell DF, Laine S, and Gatignol A (2009) Characterization of the TRBP domain required for dicer interaction and function in RNA interference. *BMC Mol Biol,* **10,** 38.
10. Diehn M, Bhattacharya R, Botstein D, and Brown PO (2006) Genome-scale identification of membrane-associated human mRNAs. *PLoS Genet,* **2,** e11.
11. Eckmann CR and Jantsch MF (1997) Xlrbpa, a double-stranded RNA-binding protein associated with ribosomes and heterogeneous nuclear RNPs. *J Cell Biol,* **138,** 239-253.
12. Eulalio A, Behm-Ansmant I, and Izaurralde E (2007a) P bodies: at the crossroads of post-transcriptional pathways. *Nat Rev Mol Cell Biol,* **8,** 9-22.
13. Eulalio A, Behm-Ansmant I, Schweizer D, and Izaurralde E (2007b) P-body formation is a consequence, not the cause, of RNA-mediated gene silencing. *Mol Cell Biol,* **27,** 3970-3981.
14. Gerst JE (2008) Message on the web: mRNA and ER co-trafficking. *Trends Cell Biol,* **18,** 68-76.
15. Gibbings D and Voinnet O (2010) Control of RNA silencing and localization by endolysosomes. *Trends Cell Biol,* **20,** 491-501.
16. Gibbings DJ, Ciaudo C, Erhardt M, and Voinnet O (2009) Multivesicular bodies associate with components of miRNA effector complexes and modulate miRNA activity. *Nat Cell Biol,* **11,** 1143-1149.
17. Gregory RI, Chendrimada TP, Cooch N, and Shiekhattar R (2005) Human RISC couples microRNA biogenesis and posttranscriptional gene silencing. *Cell,* **123,** 631-640.
18. Haase AD, Jaskiewicz L, Zhang H, Laine S, Sack R, Gatignol A, and Filipowicz W (2005) TRBP, a regulator of cellular PKR and HIV-1 virus expression, interacts with Dicer and functions in RNA silencing. *EMBO Rep,* **6,** 961-967.
19. Huizing M, Anikster Y, and Gahl WA (2000) Hermansky-Pudlak syndrome and related disorders of organelle formation. *Traffic,* **1,** 823-835.
20. Iki T, Yoshikawa M, Nishikiori M, Jaudal MC, Matsumoto-Yokoyama E, Mitsuhara I, Meshi T, and Ishikawa M (2010) In vitro assembly of plant RNA-induced silencing complexes facilitated by molecular chaperone HSP90. *Mol Cell,* **39,** 282-291.
21. Iwasaki S, Kobayashi M, Yoda M, Sakaguchi Y, Katsuma S, Suzuki T, and Tomari Y (2010) Hsc70/Hsp90 Chaperone Machinery Mediates ATP-Dependent RISC Loading of Small RNA Duplexes. *Mol Cell*.

22. Jagannath A and Wood MJ (2009) Localization of double-stranded small interfering RNA to cytoplasmic processing bodies is Ago2 dependent and results in up-regulation of GW182 and Argonaute-2. *Mol Biol Cell,* **20,** 521-529.
23. Jakymiw A, Lian S, Eystathioy T, Li S, Satoh M, Hamel JC, Fritzler MJ, and Chan EK (2005) Disruption of GW bodies impairs mammalian RNA interference. *Nat Cell Biol,* **7,** 1267-1274.
24. Janas MM, Wang B, Harris AS, Aguiar M, Shaffer JM, Subrahmanyam YV, Behlke MA, Wucherpfennig KW, Gygi SP, Gagnon E, and Novina CD (2012) Alternative RISC assembly: binding and repression of microRNA-mRNA duplexes by human Ago proteins. *RNA,* **18,** 2041-2055.
25. Johnston M, Geoffroy MC, Sobala A, Hay R, and Hutvagner G (2010) HSP90 protein stabilizes unloaded argonaute complexes and microscopic P-bodies in human cells. *Mol Biol Cell,* **21,** 1462-1469.
26. Jopling CL, Yi M, Lancaster AM, Lemon SM, and Sarnow P (2005) Modulation of hepatitis C virus RNA abundance by a liver-specific MicroRNA. *Science,* **309,** 1577-1581.
27. Jouannet V, Moreno AB, Elmayan T, Vaucheret H, Crespi MD, and Maizel A (2012) Cytoplasmic Arabidopsis AGO7 accumulates in membrane-associated siRNA bodies and is required for ta-siRNA biogenesis. *EMBO J,* **31,** 1704-1713.
28. Kanellopoulou C, Muljo SA, Kung AL, Ganesan S, Drapkin R, Jenuwein T, Livingston DM, and Rajewsky K (2005) Dicer-deficient mouse embryonic stem cells are defective in differentiation and centromeric silencing. *Genes Dev,* **19,** 489-501.
29. Kask P, Palo K, Fay N, Brand L, Mets U, Ullmann D, Jungmann J, Pschorr J, and Gall K (2000) Two-dimensional fluorescence intensity distribution analysis: theory and applications. *Biophys J,* **78,** 1703-1713.
30. Kawamata T and Tomari Y (2010) Making RISC. *Trends Biochem Sci,* **35,** 368-376.
31. Kok KH, Ng MH, Ching YP, and Jin DY (2007) Human TRBP and PACT directly interact with each other and associate with dicer to facilitate the production of small interfering RNA. *J Biol Chem,* **282,** 17649-17657.
32. Lee YS, Pressman S, Andress AP, Kim K, White JL, Cassidy JJ, Li X, Lubell K, Lim dH, Cho IS, Nakahara K, Preall JB, Bellare P, Sontheimer EJ, and Carthew RW (2009) Silencing by small RNAs is linked to endosomal trafficking. *Nat Cell Biol,* **11,** 1150-1156.
33. Lerner RS, Seiser RM, Zheng T, Lager PJ, Reedy MC, Keene JD, and Nicchitta CV (2003) Partitioning and translation of mRNAs encoding soluble proteins on membrane-bound ribosomes. *RNA,* **9,** 1123-1137.
34. Leung AK, Calabrese JM, and Sharp PA (2006) Quantitative analysis of Argonaute protein reveals microRNA-dependent localization to stress granules. *Proc Natl Acad Sci U S A,* **103,** 18125-18130.
35. Leuschner PJ, Ameres SL, Kueng S, and Martinez J (2006) Cleavage of the siRNA passenger strand during RISC assembly in human cells. *EMBO Rep,* **7,** 314-320.
36. Liu J, Carmell MA, Rivas FV, Marsden CG, Thomson JM, Song JJ, Hammond SM, Joshua-Tor L, and Hannon GJ (2004) Argonaute2 is the catalytic engine of mammalian RNAi. *Science,* **305,** 1437-1441.
37. Liu J, Valencia-Sanchez MA, Hannon GJ, and Parker R (2005) MicroRNA-dependent localization of targeted mRNAs to mammalian P-bodies. *Nat Cell Biol,* **7,** 719-723.
38. Liu Y, Ye X, Jiang F, Liang C, Chen D, Peng J, Kinch LN, Grishin NV, and Liu Q (2009) C3PO, an endoribonuclease that promotes RNAi by facilitating RISC activation. *Science,* **325,** 750-753.
39. Lu JJ, Langer R, and Chen J (2009) A novel mechanism is involved in cationic lipid-mediated functional siRNA delivery. *Mol Pharm,* **6,** 763-771.
40. MacRae IJ, Ma E, Zhou M, Robinson CV, and Doudna JA (2008) In vitro reconstitution of the human RISC-loading complex. *Proc Natl Acad Sci U S A,* **105,** 512-517.
41. Maniataki E and Mourelatos Z (2005) A human, ATP-independent, RISC assembly machine fueled by pre-miRNA. *Genes Dev,* **19,** 2979-2990.
42. Matranga C, Tomari Y, Shin C, Bartel DP, and Zamore PD (2005) Passenger-strand cleavage facilitates assembly of siRNA into Ago2-containing RNAi enzyme complexes. *Cell,* **123,** 607-620.

43. Meisner NC, Hackermuller J, Uhl V, Aszodi A, Jaritz M, and Auer M (2004) mRNA openers and closers: modulating AU-rich element-controlled mRNA stability by a molecular switch in mRNA secondary structure. *Chembiochem,* **5,** 1432-1447.
44. Meister G, Landthaler M, Patkaniowska A, Dorsett Y, Teng G, and Tuschl T (2004) Human Argonaute2 mediates RNA cleavage targeted by miRNAs and siRNAs. *Mol Cell,* **15,** 185-197.
45. Miyoshi K, Tsukumo H, Nagami T, Siomi H, and Siomi MC (2005) Slicer function of Drosophila Argonautes and its involvement in RISC formation. *Genes Dev,* **19,** 2837-2848.
46. Miyoshi T, Takeuchi A, Siomi H, and Siomi MC (2010) A direct role for Hsp90 in pre-RISC formation in Drosophila. *Nat Struct Mol Biol,* **17,** 1024-1026.
47. Noland CL, Ma E, and Doudna JA (2011) siRNA Repositioning for Guide Strand Selection by Human Dicer Complexes. *Mol Cell,* **43,** 110-121.
48. Ohrt T, Mutze J, Staroske W, Weinmann L, Hock J, Crell K, Meister G, and Schwille P (2008) Fluorescence correlation spectroscopy and fluorescence cross-correlation spectroscopy reveal the cytoplasmic origination of loaded nuclear RISC in vivo in human cells. *Nucleic Acids Res,* **36,** 6439-6449.
49. Pare JM, Tahbaz N, Lopez-Orozco J, LaPointe P, Lasko P, and Hobman TC (2009) Hsp90 regulates the function of argonaute 2 and its recruitment to stress granules and P-bodies. *Mol Biol Cell,* **20,** 3273-3284.
50. Pei Y, Hancock PJ, Zhang H, Bartz R, Cherrin C, Innocent N, Pomerantz CJ, Seitzer J, Koser ML, Abrams MT, Xu Y, Kuklin NA, Burke PA, Sachs AB, Sepp-Lorenzino L, and Barnett SF (2010) Quantitative evaluation of siRNA delivery in vivo. *RNA*.
51. Pillai RS, Bhattacharyya SN, Artus CG, Zoller T, Cougot N, Basyuk E, Bertrand E, and Filipowicz W (2005) Inhibition of translational initiation by Let-7 MicroRNA in human cells. *Science,* **309,** 1573-1576.
52. Rand TA, Petersen S, Du F, and Wang X (2005) Argonaute2 cleaves the anti-guide strand of siRNA during RISC activation. *Cell,* **123,** 621-629.
53. Rivas FV, Tolia NH, Song JJ, Aragon JP, Liu J, Hannon GJ, and Joshua-Tor L (2005) Purified Argonaute2 and an siRNA form recombinant human RISC. *Nat Struct Mol Biol,* **12,** 340-349.
54. Rüdel S, Flatley A, Weinmann L, Kremmer E, and Meister G (2008) A multifunctional human Argonaute2-specific monoclonal antibody. *RNA,* **14,** 1244-1253.
55. Sen GL and Blau HM (2005) Argonaute 2/RISC resides in sites of mammalian mRNA decay known as cytoplasmic bodies. *Nat Cell Biol,* **7,** 633-636.
56. Stalder L and Muhlemann O (2009) Processing bodies are not required for mammalian nonsense-mediated mRNA decay. *RNA,* **15,** 1265-1273.
57. Tahbaz N, Carmichael JB, and Hobman TC (2001) GERp95 belongs to a family of signal-transducing proteins and requires Hsp90 activity for stability and Golgi localization. *J Biol Chem,* **276,** 43294-43299.
58. Tahbaz N, Kolb FA, Zhang H, Jaronczyk K, Filipowicz W, and Hobman TC (2004) Characterization of the interactions between mammalian PAZ PIWI domain proteins and Dicer. *EMBO Rep,* **5,** 189-194.
59. Wilson JA, Zhang C, Huys A, and Richardson CD (2011) Human Ago2 is required for efficient microRNA 122 regulation of hepatitis C virus RNA accumulation and translation. *J Virol,* **85,** 2342-2350.
60. Ye X, Huang N, Liu Y, Paroo Z, Huerta C, Li P, Chen S, Liu Q, and Zhang H (2011) Structure of C3PO and mechanism of human RISC activation. *Nat Struct Mol Biol,* **18,** 650-657.
61. Yoda M, Kawamata T, Paroo Z, Ye X, Iwasaki S, Liu Q, and Tomari Y (2010) ATP-dependent human RISC assembly pathways. *Nat Struct Mol Biol,* **17,** 17-23.
62. Zeng Y, Sankala H, Zhang X, and Graves PR (2008) Phosphorylation of Argonaute 2 at serine-387 facilitates its localization to processing bodies. *Biochem J,* **413,** 429-436.

Supplementary Information

Supplemental Information includes five figures and one movie and can be found with this article online at www.emboj.org

Acknowledgements

We thank Julien Bethune, Witold Filipowicz and Larry Gerace for very inspiring discussions, Iwan Beuvink and the NIBR siRNA synthesis team for providing reagents, and Witold Filipowicz for providing reagents and cross reading the manuscript. The authors declare no financial competing interests.

Author contributions

The study was designed by D.M, N.M and L.St. Life cell imaging experiments in Fig. 1D and S1 were performed by W.H, tools for imaging studies were generated by M.H. Luciferase experiments in Fig.5F and Fig.S4 were performed by V.P., luciferase plasmids were cloned by F.A. The Ago2-IPs in Figs. S2F-G were performed by L.S., the experiments for Figs. S2N-P were performed by L.S., D.T. and J.Wi., the halflife measurements in Fig. S2H by P.B. Experiments for Ago2 GFP fractionation were performed by J.H, D.T. and A.F, computational analysis of siRNAs was performed by J.We. All other experiments were performed by L.St. Experiments were performed under supervision of N.M. with consultance of D.M., M.H.

N.M. and L.St. designed the experiments and wrote the manuscript.

Author information

Correspondence should be addressed to nicole.meisner-kober@novartis.com and lukas.stalder@sakk.ch, requests for materials to nicole.meisner-kober@novartis.com.

Figure legends

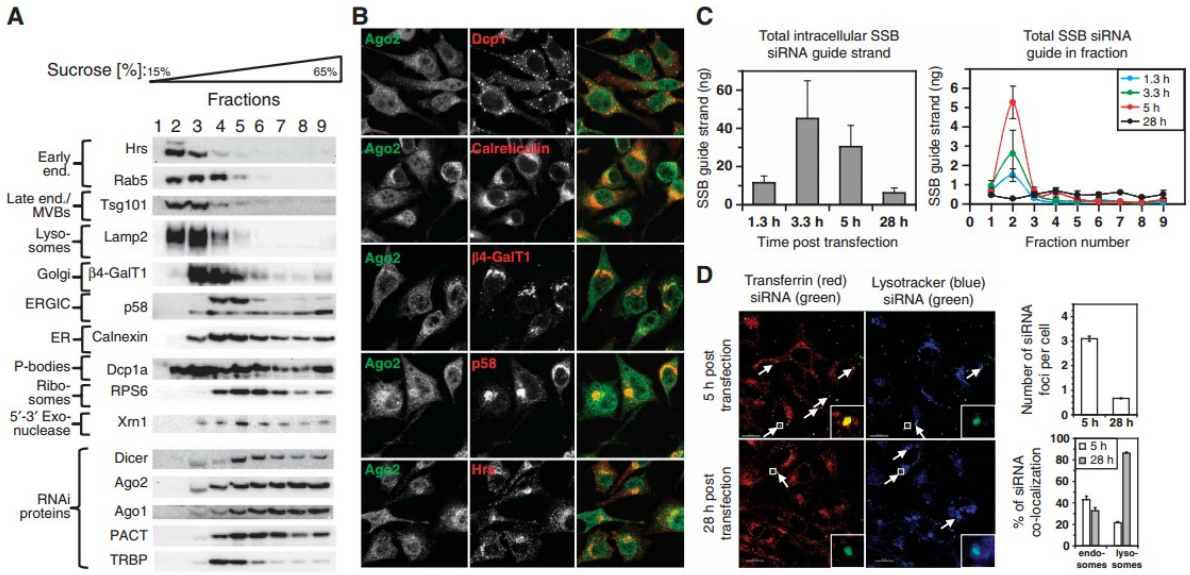

Figure 1 Ago2 and siRNAs localize to a number of different compartments

***a**, Western blot analysis of sucrose gradient fractions. **b**, immune fluorescence of HeLa cells stained with anti-Ago2 and counterstained with antibodies against marker proteins for P-bodies (Dcp1), ER (Calreticulin), Golgi (β4-GalT1), ERGIC (p58), early Endosome (Hrs). Settings were chosen so that no background was detected from cells stained only with secondary antibodies, all images were taken with the same settings. **c**, RT-qPCR Quantification of total intracellular SSB guide strand (left panel) and in the sucrose fractions (right panel) at the indicated timepoints post transfection. **d**, Life cell imaging of HeLa cells transfected with 5'TMR-labeled HuR siRNAs (green) and counterstained with Lysotracker (lysosome marker; blue) or transferrin (endosome marker; red).*

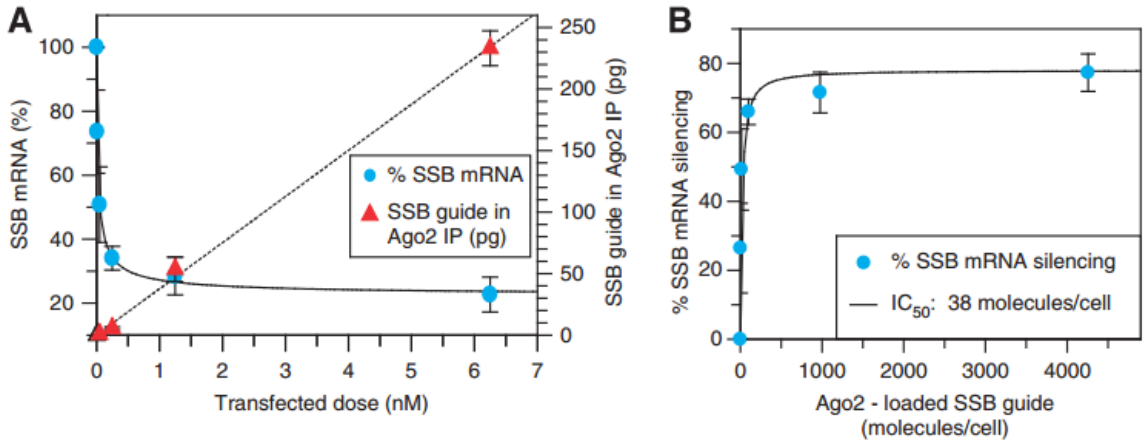

Figure 2 Excess of inactive siRNA masks active population

***a, b**, Ago2 IPs were performed in an quantitative manner 24 h after the HeLa cells were transfected with SSB siRNA. mRNA levels were determined by RT-qPCR from purified total RNA.*

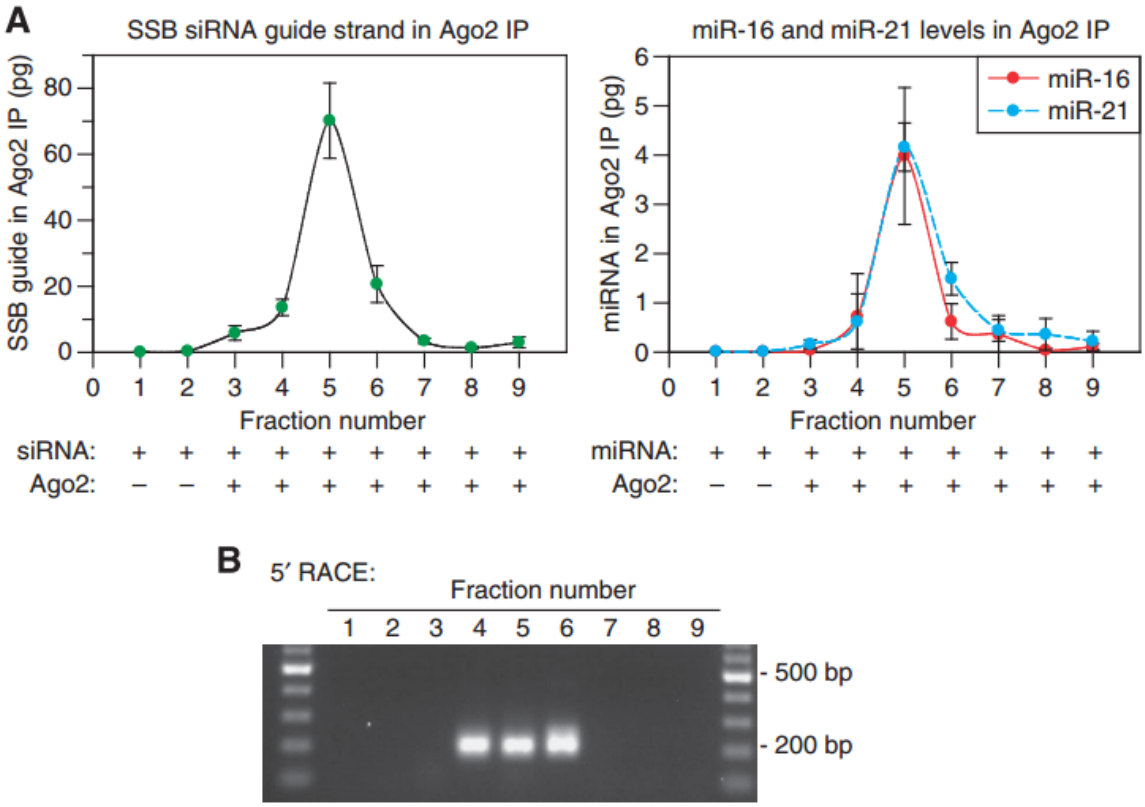

Figure 3 siRNA- and miRNA-loaded Ago2 complexes and mRNA slicing product co-sediment with ER/Golgi membranes

***a**, Ago2 IPs were performed from fractions of the sucrose gradient displayed in Fig. 1A, and SSB siRNA guide strand, miR-16 and miR-21 were quantified by RT-qPCR. **b**, 5′ RACE performed with total RNA from the sucrose gradient fractions of the gradient displayed in Fig. 1A. PCR products were separated on an agarose gel, a positive 5′RACE signal results in a 208 bp fragment.*

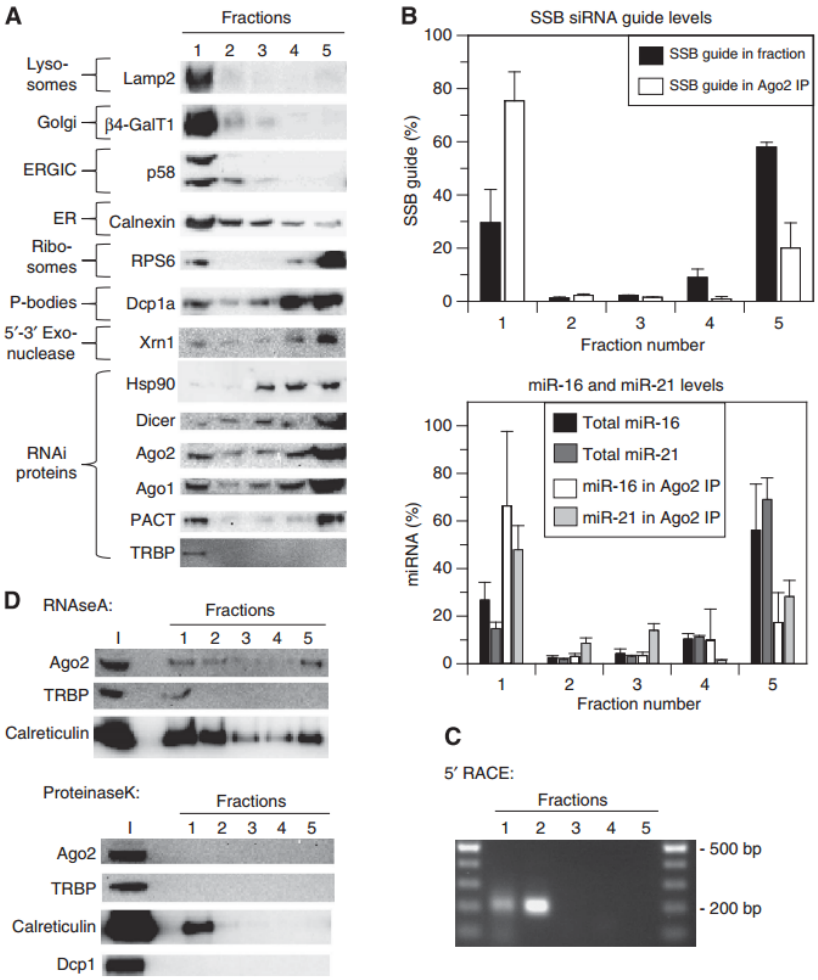

Figure 4 Active siRISC associates to the outside of membranes

*HeLa cells were transfected with SSB siRNA and subjected to a membrane floatation assay. Fractions were analyzed by western blotting (**a**), Ago2 IP and RT-qPCR (**b**) and 5'RACE (**c**) as in Fig. 3. **d**, HeLa lysates were treated with RNAseA or ProteinaseK and subjected to membrane floatation assays, fractions were analyzed by Western blotting. RNAse A activity was confirmed by analysis of GAPDH mRNA levels in the sucrose gradient fractions after the treatment (Fig. S3C).*

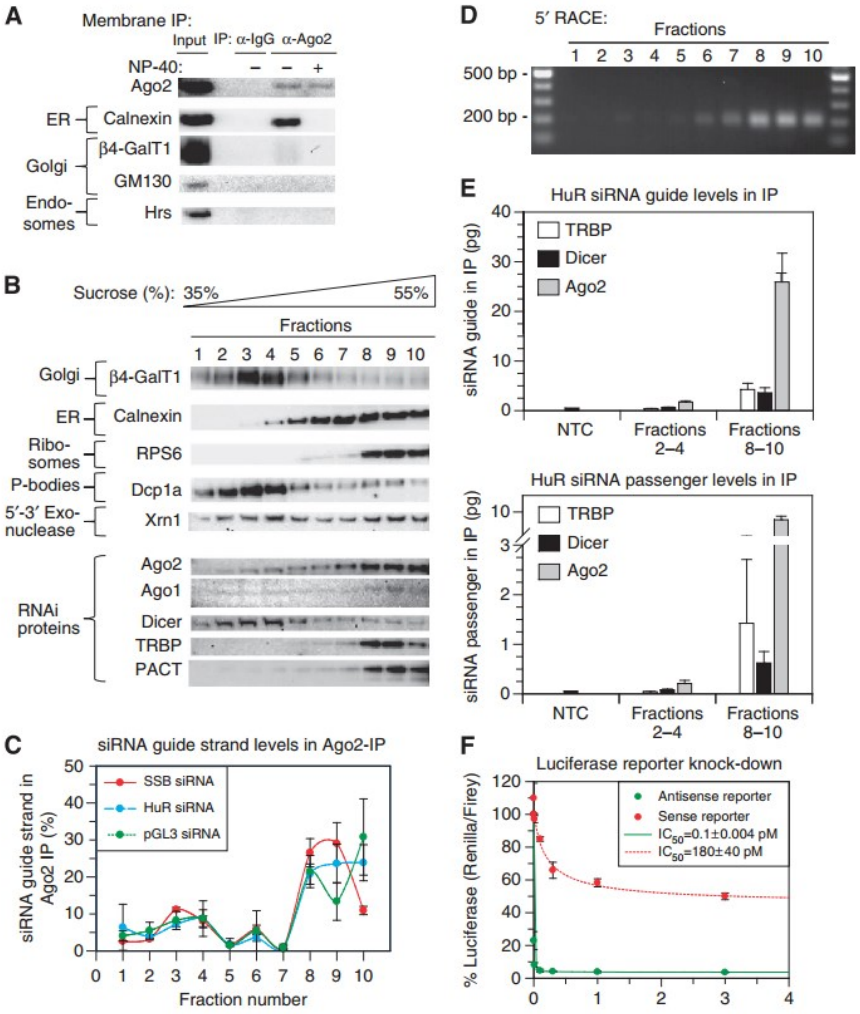

Figure 5 siRISC loading and siRNA-mediated mRNA cleavage occur on the membrane of the rough endoplasmatic reticulum

***a**, Membrane IPs were performed with HeLa lysates (as described in materials and methods) and eluates were analyzed by Western blotting. **b**, HeLa cells were transfected with SSB, HuR and pGL3 siRNA and subjected to a sucrose sedimentation gradient. Fractions were analyzed by Western blotting, Ago2 IP and RT-qPCR (**c**) and 5'RACE (**d**). **e**, HeLa cells transfected with HuR siRNA were subjected to a sucrose sedimentation gradient as in (a). The Golgi/P-body fractions (2-4) and rER fractions (8-10) were pooled and used for TRBP, Dicer and Ago2 IPs. The eluates were analyzed by RT-qPCR. Averages of one typical experiment are shown, error bars represent standard deviation of the RT-qPCR.. **f**, A dual-luciferase reporter plasmid was co-tranfected together with increasing concentrations of the HuR siRNA, luciferase activity was measured after 24 hours.*

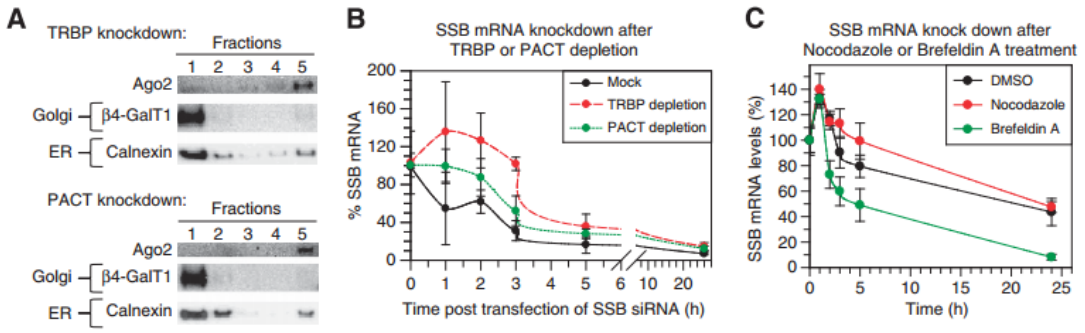

Figure 6 Membrane anchoring of RISC by TRBP/PACT accelerates RNA silencing

***a**, HeLa cells depleted of TRBP or PACT were subjected to membrane floatation assays as in Fig 4a, fractions were analyzed by western blotting. **b**, HeLa cells depleted of TRBP and/or PACT were transfected with SSB siRNA and harvested after the indicated timepoints. Relative SSB mRNA levels, normalized to GAPDH mRNA, were quantified by RT-qPCR. **c**, HeLa cells were pre-treated with Nocodazole (5 □g/ml) or Brefeldin A (10 □g/ml) for 2 hours, transfected with the SSB siRNA at 0.5 nM, and lysed at the indicated timepoints after the transfection. SSB mRNA levels were analyzed by RT-qPCR.*

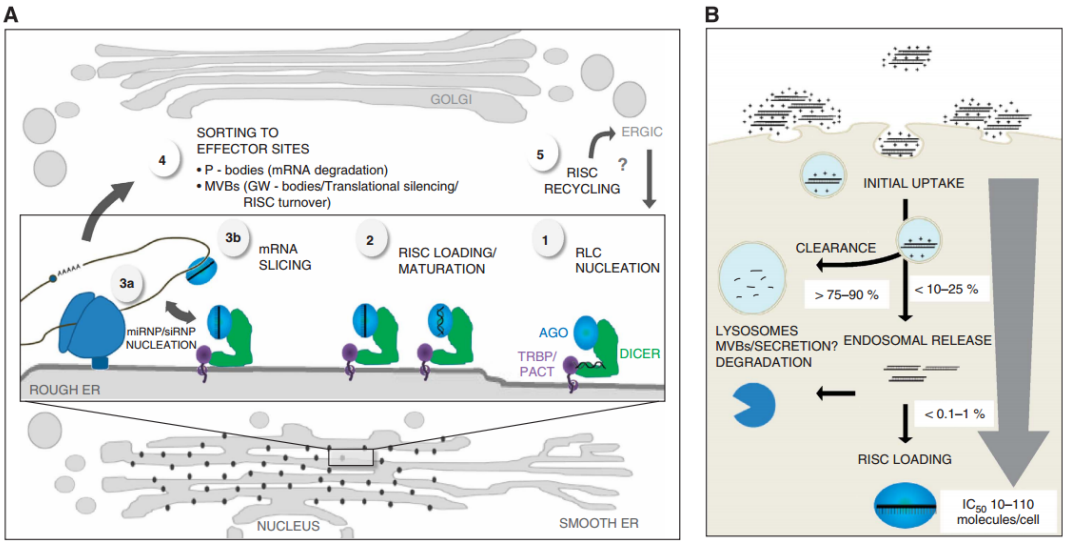

***Figure 7** Model for spatial organization of the RNAi pathway and quantitative fate of siRNA following transfection.*

***a**, Based on the data presented in this work, we propose that the central steps of RNAi occur at the cytosolic surface of the rough ER membrane. Exposure of ds siRNA to RLC, anchored to the membrane either directly or indirectly via TRBP and/or PACT, is nucleated by encounter of all partners at the rough ER (1). Upon transfer of the ds siRNA from RLC into Ago and passenger strand removal (RISC loading and maturation, (2)) mature RISC is formed. rER association provides mature RISC a privileged position to sample over translationally active mRNAs which either permanently (secreted/membrane proteins) or transiently (soluble proteins) associate with the rER (Chen et al., 2011;Gerst, 2008;Lerner et al., 2003). Upon encounter of a target mRNA, the formation of an siRNP or miRNP is nucleated (3a) and a perfect target gets endonucleolytically sliced by Ago2 (3b). Considering previous reports, it is likely that the RISC associated RNPs are then further directed to effector sites for downstream silencing events (4), such as P-bodies for*

exposure to the mRNA degradation machinery (Eulalio et al., 2007a), or MVBs/GW bodies for interaction with GW proteins and/or RISC disassembly (Gibbings et al., 2010). Finally, "consumed" RISC may get either eliminated, or reactivated and recycled back to the ER through the highly dynamic endomembrane apparatus or other routes (5). ***b****, In summary of the data presented in Figures 1 and S2, following endosomal uptake of siRNA with cationic lipofection a lion's share of the intracellular siRNA is cleared again very quickly via lysosomes and potential additional secretion or degradation pathways. Even though the RISC loading machinery is not saturated (Fig. 2A), the residual intracellular siRNA is loaded very inefficiently into Ago (less than 0.1-1 % of the initial intracellular siRNA). This explains why, although as little as 10-110 loaded RISC molecules per cell are sufficient to promote knockdown of a relatively abundant mRNA such as SSB, the cell needs to be flooded with siRNA by exposure to nanomolar concentrations to sustain significant mRNA knockdown.*

6.2 Manuscript IV

An easily accessible wide field based fluorescence imaging platform for ultrafast screening of one-bead one-compound libraries using a novel image subtraction approach.

*Wolf Heusermann[1], Beat Ludin[2], Thomas Weidemann[3], Nicole-Claudia Meisner-Kober[1], Nhan Pham[4], Manfred Auer4 and Martin Hintersteiner[1,5]**

[1] Novartis Institutes for BioMedical Research Basel, Novartis Biologics Center, Fabrikstrasse 10, 4.13, Novartis Campus, CH-4056-Basel, Switzerland

[2] Life Imaging Services, Efringerstrasse 79
CH-4057-Basel, Switzerland

[3] Technische Universität Dresden, BIOTEC/Biophysics, Tatzberg 47-51, 01307 Dresden,
Germany

[4] The University of Edinburgh, School of Biological Sciences (CSE) and School of Biomedical Sciences (CMVM), CH Waddington Building, 3.07, The King's Buildings, Mayfield Road, Edinburgh, EH9 3JD, UK

[5] Bioseutica BV, Succursale di Lugano, Corso Elvezia 4, 6900 Lugano, Switzerland

* E-mail: M.Hintersteiner@bioseutica.com

ABSTRACT. The increasing involvement of academic institutions and Biotech companies in drug discovery calls for miniaturized, cost effective methods to identify new bioactive molecules. Affinity based on-bead screening of one-bead one-compound combinatorial libraries aims at combining the advantages of miniaturized combinatorial split-mix library synthesis in generating large compound collections with a simple, cheap and generic protein binding assay format. However, due to the pronounced broad spectrum autofluorescence of library beads as well as the considerable miniaturization i.e. the need to sort objects of 50-100µm and possibly smaller, one bottle-neck in on-bead screening is still the unavailability of a widely accessible, technically simple, cheap and robust screening platform. Despite the development of all sorts of detection aids and contrast enhancement methods, a dye labeled protein in combination with fluorescence as a detection principle is arguably still the simplest assay system for on-bead screening. However, wide-field fluorescence microscopy has long been considered unsuitable due to detection of photons from outside the focal volume, a relatively broad excitation bandwidth and low detection sensitivity, all resulting in too low signal-to-noise ratios. Herein we describe the extension of a standard, commercially available wide field fluorescence microscope for on-bead screening. We demonstrate that the autofluorescence problem can be overcome by an optical image subtraction approach which leads to excellent signal-to-noise ratios and results in unambiguous detection of true hit-beads. The combination of modern sCMOS camera detection and LED based excitation with this image subtraction approach for autofluorescence correction results in a robust on-bead screening system. A polymer capillary based bead-picking device, mounted on a mechanical slider, very efficiently allows the operator to isolate individual hit beads in less than 20 seconds. The system, while easily implementable on any high-quality fluorescence microscope, can be used for ultra-fast automated screening of > 200 000 bead bound compounds in 1.5 hours, thereby making it an exceptionally fast and cost effective screening platform.

INTRODUCTION. Today, academic institutions play an increasing role in the development of novel and innovative drugs.[1][2] The emergence of chemical biology as a new discipline in the post-genomic era is one contributing factor to that development. Consequently, an ever increasing number of proteins and their

interaction networks are being studied.[3][4] This calls for efficient, miniaturized and economic approaches to identify new bioactive molecules.[5][6][7] Combinatorial Chemistry and High-throughput screening (HTS) certainly represent two enabling technologies for identifying new bioactive molecules.[8] A particularly efficient embodiment of combinatorial chemistry, the one-bead one-compound (OBOC) library concept, as invented by Lam et al.[9], allows the generation of large compound libraries of hundreds of thousands to millions of compounds on polymeric carrier beads. On-bead screening on the other hand is a particularly easy to use and efficient affinity based screening concept. It selects hit-beads based on the binding of a soluble, tagged target protein or a cell to the immobilized compound on the bead surface[10][11]. Each bead therefore represents a highly miniaturized screening assay. With beads of 90 micrometer diameter, a loading of 100 pmol of substance and a bead volume of less than 1 nl, the amount of chemical substances required for a screen and the corresponding assay volumes are several orders of magnitude lower than even highly miniaturized multi-well-plate based high-throughput screening formats in homogenous solution.[12]

This very efficient initial screening step can then be combined with different follow-up assays for further characterization and ranking of individual hit beads before resources are committed to the resynthesis of screening hits.[13][14][15][16] However, one of the major hurdles for a wider application of on-bead screening is the lack of simple, robust and easy screening platforms. In its simplest assay format, a fluorescently tagged protein can be used in on-bead screening for incubation of library beads. Hits, arising from the binding of the target protein to the bead-immobilized compounds, then need to be selected based on the fluorescence signal on the beads using a fluorescence microscope. Yet, the variable and pronounced autofluorescence intensity of library beads, which have gone through a combinatorial synthesis, makes a detection of hit beads based on their fluorescence intensity difficult. Different strategies, which were developed to overcome this autofluorescence problem, range from the immobilization of 3-Nitro-Tyrosine as an internal quencher prior to library synthesis to the use of quantum dots as secondary detection aid.[17][18] However, any non-specific binding of the secondary detection reagent in sandwich assays is hard to control.

The COPAS instrument is the only commercially available on-bead screening platform.[19,20] It essentially works as a fluorescence activated bead sorter and thereby allows a fast real-time manipulation of beads, but naturally suffers from the same binding signal versus bead autofluorescence problem. Pre-sorting of libraries to remove beads with high autofluorescence has been suggested as one possible, but time-consuming solution.[21] Alternatively, a multi-channel real-time analysis was recently shown to enhance the signal-to-noise ratio on the COPAS instrument significantly.[22] Our own group has previously developed the PickoScreen instruments, a confocal nanoscanning and bead-picking platform

(CONA), exploiting the high-resolution fluorescence imaging capabilities of confocal microscopy for overcoming the bead autoflourescence.[23] The CONA method for the first time made a precise, quantitative detection of on-bead binding events possible under high-throughput screening conditions. This methodology has recently also been used to investigate the thermodynamics and kinetics of on-bead binding events.[24] However, in CONA, the need for scanning large areas with high resolution limits the achievable speed. Furthermore, the use of lasers, sensitive confocal optics and a complex bead-picking robot leads to considerable complexity and high instrumental costs, which render this technology inaccessible to a wider research community.

We have therefore constructed an ultrafast wide field fluorescence microscopy based on-bead screening instrument featuring a capillary based high-speed, high-precision z-axis picking device, which is operated by using a kinematic guided mechanical x-axis slider. We further demonstrate herein that this fast wide-field fluorescence imaging approach opens up the possibility to use an image subtraction approach to reliably detect hit-beads despite a significant and variable autoflouresence background. The image-based autofluorescence correction, combined with the fast wide field fluorescence imaging and the robust, yet simple bead picking option for the first time generates an on-bead screening platform which can be mounted on any standard fluorescence microscope at limited costs and achieves unprecedented screening speed.

RESULTS

Library bead fluorescence

To study the fluorescence properties of typical TentaGel based one-bead one-compound combinatorial libraries, a small library containing cyclic hexapeptides of the general form NH2-Pra-Glu[-Pro-X-Y-Z-Asp-], X, Y and Z being the combinatorial positions was constructed using Fmoc- based solid phase peptide chemistry. An N-terminally allyl-protected glutamate was used for side-chain anchoring of the cyclic peptide. The head-to-tail cyclization was affected on resin after palladiumacetate based allyl-group removal. This treatment resulted in a bead population with different levels of autofluorescence, as seen from a CONA image (Figure 1a). To analyze the fluorescence properties of these beads, fluorescence excitation- and emission spectra were collected (Figure 1b). For further characterization, the average fluorescence lifetimes of these library beads were measured using a fluorescence spectrophotometer (Figure 1c). In addition, the fluorescence lifetimes of individual beads were measured using a standard wide field fluorescence microscope equipped with a commercially available module for phase-domain based fluorescence lifetime determination (LIFA from- Lambert Instruments) (Figure 1d). These fluorescence lifetime measurements revealed that

the library beads exhibited surprisingly long average fluorescence lifetimes of about 3 ns, rendering the use of fluorescence-lifetime as a detection principle for hit-bead detection impractical (Table 1). We therefore decided to focus our efforts on obtaining an efficient spectral separation of bead autofluorescence and protein-tag derived fluorescence signal for building an optimized fluorescence wide-field microscope for on-bead screening.

Figure 1

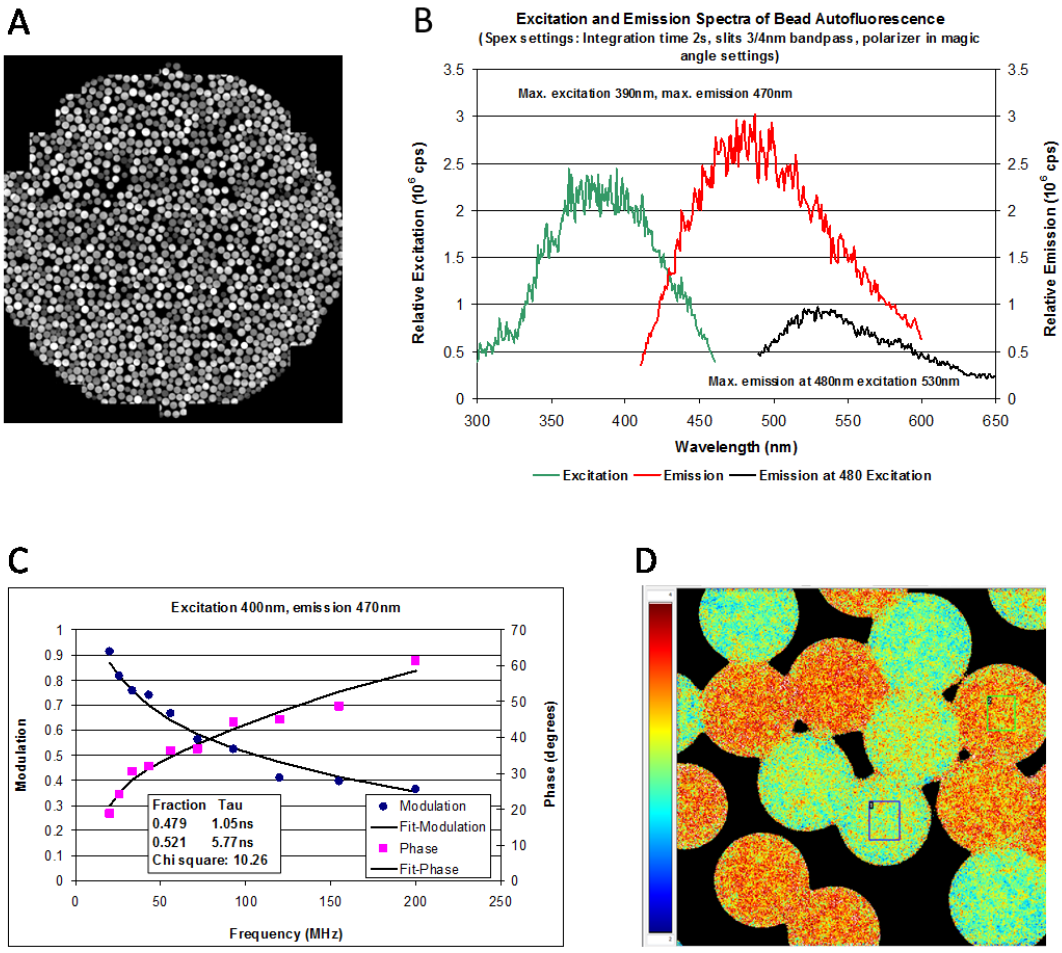

Figure 1: Fluorescence properties of TentaGel library beads. A) CONA image of a well from a 96-well microtiter plate filled with typical beads from a one-bead one-compound library, recorded with 633 nm excitation B) Fluorescence excitation and emission spectra of the same bead sample as in a. C) Fluorescence life-time determination of average autofluorescence from the bead sample in a. D) Fluorescence life-time imaging of the bead sample in a. using a commercially available phase-domain based fluorescence lifetime unit (LIFA from- Lambert Instruments) mounted on the WIOBS-1 instrument.

Table 1

Wavelength (nm)	Fraction 1	Fraction 2	Tau 1/ns	Tau2/ns	Chi square
400/470	0.435	0.565	0.953	5.118	9.47
400/470	0.373	0.626	0.787	5.004	14.1
480/530	0.37	0.63	1.07	5.651	29.4
480/530	0.489	0.511	1.243	4.854	22.37

Table 1: Fluorescence life-time data determined for the autofluorescence arising from typical one-bead one-compound library beads at different excitation/emission wavelengths.

Instrumental design elements

The instrumental design was driven by the principle of using commercially available components while avoiding complicated robotics systems (Figure 2). While wide field fluorescence microscopes often still rely on lamps for excitation, the use of cooled LEDs has become an excellent alternative. LEDs offer the advantage of delivering high intensities in a narrow wavelength range thereby overcoming the need for expensive laser equipment.

During on-bead screening many different bead populations are encountered in a single field of view. There are dark beads with hardly any signal, beads with different levels of broad spectrum autofluorescence, originating from the various chromophoric elements distributed in the entire bead volume and finally, beads which on top show the specific fluorescence signal due to protein binding within the first few micrometers of the bead surface.

This creates a need for a camera which features both, high-sensitivity as well as a wide dynamic range. We therefore decided to use a sCMOS technology based camera (Andor Technology, Belfast/UK). A standard fluorescence microscope, the Leica DMI6000B (Leica Microsystems, Wetzlar/Germany), equipped with a scanning stage, served as the platform onto which the LED lightsources and the camera were integrated. This setup was further complemented by a bead-picking device (Life Imaging Services GmbH, Basel/Switzerland) (Figure 2b). Our group's previously reported bead-picker, one of the defining elements of the PickoScreen[23] series of prototype confocal screening instruments, used a complex robotic system, which moves a picking capillary in 3D. This causes the need for an alignment procedure between an external 3D coordinate system and the 2D coordinates of the beads in the screening plate. Furthermore, the high-precision needed for the movement of the picking capillary across a distance of about 30 centimeters limits the speed with which the robotics arm can move. We therefore reasoned that it would be highly desirable to have a mechanical slider, which can

be used to manually move the picking capillary and position it right in the center of the field of view by a magnet at the end of the slider (Figure 2a, indicated). This only leaves the precise up-and-down movement of the picking capillary to be automated. To this end, a motorized z-axis (Physik Instrumente-PI GmbH & Co. KG Karlsruhe/Germany) was mounted onto the slider which performs a three-step movement of the picking capillary holder (see bead picking). Finally, the picking capillary is mounted on the holder by first gluing a polyimide tubing (Accellent Inc. MA, USA), the picking capillary, into a short metal tubule and inserting it with the metal part into a silicon lined channel on the transparent capillary holder, an polycarbonate disc. The other end of this channel, running across the capillary holder is then connected via a hydraulic pump (Kloehn Inc. USA Las Vegas, NV), which generates a precisely controllable negative pressure for sucking beads into the capillary for subsequent dispensing into a collection tube or well. We dubbed this new screening instrument WIOBS 1 for Widefield Fluorescence Imaging based On-bead Screening and bead-picking device 1.

Figure 2

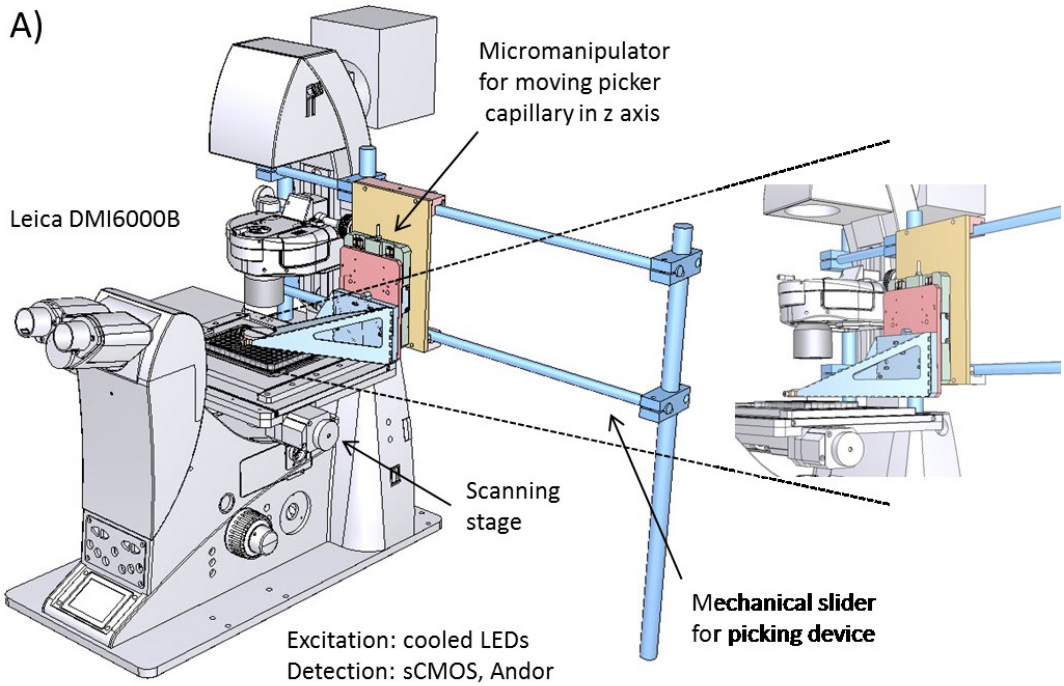

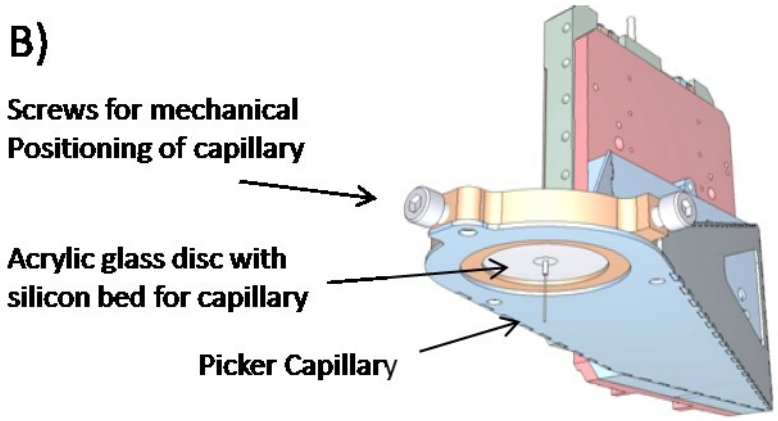

Figure 2: The WIOBS-1 instrument A) 3D overview sketch, generated with IronCAD (version 11.0), with bead picker positioned over a 96-well microtiter plate. The individual parts are indicated; the close up shows the bead picker arm above the microtiter plate and scanning stage. B) Zoom view of the bead-picker, the picker capillary, mounted into the clear polycarbonate disc is shown.

Wide field fluorescence based quantitative on-bead screening

For testing the suitability of WIOBS 1 for fast and quantitative on-bead screening we first generated model hit beads by decorating standard 90µm TentaGel S beads on their amino groups with biotin. Aliquots of 2 mg of these biotinylated beads were then filled into 1.5 ml Eppendorf test tubes and incubated for 6 hours with different concentrations of three differently labeled streptavidin conjugates, Alexa-488-streptavidin, TMR-streptavidin and Alexa-647-streptavidin. After thorough washing, 1 mg beads from each tube was then transferred into a well of a 96-well microtiter plate and fluorescence images were recorded using constant acquisition parameters (Figure 3a). Streptavidin binding to the beads was clearly detectable in all images, as seen from a pronounced fluorescence signal in the form of a halo around the beads. An analysis of the average pixel intensities for each image shows that the fluorescence signal responds linearly to the increasing incubation concentrations of all tested streptavidin conjugates with linear correlation coefficients higher than 0.9 (the highest concentration of the TMR-streptavidin series was excluded from the curve-fit due to inhomogeneous fluorescence signals on some of the beads). Thus, WIOBS1 proved to be able to specifically and quantitatively detect the binding of a fluorescently labeled target protein to TentaGel beads under typical on-bead screening conditions.

Figure 3

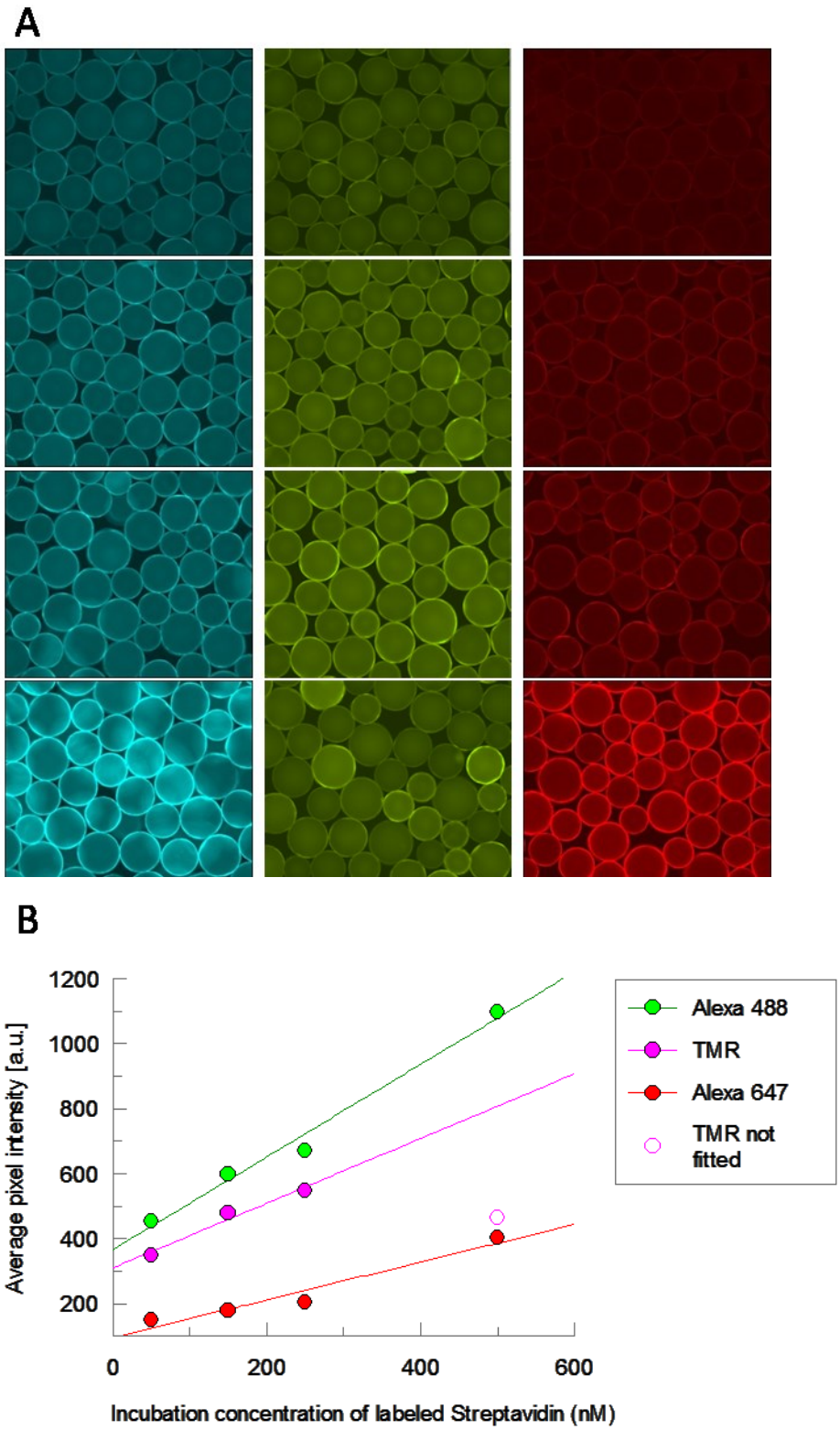

Figure 3: WIOBS 1 on-bead screening images and signal dynamics A) images of biotinylated beads incubated with increasing concentrations of different streptavidin-conjugates. Left: Alexa-488-streptavidin, Middle: TMR-streptavidin,

Right: Alexa-647-streptavidin. Top-to-bottom: 50 nM, 150 nM, 250 nM, 500 nM conjugate, after 6 h incubation. B) Linear data fit of average pixel intensities obtained from each image in a.

Image merging and screening speed

Next, we turned our attention to verifying the underlying rational that fluorescence wide-field imaging can provide an ultrafast method for on-bead screening. For that purpose, an efficient tile-image merging procedure had to be established, which would allow us to screen entire wells of a 96-well microtiter plate. Due to inhomogeneities in excitation and detection efficiency within a single image frame, the individual tile images first need to be corrected for any such optical imperfections using a previously recorded reference image. In a first step, the optimal number of tile-images for complete imaging of an entire well of a 96-well microtiter plate for 5x, 10x and 20x magnification were determined to be 9 images, 32 images and 84 images, respectively (Figure 4). The time needed for the system to record and process individual tile-images in order to obtain a merged image of a complete well of 96-well microtiter plate, containing 2000 standard 90µm TentaGel beads, under different instrumental settings was recorded (Table 2). The image acquisition times including autofocus determination ranged from 26 seconds for a well at 5x magnification to 2.5 minutes for a well at 20x magnification. The additionally required time for the image merging procedure can in principle be allocated to a second computer and done in parallel to the recording of the following well. Thus, at 5x magnification recording an entire 96-well microtiter plate, containing around 200 000 beads or bead bound compounds takes about 41 minutes. The sensitivity even at 5x magnification proved perfectly suitable for detecting the binding of Alexa-647-streptavidin to the biotinylated beads after incubating the beads with 50 nM conjugate for 6 hours (Figure 4). At higher magnification the sensitivity for detecting hit-beads further improves, however at 20x magnification, which requires 84 images per well, the recording time for a 96-well plate increases to 4 hours with an additional 7 hours of image merging time on a standard PC. The 10x magnification represents a good compromise between speed and sensitivity and allowed us to acquire data from an entire 96-well plate in less than 2 hours.

Table 2:

Objective	20x	10x	5x
Stitching format	84 images	32 images	9 images
Overlap	150 µm	400 µm	600 µm
Exposure time	200 ms	200 ms	200 ms
Image acquisition time	150 sec	65 sec	26 sec
Image merging time	290 sec	70 sec	14 sec

Table 2: Typical parameters and time for imaging of entire wells of a 96-well microtiter plate on the WIOBS-1 instrument at different magnifications

Figure 4

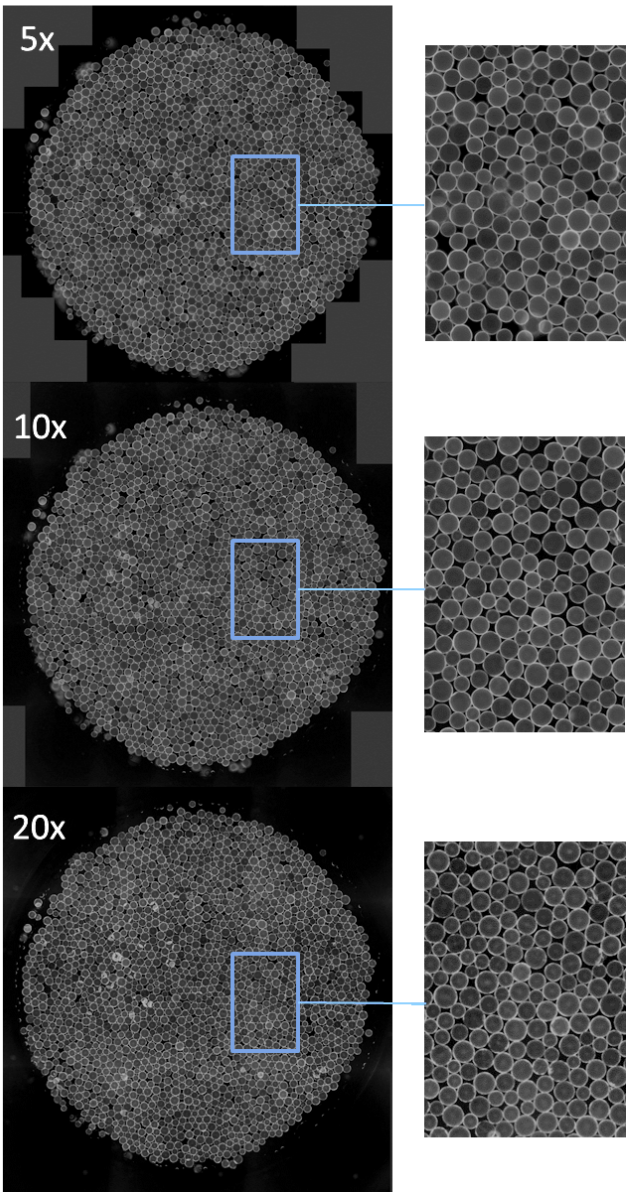

Figure 4: Images of full wells from a 96-well microtiter plate containing a monolayer of 90 ∝m Tentagel beads recorded on the WIOBS 1 instrument at different magnifications and after tile-image merging. Top: 5x, Middle 10x, Bottom: 20x.

Bead picking

The simplicity of the bead-picking device enables a fast isolation or sorting of beads both, in brightfield illumination mode (Figure 5A) or under fluorescence imaging settings (Figure 5B) in six steps:

Step 1 - Alignment: as individually cut picking capillaries vary in length, the appropriate Z-axis positions have to be determined before a picking session. These Z-axis positions are: a) The bead selection position; which is 10 to 50µm above the bead monolayer and allows the picking capillary to be seen in the microscope`s field of view. It allows fine adjustment of the capillary`s position above the bead of interest by moving the x,y-stage without disturbing the beads. b) The picking position, which is a few micrometers above the well bottom. This ensures that the bead, which is captured by the capillary, will be sucked up without creating a turbulent flow through the capillary`s opening.

Step 2 - Bead Selection: The x,y-coordinates of the beads are stored with each well image. A simple mouse click on the image allows to select the respective beads and causes the scanning stage to move to these positions, bringing the selected bead into the center of the field of view.

Step 3 – Capillary movement to bead selection position: The capillary is lowered to the position immediately above the bead monolayer and consequently becomes visible in the field of view without disturbing the beads.

Step 4 – Picking: Capillary is lowered further to the bead picking position and engulfs the selected bead. A predefined volume of liquid, ~4 µl for 90µm beads, is drawn into the capillary and the beads is sucked into the capillary.

Step 5 – Capillary withdrawal: The capillary is moved out of the well to the resting position. The slider is manually moved to the side for dispensing the bead.

Step 6 – Bead dispensing: A volume of 10 µl is dispensed through the capillary. Thereby the bead is placed along with the liquid into a well of microtiter plate, a glass vial or any other vessel.

This entire picking procedure for a single bead takes approximately 20-30 seconds.

Figure 5

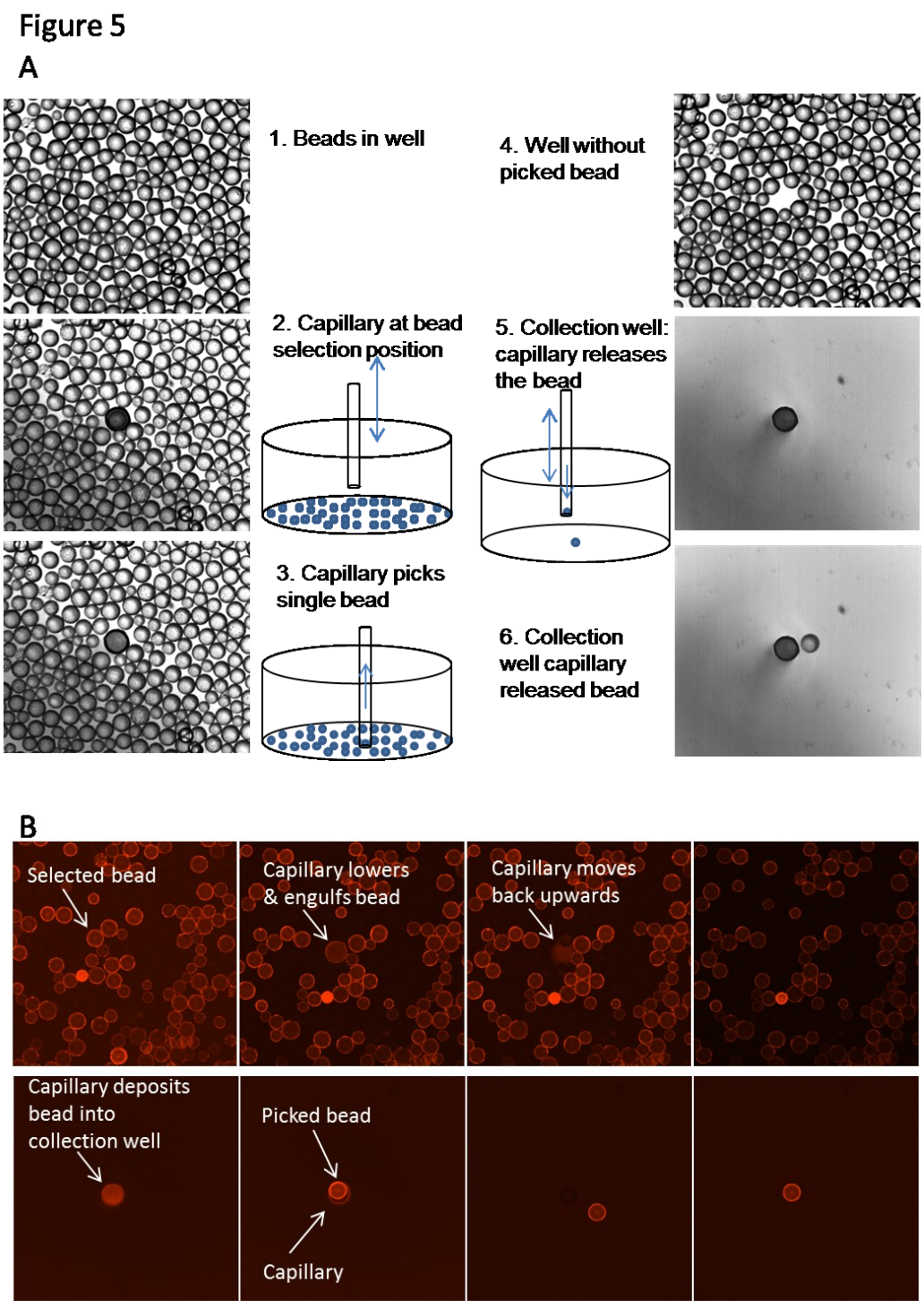

Figure 5: Bead picking on the WIOBS 1 instrument. A) Overview of the picking process, detailing the different steps and corresponding bright-field images B) Bead picking on the WIOBS 1 instrument under fluorescence imaging settings. Top row: images corresponding to different stages in the picking process; bottom-row: images corresponding to the different stages in the bead dispensing process into a separate empty well.

Image Subtraction Approach for detection of hit-beads

So far, the data recorded with three different fluorescently labeled streptavidine conjugates and biotinylated TentaGel beads demonstrate that wide-field fluorescence imaging with a fine-tuned instrument is perfectly suitable for detecting target protein binding to beads with excellent reproducibility. However, biotinylated Tentagel beads have only undergone one coupling step and therefore exhibit a uniform low autofluorescence. The discrimination of hit among a population of beads with various levels of autofluorescence, as seen a typical one-bead one-compound library is more challenging. Especially so, when lower magnifications like 5x objectives are used for ultimately fast screening. Moreover, the autofluorescence of library beads is not restricted to the specific emission range of a label and usually much broader in its emission bandwidths (Figure 1). We therefore reasoned that a second fluorescence image, taken at an excitation and emission wavelength sufficiently below or above the specific absorption and emission of the label of the target protein can be used to correct for bead-autofluorescence (Figure 6A). To demonstrate the applicability of this approach, beads from the prototypical cyclic peptide library used to measure the data shown in Figure 1 were mixed with a small number of biotinylated beads and incubated with 50 nM fluorescently tagged streptavidin conjugate for six hours. Entire wells of a 96-well microtiter plate were then imaged with two different excitation and emission wavelength settings using the WIOBS 1 instrument (Figure 6B). For the Alexa647 labeled streptavidin, the 488/520 nm channel was used for autofluorescence correction, whereas for the Alexa488 labeled streptavidin the 455/485 nm channel was used to correct for autofluorescence. In addition, the exposure parameters were adjusted so that the average signal intensities were in the same intensity range. This adjustment of exposure parameters can easily be done before a full on-bead screen is carried out using a population of typical library beads. The two set of images were then simply subtracted to generate an autofluorescence corrected image. Under all settings used, this resulted in images, where only the true hit beads are visible (Figure 6C). With this method even the 5x magnification settings proved sensitive enough to discriminate beads with bound Alexa488 labeled streptavidin from beads with high autofluorescence. This represents a worst case scenario, as the peak of the bead autofluorescence signal is around 490 nm.

Figure 6

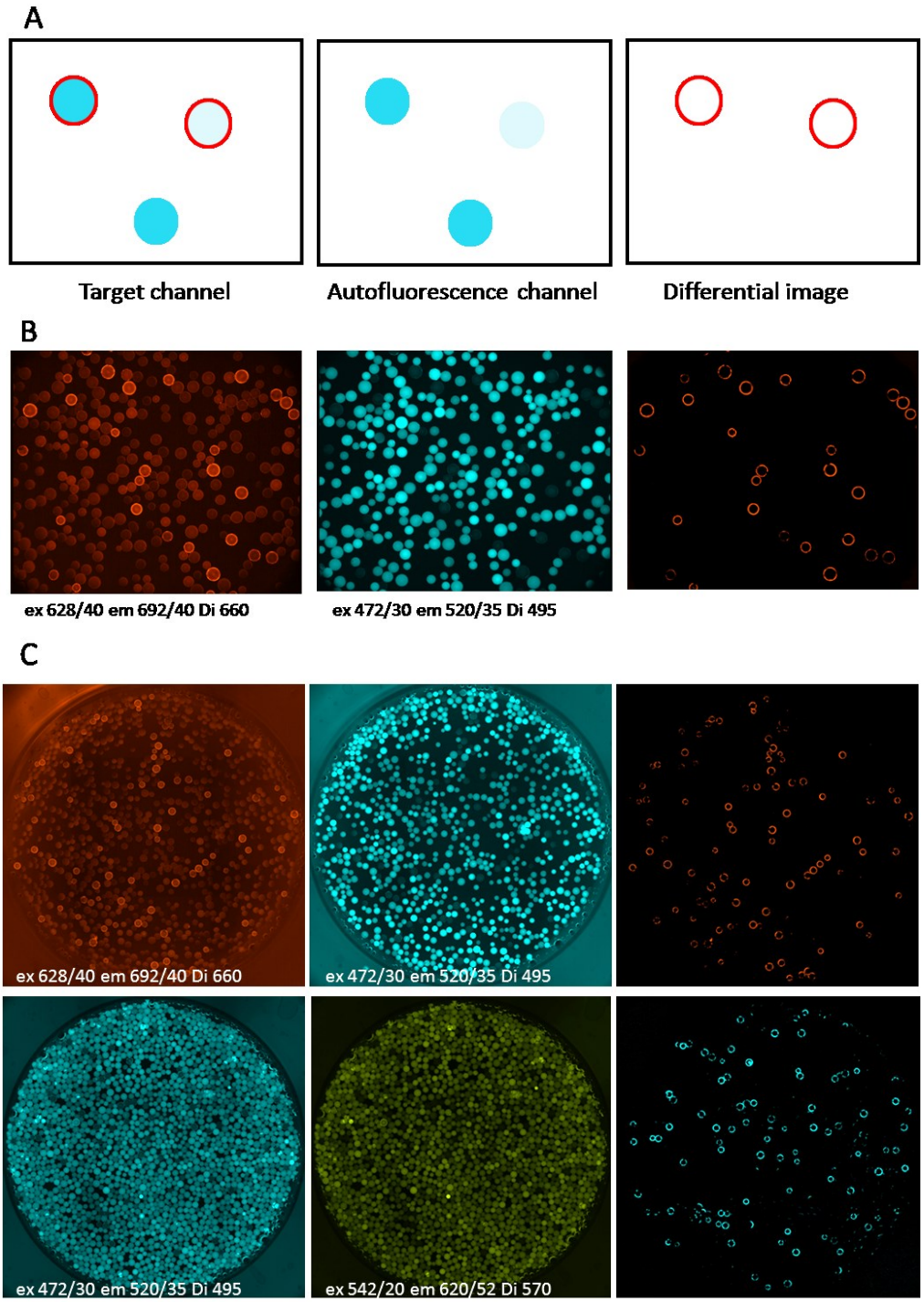

Figure 6: Image subtraction approach for on-bead screening on WIOBS 1. All images were recorded using 5 x magnification. Well were filled with beads from a one-bead one-compound library of cyclic hexapeptides, spiked with biotinylated beads and incubated with different streptavidin conjugates (50 nM, 6 h). A) schematic representation B) example from tile-images of a well incubated with Alex-647-streptavidin. C) full well 96-well microtiter plate images. Top row: Alexa-647-streptavidin conjugate. Bottom row: Alexa-488-streptavidin conjugate.

Cell based screening

One conceptual advantage of using a standard wide-field microscope for on-bead screening is that the system can also be used for selecting cell-surface binding ligands when entire cells, rather than isolated soluble proteins, are used for screening. To test the applicability of our WIOBS 1 instrument for cell-based on-bead screening, we used HeLa and Huh-7 cells and compared the cell-binding behavior of two different peptidic ligands, a cyclic disulfide bridged peptide, CRKRLDRNC[25], as well as the transferrin binding peptide HAIYPRH[26]. Both peptides were synthesized on TentaGel beads using Fmoc-chemistry. The disulfide bridged peptide was cyclized on-bead by iodine mediated disulfide formation.

Beads carrying either one of the two peptides or biotin as a ligand where incubated with HeLa cells or Huh-7 cells at 37° C in an incubator under constant shaking before being imaged on the WIOBS 1 microscope using bright field illumination setting. As soon as five minutes after incubation, a clear difference was seen between the cell lines and ligands (Figure 7). HeLa cells clearly bound specifically to the cyclic CRKRLDRNC peptide whereas, no binding was observed to the other two ligands. Also, Huh-7 cells did not bind to any of the ligands. This clearly demonstrates, that the WIOBS instrument is also suitable for cell-based on-bead screening e.g. for identification of cell-type specific targeting ligands.

Figure 7

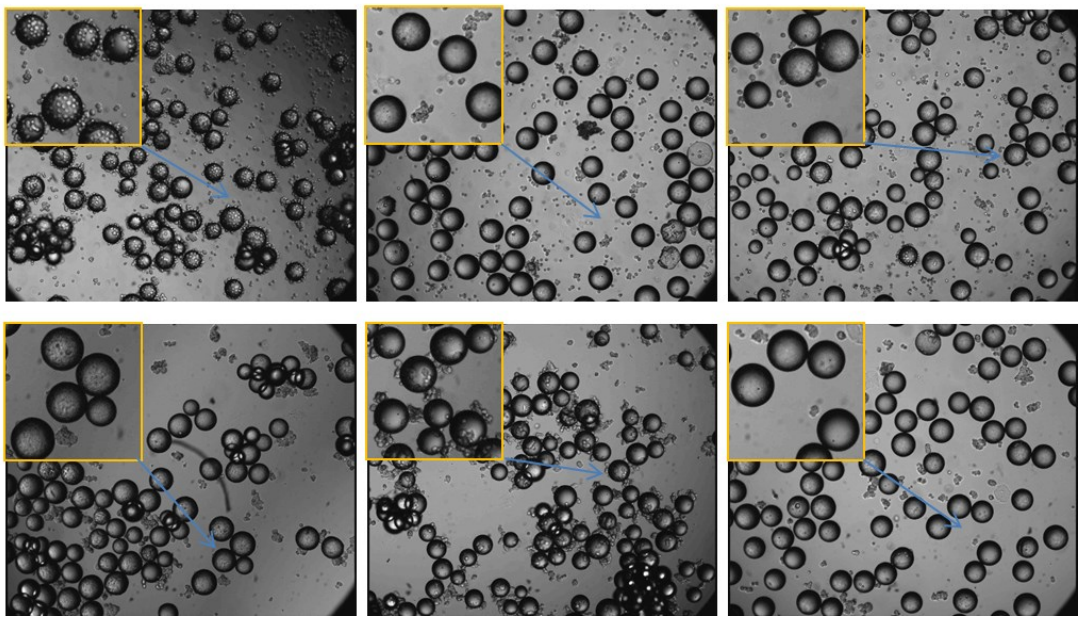

Figure 7: Cell-based on-bead screening using WIOBS 1. All images were recorded using bright-field illumination using 5x magnification. Left: beads carrying the cyclic peptide *CRKRLDRNC*[25], *Middle: beads carrying a* linear peptide, *HAIYPRH*[26], Right, biotinylated beads. Top row: HELA cells, bottom row: Huh-7 cells.

DISCUSSION. Three main factors contribute to autofluorescence of typical library beads and therefore complicate the detection of real hit beads after incubation of the library with fluorescently labeled target proteins: First, TentaGel, the most common solid support used in on-bead screening has a substantial intrinsic autofluorescence, arising from the polystyrene co-polymer. Secondly, during chemical synthesis, in-complete couplings and side reactions of reagents lead to by-products with pronounced fluorescence emission across the entire spectrum. Thirdly, individual library compounds themselves can contribute to the background fluorescence if they contain larger conjugated pi-electron systems. This third factor is the only one which can consciously be influenced and minimized during library design e.g. by selecting different building blocks or by the general compound design.

In general, the bead autofluorescence issue in on-bead screening described above can either be addressed by using a high-resolution (confocal) imaging setup which can separate the signal on the outside of the beads from the bead interior or by making use of one of the many parameters of fluorescence, such as fluorescence lifetime or specific excitation and emission wavelength i.e. spectral separation. For example, if labels are used with bright fluorescence emission in the red region of the spectrum the ratio of specific signal intensity to autofluorescence intensity gets better as autofluorescence is usually much more pronounced in the blue-to-green region of the spectrum. Another example for a smart detection principle would be fluorescence lifetime. However, when investigating this possibility for on-bead screening unexpectedly long fluorescence lifetimes of around 3 ns were measured for the autofluorescence signal. This long-lifetime background signal makes any specific detection of fluorescence signals from standard organic dyes with lifetimes of 1-4 ns very difficult under screening conditions. We therefore turned towards spectral separation as the method for dealing with autofluorescence. In order to overcome the limitation of wide-field imaging for fluorescence based detection of hit beads during on-bead screening, we first optimized the individual components of the fluorescence microscope, including cooled LEDs as powerful light source and a detection chip based on the sCMOS technology which features favorable characteristics with respect to sensitivity and linearity. As a second element we developed a new optical image-subtraction approach. This approach uses a second detection channel for correcting the fluorescence signal measured in one channel by the autofluorescence signal measured in the second channel. Ideally, the second channel should be close to the specific fluorescence emission channel of the label but well separated in order to minimize cross-talk. Although this image subtraction approach effectively doubles the measurement time, it proved to be highly efficient in dealing with autofluorescence and allowed us to detect hit-beads even with a 5x objective. The very short measurement times associated with the use of fluorescence wide field imaging instead of confocal imaging more than compensate

for this extra-measurement time. This ultimately reduced the screening time for a 96-well microtiter plate containing approximately 200 000 TentaGel S 90µm beads to less than 90 minutes for a 5x objective and to less than 3.5 hours for a 10x objective. Furthermore, there is always the possibility to take an iterative approach and use a higher magnification for individual wells of high interest.

In an attempt to also simplify the isolation of hit beads and improve the so-called bead-picking procedure, described previously[23], we constructed a bead picking device which only requires a motorized movement in one axis (z) and is mounted on a mechanical slider for moving it over the scanning stage and positioning the picking capillary in the center of the field of view. With this simplified picking device a significantly faster picking time of 20 to 30 seconds per bead was achieved.

Overall, the resulting new instrumental platform for on-bead screening is simple to operate, does not require sophisticated equipment and is suitable for both fluorescence based screening with tagged target proteins as well as bright-field imaging for cell based screening. Our new development represents a further step to make on-bead screening more easily accessible to a larger number of researchers who want to use this miniaturized, cost effective high-throughput screening platform for the identification of new bioactive molecules.

Materials and Methods

All chemicals were bought from Sigma-Aldrich. TentaGel beads (standard 90µm diameter) with either free amine, Rink linker or HMBA linker were bought from Rapp Polymers, Germany. Labeled Streptavidin conjugates were bought from Life Technologies Corporation, USA.

Chemical syntheses:

All syntheses were carried out using manual solid phase peptide synthesis equipment and standard Fmoc chemistry, following standard procedures as recommended by Novabiochem, Germany and described previously.[15][27] In brief, resin loading for HMBA resin was carried out using the MSNT/1-methylimidazole method. For couplings the individual building blocks (5.8 equ), HATU (6 equ.) was used as coupling reagent with DIPEA (12 equ.) as base and DMF as solvent. All couplings were carried out twice with each coupling time 40 min. Fmoc deprotection after extensive washing was carried by four repetitive treatments of the resin with piperidine (20% in DMF) for 5 min. For the cyclic peptide library a head-to-tail cyclization on resin was carried out following Pd(0) catalyzed removal of an ally protection group on Glutamic acid (Fmoc-Glu-OAll)

and on-resin cyclization with HATU. Final side-chain deprotection of peptides was carried out using TFA:TIS:water (95:2.5:2.5) for 2 hours. Biotinylated beads were generated by coupling Biotin to TentaGel S NH2 resin using the HATU coupling procedure. The CRKRLDRNC peptide was synthesized on TentaGel S HMBA resin, using C-terminal 8-amino-3,6-dioxaoctanoic acid as C-terminal spacer. The peptide was cyclized after on-resin side-chain deprotection by DMSO treatment for 24 hours.

Fluorescence excitation and emission spectra of TentaGel beads

Excitation and emission spectra of Tentagel beads containing a one-bead one compound library of cyclic peptides were recorded on a Fluorolog tau-3 spectrofluorometer (Horiba Jobin Yvon). All measurements were performed with a Hellma 1.5 ml cuvette under stirring. The beads were suspended in a methanol : water mixture (1:3). Instrumental parameters were: polarizers in magic angle settings (55°), integration time 2 seconds, excitation and emission slit widths 3 nm and 4 nm, respectively. All spectra shown were corrected for the blank, dark and reference contributions as well as for instrumental spectral characteristics.

Fluorescence lifetime measurements of TentaGel beads

Lifetime measurements were performed on the Fluorolog tau-3 in lifetime mode. Ludox (silica particles in water) was used as the reference. The procedure for obtaining lifetime data was according to the manufacturer's guidelines. In short: excitation and emission slits settings optimised to obtain optimum signal from the bead sample. The measurement was performed with parameters set to: integration time 10 seconds, frequency range 20 – 200 MHz, with 10 frequencies chosen as measurement points, and number of averages per measurements 5 to 7 at various excitation and emission wavelengths, respectively which were determined from the excitation and emission spectra of the library beads. The data was fitted using Horiba's own "lifetime modelling" software.

Instrumental description of WIOBS instrument

The WIOBS1 instrument is based on a Leica DMI6000B inverted Fluorescence Widefield Microscope equipped with a sCMOS NEO (Andor) camera, a high precision motorized stage (C7018-9012K VEXTA Stepping Motor - Oriental Motor CO, Ltd. Tokyo, Japan), a coolLed pE-2 LED fluorescence illuminator (4 LED`s 400/490/550/635nm) connected by 2 liquid light-guides and a TransLED white light source for bright field imaging. The light path was equipped with HC PL APO 10x/0.40, HC Plan APO 20x/0.70 HCX PL APO 40x/1.25-0.75 oil Objective and 4 fluorescence filter sets (LF 405- Ex390/40 Em452/45 Di405, GFP 3035- Ex472/30 Em520/35 Di495, TRITC- Ex542/20 Em620/52 Di570, Cy5 4040- Ex628/40 Em692/40 Di660) for fluorescence excitation and emission separation. The Bead picker system was designed by Life Imaging Services GmbH (Basel, Switzerland) and consisted of a stiff and light Carbon arm mounted on a high speed (350mm/sec) high precision (provided by a linear encoder with sensor resolution

0.1µm & a bidirectional repeatability ±1µm), motorized z-axis (travel range 50 mm) Physik Instrumente M-683.2U4 (PI GmbH & Co. KG Karlsruhe/Germany) and controller PI C-867. The end of the arm carries a clear polycarbonate disc which slides up to medial kinematic end position defined by a magnetic stop block on a manual x-axis (medial-lateral mobility 32 cm) underneath the Leica S70 WD condenser in the light path. This disc with clear design allows a bright field illumination and connects an exchangeable capillary by a silicon adaptor to the high- precision syringe pump VersaPump3 (Kloehn Inc. USA Las Vegas, NV). The stable end position of the bead picker capillary can be manually fine-tuned in the field of view by two screws in horizontal X & Y direction.

All components of the WIOBS where controlled by MetaMorph Microscopy Automation and Image Analysis Software (Molecular Devices LLC. CA/USA Version 7.7.5.0 64bit -Image acquisition, processing and analysis package). For the integration of the Kloehn pump and the additional bead picker PI z-axis in the MetaMorph software the common shared communication port was used and automated data recording for a full 96-well microtiter plate was achieved by a combination of standard MetaMorph macros and recording of new journals. Finally image analyses, quantification and image processing like stitching and image subtraction routines were accomplished with the MetaMorph Image Analysis software package.

Fluorescence based on-bead screening assay

For fluorescence based on-bead screening 2 mg of beads were distributed into 1.5 ml Eppendorf tubes and the beads were allowed to swell for several minutes in 1 ml of PBS, 0.005% Tween 20. To further dissolve any bead clusters, the test tubes were repetitively (3 times 10 sec) sonicated. Subsequently, the tubes were spun down on a table-top centrifuge, the buffer was removed and the beads were treated with a fresh aliquot of buffer containing varying concentrations of dye-labeled streptavidin. The beads were then incubated on a shaker at RT for 6 hours. Prior to fluorescence imaging and bead picking, the incubation buffer containing the fluorescently labeled target protein was removed and the beads were washed at least 3 times with fresh buffer.

Cell-based on-bead screening assay

For cell based on bead screening, adherent cells (HeLa & Huh7) where detached by 8 min incubation with Cell Dissociation Buffer (enzyme free, PBS-based - Invitrogen) and prepared by centrifugation 2 min, 300 x g, followed by a careful re-suspension in FCS free medium at high cell concentration (1x10^6 cells/ml). 1 mg beads were briefly washed with PBS and then re-suspended in 1ml FCS free cell medium. The beads were mixed with 5x10^5 cells in a total volume of 750 µl in a 1,5ml Eppendorf tube. After incubation for 10min at 37°C on a rotator wheel, free floating cells where separated by taking of the supernatant from the sedimented

beads. 200µl fresh medium was then added and beads are transferred into wells of a 96-well microtiter plate and imaged immediately and after 24h incubation at 37°C.

Fluorescence imaging, bright-field imaging and image merging on WIOBS instrument

Typically, 96 well glass bottom plates (Greiner) were filled with 1 mg of beads to obtain a bead mono layer. Typical instrumental settings for fluorescence imaging using streptavidin conjugates were as follows: Alexa488: excitation 490nm, Led intensity 50%, exposure time 200ms; TAMRA: excitation 550nm, Led intensity 100%, exposure time 250ms; Alexa647: 635nm, Led intensity 100%, exposure time 350ms. Camera settings: frames to average 3; Center Quad.). For bright- field imaging with TransLed illumination (intensity 30-80%) exposure times were set between 2 to 20ms and automated illustration (colour depth, thresholds) was turned on. Whole 96well plate well illustration in 5x, 10x and 20x magnification was achieved by a three step (recording, stacking, merging) protocol.

Bead picking on WIOBS instrument

Bead picking was set up in a semi-automated way. The procedure contains a manually initiated sequence of standard MetaMorph software features and customized journals.

Alignment: Before each picking session the standard z positions (home/bottom/top/Origin) were manually defined as follows: The bead picking arm with attached capillary was manually moved to the kinematic end position underneath the condenser and the capillary end was aligned in the center of the image by moving the polycarbonate disc of the bead picking device in x-y direction. In order to automate the capillary z movement of the picking procedure four z positions are pre-defined in the MetaMorph Z position control software. A) Bottom position: this position is defined by moving the capillary into a well of the microtiter plate and lowered until the capillary touches the well bottom. B) home/picking position: This position is one third of the bead diameter above the bottom position (e.g. 100µm bead, 33µm above the bottom position). C) Top position: This position is used for intra well movement about 120µm above the beads for capillary x-y positioning. D) Origin position: capillary position for inter well and manual slider movement.

Bead picking: Whole well stitched images still contain pixel position information and with the MetaMorph function “move selected point to center of image” mouse click selected beads are positioned underneath the capillary. In the next step the capillary end incorporates the selected bead by moving the z axis to the picking position and Kloehn pump induced negative pressure sucks up (4µl volume) including the bead of interest. To dispense the bead the capillary is moved to the Origin position and a volume of 10 µl is dispensed by the Kloehn pump after manual trigger.

REFERENCES

[1] R. Kneller, Nature Reviews Drug Discovery 2010, 9, 867–882.
[2] J. Frearson, P. Wyatt, Expert Opin Drug Discov 2010, 5, 909–919.
[3] Y. Ho, A. Gruhler, A. Heilbut, G. D. Bader, L. Moore, S.-L. Adams, A. Millar, P. Taylor, K. Bennett, K. Boutilier, et al., Nature 2002, 415, 180–183.
[4] R. B. Jones, A. Gordus, J. A. Krall, G. MacBeath, Nature 2006, 439, 168–174.
[5] N. C. Meisner, M. Hintersteiner, V. Uhl, T. Weidemann, M. Schmied, H. Gstach, M. Auer, Curr.Opin.Chem.Biol. 2004, 8, 424–431.
[6] T. Kodadek, Nature Chemical Biology 2010, 6, 162–165.
[7] J. J. az-Mochon, L. Bialy, M. Bradley, Chemical Communications (Cambridge, United Kingdom) 2006, 3984–3986.
[8] T. Kodadek, Chemical Communications 2011, 47, 9757.
[9] K. S. Lam, S. E. Salmon, E. M. Hersh, V. J. Hruby, W. M. Kazmierski, R. J. Knapp, Nature (London, United Kingdom) 1991, 354, 82–84.
[10] M. C. Sweeney, X. Wang, J. Park, Y. Liu, D. Pei, Biochemistry 2006, 45, 14740–14748.
[11] A. R. Gocke, D. G. Udugamasooriya, C. T. Archer, J.-Y. Lee, T. Kodadek, Chem. Biol. (Cambridge, MA, U. S.) FIELD Full Journal Title:Chemistry & Biology (Cambridge, MA, United States) 2009, 16, 1133–1139.
[12] M. Auer, K. J. Moore, F. J. Meyer-Almes, R. Guenther, A. J. Pope, K. A. Stoeckli, Drug Discovery Today 1998, 3, 457–465.
[13] J. M. Astle, L. S. Simpson, Y. Huang, M. M. Reddy, R. Wilson, S. Connell, J. Wilson, T. Kodadek, Chem. Biol. (Cambridge, MA, U. S.) FIELD Full Journal Title:Chemistry & Biology (Cambridge, MA, United States) n.d., 17, 38–45.
[14] T. Liu, Z. Qian, Q. Xiao, D. Pei, ACS Comb. Sci. 2011, 13, 537–546.
[15] M. Hintersteiner, T. Kimmerlin, F. Kalthoff, M. Stoeckli, G. Garavel, J.-M. Seifert, N.-C. Meisner, V. Uhl, C. Buehler, T. Weidemann, et al., Chem. Biol. 2009, 16, 724–735.
[16] M. Hintersteiner, A. J. Knox, G. Mudd, M. Auer, Journal of Chemical Biology 2012, 5, 63–79.
[17] J. Townsend, A. Do, A. Lehman, S. Dixon, B. Sanii, K. S. Lam, Comb. Chem. High Throughput Screen. 2010, 13, 422–429.
[18] H. J. Olivos, K. Bachhawat-Sikder, T. Kodadek, Chembiochem 2003, 4, 1242–1245.
[19] K. Mueller, F. O. Gombert, U. Manning, F. Grossmueller, P. Graff, helene Zaegel, jean F. Zuber, F. Freuler, C. Tschopp, G. Baumann, Journal of Biological Chemistry 1996, 271, 16500–16505.
[20] R. Pulak, Methods Mol Biol 2006, 351, 275–286.
[21] M. M. Reddy, K. Bachhawat-Sikder, T. Kodadek, Chemistry & Biology 2004, 11, 1127–1137.
[22] M. Hintersteiner, M. Auer, Methods Appl. Fluoresc. 2013, 1, 017001.
[23] M. Hintersteiner, C. Buehler, V. Uhl, M. Schmied, J. Muller, K. Kottig, M. Auer, J. Comb. Chem. 2009, 11, 886–894.
[24] M. Hintersteiner, C. Buehler, M. Auer, ChemPhysChem 2012, 13, 3472–3480.
[25] H. Hong, H. Y. Lee, W. Kwak, J. Yoo, M.-H. Na, I. S. So, T.-H. Kwon, H.-S. Park, S. Huh, G. T. Oh, et al., J. Cell. Mol. Med. 2008, 12, 2003–2014.
[26] J. H. Lee, J. A. Engler, J. F. Collawn, B. A. Moore, Eur. J. Biochem. 2001, 268, 2004–2012.
[27] M. Hintersteiner, T. Kimmerlin, G. Garavel, T. Schindler, R. Bauer, N.-C. Meisner, J.-M. Seifert, V. Uhl, M. Auer, ChemBioChem 2009, 10, 994–998.

7 Literature

1. Johnstone RM, Adam M, Hammonds JR, Turbide C. Vesicle Formation during Reticulocyte Maturation. Association of plasma membrane activities with released vesicles (exosomes). *J Biol Chem* 1987;262(1):9412-9420.
2. Trams EG, Lauter CJ, Salem N, Heine U. Exfoliation of membrane ecto-enzymes in the form of micro-vesicles. *Biochim. Biophys. Acta* 1981;645(1):63-70. doi:10.1016/0005-2736(81)90512-5.
3. Pisitkun T, Johnstone R, Knepper MA. Discovery of urinary biomarkers. *Mol. Cell. Proteomics* 2006;5(10):1760-1771. doi:10.1074/mcp.R600004-MCP200.
4. Strauss K, Goebel C, Runz H, et al. Exosome secretion ameliorates lysosomal storage of cholesterol in Niemann-Pick type C disease. *J. Biol. Chem.* 2010;285(34):26279-88. doi:10.1074/jbc.M110.134775.
5. Raposo G, Nijman HW, Stoorvogel W, et al. B lymphocytes secrete antigen-presenting vesicles. *J. Exp. Med.* 1996;183(3):1161-1172. doi:10.1084/jem.183.3.1161.
6. Hawari FI, Rouhani FN, Cui X, et al. Release of full-length 55-kDa TNF receptor 1 in exosome-like vesicles: a mechanism for generation of soluble cytokine receptors. *Proc. Natl. Acad. Sci. U. S. A.* 2004;101(5):1297-302. doi:10.1073/pnas.0307981100.
7. Clayton A, Al-Taei S, Webber J, Mason MD, Tabi Z. Cancer exosomes express CD39 and CD73, which suppress T cells through adenosine production. *J. Immunol.* 2011;187(2):676-83. doi:10.4049/jimmunol.1003884.
8. Kim SH, Bianco NR, Shufesky WJ, Morelli AE, Robbins PD. MHC Class II+ Exosomes in Plasma Suppress Inflammation in an Antigen-Specific and Fas Ligand/Fas-Dependent Manner. *J. Immunol.* 2007;179(4):2235-2241. doi:10.4049/jimmunol.179.4.2235.
9. Karlsson M, Lundin S, Dahlgren U, Kahu H, Pettersson I, Telemo E. "Tolerosomes" are produced by intestinal epithelial cells. *Eur. J. Immunol.* 2001;31(10):2892-2900. doi:10.1002/1521-4141(2001010)31:10<2892::AID-IMMU2892>3.0.CO;2-I.
10. Pêche H, Heslan M, Usal C, Amigorena S, Cuturi MC. Presentation of donor major histocompatibility complex antigens by bone marrow dendritic cell-derived exosomes modulates allograft rejection. *Transplantation* 2003;76(10):1503-1510. doi:10.1097/01.TP.0000092494.75313.38.
11. Valenti R, Huber V, Iero M, Filipazzi P, Parmiani G, Rivoltini L. Tumor-released microvesicles as vehicles of immunosuppression. *Cancer Res.* 2007;67(7):2912-2915. doi:10.1158/0008-5472.CAN-07-0520.
12. Wolfers J, Lozier A, Raposo G, et al. Tumor-derived exosomes are a source of shared tumor rejection antigens for CTL cross-priming. *Nat. Med.* 2001;7(3):297-303. doi:10.1038/85438.
13. Iero M, Valenti R, Huber V, et al. Tumour-released exosomes and their implications in cancer immunity. *Cell Death Differ.* 2008;15(1):80-88. doi:10.1038/sj.cdd.4402237.
14. Kriebel PW, Barr VA, Rericha EC, Zhang G, Parent CA. Collective cell migration requires vesicular trafficking for chemoattractant delivery at the trailing edge. *J. Cell Biol.* 2008;183(5):949-961. doi:10.1083/jcb.200808105.
15. Janowska-Wieczorek A, Wysoczynski M, Kijowski J, et al. Microvesicles derived from activated platelets induce metastasis and angiogenesis in lung cancer. *Int. J. Cancer* 2005;113(5):752-760. doi:10.1002/ijc.20657.
16. Yu X, Riley T, Levine AJ. The regulation of the endosomal compartment by p53 the tumor suppressor gene. *FEBS J.* 2009;276(8):2201-2212. doi:10.1111/j.1742-4658.2009.06949.x.
17. Chivet M, Javalet C, Hemming F, et al. Exosomes as a novel way of interneuronal communication. *Biochem. Soc. Trans.* 2013;41(1):241-4. doi:10.1042/BST20120266.
18. Izquierdo-Useros N, Naranjo-Gómez M, Erkizia I, et al. HIV and mature dendritic cells: Trojan exosomes riding the Trojan horse? *PLoS Pathog.* 2010;6(3):e1000740. doi:10.1371/journal.ppat.1000740.
19. Fevrier B, Vilette D, Archer F, et al. Cells release prions in association with exosomes. *Proc. Natl. Acad. Sci. U. S. A.* 2004;101(26):9683-8. doi:10.1073/pnas.0308413101.

20. Zhuang X, Xiang X, Grizzle W, et al. Treatment of brain inflammatory diseases by delivering exosome encapsulated anti-inflammatory drugs from the nasal region to the brain. *Mol. Ther.* 2011;19(10):1769-79. doi:10.1038/mt.2011.164.
21. Alvarez-Erviti L, Seow Y, Yin H, Betts C, Lakhal S, Wood MJA. Delivery of siRNA to the mouse brain by systemic injection of targeted exosomes. *Nat. Biotechnol.* 2011;29(4):341-5. doi:10.1038/nbt.1807.
22. Higginbotham JN, Demory Beckler M, Gephart JD, et al. Amphiregulin exosomes increase cancer cell invasion. *Curr. Biol.* 2011;21(9):779-86. doi:10.1016/j.cub.2011.03.043.
23. Segura E, Guérin C, Hogg N, Amigorena S, Théry C. CD8+ dendritic cells use LFA-1 to capture MHC-peptide complexes from exosomes in vivo. *J. Immunol.* 2007;179(3):1489-1496. doi:10.4049/jimmunol.179.3.1489.
24. Chen X, Liang H, Zhang J, Zen K, Zhang C-Y. Secreted microRNAs: a new form of intercellular communication. *Trends Cell Biol.* 2012;22(3):125-32. doi:10.1016/j.tcb.2011.12.001.
25. Ratajczak J, Miekus K, Kucia M, et al. Embryonic stem cell-derived microvesicles reprogram hematopoietic progenitors: evidence for horizontal transfer of mRNA and protein delivery. *Leukemia* 2006;20(5):847-856. doi:10.1038/sj.leu.2404132.
26. Valadi H, Ekström K, Bossios A, Sjöstrand M, Lee JJ, Lötvall JO. Exosome-mediated transfer of mRNAs and microRNAs is a novel mechanism of genetic exchange between cells. *Nat. Cell Biol.* 2007;9(6):654-9. doi:10.1038/ncb1596.
27. Skog J, Würdinger T, van Rijn S, et al. Glioblastoma microvesicles transport RNA and proteins that promote tumour growth and provide diagnostic biomarkers. *Nat. Cell Biol.* 2008;10(12):1470-6. doi:10.1038/ncb1800.
28. Smalheiser NR. Exosomal transfer of proteins and RNAs at synapses in the nervous system. *Biol. Direct* 2007;2:35. doi:10.1186/1745-6150-2-35.
29. Lima LG, Leal AC, Vargas G, Porto-Carreiro I, Monteiro RQ. Intercellular transfer of tissue factor via the uptake of tumor-derived microvesicles. *Thromb. Res.* 2013;132(4):450-6. doi:10.1016/j.thromres.2013.07.026.
30. Balaj L, Lessard R, Dai L, et al. NIH Public Access. *Nat Commun* 2011;1(2):180. doi:10.1038/ncomms1180.Tumour.
31. Pegtel DM, Cosmopoulos K, Thorley-lawson DA, Eijndhoven MAJ Van. Functional delivery of viral miRNAs via exosomes. *Proc Natl Acad Sci* 2010;107(14):6328-33. doi:10.1073/pnas.0914843107.
32. Pegtel DM, Garde MDB Van De, Middeldorp JM. Viral miRNAs exploiting the endosomal – exosomal pathway for intercellular cross-talk and immune evasion. *BBA - Gene Regul. Mech.* 2011;1809(11-12):715-721. doi:10.1016/j.bbagrm.2011.08.002.
33. Kosaka N, Iguchi H, Yoshioka Y, Takeshita F, Matsuki Y, Ochiya T. Secretory mechanisms and intercellular transfer of microRNAs in living cells. *J. Biol. Chem.* 2010;285(23):17442-52. doi:10.1074/jbc.M110.107821.
34. Kosaka N, Ochiya T. Unraveling the Mystery of Cancer by Secretory microRNA: Horizontal microRNA Transfer between Living Cells. *Front. Genet.* 2011;2(January):97. doi:10.3389/fgene.2011.00097.
35. Umezu T, Ohyashiki K, Kuroda M, Ohyashiki JH. Leukemia cell to endothelial cell communication via exosomal miRNAs. *Oncogene* 2012;32(22):2747-55. doi:10.1038/onc.2012.295.
36. Mittelbrunn M, Gutiérrez-Vázquez C, Villarroya-Beltri C, et al. Unidirectional transfer of microRNA-loaded exosomes from T cells to antigen-presenting cells. *Nat. Commun.* 2011;2:282. doi:10.1038/ncomms1285.
37. Zhang Y, Liu D, Chen X, et al. Secreted Monocytic miR-150 Enhances Targeted Endothelial Cell Migration. *Mol Cell* 2010;39(1):133-144. doi:10.1016/j.molcel.2010.06.010.
38. Yang M, Chen J, Su F, et al. Microvesicles secreted by macrophages shuttle invasion-potentiating microRNAs into breast cancer cells. *Mol. Cancer* 2011;10(1):117. doi:10.1186/1476-4598-10-117.
39. Montecalvo A, Larregina AT, Shufesky WJ, et al. Mechanism of transfer of functional microRNAs between mouse dendritic cells via exosomes. *Blood* 2012;119(3):756-66. doi:10.1182/blood-2011-02-338004.The.

40. Hergenreider E, Heydt S, Tréguer K, et al. Atheroprotective communication between endothelial cells and smooth muscle cells through miRNAs. *Nat. Cell Biol.* 2012;14(3):249-56. doi:10.1038/ncb2441.
41. Dear JW, Street JM, Bailey MA. Urinary exosomes: a reservoir for biomarker discovery and potential mediators of intrarenal signalling. *Proteomics* 2013;13(10-11):1572-80. doi:10.1002/pmic.201200285.
42. Wahlgren J, Karlson TDL, Brisslert M, Sani FV. Plasma exosomes can deliver exogenous short interfering RNA to monocytes and lymphocytes. *Nucleic Acids Res.* 2012;40(17):e130. doi:10.1093/nar/gks463.
43. El-Andaloussi S, Lee Y, Lakhal-Littleton S, et al. Exosome-mediated delivery of siRNA in vitro and in vivo. *Nat. Protoc.* 2012;7(12):2112-26. doi:10.1038/nprot.2012.131.
44. Seow Y, Wood MJ. Biological gene delivery vehicles: beyond viral vectors. *Mol. Ther.* 2009;17(5):767-77. doi:10.1038/mt.2009.41.
45. Bellingham SA, Guo BB, Coleman BM, Hill AF. Exosomes: Vehicles for the Transfer of Toxic Proteins Associated with Neurodegenerative Diseases? *Front. Physiol.* 2012;3:124. doi:10.3389/fphys.2012.00124.
46. Emmanouilidou E, Melachroinou K, Roumeliotis T, et al. Cell-produced alpha-synuclein is secreted in a calcium-dependent manner by exosomes and impacts neuronal survival. *J. Neurosci.* 2010;30(20):6838-51. doi:10.1523/JNEUROSCI.5699-09.2010.
47. Danzer KM, Kranich LR, Ruf WP, et al. Exosomal cell-to-cell transmission of alpha synuclein oligomers. *Mol. Neurodegener.* 2012;7:42. doi:10.1186/1750-1326-7-42.
48. Saman S, Kim W, Raya M, et al. Exosome-associated tau is secreted in tauopathy models and is selectively phosphorylated in cerebrospinal fluid in early Alzheimer disease. *J. Biol. Chem.* 2012;287(6):3842-9. doi:10.1074/jbc.M111.277061.
49. Marhaba R, Klingbeil P, Nuebel T, Nazarenko I, Buechler MW, Zoeller M. CD44 and EpCAM : Cancer-Initiating Cell Markers. *Curr Mol Med* 2008;8(8):784-804.
50. Hood JL, San RS, Wickline S a. Exosomes released by melanoma cells prepare sentinel lymph nodes for tumor metastasis. *Cancer Res.* 2011;71(11):3792-801. doi:10.1158/0008-5472.CAN-10-4455.
51. Suetsugu A, Honma K, Saji S, Moriwaki H, Ochiya T, Hoffman RM. Imaging exosome transfer from breast cancer cells to stroma at metastatic sites in orthotopic nude-mouse models. *Adv. Drug Deliv. Rev.* 2013;65(3):383-90. doi:10.1016/j.addr.2012.08.007.
52. Martins VR, Dias MS, Hainaut P. Tumor-cell-derived microvesicles as carriers of molecular information in cancer. *Curr. Opin. Oncol.* 2013;25(1):66-75. doi:10.1097/CCO.0b013e32835b7c81.
53. Zöller M. Tetraspanins: push and pull in suppressing and promoting metastasis. *Nat. Rev. Cancer* 2009;9(1):40-55. doi:10.1038/nrc2543.
54. Marcilla A, Martin-Jaular L, Trelis M, et al. Extracellular vesicles in parasitic diseases. *J. Extracell. vesicles* 2014;3:25040. Available at: http://www.pubmedcentral.nih.gov/articlerender.fcgi?artid=4275648&tool=pmcentrez&rendertype=abstract. Accessed August 3, 2015.
55. Miao Y, Li G, Zhang X, Xu H, Abraham SN. A TRP Channel Senses Lysosome Neutralization by Pathogens to Trigger Their Expulsion. *Cell* 2015;161(6):1306-1319. doi:10.1016/j.cell.2015.05.009.
56. Théry C, Amigorena S, Raposo G, Clayton A. Isolation and characterization of exosomes from cell culture supernatants and biological fluids. *Curr. Protoc. Cell Biol.* 2006;Chapter 3:Unit 3.22. doi:10.1002/0471143030.cb0322s30.
57. Lane RE, Korbie D, Anderson W, Vaidyanathan R, Trau M. Analysis of exosome purification methods using a model liposome system and tunable-resistive pulse sensing. *Sci. Rep.* 2015;5:7639. doi:10.1038/srep07639.
58. Clayton A, Court J, Navabi H, et al. Analysis of antigen presenting cell derived exosomes, based on immuno-magnetic isolation and flow cytometry. *J. Immunol. Methods* 2001;247(1-2):163-74. Available at: http://www.ncbi.nlm.nih.gov/pubmed/11150547. Accessed August 2, 2015.
59. Mathivanan S, Simpson RJ. ExoCarta: A compendium of exosomal proteins and RNA. *Proteomics* 2009;9(21):4997-5000. doi:10.1002/pmic.200900351.

60. Kim D-K, Kang B, Kim OY, et al. EVpedia: an integrated database of high-throughput data for systemic analyses of extracellular vesicles. *J. Extracell. vesicles* 2013;2. doi:10.3402/jev.v2i0.20384.
61. Kalra H, Simpson RJ, Ji H, et al. Vesiclepedia: a compendium for extracellular vesicles with continuous community annotation. *PLoS Biol.* 2012;10(12):e1001450. doi:10.1371/journal.pbio.1001450.
62. Ostrowski M, Carmo NB, Krumeich S, et al. Rab27a and Rab27b control different steps of the exosome secretion pathway. *Nat. Cell Biol.* 2010;12(1):19-30; sup pp 1-13. doi:10.1038/ncb2000.
63. Alexander M, Hu R, Runtsch MC, et al. Exosome-delivered microRNAs modulate the inflammatory response to endotoxin. *Nat. Commun.* 2015;6:7321. doi:10.1038/ncomms8321.
64. Villarroya-Beltri C, Gutiérrez-Vázquez C, Sánchez-Madrid F, Mittelbrunn M. Analysis of microRNA and protein transfer by exosomes during an immune synapse. *Methods Mol. Biol.* 2013;1024:41-51. doi:10.1007/978-1-62703-453-1_4.
65. Smythies J, Edelstein L. Transsynaptic modality codes in the brain: possible involvement of synchronized spike timing, microRNAs, exosomes and epigenetic processes. *Front. Integr. Neurosci.* 2012;6:126. doi:10.3389/fnint.2012.00126.
66. Korkut C, Li Y, Koles K, et al. Regulation of postsynaptic retrograde signaling by presynaptic exosome release. *Neuron* 2013;77(6):1039-46. doi:10.1016/j.neuron.2013.01.013.
67. Arroyo JD, Chevillet JR, Kroh EM, et al. Argonaute2 complexes carry a population of circulating microRNAs independent of vesicles in human plasma. *Proc. Natl. Acad. Sci. U. S. A.* 2011;108(12):5003-8. doi:10.1073/pnas.1019055108.
68. Sun D, Zhuang X, Xiang X, et al. A novel nanoparticle drug delivery system: the anti-inflammatory activity of curcumin is enhanced when encapsulated in exosomes. *Mol. Ther.* 2010;18(9):1606-14. doi:10.1038/mt.2010.105.
69. Kooijmans S a a, Vader P, van Dommelen SM, van Solinge WW, Schiffelers RM. Exosome mimetics: a novel class of drug delivery systems. *Int. J. Nanomedicine* 2012;7:1525-41. doi:10.2147/IJN.S29661.
70. Alvarez-Erviti L, Seow Y, Yin H, Betts C, Lakhal S, Wood MJ a. Delivery of siRNA to the mouse brain by systemic injection of targeted exosomes. *Nat. Biotechnol.* 2011;29(4):341-5. doi:10.1038/nbt.1807.
71. Tian Y, Li S, Song J, et al. A doxorubicin delivery platform using engineered natural membrane vesicle exosomes for targeted tumor therapy. *Biomaterials* 2014;35(7):2383-90. doi:10.1016/j.biomaterials.2013.11.083.
72. Shimbo K, Miyaki S, Ishitobi H, et al. Exosome-formed synthetic microRNA-143 is transferred to osteosarcoma cells and inhibits their migration. *Biochem. Biophys. Res. Commun.* 2014;445(2):381-7. doi:10.1016/j.bbrc.2014.02.007.
73. Bruno S, Collino F, Deregibus MC, Grange C, Tetta C, Camussi G. Microvesicles derived from human bone marrow mesenchymal stem cells inhibit tumor growth. *Stem Cells Dev.* 2013;22(5):758-71. doi:10.1089/scd.2012.0304.
74. Kooijmans SAA, Stremersch S, Braeckmans K, et al. Electroporation-induced siRNA precipitation obscures the efficiency of siRNA loading into extracellular vesicles. *J. Control. Release* 2013;172(1):229-38. doi:10.1016/j.jconrel.2013.08.014.
75. Vader P, Breakefield XO, Wood MJA. Extracellular vesicles: emerging targets for cancer therapy. *Trends Mol. Med.* 2014;(14):000044-6. doi:10.1016/j.molmed.2014.03.002.
76. Van der Vlist EJ, Arkesteijn GJA, van de Lest CHA, Stoorvogel W, Nolte-'t Hoen ENM, Wauben MHM. CD4(+) T cell activation promotes the differential release of distinct populations of nanosized vesicles. *J. Extracell. vesicles* 2012;1. doi:10.3402/jev.v1i0.18364.
77. Nolte-'t Hoen ENM, van der Vlist EJ, Aalberts M, et al. Quantitative and qualitative flow cytometric analysis of nanosized cell-derived membrane vesicles. *Nanomedicine* 2012;8(5):712-20. doi:10.1016/j.nano.2011.09.006.
78. Morelli AE, Larregina AT, Shufesky WJ, et al. Endocytosis, intracellular sorting, and processing of exosomes by dendritic cells. *Blood* 2004;104(10):3257-66. doi:10.1182/blood-2004-03-0824.

79. Svensson K, Christianson H. Exosome uptake depends on ERK1/2-heat shock protein 27 signaling and lipid raft-mediated endocytosis negatively regulated by caveolin-1. *J. Biol. …* 2013;288(24):17713-24. doi:10.1074/jbc.M112.445403.
80. Nolte-'t Hoen ENM, van der Vlist EJ, de Boer-Brouwer M, Arkesteijn GJA, Stoorvogel W, Wauben MHM. Dynamics of dendritic cell-derived vesicles: high-resolution flow cytometric analysis of extracellular vesicle quantity and quality. *J. Leukoc. Biol.* 2013;93(3):395-402. doi:10.1189/jlb.0911480.
81. Franzen CA, Simms PE, Van Huis AF, Foreman KE, Kuo PC, Gupta GN. Characterization of uptake and internalization of exosomes by bladder cancer cells. *Biomed Res. Int.* 2014;2014:619829. doi:10.1155/2014/619829.
82. Tian T, Wang Y, Wang H, Zhu Z, Xiao Z. Visualizing of the cellular uptake and intracellular trafficking of exosomes by live-cell microscopy. *J. Cell. Biochem.* 2010;111(2):488-96. doi:10.1002/jcb.22733.
83. Chiba M, Kimura M, Asari S. Exosomes secreted from human colorectal cancer cell lines contain mRNAs, microRNAs and natural antisense RNAs, that can transfer into the human hepatoma HepG2 and lung cancer A549 cell lines. 2012;28(5):1551-8. doi:10.3892/or.2012.1967.
84. Feng D, Zhao W-L, Ye Y-Y, et al. Cellular internalization of exosomes occurs through phagocytosis. *Traffic* 2010;11(5):675-87. doi:10.1111/j.1600-0854.2010.01041.x.
85. Wallace PK, Tario JD, Fisher JL, Wallace SS, Ernstoff MS, Muirhead KA. Tracking antigen-driven responses by flow cytometry: monitoring proliferation by dye dilution. *Cytometry. A* 2008;73(11):1019-34. doi:10.1002/cyto.a.20619.
86. Escrevente C, Keller S, Altevogt P, Costa J. Interaction and uptake of exosomes by ovarian cancer cells. *BMC Cancer* 2011;11(1):108. doi:10.1186/1471-2407-11-108.
87. Tian T, Zhu Y-L, Hu F-H, Wang Y-Y, Huang N-P, Xiao Z-D. Dynamics of exosome internalization and trafficking. *J. Cell. Physiol.* 2013;228(7):1487-95. doi:10.1002/jcp.24304.
88. Dragovic RA, Southcombe JH, Tannetta DS, Redman CWG, Sargent IL. Multicolor flow cytometry and nanoparticle tracking analysis of extracellular vesicles in the plasma of normal pregnant and pre-eclamptic women. *Biol. Reprod.* 2013;89(6):151. doi:10.1095/biolreprod.113.113266.
89. De La Peña H, Madrigal JA, Rusakiewicz S, et al. Artificial exosomes as tools for basic and clinical immunology. *J. Immunol. Methods* 2009;344(2):121-32. doi:10.1016/j.jim.2009.03.011.
90. Fabbri M, Paone A, Calore F, Galli R, Gaudio E, Santhanam R. MicroRNAs bind to Toll-like receptors to induce prometastatic inflammatory response. 2012;109(31). doi:10.1073/pnas.1209414109/-/DCSupplemental.www.pnas.org/cgi/doi/10.1073/pnas.1209414109.
91. Théry C, Regnault a, Garin J, et al. Molecular characterization of dendritic cell-derived exosomes. Selective accumulation of the heat shock protein hsc73. *J. Cell Biol.* 1999;147(3):599-610. Available at: http://www.pubmedcentral.nih.gov/articlerender.fcgi?artid=2151184&tool=pmcentrez&rendertype=abstract.
92. Nolte-'t Hoen ENM, Buschow SI, Anderton SM, Stoorvogel W, Wauben MHM. Activated T cells recruit exosomes secreted by dendritic cells via LFA-1. *Blood* 2009;113(9):1977-81. doi:10.1182/blood-2008-08-174094.
93. Rana S, Zöller M. Exosome target cell selection and the importance of exosomal tetraspanins: a hypothesis. *Biochem. Soc. Trans.* 2011;39(2):559-62. doi:10.1042/BST0390559.
94. Rana S, Yue S, Stadel D, Zöller M. Toward tailored exosomes: the exosomal tetraspanin web contributes to target cell selection. *Int. J. Biochem. Cell Biol.* 2012;44(9):1574-84. doi:10.1016/j.biocel.2012.06.018.
95. Christianson HC, Svensson KJ, van Kuppevelt TH, Li J-P, Belting M. Cancer cell exosomes depend on cell-surface heparan sulfate proteoglycans for their internalization and functional activity. *Proc. Natl. Acad. Sci. U. S. A.* 2013;110(43):17380-5. doi:10.1073/pnas.1304266110.

96. Parolini I, Federici C, Raggi C, et al. Microenvironmental pH is a key factor for exosome traffic in tumor cells. *J. Biol. Chem.* 2009;284(49):34211-22. doi:10.1074/jbc.M109.041152.
97. Felicetti F, Parolini I, Bottero L, et al. Caveolin-1 tumor-promoting role in human melanoma. *Int. J. Cancer* 2009;125(7):1514-22. doi:10.1002/ijc.24451.
98. Del Conde I, Shrimpton CN, Thiagarajan P, López J a. Tissue-factor-bearing microvesicles arise from lipid rafts and fuse with activated platelets to initiate coagulation. *Blood* 2005;106(5):1604-11. doi:10.1182/blood-2004-03-1095.
99. Helmuth JA, Burckhardt CJ, Koumoutsakos P, Greber UF, Sbalzarini IF. A novel supervised trajectory segmentation algorithm identifies distinct types of human adenovirus motion in host cells. *J. Struct. Biol.* 2007;159(3):347-58. doi:10.1016/j.jsb.2007.04.003.
100. Tauro BJ, Greening DW, Mathias R a, Mathivanan S, Ji H, Simpson RJ. Two distinct populations of exosomes are released from LIM1863 colon carcinoma cell-derived organoids. *Mol. Cell. Proteomics* 2013;12(3):587-98. doi:10.1074/mcp.M112.021303.
101. Crescitelli R, Lässer C, Szabó TG, et al. Distinct RNA profiles in subpopulations of extracellular vesicles: apoptotic bodies, microvesicles and exosomes. *J. Extracell. vesicles* 2013;2:1-10. doi:10.3402/jev.v2i0.20677.
102. Martin K, Vilela M, Jeon NL, Danuser G, Pertz O. A growth factor-induced, spatially organizing cytoskeletal module enables rapid and persistent fibroblast migration. *Dev. Cell* 2014;30(6):701-16. doi:10.1016/j.devcel.2014.07.022.
103. Di Giorgio FP, Boulting GL, Bobrowicz S, Eggan KC. Human embryonic stem cell-derived motor neurons are sensitive to the toxic effect of glial cells carrying an ALS-causing mutation. *Cell Stem Cell* 2008;3(6):637-48. doi:10.1016/j.stem.2008.09.017.
104. Boulting GL, Kiskinis E, Croft GF, et al. A functionally characterized test set of human induced pluripotent stem cells. *Nat. Biotechnol.* 2011;29(3):279-86. doi:10.1038/nbt.1783.
105. Gibbings DJ, Ciaudo C, Erhardt M, Voinnet O. Multivesicular bodies associate with components of miRNA effector complexes and modulate miRNA activity. *Nat. Cell Biol.* 2009;11(9):1143-9. doi:10.1038/ncb1929.
106. Sherer NM, Lehmann MJ, Jimenez-Soto LF, et al. Visualization of retroviral replication in living cells reveals budding into multivesicular bodies. *Traffic* 2003;4(11):785-801. Available at: http://www.ncbi.nlm.nih.gov/pubmed/14617360.
107. Vidal M, Mangeat P, Hoekstra D. Aggregation reroutes molecules from a recycling to a vesicle-mediated secretion pathway during reticulocyte maturation. *J. Cell Sci.* 1997;110 (Pt 1:1867-77. Available at: http://www.ncbi.nlm.nih.gov/pubmed/9296387.
108. Théry C, Boussac M, Véron P, et al. Proteomic analysis of dendritic cell-derived exosomes: a secreted subcellular compartment distinct from apoptotic vesicles. *J. Immunol.* 2001;166(12):7309-18. Available at: http://www.ncbi.nlm.nih.gov/pubmed/11390481.
109. Skokos D, Panse S Le, Villa I, Peronet R, David B. Mast Cell-Dependent B and T Lymphocyte Activation Is Mediated by the Secretion of Immunologically Active Exosomes. 2013.
110. Michaloglou C, Lehmann W, Martin T, et al. The Tyrosine Phosphatase PTPN14 Is a Negative Regulator of YAP Activity. Languino LR, ed. *PLoS One* 2013;8(4):e61916. doi:10.1371/journal.pone.0061916.
111. Culbertson MJ, Williams JTB, Cheng WWL, et al. Numerical fluorescence correlation spectroscopy for the analysis of molecular dynamics under nonstandard conditions. *Anal. Chem.* 2007;79(11):4031-9. doi:10.1021/ac062013m.
112. Simons K, Sampaio JL, Schwudke D, et al. Fluorescence Techniques to Study Lipid Dynamics. 2013. doi:10.1101/cshperspect.a009803.
113. Schwille P. Fluorescence Correlation Spectroscopy and Its Potential for Intracellular Applications. 2001;34.
114. Bolte S, Cordelières FP. A guided tour into subcellular colocalization analysis in light microscopy. *J. Microsc.* 2006;224(Pt 3):213-32. doi:10.1111/j.1365-2818.2006.01706.x.
115. Rasband WS. ImageJ, U. S. National Institutes of Health, Bethesda, Maryland, USA, http://imagej.nih.gov/ij/.

116. Stalder L, Heusermann W, Sokol L, et al. The rough endoplasmatic reticulum is a central nucleation site of siRNA-mediated RNA silencing. *EMBO J.* 2013;32(8):1115-27. doi:10.1038/emboj.2013.52.
117. Baryza J, Bowman K, Geall A, et al. Lipids, lipid compositions, and methods of using them. *US 2014/0309277 A1* 2014:191.
118. Li J, Lee Y, Johansson HJ, et al. Serum-free culture alters the quantity and protein composition of neuroblastoma-derived extracellular vesicles. *J. Extracell. Vesicles* 2015;4. Available at: http://www.journalofextracellularvesicles.net/index.php/jev/article/view/26883/xml_14. Accessed August 9, 2015.
119. Clayton A, Turkes A, Dewitt S, Steadman R, Mason MD, Hallett MB. Adhesion and signaling by B cell-derived exosomes: the role of integrins. 2004;22(2):1-22.
120. Luga V, Zhang L, Viloria-Petit AM, et al. Exosomes mediate stromal mobilization of autocrine Wnt-PCP signaling in breast cancer cell migration. *Cell* 2012;151(7):1542-56. doi:10.1016/j.cell.2012.11.024.
121. Chevillet JR, Kang Q, Ruf IK, et al. Quantitative and stoichiometric analysis of the microRNA content of exosomes. 2014;111(41). doi:10.1073/pnas.1408301111.
122. Li S, Liu L, Zhuang X, et al. MicroRNAs inhibit the translation of target mRNAs on the endoplasmic reticulum in Arabidopsis. *Cell* 2013;153(3):562-74. doi:10.1016/j.cell.2013.04.005.
123. Izquierdo-Useros N, Naranjo-Gómez M, Archer J, et al. Capture and transfer of HIV-1 particles by mature dendritic cells converges with the exosome-dissemination pathway. *Blood* 2009;113(12):2732-41. doi:10.1182/blood-2008-05-158642.
124. Gould SJ, Booth AM, Hildreth JEK. The Trojan exosome hypothesis. *Proc. Natl. Acad. Sci. U. S. A.* 2003;100(19):10592-7. doi:10.1073/pnas.1831413100.
125. Vella LJ, Sharples RA, Lawson VA, Masters CL, Cappai R, Hill AF. Packaging of prions into exosomes is associated with a novel pathway of PrP processing. 2007;(March):582-590. doi:10.1002/path.